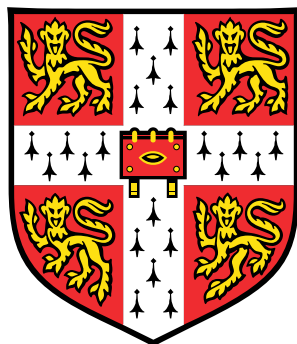


# Multi-scale multiphase modelling of granular flows



**Krishna Kumar Soundararajan**

Department of Engineering  
University of Cambridge

This dissertation is submitted for the degree of

*Doctor of Philosophy*



## Abstract

Geophysical hazards usually involve flow of dense granular solids and water as a single-phase system. Understanding the mechanics of granular flow is of particular importance in predicting the run-out behaviour of debris flows. The dynamics of a homogeneous granular flow involve three distinct scales: the microscopic scale, the meso-scale, and the macroscopic scale. Conventionally, granular flows are modelled as a continuum because they exhibit many collective phenomena. Recent studies, however, suggest that a continuum law may be unable to capture the effect of inhomogeneities at the grain scale level, such as orientation of force chains, which are micro-structural effects. Discrete element methods (DEM) are capable of simulating these micro-structural effects, however they are computationally expensive. In the present study, a multi-scale approach is adopted, using both DEM and continuum techniques, to better understand the rheology of granular flows and the limitations of continuum models.

The collapse of a granular column on a horizontal surface is a simple case of granular flow, however a proper model that describes the flow dynamics is still lacking. In the present study, the generalised interpolation material point method (GIMPM), a hybrid Eulerian – Lagrangian approach, is implemented with Mohr-Coloumb failure criterion to describe the continuum behaviour of granular flows. The granular column collapse is also simulated using DEM to understand the micro-mechanics of the flow. The limitations of MPM in modelling the flow dynamics are studied by inspecting the energy dissipation mechanisms. The lack of collisional dissipation in the Mohr-Coloumb model results in longer run-out distances for granular flows in dilute regimes (where the mean pressure is low). However, the model is able to capture the rheology of dense granular flows, such as run-out evolution of slopes subjected to impact loading, where the inertial number  $I < 0.1$ .

The initiation and propagation of submarine flows depend mainly on the slope, density, and quantity of the material destabilised. Certain macroscopic models are able to capture simple mechanical behaviours, however the complex physical mechanisms that occur at the grain scale, such as hydrodynamic instabilities and formation of clusters, have largely been ignored. In order to describe the mechanism of submarine granular flows, it is important to consider both the dynamics of the solid phase and the role of the ambient fluid. In the present study, a two-dimensional coupled Lattice Boltzmann LBM – DEM technique is developed

to understand the micro-scale rheology of granular flows in fluid. Parametric analyses are performed to assess the influence of initial configuration, permeability, and slope of the inclined plane on the flow. The effect of hydrodynamic forces on the run-out evolution is analysed by comparing the energy dissipation and flow evolution between dry and immersed conditions.

# Table of contents

<b>Table of contents</b>	<b>5</b>
<b>List of figures</b>	<b>9</b>
<b>List of tables</b>	<b>15</b>
<b>Nomenclature</b>	<b>15</b>
<b>1 Introduction</b>	<b>17</b>
1.1 Introduction . . . . .	17
1.2 Objectives . . . . .	22
1.3 Thesis outline . . . . .	23
<b>2 Granular flows</b>	<b>25</b>
2.1 Introduction . . . . .	25
2.2 Modelling the granular flows . . . . .	27
2.2.1 Kinetic theory . . . . .	28
2.2.2 Shallow-water approximation . . . . .	29
2.2.3 Rheology . . . . .	31
2.3 Studies on granular flows . . . . .	36
2.3.1 Granular column collapse . . . . .	37
2.3.2 Flow on inclined plane . . . . .	42
2.3.3 Saturated and submerged granular flows . . . . .	44
2.4 Summary . . . . .	45
<b>3 Numerical modelling of granular flows</b>	<b>47</b>
3.1 Introduction . . . . .	47
3.2 Continuum modelling of granular flows . . . . .	47
3.3 Material Point Method (MPM) . . . . .	50

---

3.3.1	Discrete formulation of the governing equations . . . . .	52
3.3.2	Boundary conditions . . . . .	54
3.3.3	Solution scheme . . . . .	56
3.4	Particulate modelling of granular flows . . . . .	60
3.4.1	Introduction . . . . .	60
3.5	Discrete Element Method . . . . .	61
3.5.1	The Forces . . . . .	63
3.5.2	Numerical algorithm and integration scheme . . . . .	67
3.5.3	Boundary conditions . . . . .	74
3.5.4	Particle Assembling Methods . . . . .	76
3.5.5	Voronoi Tesselation . . . . .	79
<b>4</b>	<b>Multi-scale modelling of dry granular flows</b>	<b>81</b>
4.1	Introduction . . . . .	81
4.2	Granular column collapse . . . . .	82
4.2.1	Numerical set-up . . . . .	83
4.2.2	Deposit morphology . . . . .	87
4.2.3	Flow evolution and internal flow structure . . . . .	90
4.2.4	Energy dissipation mechanism . . . . .	98
4.2.5	Role of initial grain properties . . . . .	106
4.3	Slopes subjected to impact loading . . . . .	112
4.3.1	Numerical set-up . . . . .	112
4.3.2	Evolution of pile geometry and run-out . . . . .	115
4.3.3	Decay of kinetic energy . . . . .	120
4.3.4	Effect of friction . . . . .	126
4.3.5	Effect of mesh size and number of material points per cell . . . . .	128
4.3.6	Comparison with granular column collapse . . . . .	139
4.4	Summary . . . . .	139
<b>5</b>	<b>Numerical modelling of fluid–grain interactions</b>	<b>143</b>
5.1	Fluid simulation using lattice Boltzmann method . . . . .	143
5.1.1	Formulation . . . . .	145
5.1.2	Lattice Boltzmann - Multi-Relaxation Time (LBM-MRT) . . . . .	149
5.1.3	Boundary conditions . . . . .	152
5.2	Validation of the lattice Boltzmann method . . . . .	155
5.3	Turbulence in lattice Boltzmann method . . . . .	159
5.4	Coupled LBM and DEM for fluid-grain interactions . . . . .	162

5.4.1	Draft, kiss and tumbling: Sedimentation of two grains . . . . .	169
5.5	GP-GPU Implementation . . . . .	172
<b>6</b>	<b>Underwater granular flows</b>	<b>179</b>
6.1	Introduction . . . . .	179
6.2	Granular collapse in fluid . . . . .	180
6.2.1	LBM-DEM Coupling . . . . .	180
6.2.2	Permeability . . . . .	181
6.2.3	Collapse in fluid: Flow evolution . . . . .	185
6.2.4	Effect of permeability . . . . .	190
6.2.5	Effect of initial packing density . . . . .	207
6.3	Submarine granular flows down incline plane . . . . .	207
6.3.1	Effect of initial density . . . . .	216
6.3.2	Effect of permeability . . . . .	224
6.3.3	Tall columns . . . . .	235
6.3.4	Summary . . . . .	235
<b>7</b>	<b>Conclusions and future work</b>	<b>237</b>
7.1	Introduction . . . . .	237
7.2	Recommendations for future research . . . . .	237
7.2.1	Multi-scale simulations of granular flows . . . . .	238
7.2.2	Developments in Material Point Method . . . . .	239
7.2.3	The I rheology . . . . .	240
7.2.4	Homogenization of granular flows . . . . .	241
7.2.5	Slope subjected to impact . . . . .	242
<b>References</b>		<b>243</b>



# List of figures

1.1	Debris slide in Las Colinas, El Salvador, January 2001 . . . . .	19
1.2	The extent of the Storegga landslide . . . . .	21
2.1	Particle size range and their predominant characteristics . . . . .	26
2.2	Illustration of the Savage-Hutter model . . . . .	30
2.3	Plane stress at a constant pressure . . . . .	32
2.4	Dependence of frictional coefficient $\mu$ with dimensionless shear rate $I$ . . . . .	33
2.5	Variation of dimensionless parameters for various flow regimes . . . . .	34
3.1	Multi-scale modelling of granular materials . . . . .	48
3.2	Typical discretization of a domain in MPM . . . . .	51
3.3	Cell crossing noise . . . . .	55
3.4	Illustration of the MPM algorithm for particles occupying a single cell in the background grid . . . . .	58
3.5	Calculation of normal force . . . . .	64
3.6	Verlet list . . . . .	69
3.7	Checking the validity of Verlet list . . . . .	71
3.8	Verlet integration scheme . . . . .	73
3.9	A 2D simulation cell $\omega$ with its basis vectors in an absolute frame . . . . .	75
3.10	(a)Ballistic deposition: first contact followed by steepest descent; (b) small-scale periodic sample ( <a href="#">Radjai and Dubois, 2011</a> ) . . . . .	78
3.11	Voronoi tessellation to average bulk properties . . . . .	79
4.1	Schematic of experimental configuration for 2-D collapse in a rectangular channel, ( <a href="#">Lajeunesse et al., 2004</a> ) . . . . .	83
4.2	DEM sample characteristics . . . . .	85
4.3	Periodic shear test . . . . .	88
4.4	Normalised final run-out distance for columns with different initial aspect ratios	90
4.5	Normalised final collapse height for columns with different initial aspect ratios	91

---

4.6	Velocity profile of a granular column collapse ( $a = 0.4$ & $t = \tau_c$ ) . . . . .	93
4.7	Velocity profile of a granular column collapse ( $a = 0.4$ & $t = 3 \times \tau_c$ ) . . . . .	94
4.8	Velocity profile of a granular column collapse ( $a = 6$ & $t = \tau_c$ ) . . . . .	96
4.9	Velocity profile of a granular column collapse ( $a = 6$ & $t = 3 \times \tau_c$ ) . . . . .	97
4.10	Flow evolution of granular column collapse . . . . .	99
4.11	Scheme of collapse for small aspect ratio columns. The amount of energy $\delta E$ lost in the process can be evaluated from the run-out distance $L_f - L_0$ (after <a href="#">Staron and Hinch (2007)</a> ). . . . .	100
4.12	Energy evolution of granular column collapse . . . . .	103
4.13	Flow evolution of granular column collapse using $\mu(I)$ rheology . . . . .	104
4.14	Evolution of inertial number with time for columns with $a = 0.4$ and $a = 6$ . .	105
4.15	Effect of density on run-out evolution $a = 0.8$ . . . . .	107
4.16	Evolution of local packing density $a = 0.8$ . . . . .	108
4.17	Effect of density on energy evolution $a = 0.8$ . . . . .	109
4.18	Effect of density on run-out evolution $a = 0.8$ (poly-dispersity ‘r’ = 6) . . . .	110
4.19	Snapshots of granular column collapse $t = 6\tau_c$ . . . . .	110
4.20	Effect of density on energy and packing fraction evolution $a = 0.8$ (poly-dispersity ‘r’ = 6) . . . . .	111
4.21	Effect of density on run-out behaviour and energy evolution $a = 0.6$ . . . . .	113
4.22	Initial geometry and dimensions of the pile . . . . .	114
4.23	Periodic shear test using CD ( <a href="#">Mutabaruka, 2013</a> ). . . . .	115
4.24	MPM simulation of the initial stages of granular pile subjected to a gradient impact energy. . . . .	116
4.25	CD simulation of the initial stages of granular pile subjected to a gradient impact energy. ( <a href="#">Mutabaruka, 2013</a> ). . . . .	117
4.26	Run-out behaviour of a pile subjected a gradient impact energy . . . . .	119
4.27	Evolution of kinetic energy with time (MPM) . . . . .	121
4.28	Evolution of normalised kinetic energy with normalised time . . . . .	122
4.29	Evolution of packing density with time $E_0 = 152mgd$ (DEM) . . . . .	122
4.30	Evolution of vertical and horizontal kinetic energy with time (MPM) . . . . .	123
4.31	Evolution of kinetic energy in the $x$ component of the velocity field normalized by the available kinetic energy at the end of the transient as a function of time elapsed since the same instant (MPM). . . . .	124
4.32	Evolution of kinetic energy in the $x$ component of the velocity field normalized by the available kinetic energy at the end of the transient as a function of normalized time (MPM). . . . .	125

---

4.33	Decay time and run-out time as a function of the normalised kinetic energy $E_{kx0}$ .	127
4.34	Effect of friction on the run-out behaviour . . . . .	129
4.35	Snapshots of MPM simulations of the evolution of granular pile subjected to a gradient impact energy $E_0 = 61 \text{ mgd}$ . . . . .	130
4.36	Snapshots of DEM simulations of the evolution of granular pile subjected to a gradient impact energy $E_0 = 61 \text{ mgd}$ . . . . .	131
4.37	Effect of input velocity distribution on the run-out behaviour . . . . .	132
4.38	Evolution of run-out with time for varying material points per cell. . . . .	134
4.39	Effect of number of material points on cell on the run-out behaviour $E_0 = 12.7 \text{ mgd}$ . Velocity profile (m/s) of granular pile subjected to gradient impact loading. . . . .	135
4.40	Effect of number of material points on cell on the run-out behaviour $E_0 = 152 \text{ mgd}$ . Velocity profile (m/s) of granular pile subjected to gradient impact loading. . . . .	136
4.41	Evolution of kinetic with time for varying material points per cell . . . . .	137
4.42	Evolution of run-out and duration of flow for varying material points per cell. . . . .	138
4.43	Comparison of column collapse with slope subjected to impact loading. . . . .	140
5.1	The lattice Boltzmann discretisation and D2Q9 scheme . . . . .	145
5.2	Illustration of the streaming process on a <i>D2Q9</i> lattice . . . . .	147
5.3	Illustration of the collision process on a <i>D2Q9</i> lattice . . . . .	148
5.4	Half-way bounce back algorithm for the <i>D2Q9</i> model . . . . .	153
5.5	Velocity profile: LBM Simulation of a laminar flow through a channel. . . . .	156
5.6	Finite Volume mesh used in the CFD analysis of laminar flow through a channel.	157
5.7	Velocity profile: CFD analysis of laminar flow through a channel. . . . .	157
5.8	Development of the Poiseuille velocity profile in time: comparison between LBM simulation, CFD simulation and the analytical solution. Time is made dimensionless by $H/U_0$ . . . . .	158
5.9	LBM simulation of velocity profile for a laminar flow through a pipe with an obstacle at $L/4$ . . . . .	159
5.10	CFD simulation of velocity contour for a laminar flow through a pipe with an obstacle at $L/4$ . . . . .	159
5.11	LBM and CFD simulation of a flow around an obstacle. . . . .	160
5.12	Kármán vortex street . . . . .	163
5.13	Bounce back boundaries for different values of $\delta$ . . . . .	167
5.14	Time series of draft, kiss and tumble of two grains during sedimentation in a viscous fluid. . . . .	170

5.15 Time history of two circular grains during sedimentation. . . . .	171
5.16 Schematics of a heterogeneous CPU/GPU system. . . . .	173
5.17 GPU scalability with increase in LBM nodes . . . . .	177
6.1 Underwater granular collapse set-up. . . . .	181
6.2 Discretisation of solid grains in LBM grid. Shows the step-wise representation of circular disks in the lattice. . . . .	182
6.3 Schematic representation of the hydrodynamic radius in LBM-DEM computation	183
6.4 Evaluation of the horizontal permeability for a hydrodynamic radius of $0.7R$ . .	184
6.5 Variation of the mean flow velocity with pressure gradient for different hydrodynamic radius. . . . .	184
6.6 Relation between permeability and porosity for different hydrodynamic radius and comparison with the analytical solution. . . . .	186
6.7 Flow evolution of a granular column collapse in fluid ( $a = 0.4$ ). Shows the velocity profile of fluid due to interaction with the grains (red - higher velocity).	188
6.8 Evolution of run-out for a column collapse in fluid ( $a = 0.4$ ) . . . . .	189
6.9 Evolution of height with time for a column collapse in fluid ( $a = 0.4$ ) . . . . .	189
6.10 Evolution of kinetic energies with time for a granular column collapse in fluid ( $a = 0.4$ ) . . . . .	191
6.11 Evolution of the potential energy with time for a granular column collapse in fluid ( $a = 0.4$ ) . . . . .	192
6.11 Flow evolution of a granular column collapse in fluid ( $a = 4$ ). Shows the velocity profile of fluid due to interaction with the grains (red - higher velocity).	194
6.12 Evolution of run-out for a column collapse in fluid ( $a = 4$ ) . . . . .	195
6.13 Evolution of height with time for a column collapse in fluid ( $a = 4$ ) . . . . .	195
6.14 Evolution of kinetic energies with time for a granular column collapse in fluid ( $a = 4$ ) . . . . .	196
6.15 Evolution of the potential energy with time for a granular column collapse in fluid ( $a = 4$ ) . . . . .	197
6.16 Normalised final run-out distance for columns with different initial aspect ratios. Comparison of dry and submerged granular column collapse. . . . .	198
6.17 Normalised final collapse height for columns with different initial aspect ratios. Comparison of dry and submerged granular column collapse. . . . .	199
6.18 Effect of permeability on the deposit morphology of a granular column collapse in fluid ( $a = 0.8$ ) . . . . .	200
6.19 Effect of permeability on the evolution of run-out for a column collapse in fluid ( $a = 0.8$ ) . . . . .	201

6.20 Effect of permeability on the evolution of kinetic energies with time for a granular column collapse in fluid ( $a = 0.8$ ) . . . . .	202
6.21 Effect of permeability on the evolution of the potential energy with time for a granular column collapse in fluid ( $a = 0.8$ ) . . . . .	203
6.22 Effect of permeability on the evolution of packing density for a granular column collapse in fluid ( $a = 0.8$ & dense initial packing) . . . . .	204
6.23 Normalised final run-out distance for columns with different initial aspect ratios. Comparison of dry and submerged granular column collapse for different hydrodynamic radius ( $0.7R$ , $0.8R$ and $0.9R$ ). . . . .	205
6.24 Normalised final run-out distance for columns as a function of peak kinetic energy. Comparison of dry and submerged granular column collapse for different hydrodynamic radius ( $0.7R$ , $0.8R$ and $0.9R$ ). . . . .	206
6.25 Effect of permeability on the evolution of run-out for a column collapse in fluid ( $a = 0.8$ & loose packing) . . . . .	207
6.26 Effect of permeability on the excess pore water pressure distribution for a granular column collapse in fluid ( $a = 0.8$ & loose packing) at $t = \tau_c$ . . . . .	208
6.27 Effect of permeability on the excess pore water pressure distribution for a granular column collapse in fluid ( $a = 0.8$ & loose packing) at $t = 2\tau_c$ . . . . .	209
6.28 Particle tracking of the deposit morphology for a granular column collapse in fluid ( $a = 0.8$ & loose packing), influence of permeability . . . . .	210
6.29 Effect of permeability on the normalised effective stress for loose initial packing at $t = \tau_c$ . . . . .	211
6.30 Effect of permeability on the evolution of kinetic energies with time for a granular column collapse in fluid ( $a = 0.8$ & loose packing) . . . . .	212
6.31 Effect of permeability on the evolution of the potential energy with time for a granular column collapse in fluid ( $a = 0.8$ & loose packing) . . . . .	213
6.32 Effect of permeability on the evolution of packing density for a granular column collapse in fluid ( $a = 0.8$ & loose initial packing) . . . . .	214
6.33 Effect of initial density on the deposit morphology for a granular column collapse in fluid ( $a = 0.8$ ). Dense vs loose initial packing fraction. . . . .	215
6.34 Evolution of packing fraction at $t = \tau_c$ for dense and loose initial packing fraction.	215
6.35 Evolution of run-out with time (dense) . . . . .	217
6.36 Evolution of Kinetic Energy with time (dense case) . . . . .	218
6.37 Flow morphology at critical time for different slope angles (dense) . . . . .	219
6.38 Evolution of run-out with time (loose) . . . . .	220
6.39 Flow morphology at critical time for different slope angles (loose) . . . . .	221

6.40 Evolution of Kinetic Energy with time (loose) . . . . .	222
6.41 Evolution of packing density with time . . . . .	223
6.42 Evolution of run-out with time for different permeability (loose slope 5°) . . .	225
6.43 Evolution of height with time for different permeability (loose slope 5°) . . .	226
6.44 Evolution of Kinetic Energy with time for different permeability (loose slope 5°)	227
6.45 Evolution of packing density with time for different permeability (loose slope 5°)	228
6.46 Flow evolution of a granular column collapse in fluid ( $a = 6$ ) on a horizontal surface . . . . .	229
6.46 Flow evolution of a granular column collapse in fluid ( $a = 6$ ) on a slope of 5°. Shows the velocity profile of fluid due to interaction with the grains (red - higher velocity). . . . .	231
6.47 Evolution of run-out for a column collapse in fluid ( $a = 6$ ) on a slope of 5° . .	232
6.48 Evolution of height with time for a column collapse in fluid ( $a = 6$ ) on a slope of 5° . . . . .	232
6.49 Evolution of the kinetic and the potential energy with time for a granular column collapse in fluid ( $a = 6$ ) on a slope of 5° . . . . .	233
6.50 Evolution of the kinetic energies with time for a granular column collapse in fluid ( $a = 6$ ) on a slope of 5° . . . . .	234
6.51 Packing density of a granular column collapse in fluid ( $a = 6$ ) on a slope of 5°.	235
7.1 Identification of dynamic solid-fluid boundary . . . . .	240

# List of tables

4.1	Material properties of glass ballotini (Lajeunesse et al., 2004) . . . . .	84
4.2	Micro-mechanical parameters used in DEM simulations . . . . .	86
4.3	Parameters used in continuum simulations . . . . .	88
5.1	LBM parameters used in simulating laminar flow through a circular pipe. . .	155
5.2	Computed Strouhal number for fluid flows with different Reynolds number .	164
5.3	GPU vs CPU parallelisation . . . . .	176



# Chapter 1

## Introduction

### 1.1 Introduction

Avalanches, debris flows, and landslides are geophysical hazards which involve rapid mass movement of granular solids, water and air as a single phase system. The presence of water in a granular flow distinguishes '*mud and debris flow*' from '*granular avalanches*'. Debris flow is a rapid mass movement of liquefied, unconsolidated, saturated soil. The speed of the debris flow varies from 3 mph to 50 mph in extreme cases, transporting 100 to 100,000 cubic meters of unconsolidated sediments down very steep slopes. Figure. 1.1 shows the debris flow that occurred during an earthquake-triggered landslide in Las Colinas, El Salvador. Submarine landslides are marine landslides that transport sediments across continental shelves. Unlike a debris flow, the submarine landslides can occur on slopes as flat as  $1^{\circ}$  and can reach speeds of 50 mph. figure 1.2 shows the Storegga Landslide, the largest recorded continental slope failure, which struck off the coast of central Norway, transporting materials over 300 miles ([Ward and Day, 2002](#)). Granular avalanches, debris flow and submarine landslides cause significant damage to life and property. Globally, landslides cause billions of pounds in damage, and thousands of deaths and injuries each year. In July 2011, at least 32 people were killed in a debris flow induced by a rainfall-triggered landslide in South Korea (Source: BBC, 2011). Understanding the triggering mechanism and the granular flow process provides an insight into the force and velocity distribution in a granular flow, enabling us to design appropriate defensive measures.

Granular flows have been extensively studied during the past two decades through experimental and numerical simulations ([Jaeger et al., 1996](#)). In most cases, granular flows exhibit three distinct regimes: the slow quasi-static regime, a dilute collisional regime and an intermediate regime. Kinetic theory ([Jenkins and Savage, 1983; Savage and Jeffrey, 1981](#)) which assumes binary collision between particles, captures the rapid-collisional regime, but

1 is incapable of predicting the dense quasi-static behaviour. By drawing a simple analogy  
2 from fluid dynamics one can model granular flows as non-Newtonian fluids using a variant  
3 of the Navier-Stokes equation; one such approach is the depth-averaged shallow water equa-  
4 tion ([Savage and Hutter, 1991](#)), which has been applied to solve granular flow dynamics with  
5 a reasonable amount of success. However, the basic assumption of neglecting the effect of  
6 vertical acceleration restricts the approach from describing the triggering mechanism, in which  
7 vertical acceleration plays a significant role. The dynamics of a homogeneous granular flow  
8 involve at least three distinct scales: the *microscopic scale* which is characterized by contact  
9 between particles, the *meso-scale* which represents micro-structural effects such as particle  
10 rearrangement, and the *macroscopic scale*. A continuum description of granular flows is  
11 incapable of revealing inhomogeneities at particle level, such as force chains, which are purely  
12 due to micro-structural effects. Non-trivial relations have been found between the run-out  
13 distance and the initial aspect ratio of a granular column ([Lajeunesse et al., 2005](#); [Lube et al.,](#)  
14 [2005](#); ?). Simple mathematical models based on conservation of horizontal momentum capture  
15 the scaling laws of the final deposit, but fail to describe the initial transition regime. Rheology  
16 is concerned with describing the mechanical behaviour of those materials which cannot be  
17 described using classical theories, by establishing an empirical relation between deformations  
18 and stresses. Recently, [Midi \(2004\)](#) proposed a new rheology based on extensive experimental  
19 and numerical investigation on gravity-driven dry granular flows. The spreading dynamics  
20 are found to be similar for the continuum and particle approaches, however the rheology falls  
21 short in predicting the run-out distance for steeper slopes and in the transition regime where  
22 the shear-rate effect diminishes. The flow of granular materials in a fluid remains largely  
23 unexplored.

24 Geophysical hazards usually involve multi-phase interactions. The momentum transfer  
25 between the discrete and continuous phases significantly affects the dynamics of the flow.  
26 Certain macroscopic models were unable to capture the complex physical mechanisms occurring  
27 at the particle scale, i.e. the hydrodynamic instabilities, formation of clusters, collapse, and  
28 transport phenomena. In order to describe the mechanism of multi-phase granular flows, it is  
29 important to consider both the dynamics of the solid phase and the role of the ambient fluid.  
30 Most models which simulate submarine landslides assume a single homogeneous grain-fluid  
31 mixture governed by a non-Newtonian fluid behaviour ([Denlinger and Iverson, 2001](#); [Iverson,](#)  
32 [2000](#)). Although successful in accounting for the general phenomenology on analytical grounds,  
33 such models fail to capture certain phenomena such as porosity gradient and fluid-induced  
34 size-segregation. Moreover, application of these models involves additional assumptions about  
35 the boundary/interface between the grains and the fluid, and the transition between high and  
36 low shear stresses. The  $\mu(I)$  rheology is found to capture the dense submarine granular flows,



Figure 1.1 Initiation, channelling, spreading and deposition of debris slide in Las Colinas, El Salvador, January 2001. The debris flow buried as many as 500 homes. (Source: USGS report on '*Landslides in Central America*', 2001)

if the inertial time scale in the rheology is replaced with a viscous time scale. However, the transition to the quasi-static regime where the shear rate vanishes is not captured by the simple model. The flow threshold or the hysteresis characterizing the flow or no-flow condition is also not correctly captured by the model. When the scale of the system is larger than the size of the structure, a simple rheology is expected to capture the overall flow behaviour, however the size of the correlated motion is of the same size as the system, causing difficulties in modelling the flow behaviour. Hence, it is essential to study the behaviour of granular flows at various scales, i.e. microscopic, meso-scale and continuum-scale levels, in order to develop a constitutive model that captures the entire flow process.

Typical continuum laws are only used when there is a strong separation of scales between the micro-scale and the macro-scale sizes of the flow geometry. Although granular materials are composed of discrete grains which interact only at contacts, the deformations of individual grains are negligible in comparison with the deformation of the granular assembly as a whole. Hence, the deformation is primarily due to the movements of grains as rigid bodies. Therefore, continuum models are still widely used to solve engineering problems associated with granular materials and flows. Conventional mesh-based approaches, such as Finite Element (FE) and Finite Difference (FD) methods, involve complex re-meshing and remapping of variables, which cause additional errors in simulating large deformation problems. Mesh-free methods, such as the Material Point Method (MPM) and Smooth Particle Hydrodynamics (SPH), are not constrained by the mesh size and its distortion, and hence are effective in simulating large deformation problems such as debris flow and submarine landslides. The analytical and finite element models which consider granular materials as a continuum cannot take into account the local geometrical processes that govern the mechanical behaviour of non-homogeneous soils, and pose subtle problems for statistical analysis. The particle level description of the granular material enriches the macro-scale variables that happen to poorly account for the local rheology of the materials. Numerical models based on the Discrete Element Method (DEM) allow us to evaluate quantities which are not accessible experimentally, thus providing useful insight into the flow dynamics. Particle-fluid interactions can now be simulated by interfacing discrete-element methods with a Lattice Boltzmann solver or a fluid-coupled continuum model, however both methods have their inherent limitations. Even though millions of particles can be simulated, the possible length of such a particle system is generally too small to regard it as '*macroscopic*'. Therefore, methods to perform a micro-macro transition are important and these '*microscopic*' simulations of a small sample, i.e. the '*representative volume element*', can be used to derive a macroscopic constitutive relation which describes the material within the continuum framework.

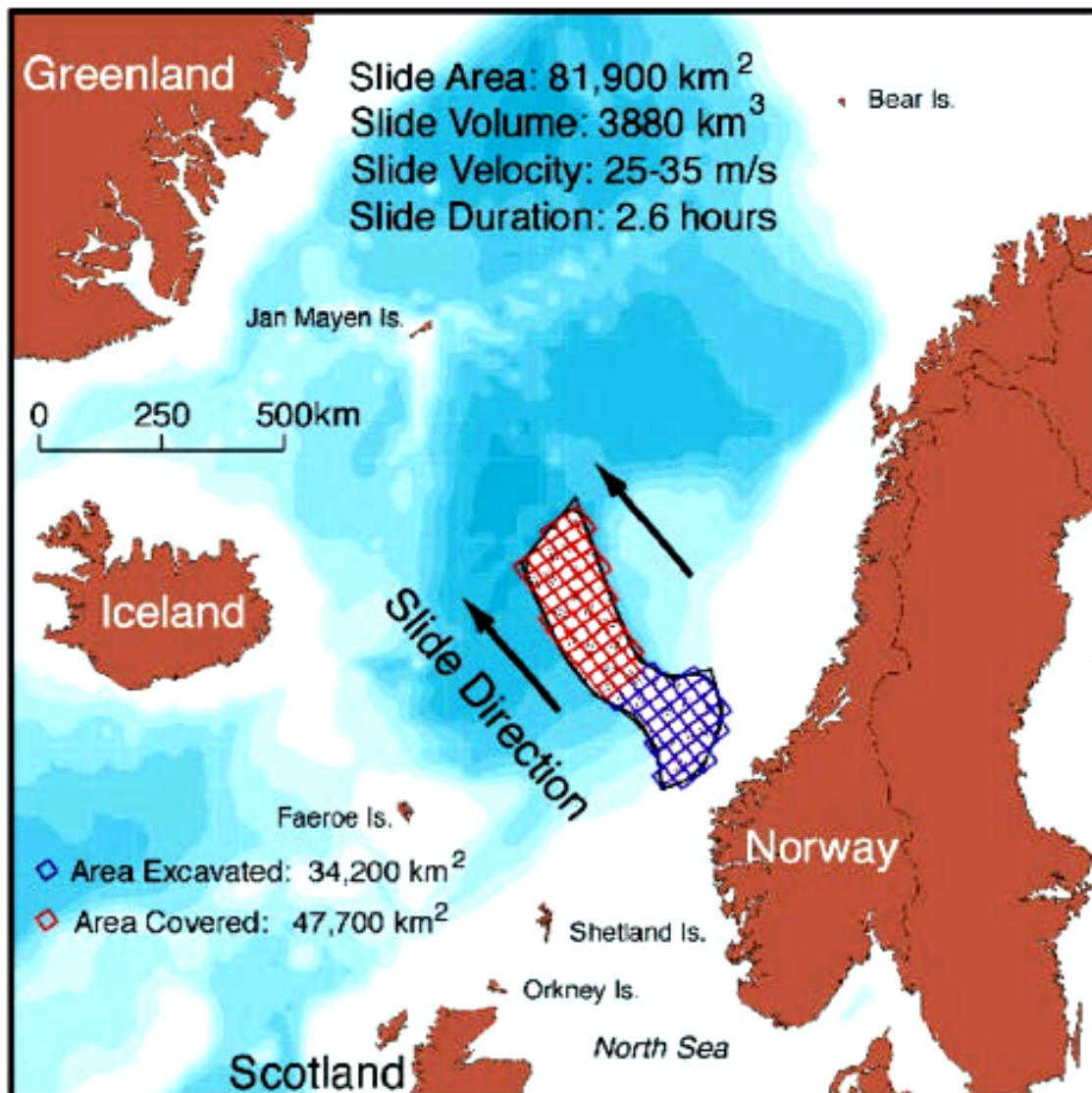


Figure 1.2 The extent of the Storegga landslide (Source: School of geoscience, University of Sydney)

## 4 1.2 Objectives

5 The aim of this research work is to understand and describe the mechanism of granular flows  
6 in dry and submerged conditions using a multi-scale approach. This research work involves  
7 identification of fundamental microscopic parameters that control the granular flow dynamics.  
8 Continuum and discrete-element modelling of granular flows will be performed to understand  
9 the limits of the continuum approach in modelling large deformation granular flow problems.  
10 This study will provide an insight into the mechanics of granular flows, and will enable us to  
11 understand geophysical hazards, such as avalanches, debris flows and sub-marine landslides.  
12 The study involves, but is not limited to, the following goals:

13 **Multi-scale simulation of dry granular flows**

14 Two-dimensional simulations of the collapse of a dry granular column and the flow of dry granular  
15 material on an inclined plane will be performed in particulate and continuum scales, using  
16 the Molecular Dynamics and Material Point Method, respectively. It involves understanding the  
17 parameters influencing the granular flow, i.e. the mechanism of flow initiation, flow propagation  
18 and the energy dissipation process. The study will highlight the limitations of the continuum  
19 and the microscopic approaches in capturing the mechanics behind the complex-flow problems.

20 **Constitutive modelling and fluid coupling in Material Point Method**

21 Advanced constitutive models, such as NorSand constitutive law and  $\mu(I)$  rheology models  
22 will be implemented in the Material Point Method. Large deformation plasticity theory and  
23 objective stress rates will be implemented in the MPM code to describe the granular flow dynamics.  
24 The coupling of soil and fluid material points, which considers the dynamic fluid-solid interface  
25 will be developed. The effect of fluid pressure oscillations at the fluid-solid interface, will be  
26 studied. The fluid-coupled *MPM* code will be implemented in a structured framework and  
27 robust visualization and parallelization algorithms will be implemented.

28 **Multi-scale simulation of saturated granular flows**

29 The Molecular Dynamics technique has been coupled with the Lattice Boltzmann method to  
30 simulate granular flows in a fluid domain. The validity of  $\mu(I)$  rheology in simulating granular  
31 flow in a fluid will be investigated. Continuum and particle level simulations of granular flows  
in fluids will be performed. The triggering mechanism, spreading dynamics and the energy  
dissipation mechanism between the dry and fluid saturated granular flows will be compared.  
The parameters influencing the granular collapse in fluids will also be investigated.

## 1.3 Thesis outline

This thesis consists of seven chapters. Chapter one gives a brief introduction to geophysical hazards, such as submarine landslides, granular avalanches and debris flow. The behaviour of granular materials and the mechanism of granular flow is discussed in detail in chapter two, drawing attention to previous research on granular flow regimes. Experimental and numerical investigations on various granular flow problems and modelling techniques are also discussed in this chapter. By exploring different regimes in a granular flow and the limitations of various theoretical models, potential areas of improvement and future research in describing the mechanics of granular flow are identified. Continuum modelling of granular flow, the possibility of using a continuum model to describe the flow dynamics, and the limitations of a continuum approach are discussed in chapter three. Chapter three also elaborates on the Material Point Method, a Eulerian-Lagrangian approach, and its implementation in the present study to model granular flows. Chapter four explains the various discrete-element modelling techniques and explains the implementation of the Molecular Dynamics technique in modelling granular flow problems. The particle-assembling method adopted in the present study and the results of statistical analysis performed to verify the homogeneity of the prepared sample are also discussed in this chapter. Chapter five elaborates on the Lattice Boltzmann approach in modelling fluid flow and the coupling of the LBM approach with the Molecular Dynamics technique to simulate fluid-particle interactions. The validation of the Lattice Boltzmann technique in simulating fluid flow through a pipe with Computational Fluid Dynamics simulations is also discussed. The multi-scale simulations of granular column collapse using the Molecular Dynamics and the Material Point Method are discussed in chapter six. The final chapter summarizes the mechanics involved in a granular flow and outlines the goals and time-line of future research.

4

5

6

7

8

9

10

11

12

13

14

15

16

17

18

19

20

21

22

23

1

2

3



# Chapter 2

4

## Granular flows

5

### 2.1 Introduction

6

A granular material is a conglomeration of large number of discrete solid particles of sizes greater than  $1\mu m$  whose behaviour is governed by frictional contact and inelastic collisions. A schematic representation of the size range of the granular materials is presented in figure 2.1. Granular materials, characterized by interaction between individual particles, lie between two extremes scales: the molecular-scale range predominated by electrostatic force, i.e. Van der Waals forces, and the continuum scale which is described by the bulk property of the material. In various soil classification systems adopted in soil mechanics, sand is classified as a granular material having particle sizes greater than  $75\mu m$ . Particle size of  $75\mu m$  is an important transition point, where the frictional effect starts to dominate the material behaviour and the effect of the electrostatic Van der Waals forces diminishes. The extent of the particle size range of the granular materials from the molecular size to a continuum scale indicates that they have a complex behaviour, demonstrating a mix of particle-like and continuum-like behaviour. The physics of non-cohesive granular assemblies is intriguing. Despite being ubiquitous in nature, granular materials are the most poorly understood materials from a theoretical standpoint. For such a poorly understood area, the flow of granular materials has a surprising range of geo-hazard predictions and industrial applications. For years, granular materials have resisted theoretical development, demonstrating non-trivial behaviour that resembles solid and/or fluid-like behaviour under different circumstances. Even in the simplest of situations, granular materials can exhibit surprisingly complex behaviour. Macroscopically, the complex mix of solid and fluid-like behaviour can be illustrated by a simple example; while one walks on the beach, the solid-like behaviour of soil becomes evident as it supports one's weight, but if we scoop a handful of soil and allow it to run through the fingers, the fluid-like nature becomes obvious. Microscopically this complex behaviour has various reasons. The range of

<sup>1</sup> the beach, the solid-like behaviour of soil becomes evident as it supports one's weight, but  
<sup>2</sup> if we scoop a handful of soil and allow it to run through the fingers, the fluid-like nature  
<sup>3</sup> becomes obvious. Microscopically this complex behaviour has various reasons. The range of

the particle size gives rise to complex interactions between grains constituting the granular media. Unlike other micro-scale particles, granular particles are insensitive to thermal energy dissipation (Mehta, 2011), because the thermal energy dissipation in a granular material is several orders of magnitude smaller in comparison with the energy dissipation due to interaction between the grains. The thermal energy scales are small when compared to the energy required to move grains. The granular material reaches the static equilibrium quickly due to its dissipative nature, unless an external source of energy is constantly applied (Choi, 2005). Our knowledge of the behaviour of granular assemblies is restricted to two extremes: the solid-like behaviour of dense granular assemblies that resist the shearing force by undergoing plastic deformations, and the fluid-like flow behaviour characterized by high shear rates. Granular media are *a priori* simple systems made of solid particles interacting through their contacts. However, they still resist our understanding and no theoretical framework is available to describe their behaviour (Pouliquen et al., 2006). The strong dependency of the behaviour of granular material on its surrounding environment makes it difficult to have a unified theoretical framework. When strongly agitated, the granular material behaves like a dissipative gas, and kinetic theories have been developed to describe this regime (Popken and Cleary, 1999; Xu et al., 2003). On the other hand, during slow deformations, the quasi-static regime is dominated by steric hindrance and friction forces are often described using plasticity theories. In between the two regimes, the material flows like a fluid, and the particles experience enduring contacts, which is incompatible with the assumptions of the kinetic theory (Pouliquen et al., 2006) that describes the dilute regime of a granular flow. Typical granular flows are dense and hence a fundamental statistical theory is not appropriate to describe their properties. Moreover, during the process of granular flow, the material can exist in all the above-mentioned states, which further complicates our understanding of granular flows.

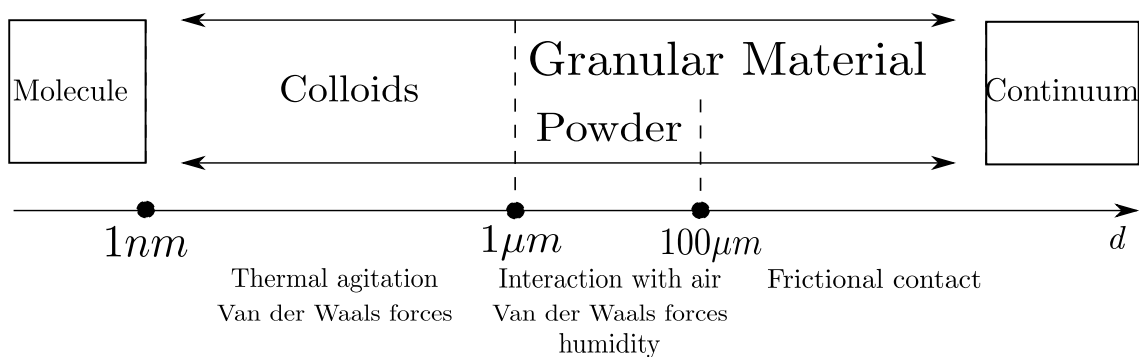


Figure 2.1 Particle size range and their predominant characteristics

## 2.2 Modelling the granular flows

Granular flows can be classified into three different regimes (Jaeger et al., 1996): the dense slow quasi-static regime characterized by long duration between contacts and particle interaction via frictional contact (Roux and Combe, 2002); the rapid and dilute flow regime characterized by particles moving freely between successive collisions (Goldhirsch, 2003); and an intermediate fluid-like regime in which the material is dense but still flows like a fluid and the particles interact both by collision and through friction (Midi, 2004; Pouliquen and Forterre, 2002). Transfer of particle kinetic energy and momentum within a rapidly flowing granular medium occurs during these collisions (Popken and Cleary, 1999). Different approaches have been used to model granular flows at different scales of description. The dynamics of a homogeneous granular flow involve at least three distinct scales: (1) the *Microscopic scale* characterized by small time and length scales representing contact/particle interactions, (2) the *Mesoscopic scale*, where particle rearrangements, development of micro-structures and shear rates have a dominant influence on the granular flow behaviour, and (3) the *Macroscopic scale* which involves large length scales that are related to geometric correlations at even larger scales. The interesting issue is whether one should consider or neglect a particular scale while modelling the granular dynamics (Radjai and Richefeu, 2009). However, the difficulty in modelling the granular flows originates from the fundamental characteristics of the granular matter such as negligible thermal fluctuations, highly-dissipative interactions, and a lack of separation between the microscopic grain scale and the macroscopic scale of the flow (Goldhirsch, 2003).

Granular flow modelling began as early as 1776 with Coulomb's paper describing the yielding of granular material as a frictional process (Coulomb, 1776). Although it was not about granular flows, *per se*, the prediction of soil failure for Civil engineering applications describes the onset of structural collapse leading to catastrophe (Campbell, 2006). Mohr-Coulomb's yield criterion along with a flow rule from metal plasticity is sufficient to describe the behaviour of granular flow as a continuum process, without considering the interaction of individual particles. Advanced models based on the critical state concept (Schofield and Wroth, 1968) provides further insight into continuum description of granular flows. According to the critical state theory, the 'under consolidated' or loose soil tends to increase in density upon shearing, while the dense 'over consolidated' soil dilates when sheared, until it reaches the critical state. As dense granular flow involves large shear stresses, it is reasonable to assume that the shearing occurs at the critical state. Large applied stress can cause the granular particles to deform at the grain scale and squeeze them into the inter-particle pores. However, the critical state is independent of the applied stress. In granular flows, the applied stress during the actual flow is less in comparison with the stress on the soil underneath a structure, where the soil is subjected to large shear strains. It is therefore reasonable to assume that the flow

is incompressible and takes place at the critical state (Campbell, 2006). The main limitation of the continuum approach is the assumption that the friction angle,  $\phi$  is a constant material parameter, which is found to vary by a factor of 3, violating the fundamental assumption of quasi-static flow theories (Potapov and Campbell, 1996). Although the mechanism of dense granular flow is attributed to the bulk friction, it is the formation of force chains and the rearrangement of internal structure of the granular assembly that causes friction-like behaviour. Experiments (Savage and Sayed, 1984; Savage, 1984) and computer simulations (Campbell and Brennan, 1985) indicate a weak relation between the bulk friction and the packing density, due to the micro-structural rearrangement of particles (Campbell, 1986). As the packing density increases, the particles tend to arrange themselves in a regular order when sheared. In order to understand the development of micro-structure, it is important to look at the particle-level interactions. Bagnold (1954) was the first to try and model granular materials as individual particles. Bagnold's theory of motion of individual particles in a shear flow and inter-particle friction inducing random velocities is reminiscent of the thermal motion of molecules in the kinetic theory of gases. The two common approaches in modelling the granular flow: the kinetic theory and the shallow water theory, are discussed below.

### 2.2.1 Kinetic theory

The gas kinetic theory assumes that the particles interact by instantaneous collisions, which implies only binary (two-particle) collisions. The particles are modelled using a single coefficient of restitution, to represent the energy dissipated by the impact normal to the point of contact between the particles, and for the most part, the surface friction or any other particle interactions tangential to the point of contact are ignored (Campbell, 1990). Jenkins and Savage (1983) extended the kinetic theory for thermal fluids to idealized granular mixtures to predict the rapid deformation of granular material by including energy dissipation during collision for nearly inelastic particles. Savage and Jeffrey (1981) extended the kinetic theory to predict simple shear flow behaviour for a wide range of coefficients of restitution. The kinetic theory is capable of predicting the shear flow behaviour only for mixtures composed of particles with identical density and size (Iddir and Arastoopour, 2005), however real systems are composed of particles that vary in size, and segregation of particles can occur.

The kinetic theory is valid for dispersed granular flows (Ng et al., 2008), however ? observed that the numerical simulations of dense granular flow based on kinetic theory were poor in comparison with the experimental data on fluidized bed expansion. Confined granular flows are usually dense, because of their mechanism of energy dissipation and their tendency to form clusters. The dense granular flows lie in an intermediate regime, where both the grain inertia and the contact network has significant influence on the flow behaviour (Pouliquen and Forterre,

2002). Thus, a part of the force is transmitted through the force network, which contradicts the two basic assumptions in the kinetic theory, i.e. binary collision and molecular chaos. For dense granular flow conditions, the total stress transmission in the flow regime is the sum of the rate-dependent (collision-transition) and the rate-independent (friction) components (Ng et al., 2008). Addition of frictional stress component (?) to the kinetic theory improves the ability of the model to predict the dense granular flows. The main advantage of kinetic theories is that they can be used to derive deterministic constitutive laws to describe the behaviour of granular flows in a theoretical framework (Jenkins and Savage, 1983). Kinetic theories formulated on the assumption of solid phase stress as a viscous response have limitations when applied to granular flows. A viscous material produces no force unless it is in motion, hence the kinetic theory based on viscous solid phase cannot explain the static force exerted by the granular materials on the walls, as observed in experiments. The addition of a frictional component to the kinetic theory improves its prediction of granular flows. However, the frictional component that is based on long-duration contact is added to the instantaneous collision contact term. Also, the rapid-flow models based on gas kinetic theory assume that the molecular collisions are elastic, which means that they do not dissipate energy (Campbell, 2006), which is in contrast to the reality. Finally, the important assumption of gas kinetic theory is molecular chaos, which assumes no correlation between the velocities or positions of the colliding particles, which is not true especially in a dense granular flow where the particles interact many times with their neighbours and a strong correlation between their velocities is inevitable.

### 2.2.2 Shallow-water approximation

The Navier-Stokes equation in fluid mechanics is capable of describing the dynamics of fluid flow under different conditions. However, the proposed models for granular flows tend to be specialized for a particular situation. By drawing a simple analogy from fluid dynamics one can model granular flows as non-Newtonian fluids using a variant of the Navier-Stokes equation; one such approach is the depth-averaged shallow-water equation, which has been applied to solve granular flow dynamics with a reasonable amount of success. The Savage-Hutter model (Savage and Hutter, 1991), is a depth-average continuum-mechanics based approach which consists of hyperbolic partial differential equations to describe the distribution of the depth and the topography of an avalanching mass of cohesion-less granular media (Hutter et al., 2005). This approach is based on the assumption that the horizontal length scale is very large in comparison with the vertical length scale, which allows us to neglect the horizontal partial derivatives relative to the vertical partial derivatives. Field observations indicate an aspect ratio of  $10^{-3}$  to  $10^{-4}$  for natural avalanches (?). By neglecting the vertical length scale, the

5 continuum equation for conservation of mass and momentum can be written as:

6  $\partial_x u + \partial_y v = 0$  (2.1)

7  $\partial_t u + u \partial_x u + v \partial_y u = (\nabla \cdot \sigma)_x + F_x$  (2.2)

9 The continuum equation requires determining the components of the stress tensor and a suitable  
 10 constitutive law. *Savage-Hutter (SH) model* uses the Mohr-Coulomb law to describe the  
 11 constitutive relation. The conservation of mass and momentum in the SH model is based on  
 12 the assumption of granular flow as an incompressible fluid flow, which means that throughout  
 13 the avalanche, the density of the avalanching material remains constant. Although [Hutter et al.](#)  
 14 ([1995](#)) observed the density of the granular flow to remain almost constant in a flow down a  
 15 curved chute, the destructive nature of landslides and avalanches restricts us from inferring a  
 16 conclusive result. The SH model involves the following assumptions: (1) Coulomb-type sliding  
 17 takes place with a bed friction angle  $\delta$ , (2) Mohr-Coulomb frictional behaviour occurs inside  
 18 the material with internal angle of friction,  $\phi \geq \delta$ , and (3) the velocity profile is assumed to be  
 uniform throughout the avalanche depth. The granular flow over a rigid plane inclined at an  
 angle,  $\theta$  is shown in figure 2.2. The mass and momentum balance in the SH model is written  
 as:

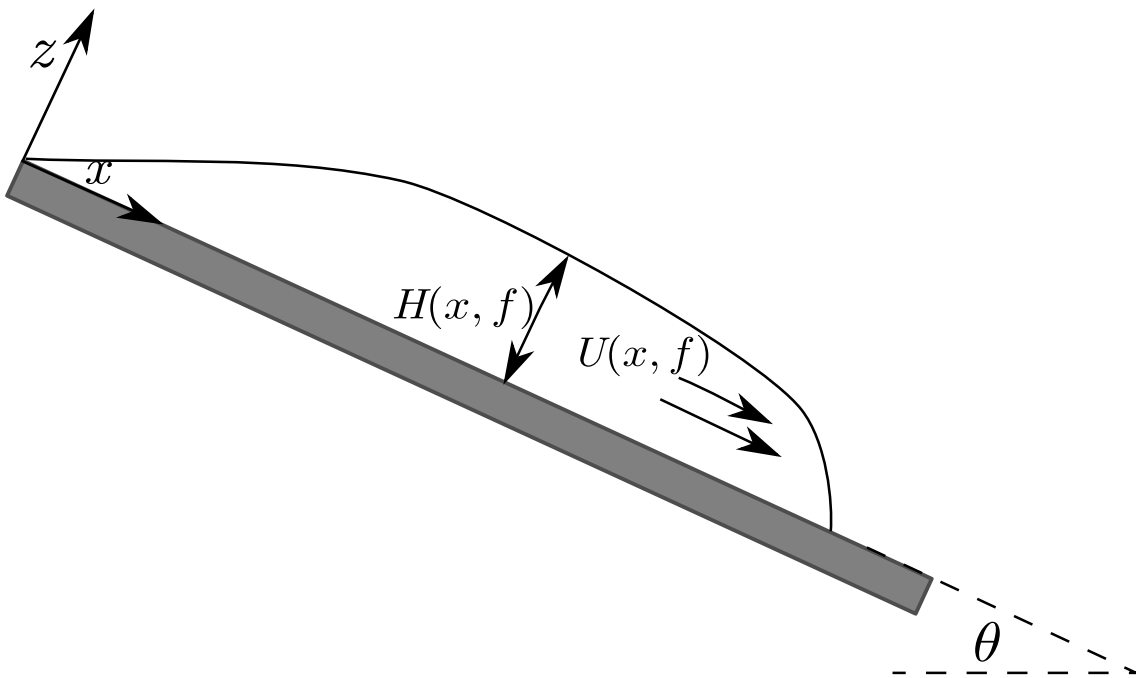


Figure 2.2 Illustration of the Savage-Hutter model

$$\frac{\partial H}{\partial T} + \frac{\partial}{\partial X}(HU) = 0 \quad (2.3)$$

$$\frac{\partial U}{\partial T} + U \frac{\partial U}{\partial X} = (\sin \theta - \tan \delta sgn(U) \cos \theta) - \beta \frac{\partial H}{\partial X} \quad (2.4)$$

where capital letters denote non-dimensional quantities with respect to the typical horizontal and vertical length scales ( $L^*, H^*$ ) and the time scale  $\sqrt{L^*/g}$ . The key feature in the shallow water approximation is the Mohr-Coulomb constitutive law, which is applied at the free surface and at the base, to describe the granular flow. Comparison of the model with the post-calculation of Madlein avalanche in Austria indicates that the Coulomb basal friction is insufficient and requires an additional viscous component. The SH model's predictions were not satisfactory for granular flows down gentle slopes of inclination angle  $\leq 30^\circ$ , where granular materials exhibit a different behaviour (Hutter et al., 2005).

### 2.2.3 Rheology

Rheology is the science of flow of materials with solid and fluid characteristics. In practice, rheology is principally concerned with describing the mechanical behaviour of those materials that cannot be described by the classical theories, by establishing an empirical relation between deformation and stresses. Consider a granular assembly of particles having diameter  $d$  and density  $\rho_d$  under a confining pressure  $P$  (see figure 2.3). If the material is sheared at a constant shear rate,  $\dot{\gamma} = V_w/L$  is imposed by the relative movement of the top plate with a velocity  $V_w$ . In the absence of gravity, the force balance implies that the shear stress,  $\tau = \sigma_{xy}$ , and normal stress,  $P = \sigma_{xx}$ , are homogeneous across the cell. This configuration is the simplest configuration to study the rheology of granular flow, i.e. to study the effect of the strain rate,  $\dot{\gamma}$ , and pressure,  $P$  on the volume and shear stress,  $\tau$ . Even though the granular materials have been extensively researched at microscopic level, the continuum representation of granular materials in terms of conservation of mass and momentum is still an area of concern (Daniel et al., 2007; Midi, 2004). The prediction of rheology of granular materials even in the simplest case is complicated as they exhibit rate-dependent behaviour and no single constitutive equation is able to describe the behaviour over a range of shear stress rates. Da Cruz et al. (2005) developed a very famous rheology for granular flows, that is based on the simple two-dimensional shear in the absence of gravity and establishes that the flow regime and rheological parameters scale with a dimensionless number that represents the relative strength of inertia forces with respect to the confining pressure (Daniel et al., 2007), along the lines of Savage and Hutter (1991). The

- <sup>2</sup> shear stress,  $\tau$ , is proportional to the confining pressure,  $P$ , and is written as:

<sup>3</sup>

$$\tau = P\mu(I) \quad (2.5)$$

- <sup>5</sup> The friction coefficient  $\mu$  depends on the single non-dimensional parameter  $I$ , expressed as:

<sup>6</sup>

$$I = \frac{\dot{\gamma}d}{\sqrt{P\rho_p}} \quad (2.6)$$

<sup>7</sup>

- <sup>8</sup> The parameter  $I$  can be interpreted in terms of different time scales controlling the grain flow.  
<sup>9</sup> If the particles are rigid, i.e. neglecting the elastic properties of the particles, then  $I$  is the only  
<sup>10</sup> non-dimensional parameter in the problem. Hence, the shear stress,  $\tau$ , has to be proportional  
<sup>11</sup> to the pressure,  $P$ , times a function of  $I$ . Comparing the shape of the function  $\mu(I)$  with the  
<sup>12</sup> experimental results of flow down an inclined plane, Jop et al. (2006) observed that the frictional  
<sup>13</sup> coefficient increases from a minimal value of  $\mu_s$  to an asymptotic value of  $\mu_2$ , when the value  
<sup>14</sup> of  $I$  increases. The variation of friction coefficient with  $I$  is shown in figure 2.4. To formulate  
<sup>15</sup> a complete constitutive model, it is essential to describe the volumetric behaviour. Based  
<sup>16</sup> on the dimensional analysis, it can be argued that the volume change is also a function of  
<sup>17</sup> dimensionless parameter  $I$  and that it also depends on the maximum and the minimum possible  
void ratios and the time for microscopic rearrangement of particles.

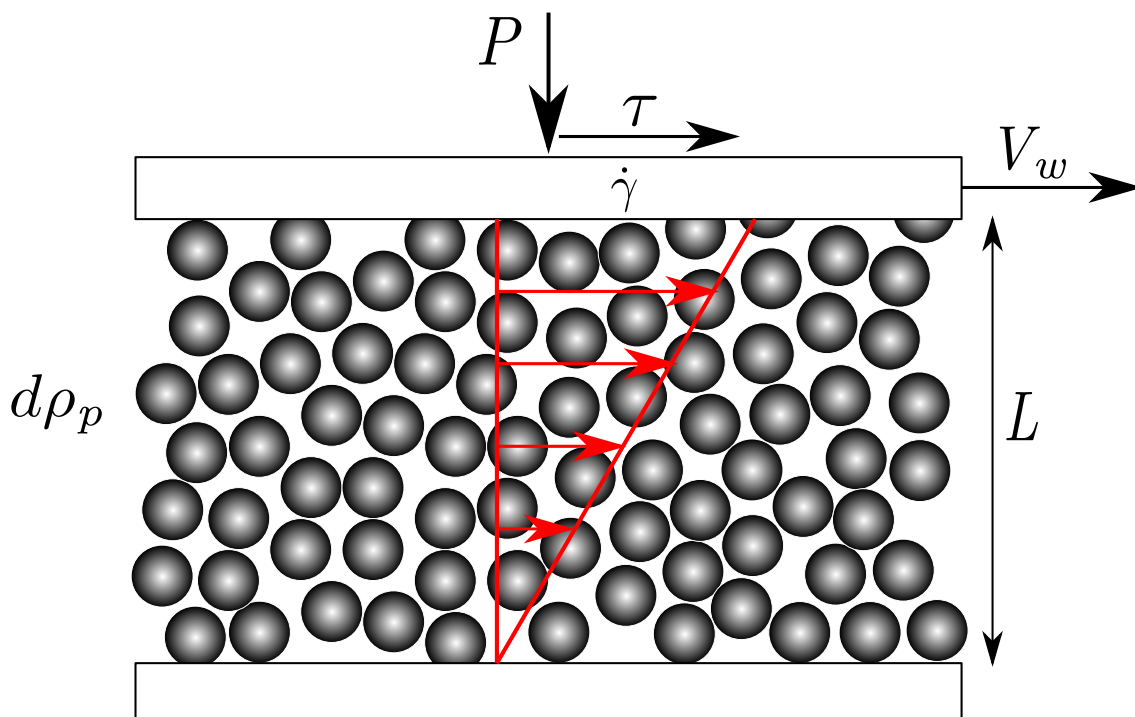


Figure 2.3 Plane stress at a constant pressure

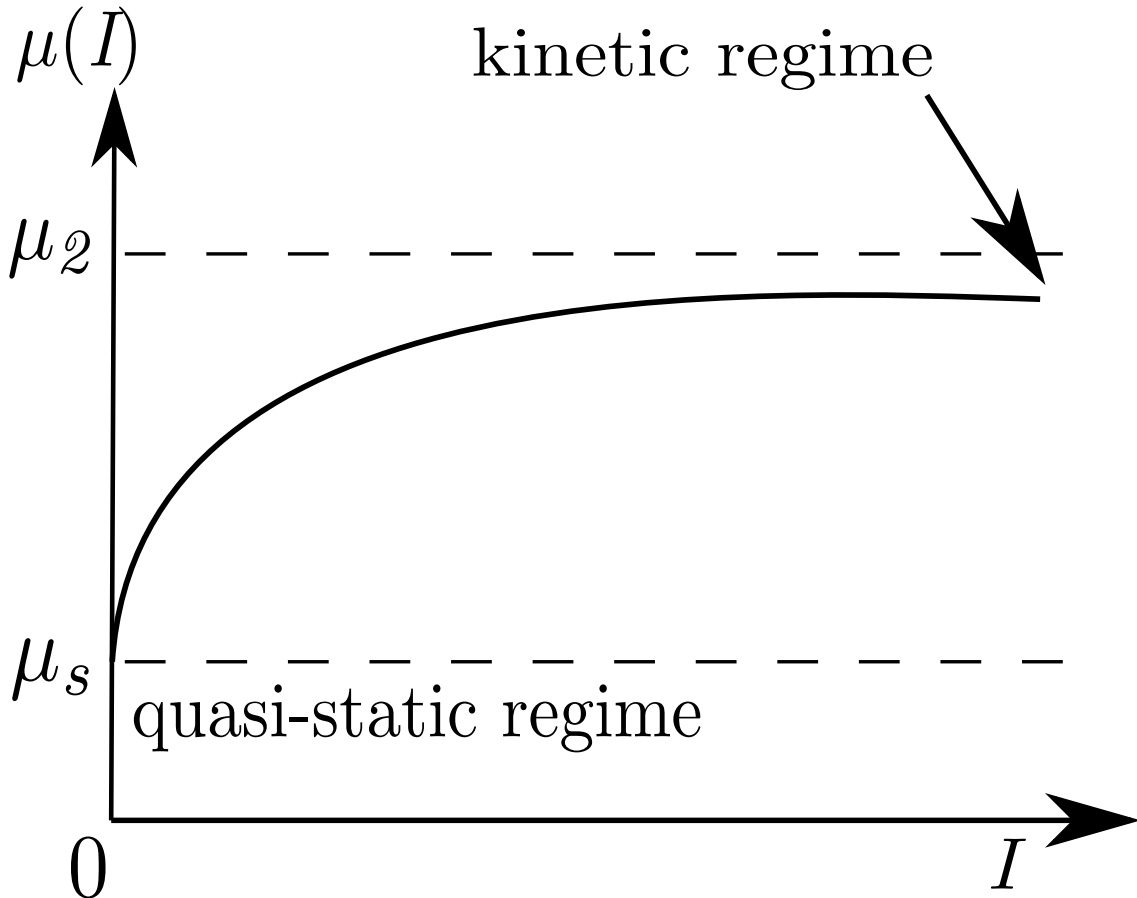


Figure 2.4 Sketch of dependence of frictional coefficient  $\mu$  with dimensionless shear rate  $I$ , reproduced after [Pouliquen et al. \(2006\)](#)

<sup>18</sup> In general, the flow regimes can be classified based on the dimensionless number  $I$  ([Da Cruz et al., 2005](#)). Dilute or “collisional” flow occurs for  $I > 10^{-1}$  and the particle collision  
<sup>1</sup> is chiefly binary, accompanied by additional “bounce-back” akin to gases ([Kamrin, 2008](#)). In  
<sup>2</sup> the dilute flow regime, the particles are rarely in long-duration contacts and can be described  
<sup>3</sup> by dissipative Boltzmann kinetics. The “quasi-static” regime occurs at the other extreme of  
<sup>4</sup> the spectrum,  $I < 10^{-3}$ , where the intermittent motion is prevalent. The inertial time is always  
<sup>5</sup> small enough for the particles to align to a dense compaction, without significant collisional  
<sup>6</sup> dissipation. The frictional sliding and stick-slip dynamics dominate the dissipation mechanism.  
<sup>7</sup> The moderate-flow regime is observed for  $I$  between  $10^{-3}$  and  $10^{-1}$ , characterized by faster  
<sup>8</sup> flows, with a high rate of contact formation and more energy dissipation per impact. In this  
<sup>9</sup> regime,  $I$  has a one-one relationship with  $\mu$  and is large enough for rate dependence, but small  
<sup>1</sup> enough for the flow to remain dense. Moderate flows also exhibit the property of *shearing*  
<sup>2</sup> *dilation*, where an increase in the normalized flow rate causes the steady-state packing fraction  
<sup>3</sup>

to decrease, which is different from *shear dilation*, which refers to a decrease in the packing density as a function of total shear. Flows which are too slow to be moderate still undergo shear dilation due to geometric packing constraints, but shearing dilation occurs only in faster flows due to rate effects (Kamrin, 2008). figure 2.5 shows the variation of frictional coefficient  $\mu$  and packing fraction  $\phi$  with dimensionless number  $I$  for various flow regimes.

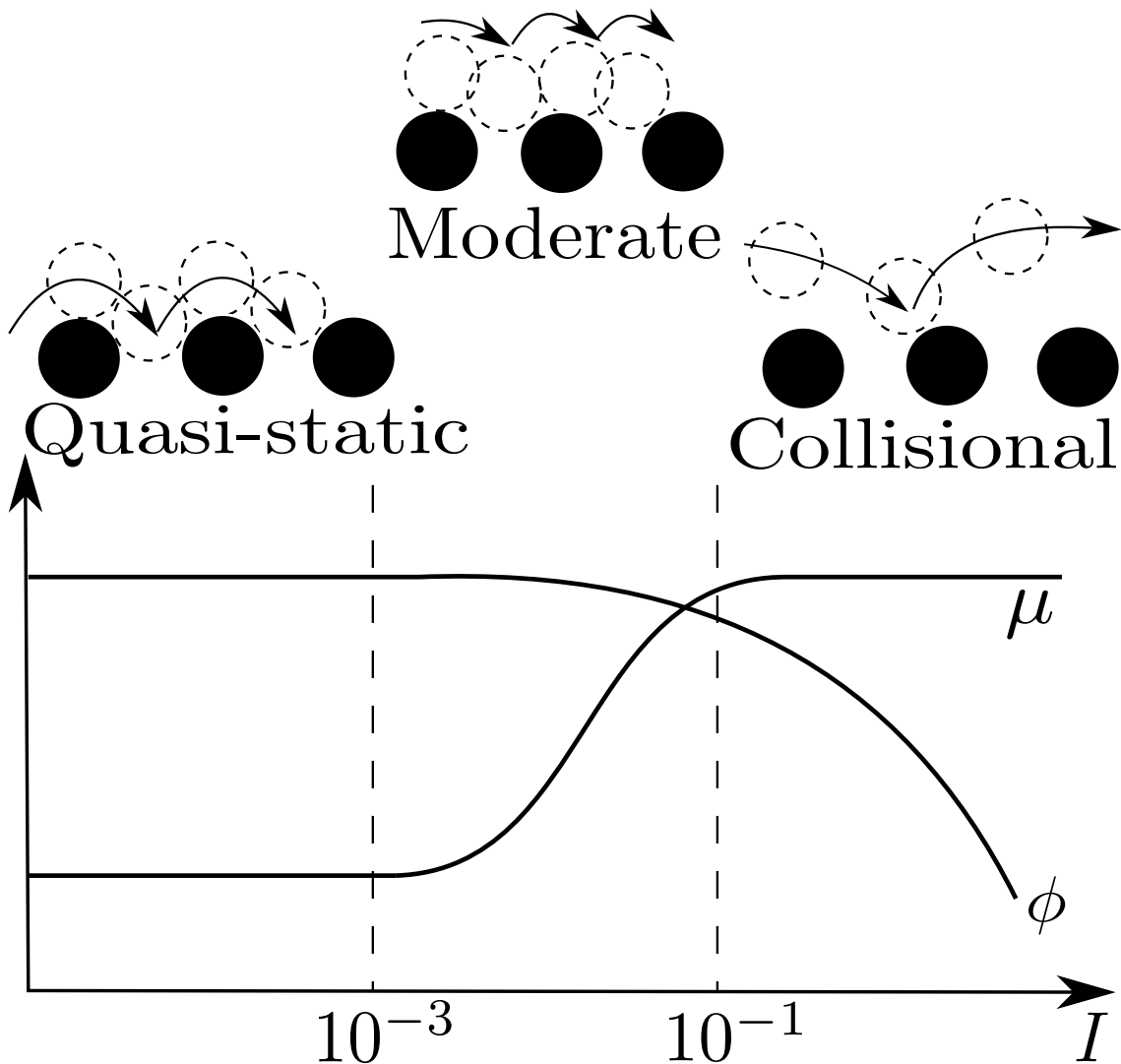


Figure 2.5 Variation of dimensionless parameters through the various flow regimes under simple shearing, reproduced after (Kamrin, 2008)

Campbell (2002) described the “Moderate regime” as an elastic granular flow regime, where the inter-particle stiffness governs the overall flow behaviour of the granular assembly. At high concentration, the stresses are proportional to the contact stiffness, and the streaming stiffness is negligible. When a dense granular assembly is sheared, the force chains that transmit the forces continue to rotate until it becomes unstable and collapses. As the force-chain

rotates, the granular material tend to dilate, however it is restricted due to the constant volume constraint; instead, the rotation compresses the chain, generating an elastic response (Campbell, 2006). Campbell (2002) divided the flow into the elastic and the inertial regimes. In the Elastic regime, the force is transmitted principally through the deformation of force chains with a natural stress scaling of  $\tau d/k$ . The force chain forms when the particles are sheared at the rate of  $\dot{\gamma}$ , and hence the rate of chain formation is proportional to the shear rate  $\dot{\gamma}$ . This transition regime can be explained using the force-chain concept. The lifetime of a force chain is proportional to  $1/\dot{\gamma}$ , consequently the product of rate of formation and the lifetime of the force chain is independent of  $\dot{\gamma}$ , and the stresses generated are quasi-static. However at higher shear rates, the elastic forces in the chain have to absorb the additional inertial force of the particles, requiring extra force to rotate the chain proportional to the shear rate. Even though the particles are locked in force chains, the forces generated must reflect the particle inertia. The ratio of elastic to inertial effects is governed by a dimensionless parameter:

$$k^* = \frac{k}{\rho d^3 \dot{\gamma}^2} \quad (2.7)$$

where  $k/\rho d^3 \dot{\gamma}^2 = (\tau/\rho d^2 \dot{\gamma}^2)/(\tau d/k)$  is the ratio of Bagnold's inertial to the elastic stress scaling. The important dimensionless parameter is  $k^*$ , which is a measure of inertially-induced deformation, reflects the relative effects of elastic to inertial forces, i.e. at large  $k^*$ , the elastic forces dominate and at small  $k^*$ , inertial forces dominate (Campbell, 2006). Campbell (2002) observed a strong correlation between the coefficient of friction and the dimensionless parameter,  $k$  as the flow progresses through different regimes, similar to the observation made by Kamrin (2010).

<sup>1</sup> Constitutive laws, which describe the dilatancy and friction, allow us to deduce the dependency of pressure and shear stress on shear rate and solid fraction. In contrast to the observation of Campbell (2002), Da Cruz et al. (2005) found that the elastic stiffness has little effect on the constitutive law, for values greater than  $10^4$ , however that it does affect the coordination number. Da Cruz et al. (2005) also observed that the microscopic friction coefficient,  $\mu$ , has a significant influence on the dilatancy, and the solid fraction remains a linearly-decreasing function of  $I$ . The frictional properties of the material are found to control the solid fraction, from the critical state to the collisional regime (Da Cruz et al., 2005). Although the rheology tends to describe the behaviour of granular flows, the mechanism of granular flows was found to vary with time, position and feedback mechanism (Iverson, 2003). Rheology summarizes the mechanical behaviour at scales smaller in comparison with the Representative Elemental Volume (REV), for a substance modelled as a continuum. Rheology-based descriptions are generally restricted to homogeneous materials that exhibit time-independent behaviour, hence

<sup>14</sup> are unsuitable for describing granular flows where the stress history has a significant effect  
<sup>15</sup> on the flow dynamics. The estimation of debris flow yield strength highlights the limitation  
<sup>16</sup> of rheologies which do not consider the development of strength with evolution of time and  
<sup>17</sup> space. [Johnson \(1965\)](#) emphasized that debris yield strength is predominantly a frictional phe-  
<sup>18</sup>nomenon analogous to the Coulomb strength of granular soils, and that strength consequently  
<sup>19</sup> varies with effective normal stress. Treatment of yield strength as an adjustable rheological  
<sup>20</sup> property contradicts the basic understanding that the strength evolves as the debris-flow motion  
<sup>21</sup> progresses. Frictional behaviour implies no explicit dependence of shear resistance on shear  
<sup>22</sup> rate, whereas rheological formulas commonly used to model debris flows generally include a  
<sup>23</sup> viscous component that specifies a fixed functional relationship between shear resistances and  
<sup>24</sup> shear rate. Although rate-dependent shear resistance is observed in debris flows, its magnitude  
<sup>25</sup> and origin indicate that it is ancillary rather than essential ([Iverson, 2003](#)).

<sup>26</sup> The two main modelling techniques that are commonly employed to describe the granular  
<sup>27</sup> flow are the continuum approach and the discrete element approach. The continuum approach  
<sup>28</sup> involves treating granular assembly as a continuum and describing its response using consti-  
<sup>29</sup>tutive laws, while the discrete approach involves considering the individual particles of the  
<sup>30</sup> granular material and applying Newton's laws of motion to describe the deformation of the  
<sup>31</sup> granular material. These approaches are adopted in the present study and detailed discussions  
<sup>32</sup> are provided in the subsequent chapters.

### <sup>33</sup> 2.3 Studies on granular flows

<sup>34</sup> The flow of dense granular material is a common phenomenon in engineering predictions, such  
as avalanche, landslides, and debris-flow modelling. Despite the huge amount of research that  
has gone into describing the behaviour of granular flow, a constitutive equation that describes  
the overall behaviour of a flowing granular material is still lacking. To circumvent this  
difficulty, depth-averaged constitutive equations have been employed along with an empirical  
friction coefficient and a velocity profile deduced from experiments ([Iverson, 2003; Midi, 2004;](#)  
[Pouliquen, 1999](#)). Although this approach has been successful to a certain extent in predicting  
geophysical flows ([Hutter et al., 1995; Pouliquen and Chevoir, 2002](#)), it presents two important  
shortcomings ([Lajeunesse et al., 2005](#)). First, the depth-average method is true only if the  
thickness of the flowing layer is thin in comparison with the lateral dimension, and second, the  
empirical laws are deduced from experiments performed under steady-flow conditions. These  
cast doubts on the validity of the depth-averaged approach. Two simple granular flow studies,  
granular column collapse and granular flow down an inclined plane, have been carried out by  
various researchers to understand the flow behaviour.

1  
2  
3  
4  
5  
6  
7  
8  
9  
10  
11  
12  
13

### 2.3.1 Granular column collapse

Lube et al. (2005) and Lajeunesse et al. (2004) have carried out experimental investigation on the collapse behaviour of a granular column on a horizontal plane. Both the experiments involved filling a cylinder of height  $H_i$  and radius  $R_i$  with granular material of mass  $m$ . The granular column is then released *en masse* by quickly removing the cylinder, thus allowing the granular material to collapse onto the horizontal surface, forming a deposit having a final height  $H_f$  and radius  $R_f$ . Although the experiment is simple and attractive allowing us to explore the limitations of depth-average modelling techniques, a constitutive law that could describe the entire flow behaviour is still lacking. The primary aim of these experiments was to determine the scaling laws for the run-out distance.

#### Deposit morphology

Lajeunesse et al. (2005) observed that the flow dynamics and the final deposit remain independent of the volume of granular material that is released, but depend only on the initial aspect ratio ‘ $a$ ’ of the granular column. The experiment was carried out to understand the effect of the geometrical configuration on the run-out, the mechanism of initiation of the flow, the evolution of flow with time, and to understand how such complex flow dynamics could produce deposits obeying simple power laws. Lube et al. (2005) explored the effect of density and shape of

1 grains on flow dynamics, whereas Lajeunesse et al. (2004) worked with glass beads to study the  
 2 influence of bead size and substrate properties on the deposit morphology. Surprisingly, both  
 3 drew the striking conclusion that the flow duration, the spreading velocity, the final extent of  
 4 the deposit, and the fraction of energy dissipated during the flow can be scaled in a quantitative  
 5 way independent of substrate properties, bead size, density, and shape of the granular material  
 6 and released mass,  $M$  (Lajeunesse et al., 2005). Lube et al. (2005) scaled the run-out distance  
 7 as:

$$\frac{R_f - R_i}{R_f} \approx \begin{cases} 1.24a, & a \lesssim 1.7 \\ 1.6a^{1.2}, & a \gtrsim 1.7 \end{cases} \quad (2.8)$$

10 while Lajeunesse et al. (2004) scaled run-out as:

$$\frac{R_f - R_i}{R_f} \approx \begin{cases} 1.35a, & a \lesssim 0.74 \\ 2.0a^{1.2}, & a \gtrsim 0.74 \end{cases} \quad (2.9)$$

13 Quasi-two-dimensional collapse of a granular column on a horizontal surface (Lajeunesse et al.,  
 14 2005) reveals that the geometric configuration influences the scaling of the run-out distance.

- <sup>15</sup> The run-out in a quasi-two-dimensional collapse of a granular column in a rectangular channel,  
<sup>16</sup> is scaled as:

$$\frac{R_f - R_i}{R_f} \approx \begin{cases} 1.2a, & a \lesssim 2.3 \\ 1.9a^{2/3}, & a \gtrsim 2.3 \end{cases} \quad (2.10)$$

<sup>19</sup> At large aspect ratios, the run-out is well represented by a simple power-law dependence. The  
<sup>20</sup> exponent is found to vary with the channel width:  $\Delta R/R_i \approx \lambda a^{0.65}$  for narrow channels and  
<sup>21</sup>  $\Delta R/R_i \approx \lambda a^{0.9}$  for wide channels. The constant of proportionality  $\lambda$  is found to vary with  
<sup>22</sup> the internal friction angle of the granular material, which contradicts the findings of previous  
<sup>23</sup> authors, especially Lube et al. (2005) who found that the scaling of run-out is independent  
<sup>24</sup> of the granular material, perhaps due to a narrow range of experimental materials (Staron  
<sup>25</sup> et al., 2005). However, scaling found for quasi-two-dimensional experiments in the narrow gap  
<sup>26</sup> configuration gives similar results as (Lube et al., 2005) and roughly a scaling of  $R_f/(R_f - R_i) \propto$   
<sup>27</sup>  $a^{2/3}$ . Numerical simulations of granular column collapse by Zenit (2005) and Staron et al.  
<sup>28</sup> (2005) yielded similar scaling of run-out with aspect ratio ‘ $a$ ’, unlike other authors, Zenit (2005)  
<sup>29</sup> did not observe any transition in the run-out behaviour of a granular column collapse with  
<sup>30</sup> the aspect ratio ‘ $a$ ’. The origin of the exponents is still under discussion. No model has yet  
<sup>31</sup> achieved a comprehensive explanation of the dependence of the complex-collapse dynamics on  
<sup>32</sup> simple power laws. However, it was observed that a simple friction model cannot effectively  
<sup>33</sup> describe the collapse dynamics. Staron et al. (2005) explained the mechanism of spreading  
<sup>1</sup> using an initial potential energy approach. For higher aspect ratios, the free fall of the column  
<sup>2</sup> controls the dynamics of the collapse and the energy dissipation at the base is attributed to the  
<sup>3</sup> coefficient of restitution. Thus, the initial potential energy stored in the system is dissipated  
<sup>4</sup> by sideways flow of material and the mass ejected sideways is found to play a significant role  
<sup>5</sup> in the spreading process, i.e. as ‘ $a$ ’ increases, the same fraction of initial potential energy  
<sup>6</sup> drives an increasing proportion of initial mass against friction, thus explaining the power-  
<sup>7</sup> law dependence of the run-out distance on ‘ $a$ ’. Taking advantage of the similarity between  
<sup>8</sup> granular slumping and the classical “dam break” problem in fluid mechanics, ? solved both  
<sup>9</sup> the axis-symmetric and two-dimensional granular-collapse problem using the shallow-water  
<sup>10</sup> approximation. Although the results of the shallow-water approximation have good agreement  
<sup>11</sup> with experimental results, the shallow-water approximation overestimates the run-out distance  
<sup>12</sup> for columns with aspect ratio ‘ $a$ ’ greater than unity. The shallow-water equation does not take  
<sup>13</sup> into account the effect of vertical acceleration (Lajeunesse et al., 2005), which has been found  
<sup>14</sup> to play a significant role in controlling the collapse dynamics Staron et al. (2005), thus resulting  
<sup>15</sup> in overestimation of run-out. The evolution of the scaled deposit height  $H_f/R_i$  with the aspect

ratio ‘ $a$ ’ for axis-symmetric collapse ([Lajeunesse et al., 2005](#)) is given as:

$$H_f/R_i \approx \begin{cases} a, & a \lesssim 0.74 \\ 0.74, & a \gtrsim 0.74 \end{cases} \quad (2.11)$$

16  
17  
18

and for two-dimensional collapse:

$$H_f/R_i \approx \begin{cases} a, & a \lesssim 0.7 \\ a^{1/3}, & a \gtrsim 0.7 \end{cases} \quad (2.12)$$

19  
20  
21

The scaling of the final collapse height is found to be similar with the experimental results of [Lube et al. \(2005\)](#) and [Balmforth and Kerswell \(2005\)](#), and the numerical simulation of [Staron et al. \(2005\)](#). Numerical simulation of granular column collapse ([Lacaze et al., 2008](#); [Staron et al., 2005](#)) showed a transition in the flow behaviour at ‘ $a$ ’ $\geq 10$ , which was not observed in granular collapse experiments ([Balmforth and Kerswell, 2005](#); [Lajeunesse et al., 2004](#); [Lube et al., 2005](#)). In the depth-averaged shallow-water model, which integrates over the depth, the emphasis was on capturing the scaling of the final deposit, rather than trying to reproduce the internal structure of the flow. The shallow-water model captures well the final deposit scaling for lower aspect ratios, however fails to capture the flow dynamics for granular columns with higher aspect ratios, where the flow is governed mainly by the vertical collapse of the granular column as a whole. The run-out distance predicted is clearly erroneous in the collapse regime where there is a sudden drop in efficiency by which the initial potential energy of the system is converted into the kinetic energy for spreading. Even a more sophisticated basal drag law will not be sufficient to model the mechanism of granular column collapse realistically using the shallow-water approximation (?).

22  
23  
24  
25  
26  
27  
28  
29  
30  
31

## 6 Flow dynamics

The variation of final scaled deposit with aspect ratio ‘ $a$ ’ shows a transition in the run-out behaviour for an aspect ratio of 1.7, indicating a transformation in the spreading process or the collapse mechanism. To understand the collapse mechanism, it is insufficient to study only the final scaled profile, and hence the entire flow process should be analysed. [Lajeunesse et al. \(2005\)](#) observed the flow regime and deposit morphology for a quasi-two-dimensional granular collapse in a rectangular channel. The flow phenomenology of a granular column collapse in a rectangular channel was surprisingly similar to that observed in the axis-symmetric collapse ([Lajeunesse et al., 2004](#); [Lube et al., 2005](#)), depending mainly on the initial aspect ratio ‘ $a$ ’. The flow dynamics involve spreading of granular mass by avalanching of flanks producing

<sup>16</sup> a truncated cone for  $a \lesssim 0.74$  and a cone for  $a \gtrsim 0.74$ ; the transition of flow dynamics occurs  
<sup>17</sup> as the value of ‘ $a$ ’ is increased. The evolution of the deposit height remains independent of the  
<sup>18</sup> flow for  $a \lesssim 0.7$ , however it exhibits significant dependence on the geometrical configuration  
<sup>19</sup> for  $a \gtrsim 0.7$ . In rectangular channels, the effect of sidewall on the run-out behaviour was  
<sup>20</sup> observed; the surface velocity profile between the sidewalls is that of a plug flow with a high  
<sup>21</sup> slip velocity at the wall and low shear along the direction transverse to the flow. Systematic  
<sup>22</sup> measurements indicate that the ratio of the maximum surface velocity to the surface velocity at  
<sup>23</sup> the wall is between 1.2 and 1.4. [Lajeunesse et al. \(2005\)](#) observed that the difference between  
<sup>24</sup> the evolution of  $H_f$  in the axis-symmetric geometry and in the rectangular channel is not an  
<sup>25</sup> experimental artefact due to the side wall friction, but is a *geometrical effect*.

<sup>26</sup> Understanding the internal flow structure will provide an insight into the complex collapse  
<sup>27</sup> dynamics. For smaller values of aspect ratio ‘ $a$ ’  $\leq 0.7$ , the flow is initiated by a failure at  
<sup>28</sup> the edge of the pile along a well-defined fracture surface above which material slides down  
<sup>29</sup> and below which the grains remain static. The grains located above the fracture move “*en*  
<sup>30</sup> *masse*” and most of the shear is concentrated along this surface forming a “*truncated-cone-like*”  
<sup>31</sup> deposit with a central motionless plateau. For columns with larger aspect ratios, the flow is still  
<sup>32</sup> initiated by failure along a well-defined surface, an inclined plane in two-dimensional geometry  
<sup>33</sup> or a cone in the axis-symmetric case. However, the initial height of the column is much higher  
<sup>34</sup> than the top of the failure surface, causing a vertical fall of grains until they reach the summit  
<sup>35</sup> where they diverge along the horizontal direction, dissipating a lot of kinetic energy, resulting  
<sup>36</sup> in a final conical deposit. Interestingly, the final deposit height coincides with the summit of  
<sup>1</sup> the failure surface in the axis-symmetric geometry, whereas in the rectangular channel, the  
<sup>2</sup> deposit summit always lies above the top of the failure surface ([Lajeunesse et al., 2005](#)).  
<sup>3</sup>

<sup>4</sup> Identification of the static region is an important task, as it is a prime component in  
<sup>5</sup> describing the collapse mechanism. Regardless of the experimental configuration, for all values  
<sup>6</sup> of ‘ $a$ ’ the flow is initiated by rupture along a well-defined failure surface and the failure angle  
<sup>7</sup> remains of the order of  $50^\circ$  to  $55^\circ$ . The failure angle is consistent with an interpretation of  
<sup>8</sup> *active Coulomb failure*, which leads to a failure angle  $\phi_f = 45^\circ + \delta/2$ , where  $\delta$  is the internal  
<sup>9</sup> friction angle of the granular material. Estimating the internal friction angle of glass beads from  
<sup>10</sup> the angle of repose as  $22^\circ$ , the failure angle is estimated as  $56^\circ$ , which is in good agreement  
<sup>11</sup> with the experimental findings. Contrary to the suggestion of [Lajeunesse et al. \(2004\)](#), the  
<sup>12</sup> fracture angle was found to have no direct effect on the transition between truncated cone and  
<sup>13</sup> conical deposit occurring at aspect ratio ‘ $a$ ’ of 0.7 ([Lajeunesse et al., 2005](#)). ? observed the  
<sup>14</sup> onset of instability, when the neutrally stable plane waves makes an angle of  $\phi_I$  with the major  
<sup>15</sup> principle stress axis. The onset of instability triggers unstable plane waves in a narrow wedge of  
<sup>16</sup>  $56^\circ$  to  $65^\circ$ , which corresponds to the angle of shear bands: this observation matches well with  
<sup>17</sup>

the failure angle observed in the granular flow. A rate-dependent constitutive relationship (Jop et al., 2006) for dense granular flows indicates the angle of shear-band orientation depends on the inertial number  $I$ . For small to moderate values of  $I$ , the orientation of shear bands is found to vary from the Roscoe and the Coulomb solutions to a unique admissible angle (Lemiale et al., 2011). Daerr and Douady (1999) observed active Coulomb-type yielding in transient surface flows for granular materials having a packing density of 0.62 to 0.65. The comparison of initial and final areas indicates a change in the packing; the initial area is systematically smaller than the final area. This change in packing is typical of granular slumping in a channel and reflects that the pile, which initially had a relatively close packing, expanded (by about 10%) as the flow progressed, to form the final deposit (Balmforth and Kerswell, 2005).

A critical time  $\tau_c$  is defined as the transition time at which the flow is fully developed. The velocity field then depends on the position of grains along the pile, see Lajeunesse et al. (2005). In the front, the flow involves the entire thickness of the pile and corresponds to a plug flow in the horizontal direction. In the region above the static core, the flow is locally parallel to the failure surface and has an upper linear part and a lower exponential tail near the static bed (Lajeunesse et al., 2005). The velocity flow profile is similar to that of a steady granular flow (Midi, 2004). As the pile spreads, interface separation occurs as the flow diverges and the static region starts to move inwards; this effect is predominant in the case of granular flows in a rectangular channel. The typical velocity observed at the front of the ejecting mass is  $v = \sqrt{2gR_i}$ . The flow evolution as per Staron et al. (2005) involves three stages. The first stage involves conversion of the initial potential energy of the grains into vertical motion, resulting in downwards acceleration of grains. In the second stage, the grains undergo collision with the base and/or neighbouring grains, and their vertical motion is converted into horizontal motion. In the final stage, the grains eventually leave the base area of the column and flow sideways. The typical time required for the flow to cease and form the final deposit, from the instant of its release, is  $T = \sqrt{2H_i/g}$  (Staron et al., 2005). While plotting the variation of normalized potential and kinetic energy with normalized time, Staron et al. (2005) observed that the flow ceases when the normalized time  $t/T_0$  is 2.5, i.e. the flow is assumed to have stopped when the total normalized energy is almost zero. This observation is consistent with the experimental results of Lube et al. (2005) and Lajeunesse et al. (2005). The transition of the flow occurs when the normalized time  $t/T_0$  is 1.0 or at critical time  $\tau_c$ , which is defined as the time at which the flow is fully mobilized.

### 13 Comments on modelling

14 In order to have a detailed understanding of the final profile of the collapsed granular column, it  
 15 is important to solve the collapse problem as an *initial-value problem* (Balmforth and Kerswell,

<sup>16</sup> 2005), beginning from the instant of release and extending to the time when the material  
<sup>17</sup> finally ceases to flow, forming the final deposit. As the process of granular collapse involves  
<sup>18</sup> collective dynamics of collisions and momentum transfer, the prediction of the trajectory of  
<sup>19</sup> a single grain is difficult. In fact, there are quantitative disagreements between theory and  
<sup>20</sup> experiments; the final shapes are reproducible, but not perfectly. Some of the disagreement  
<sup>21</sup> arises because the experiments did not have exactly the same amount of materials; it is indeed  
<sup>22</sup> difficult to fill the pile with exactly the same amount of material, which results in differences in  
<sup>23</sup> packing. However, the theoretical errors are due to the incapability of the models to capture  
<sup>24</sup> the physics that governs the flow dynamics (Balmforth and Kerswell, 2005). Shallow water  
<sup>25</sup> models fail to account for the vertical acceleration, which is responsible for the momentum  
<sup>26</sup> transfer and, in turn, the spreading process. This restricts the shallow water model to capture  
<sup>27</sup> the mechanism of collapse until the critical time  $\tau_c$ . Surprisingly, shallow-water models capture  
<sup>28</sup> certain experimental aspects for columns with lower aspect ratios (Balmforth and Kerswell,  
<sup>29</sup> 2005; Mangeney et al., 2010; ?), even though the contrast between surface flows and the static  
<sup>30</sup> region is important in this range of aspect ratio. Thus, the assumption of plug flow in the  
<sup>31</sup> horizontal direction is not critical in capturing the run-out behaviour, especially if the basal  
<sup>32</sup> friction coefficient is used as a fitting parameter (Lajeunesse et al., 2005).

<sup>33</sup> Simple mathematical models based on conservation of horizontal momentum capture the  
<sup>34</sup> scaling laws of the final deposit, however they fail to describe the initial transition regime,  
<sup>35</sup> indicating that the initial transition has negligible effect on the run-out, which is incorrect.  
Models based on the initial potential energy show promise, but the effect of material properties,  
such as basal friction and coefficient of restitution, on the run-out behaviour is still unclear  
and produces non-physical run-outs. The famous  $\mu(I)$  rheology predicts well the normalized  
run-out behaviour in comparison with the experimental results, for lower aspect ratios. The  
spreading dynamics is found to be similar for the continuum and particle approaches; however,  
the rheology falls short in predicting the run-out distance for higher aspect ratios. Unlike Lube  
et al. (2005), many researchers (Balmforth and Kerswell, 2005; ?) observed strong dependency  
of material properties on the run-out distance, moistening the materials or the sides of the  
channel even by a small amount leads to markedly different results. ? observed that the friction  
has little effect on the run-out for granular column collapse for high aspect ratios, which are  
driven mainly by the free vertical fall of grains. The initial conditions have a significant impact  
on the overall behaviour of the granular system, indicating the significance of the triggering  
mechanism in case of the natural flows (?). Numerical investigations, such as Discrete Element  
Method techniques, allow us to evaluate quantities which are not accessible experimentally, thus  
providing useful insight into the flow dynamics. Subsequent chapters discuss the methodology  
and modelling of granular column by continuum- and discrete-element approaches.

1  
2  
3  
4  
5  
6  
7  
8  
9  
10  
11  
12  
13  
14  
15  
16

### 2.3.2 Flow on inclined plane

17

Studies on the flow of granular materials down inclined planes are important to understand the mechanism of geophysical hazards, such as granular avalanches, debris flows and submarine landslides. Large scale field tests on dry and saturated granular materials were carried out to capture the mechanism of granular flows down an inclined plane (Denlinger and Iverson, 2001; Okada and Ochiai, 2008). The granular material stored in a reservoir at the top of the inclined plane is released by opening a gate; the material flows down and develops into a dense granular flow. A variant of this experiment is the experiment on fluidized beds which involves an initial bed of granular material of thickness ‘ $h$ ’ which is inclined gradually until the granular material flows. When the plane inclination reaches a critical angle,  $\theta_{start}$ , the material starts to flow and reaches a sustained flow until the inclination is decreased down to a second critical angle,  $\theta_{stop}$  (Midi, 2004). The occurrence of two critical angles indicates the hysteretic nature of granular materials. Reciprocally, the critical angle thresholds can be interpreted in terms of critical layer thicknesses  $h_{stop}(\theta)$  and  $h_{start}(\theta)$ . The measurement of  $h_{stop}(\phi)$  is easier as it corresponds to the thickness of the deposit remaining on the plane once the flow has ceased. Three regions can be observed: a region where no flow occurs, ( $h < h_{stop}(\theta)$ ), a sub-critical region where both static and flowing layers can exist ( $h_{stop}(\theta) < h < h_{start}(\theta)$ ) and a region where flow always occurs, ( $h > h_{start}(\theta)$ ). In the flow regime, i.e. ( $h > h_{start}(\theta)$ ), the flow is steady and uniform for moderate inclination, but accelerates along the plane for large inclinations (Midi, 2004). The critical angle controlling the flow behaviour tends to increase

- 1 when the thickness of the bed decreases (Daerr and Douady, 1999; Pouliquen and Chevoir,
- 2 2002), which can be attributed to the non-trivial finite-size effects and/or boundary effects that
- 3 are not well understood (Forterre and Pouliquen, 2008).

4 Fast moving granular flows can undergo a motion-induced self-fluidization process under  
 5 the combined effects of front instabilities setting on at large values of the Froude number which  
 6 are responsible for extensive air entrainment, and small deflation rates associated with small  
 7 incipient fluidization velocities and longer collapse time of the bed solids. Self-fluidization  
 8 results in enhanced mobility of the solids, causing an inviscid flow to an extent that may largely  
 9 exceed the establishment of a “*granular liquid*” state in purely granular flow (Bareschino  
 10 et al., 2008). It is understood that, for a granular material to flow, it has to exceed a certain  
 11 critical threshold, i.e. the friction criterion: the ratio of shear stress to normal stress. As  
 12 there is no internal stress scale for a granular material, granular materials exhibit solid-fluid  
 13 transition behaviour based on the friction criterion (Forterre and Pouliquen, 2008). The stress  
 14 ratio in the flowing regime above the static bed indicates the solid-to-fluid transition is a  
 15 yielding phenomenon and can be described by Mohr-Coulomb-like failure criterion (Zhang and  
 16 Campbell, 1992). This is in contrast to the mechanism of behaviour of other complex fluids,

where there is an internal stress scale linked to the breakage of microscopic structure. From a microscopic point of view, the strength of the granular materials is due to the internal friction between grains, but packed frictionless materials still exhibit macroscopic friction.

Constitutive laws based on Plasticity-theories relate the micro-structure to the macroscopic behaviour (Roux and Combe, 2002), which provide useful insight into the mechanism of granular flow. However, at present they are limited to initiation of deformation and do not predict the quasi-static flow. Material Point Method simulation of granular flow down an inclined plane (??) captures the flow behaviour in the initial stages, however it exhibits inconsistent behaviour when the granular material ceases to flow. This may be due to the application of small deformation theory to a large deformation problem and to the use of zero dilation. In the case of flow down an inclined plane, the only control parameter is the flow rate,  $Q$ , and uniform, steady flows are possible if the system is confined between walls. The additional friction induced by the lateral walls has a significant effect on the flow and causes localization at the free surface. The  $\mu(I)$  friction law captures the velocity profile and the localization at the free surface. However, the model fails to capture the transition from a continuous flow to an avalanching regime as the flow rate is decreased (Pouliquen et al., 2006). The flow can cause strong Coulomb shear stresses to develop on a plane normal to the basal flow boundary. The stresses dissipate energy as the flow encounters obstructions: models that lack multi-dimensional momentum transport or Coulomb friction cannot represent this energy dissipation and lodging.

1

### 2.3.3 Saturated and submerged granular flows

Geophysical hazards, such as debris flows and submarine landslides, usually involve flow of granular solids and water as a single-phase system. The momentum transfer between the discrete and continuous phases significantly affects the dynamics of the flow as a whole (Topin et al., 2011). Although certain macroscopic models were able to capture simple mechanical behaviours (Peker and Helvacı, 2007), the complex physical mechanisms occurring at the particle scale, such as hydrodynamic instabilities, formation of clusters, collapse, and transport (Topin et al., 2011), have largely been ignored. In particular, when the solid phase reaches a high volume fraction, the strong heterogeneity arising from the contact forces between the particles, and the hydrodynamic forces, are difficult to integrate into the homogenization process involving global averages (Topin et al., 2011). In two-phase models (Pitman and Le, 2005), the momentum transfer between the particles and the suspension fluid depends on the momentum equations of both the phases. In case of mixture theory based models (Meruane et al., 2010), the shear-induced migration and particles collisions are considered in an average sense. In order to describe the mechanism of saturated and/or immersed granular flows, it

2

3

4

5

6

7

8

9

10

11

12

13

14

15

16

is important to consider both the dynamics of the solid phase and the role of the ambient fluid (Denlinger and Iverson, 2001; Iverson, 1997). The dynamics of the solid phase alone are insufficient to describe the mechanism of granular flow in a fluid; it is important to consider the effect of hydrodynamic forces that reduce the weight of the solids inducing a transition from dense-compacted to dense-suspended flows, and the drag interactions which counteract the movement of the solids (Meruane et al., 2010). Cassar et al. (2005) carried out experimental investigation on the flow of dense granular material down an inclined plane fully-immersed in water. The velocities observed in the submarine case were found to be a magnitude smaller than the dry condition. However,  $\mu(I)$  rheology for dry dense flows captures the behaviour of dense submarine granular flows, if the inertial time scale in the rheology is replaced with a viscous time scale. In the case of dry granular flows, the parameter  $I$  is defined as the ratio between the time taken for a particle to fall into the hole,  $t_{micro}$ , and the meantime,  $t_{mean}$ , which is inversely related to the shear rate. Pitman and Le (2005) observed that if the fluid inertial effects are small enough, then a simpler model can be adopted. Hence, assuming that the fluid velocity is low enough for the contact interaction between particles to be significant, the time taken by the particle to fall into a hole,  $t_{micro}$ , is then controlled by the viscosity of the ambient fluid. Thus, the dimensionless parameter can be modified to incorporate the viscous time to describe granular flow in a fluid (Pouliquen et al., 2005).

The constitutive law is found to be valid only for the steady uniform regime; unsteady phenomena such as the triggering of avalanches result in coupling between the granular particles and the ambient fluid and are much more complex to model. Transient regimes characterized by change in solid fraction, dilation at the onset of flow and development of excess pore pressure, result in altering the balance between the stress carried by the fluid and that carried by the grains, thereby changing the overall behaviour of the flow (Denlinger and Iverson, 2001). The  $\mu(I)$  rheology seems to predict well the flow of granular materials in the dense regime. However, the transition to the quasi-static regime where the shear rate vanishes is not captured by the simple model. Also, shear band formation observed under certain flow configurations is not predicted. The flow threshold or the hysteresis characterizing the flow or no-flow condition is not correctly captured by the model, which can be due to the discrepancies between the physical mechanism controlling the grain level interactions, clustering, and vortex formations. When the scale of the system is larger than the size of the structure, a simple rheology is expected to capture the overall flow behaviour, however the size of the correlated motion is the same as that of the system, causing difficulties in modelling the flow behaviour (Pouliquen et al., 2005). Hence, it is essential to study the behaviour of granular flows at various scales, i.e. microscopic, meso-scale and at continuum level, in order to develop a constitutive model that captures the entire flow process.

**2.4 Summary**

13

Granular flow involves three distinct regimes: the dense quasi-static regime, the rapid and dilute flow regime, and an intermediate regime. Many models, such as the shallow-water approximation, kinetic theory approach, and rheologies based on shear rate, have captured the basic flow dynamics, but have failed to describe the complete mechanics of the granular flow.

14

The dynamics of homogeneous granular flow involve at least three different scales, making it difficult to describe the mechanics of granular flow by simple theories. It is important to describe the granular dynamics as an initial-value problem, beginning from the instance of its initiation to the time at which the material ceases to flow, forming a final deposit. During this process, the granular materials undergo phase transition, in addition to the transition in their flow dynamics. Most theoretical models are incapable of capturing these transition regimes. Experimental

15

- 1 conditions are too difficult to reproduce precisely, resulting in inherent inconsistencies in the
- 2 results. Discrete numerical approaches, such as Discrete Element Method, allow us to evaluate
- 3 quantities which are not accessible experimentally, thus providing useful insight into the flow
- 4 dynamics, thereby enabling us to develop better constitutive laws. Subsequent chapters discuss
- 5 the continuum and particle-scale modelling of granular flows.

16

17

18

19

20

21

22

23

## <sup>6</sup> Chapter 3

### <sup>7</sup> Numerical modelling of granular flows

#### <sup>8</sup> 3.1 Introduction

<sup>9</sup> The dynamics of a homogeneous granular flow involve at least three distinct scales: the  
<sup>10</sup> *microscopic scale*, which is characterised by the contact between grains, the *meso-scale* that  
<sup>11</sup> represents micro-structural effects such as grain rearrangement, and the *macroscopic scale*,  
<sup>12</sup> where geometric correlations can be observed (see figure 3.1). Conventionally, granular flows  
<sup>13</sup> are modelled as a continuum because they exhibit many collective phenomena. However, on  
<sup>14</sup> a grain scale, the granular materials exhibit complex solid-like and/or fluid-like behaviour.  
<sup>15</sup> Recent studies, however, suggest that a continuum law may be unable to capture the effect  
<sup>16</sup> of inhomogeneities at the grain scale level, such as orientation of force chains, which are  
<sup>17</sup> micro-structural effects. Discrete element methods (DEM) are capable of simulating these  
<sup>18</sup> micro-structural effects, however they are computationally expensive. In the present study,  
<sup>19</sup> a multi-scale approach is adopted, using both DEM and continuum techniques, to better  
<sup>20</sup> understand the rheology of granular flows and the limitations of continuum models.

#### <sup>21</sup> 3.2 Continuum modelling of granular flows

<sup>22</sup> The most powerful way of modelling the granular assembly is through numerical techniques. It  
is important to argue, why it is acceptable to model the granular materials as a continuum. At  
the outset, it may even appear for some reasons why such a treatment is objectionable. Most  
obvious is the fact that the micro-constituents of granular matter, i.e. the individual grains are  
not small enough to warrant a continuum description ([Kamrin et al., 2007](#)). Typical continuum  
laws are only expected to apply when there is a strong separation of scales, i.e. separation  
of the micro-scale from the macro-scale, in the flow geometry. Continuum mechanics relies

1  
2  
3  
4  
5  
6

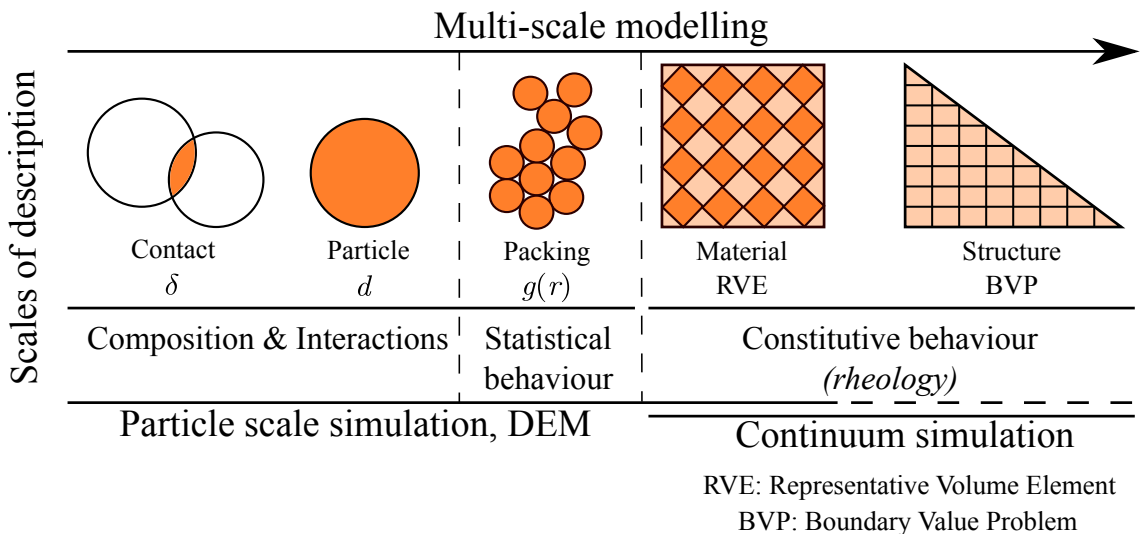


Figure 3.1 Multi-scale modelling of granular materials

on the fundamental notion of a representative volume element, in which properties averaged over discrete particles exhibit deterministic relationships. Recent works on granular materials suggest that a continuum law may be incapable of revealing in-homogeneities at the particle-scale level, such as force chains (?). Granular materials exhibit many collective phenomenon (Jaeger et al., 1996). However, no continuum model is still capable of describing the parabolic flow, the plug flow (Rycroft et al., 2006) and the occurrence of localized shear bands in the granular materials. This is in contrast to the hydrodynamics of dilute granular materials and the molecular fluids for which accurate continuum models can be systematically derived, by averaging over particle collisions in an idealized element (Jenkins and Savage, 1983). The fundamental question is how to model granular materials which exhibit complex phenomenon, meaningfully.

The oldest approach involves modelling the granular material as a rigid solid, which behaves as an ideal Coulomb material and undergoes failure if the ratio of the shear stress to the normal stress in any plane reaches a critical value of the Coulomb internal friction coefficient  $\mu$ . The stress is determined based on the mechanical equilibrium of the system along with the hypothesis of *incipient yield*, i.e. the yield criterion is attained everywhere at all times. In limit-state Mohr-Coulomb plasticity, these conditions are assumed to hold even if the wall allows for a plastic yielding, due to the assumption of coaxiality (?). The fundamental assumption of a limit-state stress field at incipient yield everywhere is questionable. Granular flows can contain regions lying within the yield surface. For example, in the case of a granular column collapse the central cone remains stagnant, and thus cannot be considered as yielded. In fact, discrete-element simulations show that the grains in this region essentially remain static (Staron

et al., 2005). The coaxiality feature of Mohr-Coulomb plasticity is useful in describing the debris flow. Granular material deforms solely based on the alignment of the principle plane. In general, the major principle plane is usually vertical due to gravity, and the coaxiality rule requires the material to expand horizontally, which is the case for granular column collapse. However, the coaxiality can be troubling depending on the circumstances, for example, in a slow dense granular flow through a silo, the principle plane remains vertical and the coaxiality requires the granular material to expand horizontally, thus making it geometrically impossible for the granular material to converge and exit through the orifice. Depending on the boundary conditions, Mohr-Coulomb plasticity can result in discontinuity or jumps in the velocity and stress fields (Rycroft et al., 2006). Advanced elasto-plastic models based on *critical state* theories provide a better representation of granular flows in quasi-static regime, but they fail to capture the mechanism of rapid granular flows which involves rate dependent behaviour. Another continuum based model is the partial fluidization model, which uses a set of equations that describes the flow velocity and the shear stresses along with a auxiliary order parameter to predict the granular flow behaviour. The order parameter of the granular media controls the size of the viscous-like contribution to the stress tensor, and describes the transition between the flowing and the static components of the granular system (Aranson and Tsimring, 2001). A constitutive model, which considers the solid fraction as the main microscopic parameter for describing dense granular flow was proposed by Josserand et al. (2004). The stress in the granular material is divided into rate-dependent part representing the rebound-less impact between grains, and a rate-independent part associated with longer contacts, i.e. quasi-static regime. Although, the model captures shear localization behaviour, it fails to describe the granular flow behaviour at rough boundaries.

Granular materials are composed of distinct grains, which displace independently from one another and interact only at contact points. It is assumed that the deformations of individual grains are negligible in comparison with the deformation of the granular assembly as a whole. The latter deformation is primarily due to the movement of the grains as a rigid body. Therefore, it can be argued that precise modelling of particle deformation is not necessary to obtain a good approximation of the overall mechanical behaviour. An Eulerian grain-level continuum model describes the response of individual grains to the applied loads. However, continuum mechanics solves over the whole domain using initial and boundary conditions appropriate for the problem. Hence, continuum models are still widely used to solve engineering problems associated with granular materials and flows. Conventional mesh based approaches, such as Finite Element Method or Finite Difference Method involves complex re-meshing and remapping of variables, which causes additional errors in simulating large deformation problems (Li and Liu, 2002). Mesh free methods such as Material Point Method are not constrained by the mesh size and

<sup>29</sup> mesh distortion, and hence can be effectively used in simulating large deformation problems,  
<sup>1</sup> such as debris flow and submarine landslides.

### <sup>2</sup> 3.3 Material Point Method (MPM)

<sup>3</sup> Material Point Method (MPM) ([Sulsky et al., 1994, 1995](#)) is a particle based method that  
<sup>4</sup> represents the material as a collection of *material points*, and their deformations are deter-  
<sup>5</sup> mined by *Newton's laws of motion*. [Sulsky et al. \(1994\)](#) extended the Particle-in-Cell (PIC)  
<sup>6</sup> method ([Harlow, 1964](#)) to computational solid mechanics by taking advantage of the combined  
<sup>7</sup> Eulerian-Lagrangian approach. Material Point Method is a hybrid Eulerian-Lagrangian ap-  
<sup>8</sup> proach, which uses moving material points, and computational nodes on a background mesh.  
<sup>9</sup> This approach is very effective particularly in the context of large deformations ([??](#)). Although,  
<sup>10</sup> not derived directly from what is classically considered as mesh-free or mesh-less methods,  
<sup>11</sup> MPM is still considered as a mesh-free approach, primarily because the initial discretization of  
<sup>12</sup> the material does not involve a polygonal tessellation, as in Finite Element Method. However,  
<sup>13</sup> MPM utilizes a background mesh to perform differentiation, integration, and to solve equations  
<sup>14</sup> of motions ([Steffen et al., 2008](#)). The background mesh can be of any form, however for  
<sup>15</sup> computational efficiency a Cartesian lattice is adopted. A typical 2D discretization of a solid  
<sup>16</sup> body is shown in figure [3.2](#).

<sup>17</sup> The grey-shaded circles are the material points ( $X_p$ , where 'p' represents a material point)  
<sup>18</sup> and the computational nodes are the points of intersection of the grid (denoted as  $X_i$ , where  
<sup>19</sup>  $i$  represents a computational node). The Material Point Method involves discretizing the  
<sup>20</sup> domain  $\Omega$  with a set of material points. The material points are assigned an initial value of  
<sup>21</sup> position, velocity, mass, volume, and stress denoted as  $\mathbf{x}_p$ ,  $v_p$ ,  $m_p$ ,  $\mathbf{V}_p$  and  $\sigma_p$ . Depending on  
<sup>22</sup> the material being simulated, additional parameters, like pressure, temperature, etc., should be  
<sup>23</sup> specified at the material points. The material points are assumed to be within the computational  
<sup>24</sup> grid, which is assumed to be a Cartesian lattice for convenience (see figure [3.2](#)). At every  
<sup>25</sup> time step  $t_k$ , the MPM computation cycle involves projecting the data, such as position, mass,  
<sup>26</sup> and velocity from the material points to the computational grid using standard nodal basis  
<sup>27</sup> functions, called *shape functions*, derived based on the position of particle with respect to the  
<sup>28</sup> grid. Gradient terms are calculated in the computational grid and the governing equation, i.e.  
<sup>1</sup> the equation of motion, is solved and the updated position and velocity values are mapped back  
<sup>2</sup> to the material points. The mesh is reinitialized to its original state and the computational cycle  
<sup>3</sup> is repeated.

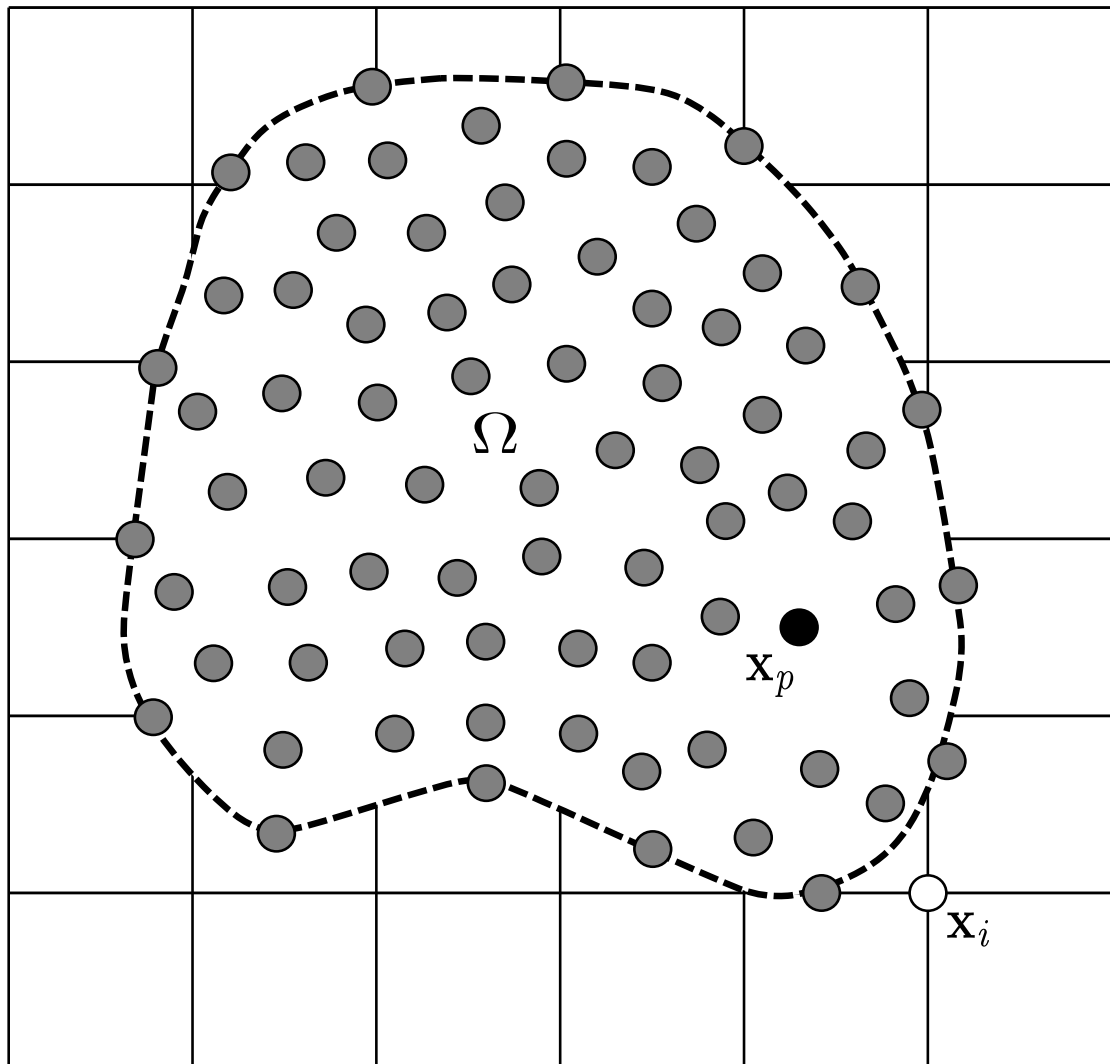


Figure 3.2 Typical discretization of a domain in MPM. The dotted line represents the boundary of the simulated object  $\Omega$  and each closed point represents a material point used to discretize  $\Omega$ . The square mesh represents the background grid. Each square in the background grid is a grid cell, and grid nodes are located at the corners of grid cells.

### 3.3.1 Discrete formulation of the governing equations

The governing differential equation for a continuum is derived from the conservation of mass and momentum.

$$\frac{\partial \rho}{\partial t} \rho \Delta \cdot v = 0 \quad (3.1)$$

and

$$\rho a = \Delta \cdot \sigma + \rho b \quad (3.2)$$

where  $\rho(\mathbf{x}, t)$  is the mass density,  $\mathbf{v}(\mathbf{x}, t)$  is the velocity,  $\mathbf{a}(\mathbf{x}, t)$  is the acceleration,  $\sigma(\mathbf{x}, t)$  is the Cauchy's stress tensor, and  $\mathbf{b}(\mathbf{x}, t)$  is the body force. The vector  $\mathbf{x}$  represents the current position of any material point in the continuum, at time  $t$ . MPM discretizes the continuum body into finite number of material points  $N_p$ . Let  $\mathbf{x}_p^t$  ( $p = 1, 2, \dots, N_p$ ) denote the current position of material point  $p$  at time  $t$ . Each material point, at any given time  $t$ , has an associated mass  $m_p^t$ , density  $\rho_p^t$ , velocity  $v_p^t$ , Cauchy stress tensor  $\sigma_p^t$ , strain  $\epsilon_p^t$ , and other necessary internal state variables based on the adopted constitutive model. These material points provide a Lagrangian description of the continuum body, since material points have a fixed mass at all times, eq. 3.1 is satisfied. The data from the material points are mapped on to the nodes of the computational grid, where the discrete form of eq. 3.2 is described. The weak form of eq. 3.2 is obtained by multiplying eq. 3.2 with a test function  $w(\mathbf{x}, t)$ .

$$\int_{\Omega} \rho \mathbf{w} \cdot a d\Omega = - \int_{\Omega} \rho \sigma^s : \Delta w d\Omega + \int_{\partial\Omega_t} w \cdot \tau dS + \int_{\Omega} \rho w \cdot \mathbf{b} d\Omega \quad (3.3)$$

where  $\sigma^s$  is the specific stress (i.e. stress divided by mass density,  $\sigma^s = \sigma/\rho$ ),  $\Omega$  is the current configuration of the continuum,  $\tau$  is the traction. eq. 3.3 is obtained by applying the divergence theorem, similar to the standard procedure adopted in Finite Element Methods (Chen and Brannon, 2002; Sulsky et al., 1994, 1995). The differential volume and the surface elements are denoted by  $d\Omega$  and  $dS$ , respectively.

- <sup>1</sup> As the whole continuum is discretized into a finite set of material points, the mass density can
- <sup>2</sup> be written as:

$$\rho(\mathbf{x}, t) = \sum_{p=1}^{N_p} M_p \delta(x - x_p^t) \quad (3.4)$$

## 3.3 Material Point Method (MPM)

## 53

5 where  $\delta$  is the Dirac delta function. Substituting [eq. 3.4](#) in [eq. 3.3](#), the sum of quantities of  
6 material points can be evaluated as:

$$7 \quad \sum_{p=1}^{N_p} M_p [w(x_p^t, t) \cdot \mathbf{a}(x_p^t, t)] = \sum_{p=1}^{N_p} M_p [-\boldsymbol{\sigma}^s(x_p^t, t) : \Delta w|_{x_p^t} \\ 8 \quad + w(x_p^t, t) \cdot \boldsymbol{\tau}^s(x_p^t, t) h^{-1} + w(x_p^t, t) \cdot b(x_p^t, t)] \quad (3.5)$$

10 where  $h$  is the thickness of the boundary layer. It can be noted from [eq. 3.5](#) that the interactions  
11 between different material points are reflected only through the gradient terms. In MPM, a  
12 background computational mesh is used to calculate the gradient terms. The computational  
13 mesh is constructed using 2-node cells for 1-D, 4-node cells for 2-D, and 8-node cells for  
14 3-D problems. These elements are used to define the standard nodal basis functions,  $N_i(\mathbf{x})$ ,  
15 associated with the spatial nodes  $x_i(t), i = 1, 2, \dots, N_n$ , where  $N_n$  represents the total number of  
16 mesh nodes. The nodal basis functions are assembled by using the conventional finite-element  
17 shape functions ([Chen and Brannon, 2002](#)). The co-ordinates of any material point in a cell can  
18 be represented by

$$19 \quad x_p^t = \sum_{i=1}^{N_n} x_i^t N_i(\mathbf{x}_p^t) \quad (3.6)$$

21 Similarly the nodal displacements, velocity and acceleration of any material point in a cell are  
22 represented using the basis functions. Thus, the test function has to be of the form:

$$23 \quad w_p^t = \sum_{i=1}^{N_n} w_i^t N_i(\mathbf{w}_p^t) \quad (3.7)$$

25 [eq. 3.6](#) and [3.7](#) ensures that the associated vectors are continuous across the cell boundary.  
26 However, the gradient of these functions are not continuous, due to the use of linear shape  
27 functions. Substituting, [eq. 3.6](#) and [3.7](#) into [eq. 3.5](#), the weak form of the equation of motion  
28 reduces to:

$$29 \quad \sum_{j=1}^{N_n} m_{ij}^t \mathbf{a}_j^t = \mathbf{f}_i^{int,t} + \mathbf{f}_i^{ext,t} \quad (3.8)$$

31 where the nodal mass,  $m_{ij}^t$  is represented as:

$$m_{ij}^t = \sum_{p=1}^{N_p} M_p N_i(x_p^t) N_j(x_p^t) \quad (3.9)$$

The nodal internal force,  $\mathbf{f}_i^{int,t}$  and the nodal external force,  $\mathbf{f}_i^{ext,t}$  are defined as:

$$\mathbf{f}_i^{int,t} = - \sum_{p=1}^{N_p} M_p \mathbf{G}_{ip}^t \cdot \boldsymbol{\sigma}_p^{s,t} \quad 4$$

$$\mathbf{f}_i^{int,t} = - \sum_{p=1}^{N_p} M_p \mathbf{b}_p^t N_i(\mathbf{x}_p^t) + \sum_{p=1}^{N_p} M_p N_i(\mathbf{x}_p^t) \tau_p^{s,t} h^{-1} \quad 5$$

where  $\mathbf{G}_{ip}^k = \Delta N_i(x)|_{x=X_p^t}$ . The nodal accelerations are obtained by explicit time integration of eq. 3.8. To obtain stable solutions, the time step used in the analysis should be less than the critical time step, which is defined as the ratio of the smallest cell size to the wave speed (Chen and Brannon, 2002). The boundary conditions are enforced on the cell nodes and the nodal velocities are obtained by solving the equation of motion at each node. The strain increment for each material point is determined using the gradients of the nodal basis functions. The corresponding stress increments are computed using the adopted constitutive law. After all the material points have been completely updated, the computational mesh is discarded, and a new mesh is defined for the next time step.

### 1 3.3.2 Boundary conditions

2 The Material Point Method uses standard shape functions, similar to those used in the Finite  
 3 Element Methods, hence the essential and the natural boundary conditions can be applied  
 4 to the background grid nodes in the same way as in the traditional FEM. The free surface  
 5 boundary conditions are satisfied, as MPM is formulated in the weak form. Implementation  
 6 of traction boundary conditions requires a set of material points to represent the boundary  
 7 layer. ? proposed a friction interaction for the planar boundary condition, using Coulomb's  
 8 friction criterion. The nodal accelerations were considered to include the frictional effects  
 9 instead of the forces, as the forces are proportional to the corresponding accelerations. The  
 10 static and kinematic frictions are applied tangential to the nodal boundary. Friction forces  
 11 are applied, only if the particles are in contact. The normal velocity and acceleration on the  
 12 boundary plane is zero. The shape functions used in the MPM are continuous, and hence  
 13 penetration between bodies are handled automatically without the need for any supplemental  
 14 contact algorithm (Chen and Brannon, 2002). In the MPM, the continuum body deforms and  
 15 moves in an arbitrary computation grid and all the boundary conditions are carried by the  
 16 boundary particles. If a boundary particle is present in a cell, then the cell boundary becomes a  
 17 part of the continuum body, and the cell size represents the thickness of the boundary. However,  
 18 in certain cases both the boundary particle and an interior particle can be found in a cell, in

which case the cell is still treated as a boundary cell, and the interior particle temporarily acts as a boundary particle. To avoid numerical errors, it is essential to consider smaller cell size along the boundary ([Chen and Brannon, 2002](#)).

In the MPM simulations, numerical noises are observed when the material points crosses the cell boundaries during deformation of the material, this is termed as cell crossing noise. If a material point is located very close to the cell boundary, it results in discontinuous nature of the gradient of the weighing function causing a force imbalance on the grid ([Bardenhagen and Kober, 2004](#)). This results in large non-physical acceleration values resulting in separation of material points from the continuum ([Sulsky et al., 1995](#)). [figure 3.3](#) illustrates the problem of cell crossing noise. The main reason for the occurrence of cell crossing noise is the use of piecewise linear shape functions. However, this problem, which is predominant when using fine mesh size, can be overcome by changing the order of arithmetic operation as proposed by [Sulsky et al. \(1995\)](#). To overcome the problem of cell crossing noise, [Bardenhagen and Kober \(2004\)](#) proposed an alternate method called the Generalized Interpolation Material Point Method that uses smoother shape functions and a larger influence region for each grid node. This approach minimizes the cell crossing noise. However, special attention is required to simulate the boundaries in the Generalized Interpolation Material Point Method (GIMP).

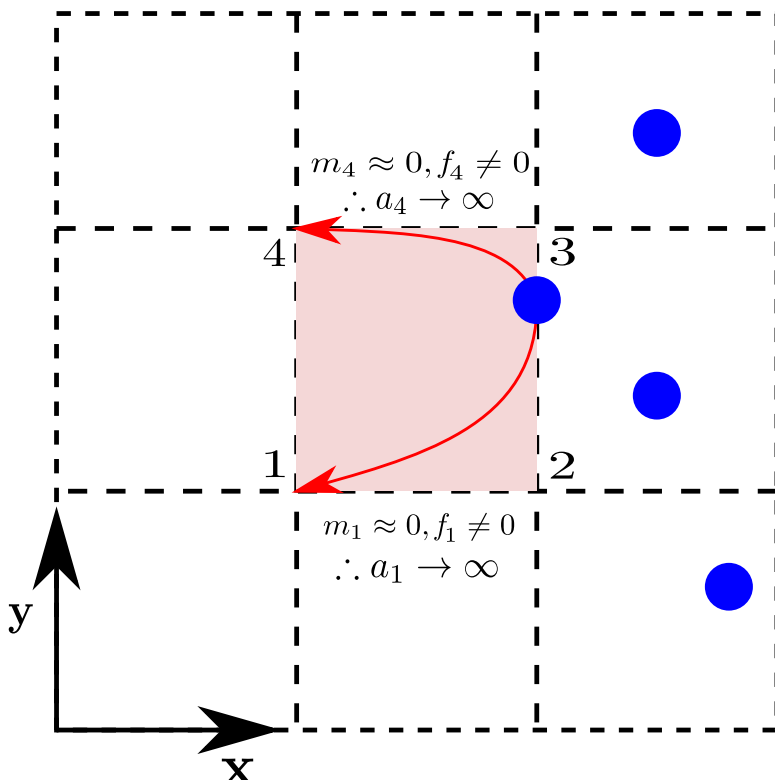


Figure 3.3 Cell crossing noise

**3.3.3 Solution scheme**

11

A step-by-step solution scheme for Material Point Method (?) is described below. It involves three stages: preprocessing, computation, and post-processing:

12

13

**Preprocessing**

14

- A continuum body is discretized into a finite set of material points corresponding to the original configuration of the body. The number of material points corresponds to the resolution of the mesh size adopted in Finite Element Method. The material points are followed throughout the deformation of the material, which gives a Lagrangian description of the motion.
- An arbitrary computational grid is initialized to describe the natural coordinates of the material points. For the purpose of simplicity, a Cartesian grid is usually adopted.
- The state variables (mass/density, velocity, strain, stress, other material parameter corresponding to the adopted constitutive relation) are initialized at every material point.

15

16

17

18

19

20

21

22

23

**Computation scheme**

24

- For each material point, the mapping of the properties from the particles to the cell nodes is accomplished using the shape functions computed from the particle position. The nodal mass matrix is obtained as:

$$m_i^k = \sum_{p=1}^{N_p} M_p N_{ip}^k \quad (3.11)$$

2

3

where  $m_i^t$  is the mass at node  $i$  at time  $t$ ,  $M_p$  the particle mass,  $N_i$  the shape function associated with node  $i$ , and  $x_p^t$  the location of the particle at  $t$ .

4

5

- The nodal velocity is obtained by mapping the particle velocity to the nodes using the shape functions:

$$v_i^k = \sum_{p=1}^{N_p} m_p v_p^t N_{ip}^t / m_i^t \quad (3.12)$$

6

7

8

9

- Strain increment  $\Delta\epsilon_p^{t+1}$  for particle is then computed as:

$$\Delta\epsilon_p^{t+1} = \frac{\Delta t}{2} \sum_{i=1}^{N_n} \mathbf{G}_{ip}^t \mathbf{v}_i^t + (\mathbf{G}_{ip}^t \mathbf{v}_i^t)^T \quad (3.13) \quad \begin{matrix} 11 \\ 12 \end{matrix}$$

- The stress increment for the particle  $\Delta\sigma_p^{t+1}$  is computed from the strain increment using the constitutive model adopted in the simulation

$$\Delta\sigma_p^{t+1} = \mathbf{D} : \Delta\epsilon_p^{t+1} \quad (3.14) \quad \begin{matrix} 15 \\ 16 \end{matrix}$$

- The stress and the strain of the material points are updated based on:

$$\begin{aligned} \sigma_p^{t+1} &= \sigma_p^t + \Delta\sigma_p^{t+1} \\ \epsilon_p^{t+1} &= \epsilon_p^t + \Delta\epsilon_p^{t+1} \end{aligned} \quad (3.15) \quad \begin{matrix} 18 \\ 19 \\ 20 \end{matrix}$$

- The material point density is then updated as:

$$\rho_p^{t+1} = \frac{\rho_p^t}{\{1 + \text{tr}(\Delta\epsilon_p^{t+1})\}} \quad (3.16) \quad \begin{matrix} 22 \\ 23 \end{matrix}$$

- Then the nodal acceleration is computed using the equation of motion as:

$$\mathbf{a}_i^t = (\mathbf{f}_i^{int,t} + \mathbf{f}_i^{ext,t}) / m_i^t \quad (3.17) \quad \begin{matrix} 25 \\ 26 \end{matrix}$$

- The nodal velocity is obtained from the computed nodal acceleration as:

$$v_i^L = \mathbf{v}_i^k + a_i^k \Delta t \quad (3.18) \quad \begin{matrix} 28 \\ 29 \end{matrix}$$

- Finally, the particle position and its velocity are updated according to:

$$\mathbf{x}_p^{t+1} = \mathbf{x}_p^t + \Delta t \sum_{i=1}^{N_n} v_i^L N_{ip}^t \quad (3.19) \quad \begin{matrix} 31 \\ 32 \end{matrix}$$

$$\mathbf{v}_p^{t+1} = \mathbf{v}_p^t + \Delta t \sum_{i=1}^{N_n} a_i^t N_{ip}^t \quad (3.19) \quad \begin{matrix} 32 \\ 33 \end{matrix}$$

- At the end of every time step, all the variables on the grid nodes are initialized to zero.

<sup>1</sup> figure 3.4 illustrates the steps involved in a MPM analysis.

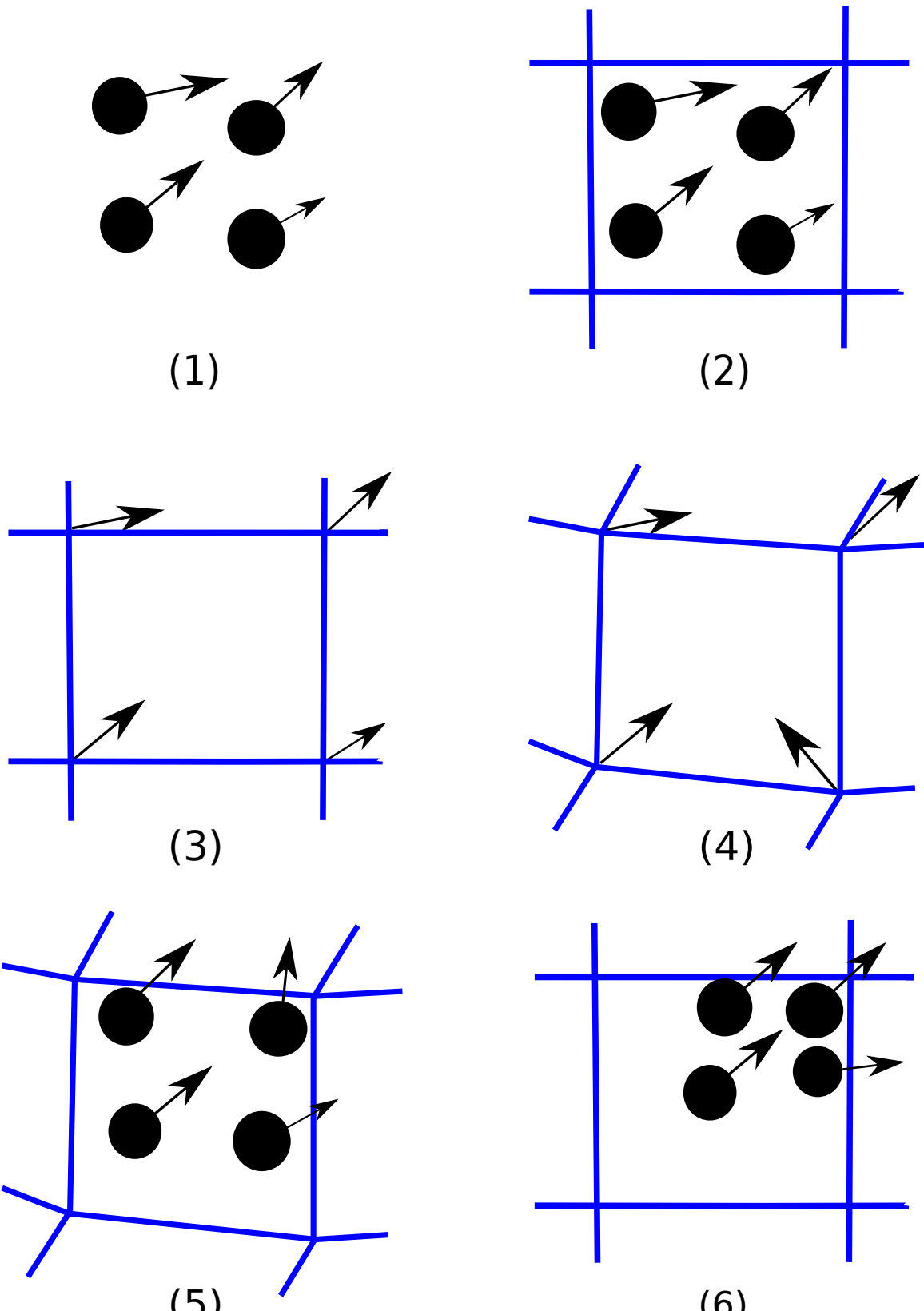


Figure 3.4 Illustration of the steps in the MPM algorithm for particles occupying a single cell in the background grid. (1). A representation of four material points (filled circles), overlaid with the computational grid (solid lines). Arrows represent displacement vectors. (2). The material point state vector (mass, volume, velocity, etc.) is projected to the nodes of the computational grid. (3). The discrete form of the equations of motion is solved on the computational grid, resulting in updated nodal velocities and positions. (4). The updated nodal kinematics are interpolated back to the material points and their state updated. (5). The computational grid is reset to its original configuration and the process repeated. Reproduced after [Bigler et al. \(2006\)](#)

## 2 Post processing

3 The final step in any analysis is post-processing. It involves visualization and extraction of  
4 the data from the analysis. In mesh-less methods, like the Material Point Method, structures  
5 are generally represented as points which represent a discrete region of the body. The MPM  
6 facilitates representation of arbitrarily complex geometries and is robust in computing large  
7 deformation problems. It has advantages over strictly grid based methods in simulations  
8 involving contact between multiple objects ([Bardenhagen et al., 2000](#)). The MPM poses a  
9 whole new set of visualization problem, it is essential to visualize the general configuration of  
10 the body as well as to observe the finer details like development of cracks or separation of chunk  
11 of material from the body. The body is discretized into conceptual material points, which carry  
12 all the relevant information of the corresponding segment. The unique qualities of the MPM  
13 necessitate the need to visualize the particle data in a way that is informative and appropriate.  
14 In the MPM, the particle data represents the finite portion of a larger continuum, and the  
15 ability to see and interpret the macroscopic structure created by these particles is vital ([Bigler](#)  
16 [et al., 2006](#)). There are two vital aspects in visualizing the MPM data: (1) visualization of the  
17 structure represented by material points, and (2) understanding the qualitative trend associated  
18 with the material points like mass, velocity or stress. The MPM output data contains both the  
19 material point and the grid data, one approach in visualizing the MPM data is by rendering the  
20 interpolated particle values on grid nodes using *iso-surfacing* ([Lorensen and Cline, 1987](#)) or  
21 *volume rendering* ([Levoy, 1988](#)) technique. In regions where the material points are sparse, it is  
22 necessary that the grid resolution to be sufficiently fine to compensate for the missing features.  
23 This results in storing large amount of unnecessary data in regions where sufficient material  
24 points are present. Thus, it is advantageous to visualize the MPM data of the material points as  
25 particles ([Bigler et al., 2006](#)). Particle visualization involves rendering the particles as a sphere  
26 or an ellipsoid representing the size and location of the fraction of the continuum ([Gumhold,](#)  
27 [2003; Krogh et al., 1997; Kuester et al., 2001](#)). Colour mapping of scalar quantities such as  
28 mass, velocity, or stress of a material point provide additional qualitative understanding of data.

29 The accuracy of the MPM simulations largely depends on the number of material points  
30 representing the continuum. The MPM utilizes a grid to compute the deformation of the  
31 continuum, hence the size of the cells affects the accuracy of the results. Generally in the MPM,  
32 the number of particles per cell controls the accuracy of the simulation. [Guilkey et al. \(2003\)](#)  
33 recommends higher particle density, such as 4 particles per cell, for large deformation problems.  
34 Very low particle density will result in non-physical opening of cracks in large deformation  
35 simulations and can be a source for the cell crossing noise. However, higher value of particle  
density affects the computation time.

## 3.4 Particulate modelling of granular flows

### 3.4.1 Introduction

Granular materials often exhibit different behaviour under different circumstances. Fluidized granular material often resembles a liquid, and reveals surface waves. In certain situations, granular materials behave more like a solid exhibiting plastic deformations. Despite the wide variations in the physical and chemical properties of the grains, the discrete granular structure has a rich generic phenomenology, which motivates us to understand the fundamental behaviour of these materials. A granular material can be considered as a continuous material if it is viewed at a macroscopic scale, ignoring the fact that it is composed of grains. On a macroscopic scale, the behaviour of the granular material could be approximately defined using continuum mechanics. However, On a particle level, the granular materials exhibit complex solid-like and/or fluid like behaviour depending on the way the grains interact with each other. The Analytical and Finite Element models, which consider granular materials as continuum cannot take into account the local geometrical processes that govern the mechanical behaviour of a non-homogeneous soil. The application of continuum models to describe granular flow poses subtle problems for statistical analysis (Mehta and Barker, 1994). The particle level description of the granular material enriches the macro-scale variables which poorly account for the local rheology of the materials. Numerical models based on the Discrete Element approach proposed by ? are capable of simulating the granular material as a discontinuous system. Although, modern measurement techniques can probe into the local granular variables, like particle position, velocities, contact forces, etc., they have inherent limitations in acquiring those variables. The *discrete-element* approach is a powerful and reliable research tool to study the behaviour granular materials at the grain-scale. This approach involves applying Newton's equation of motion simultaneously to all particles described as rigid solid bodies by considering the contact forces and the external forces acting on the particles. For a given boundary condition, the collective mechanical response of particles to the external force leads to the relative motion between particles constrained in a dense state and/or by in-elastic collisions in the loose state. ? applied this method to granular geomaterials, and called it the *Distinct Element Method*, to differentiate from the existing *Finite Element method* used in geomechanics. The attribute "distinct" refers to the degrees of freedom of individual particles, but it was later replaced by "discrete" to underline the discrete nature of the system. A similar method called *Discrete Element Method* (DEM) was used at the same time for the simulation of molecular systems

<sup>1</sup> with classical schemes that could be directly applied to granular materials. Hence, the acronyms

<sup>2</sup> DEM and DEM are used synonymously to describe the methods of simulating granular materials

<sup>3</sup> at particle scale. In-spite of the formal analogy (particles and force laws) between granular and

4 molecular systems, the physics is fundamentally different. The interactions between individual  
 5 grains are governed by unilateral contact laws, and the mechanism of energy dissipation is  
 6 through friction and inelastic collisions. Moreover, granular materials have a wide variation in  
 7 their particle shape and size distribution that require appropriate numerical treatments. In the  
 8 Molecular Dynamics approach, the normal reaction force, which prevents the interpenetration  
 9 of two grains is proportional to the depth of penetration. Thus, frictional contact between grains  
 10 can be expressed as a function of the configuration variables, which describe the positions and  
 11 velocities of the grains ([Radjai and Dubois, 2011](#)). Discrete-Element methods, which describe  
 12 interactions between grains based on the explicit overlap between the grains are termed as  
 13 *smooth methods*. Another approach is the *non-smooth approach* ([Jean, 1999](#)), which describes  
 14 the behaviour of discrete elements using the main features of uni-laterality and Coulomb  
 15 friction, and by neglecting the finer details such as interpenetration and overlap between grains.  
 16 The fundamental difference between the non-smooth method and the common DEM or Discrete  
 17 Element Method (DEM) approach lies in the treatment of small length and time scales involved  
 18 in the dynamics of granular media. In DEM-type DEM, the particles are treated as rigid bodies  
 19 but the contacts between particles are assumed to obey the visco-elastic constitutive law. The  
 20 time-stepping schemes used for the numerical integration of the equations of motion in Discrete  
 21 Element Method, imply that the contact interactions involve smaller time and length scales. In  
 22 the CD method, these small scales are neglected and their effects are absorbed into the contact  
 23 laws. In non-smooth formulation, the particle dynamics is described at a larger scale than the  
 24 elastic response time and displacement scales ([Jean, 1999; Radjai and Richefeu, 2009](#)).

## 25 **3.5 Discrete Element Method**

26 Discrete Element Method computes the equilibrium and the trajectories of a classical multi-body  
 27 system. The Discrete Element Method is a simple and flexible discrete-element approach, which  
 28 involves applying Newton's second law of motion to each grain to describe the deformation of  
 29 the granular assembly.

$$25 \quad m_i \frac{d^2x_i}{dt^2} = \mathbf{F}_i, (i = 1, \dots, N) \quad (3.20)$$

where  $N$  is the number of grains in the simulation,  $m_i$  is the mass of grain  $i$ ,  $x_i$  is its position, and  
 $\mathbf{F}_i$  is the force exerted on grain. The method consists of calculating the forces  $\mathbf{F}_i$  and then solving  
 the ordinary differential in [eq. 3.20](#). In general the system of coupled non-linear differential  
 equations cannot be solved analytically. The approximate numerical solution of these equations,  
 which describes the trajectories of all the particles of the system is called as Discrete Element  
 Method. The idea of Discrete Element Method goes back to Alder and Wainwright who in

1957 investigated the physics of hard sphere gases. The name implies that it was first applied to  
molecular scale problems before being applied to granular materials by ?. Discrete Element  
Method simulations are identical to the real experiments, this involve generation of samples  
(initial conditions) with  $N$  particles and solving the Newton's equation of motion for the system  
until the properties of the system no longer change with time (equilibration of the system).  
After equilibration, the actual analysis is performed.

The computation of the forces and torques is the central part of the Discrete Element  
Method simulation. The dynamics of the granular material is governed by Newton's equation of  
motion which depends on the centre-of-mass coordinates and the Euler angles of the particles  $i$   
( $i=1,\dots,N$ ):

$$\frac{\partial^2 \vec{r}_i}{\partial t^2} = \frac{1}{m_i} \vec{\mathbf{F}}_i(\vec{r}_j, \vec{v}_j, \vec{\varphi}_j, \vec{\omega}_j) \quad 18$$

$$\frac{\partial^2 \vec{\varphi}_i}{\partial t^2} = \frac{1}{\hat{J}_i} \vec{\mathbf{M}}_i(\vec{r}_j, \vec{v}_j, \vec{\varphi}_j, \vec{\omega}_j), (j = 1, \dots, N) \quad 19$$

The force  $\vec{\mathbf{F}}_i$  and the torque  $\vec{\mathbf{M}}_i$ , which act on particle  $i$  of mass  $m_i$  and the tensorial moment  
of inertia  $\hat{J}_i$  are (sometimes complicated) functions of the particle positions  $\vec{r}_j$ , their angular  
orientations  $\vec{\varphi}_j$ , and their corresponding velocities  $\vec{v}_j$  and  $\vec{\omega}_j$ . In a two-dimensional system,  
the angular orientation of a particle is described by a single (scalar) quantity  $\varphi_i$  and the moment  
of inertia reduces to a scalar value  $J_i$ . The Newton's equation of motion can be written as:

$$\frac{\partial^2 \vec{r}_i}{\partial t^2} = \frac{1}{m_i} \vec{\mathbf{F}}_i(\vec{r}_j, \vec{v}_j, \vec{\varphi}_j, \vec{\omega}_j) \quad 26$$

$$\frac{\partial^2 \vec{\varphi}_i}{\partial t^2} = \frac{1}{J_i} \vec{\mathbf{M}}_i(\vec{r}_j, \vec{v}_j, \vec{\varphi}_j, \vec{\omega}_j), (j = 1, \dots, N) \quad 27$$

For granular particles in the absence of long range fields, the force  $\vec{\mathbf{F}}_i$  and the torque  $\vec{\mathbf{M}}_i$   
1 acting upon the particle  $i$  are given as sum of the pairwise interaction of particle ‘ $i$ ’ with all  
2 other particles of the system:

$$\vec{\mathbf{F}}_i = \sum_{j=1, j \neq i}^N \vec{\mathbf{F}}_{ij}, \quad \vec{\mathbf{M}}_i = \sum_{j=1, j \neq i}^N \vec{\mathbf{M}}_{ij} \quad (3.21)$$

5 The limitation to pairwise interaction is an abstraction, which is justified if the particles  
6 deformation at the contact is trivial. To describe the deformation of granular assemblies one  
7 has to take into account the effect of multi-particle interactions. This method is general and can

8 be applied to a wide range of systems. The Discrete Element Method can be used to study the  
 9 behaviour of grains in rapid flows to static assemblies. The method treats both the conditions  
 10 in exactly the same way, it is not necessary to divide the system and then treat each condition  
 11 differently. The simplest model for granular particle is a sphere. In a two-dimensions case, the  
 12 sphere is reduced to a circular disk. Simulations using spherical particles are numerically very  
 13 effective since particle collisions can be easily identified and described in a simple way (?).

### <sup>14</sup> 3.5.1 The Forces

<sup>15</sup> The force  $\mathbf{F}_i$  in [eq. 3.20](#) represents both the grain to grain interaction force, and other external  
 16 forces acting on the system. Therefore, the force  $\mathbf{F}_i$  is expressed as:

$$\mathbf{F}_i = \sum_{j \neq 1} \mathbf{F}_{ij} + \mathbf{F}_{ext,i} \quad (3.22)$$

where  $\mathbf{F}_i$  is the force exerted by grain  $j$  on  $i$ . The external force  $\mathbf{F}_{ext,i}$  is most often the force  
 2 of gravity,  $\mathbf{F}_{ext,i} = m_i \mathbf{g}_i$ . The methodology to incorporate any other external forces in the  
 3 simulation is the same. However, the computation of the interaction forces depends on the  
 4 numerical method adopted in the study. The methodology used in the present study is described  
 5 below.  
 6

Let us consider two grains  $i$  and  $j$ , in contact (see figure [3.5](#)). The contact force can be  
 7 decomposed into two components, as the normal ( $F_n$ ) and the tangential ( $F_t$ ) components:  
 8

$$\mathbf{F}_{ij} = F_n \mathbf{n} + F_t \mathbf{t} \quad (3.23)$$

where  $\mathbf{n}$  and  $\mathbf{t}$  are unit vectors, pointing in the normal and the tangential directions. The  
 11 procedure adopted to calculate the normal and tangential forces are discussed.  
 12

#### Normal force

When granular particles collide, part of the kinetic energy is dissipated as heat and the other  
 14 part causes deformation of the particle. These deformations generate interaction forces. The  
 15 grains are considered to be rigid while their contact is assumed to be soft. Thus, the grains do  
 16 not change their shape, instead they overlap. The shapes of the particles are conserved on an  
 17 average, after many collisions. The overlap at the contact is limited to very small deformations,  
 18 which are achieved by defining a repulsive normal force that opposes the overlap. The mutual  
 19

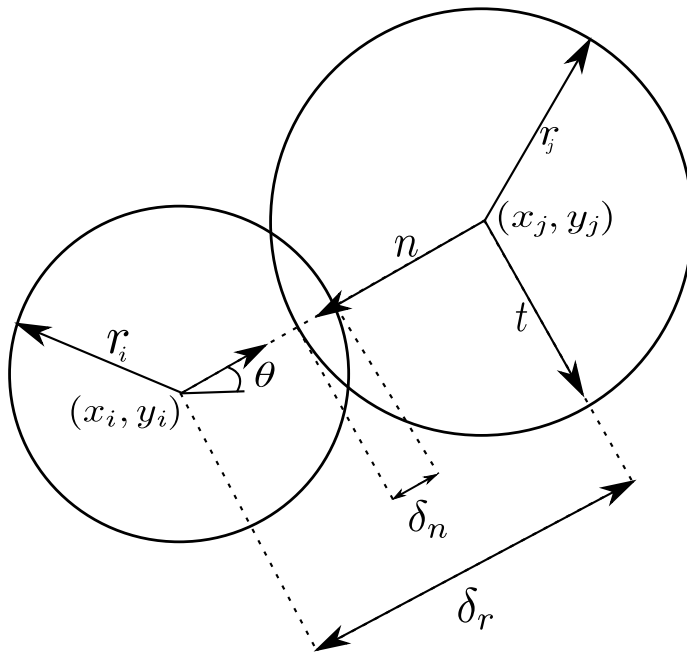


Figure 3.5 Grains  $i$  and  $j$  in contact, and the separation  $\delta_n$  is used to calculate the normal force

compression ( $\delta_n$ ) of the particles  $i$  and  $j$  is defined as:

$$\delta_n = |x_i - x_j| - r_i - r_j \quad (3.24)$$

where  $x_i$  and  $x_j$  are the centres of the grains and  $r_i$  and  $r_j$  are their radii (see Figure 3.5). When  $\delta_n > 0$ , the two grains are not in contact, and there is no interaction. When  $\delta_n < 0$ , the two grains overlap, and there is a repulsive normal force that pushes the two grains apart. The simplest model is to consider the contact as a linear spring with damping. The repulsive force depends linearly on  $\delta_n$ , and is controlled by the stiffness of the grain. The energy dissipation due to the interaction between grains is an intrinsic characteristic of the granular material and is incorporated by adding a damping force that opposes the relative velocity for the duration of the contact. The interaction force at the contact is idealized as a simple spring-dashpot system, with elastic and dissipative constants (Luding et al., 1994).

$$F_n = \begin{cases} 0, & \delta_n > 0 \\ -k_n \delta_n - \gamma_n \frac{d\delta_n}{dt}, & \delta_n < 0 \end{cases} \quad (3.25)$$

<sup>3</sup> The constant  $k_n$  characterises the stiffness of the grain, and must be chosen sufficiently large so  
<sup>4</sup> that the overlap between the grains remain small. Nevertheless, the solution has an undesirable  
<sup>5</sup> property of generating an attractive force (?). It arises just before the two particles separate.

6 In this case, we have  $d\delta_n/dt > 0$  while  $\delta_n$  approaches zero. To avoid the attractive force, the  
 7 force is computed in two stages: a candidate force  $\hat{F}_n$  is calculated, and verified whether it is  
 8 non-negative:

$$9 \quad \hat{F}_n = -k_n \delta_n - \gamma_n \frac{d\delta_n}{dt}, \quad F_n = \begin{cases} 0, & \hat{F} \leq 0 \\ \hat{F}_n, & \hat{F} > 0 \end{cases} \quad (3.26)$$

10

11 For pairwise collisions, the normal force ( $F_n$ ) represented as  $k_n \delta_n + \gamma_n$  causes a decrease in  
 12 the relative normal velocity of the particles by a factor  $\varepsilon$ . This factor is the *coefficient of*  
 13 *restitution*, and is defined as  $\varepsilon \approx g'/g$ , where  $g$  is the absolute normal relative velocity before  
 14 the collision and  $g'$  corresponds to the post-collision value. The relative velocity,  $d\delta_n/dt > 0$ ,  
 15 can be obtained by differentiating eq. 3.24. Thus we obtain:

$$16 \quad \frac{d\delta_n}{dt} = (\mathbf{v}_i - \mathbf{v}_j) \cdot \mathbf{n} \quad (3.27)$$

17 where  $\mathbf{v}_i = dx_i/dt$  is the velocity of grain  $i$  and  $\mathbf{v}_j = dx_j/dt$  is the velocity of grain  $j$ . The  
 18 numerical integration of eq. 3.27 yields the separation  $\delta_n$  and permits us to generalise the model  
 19 and treat the tangential forces as well, as explained in the next section. By integrating Newton's  
 20 equation of motion it is found that the linear force corresponds to the co-efficient of restitution,  
 21 which is defined as:

$$22 \quad \varepsilon = \exp\left(-\frac{\pi \gamma_n}{2m^{eff}} / \sqrt{\frac{Y}{m^{eff}} - \frac{\gamma_n^2}{2m^{eff}}}\right) \quad (3.28)$$

23

## 24 Tangential force

25 Granular particles are not perfect spheres, but have a complicated surface texture, therefore  
 26 at oblique collisions, besides the normal force there is a tangential force too. Even perfectly  
 27 smooth spheres exert a tangential force due to their bulk viscosity (?). To build a heap of spheres  
 28 on a flat surface, the particles as well as the surface has to be sufficiently rough, indicating  
 29 the dependence of the tangential force on the surface properties of the granular materials. For  
 realistic simulation of granular materials, it is important to consider the tangential force in  
 Discrete Element Method. The tangential force is considered in a similar fashion as the normal  
 force, arising from a spring stretched by the relative motion of the grain. Tangential forces are  
 modelled by considering the relevant relative tangential velocity of the particle surfaces at the  
 point of contact. The point of contact is an approximation, as the description of the normal  
 force assumes a compression  $\delta_n$ , which implies a contact surface in 3-D or a contact line in 2-D.  
 Assuming a tangential spring of length  $\delta_t$  exerts an opposing force to the relative tangential

1  
2  
3  
4  
5  
6  
7

displacements (ignoring the effect of relative rolling between the particles), the tangential force can be postulated similar to the normal force ( eq. 3.27) as:

$$\frac{d\delta_t}{dt} = (\mathbf{v}_i - \mathbf{v}_j) \cdot \mathbf{t} \quad (3.29)$$

This equation must also be numerically integrated, just like eq. 3.20. The grains are in contact when  $\delta_t < 0$ , and when  $\delta_t = 0$ , the grains no longer exert a force on each other. With these assumptions,  $\delta_t$  can be calculated similar to the normal force. The tangential force is assumed to be governed by Coulomb's friction law.

$$|F_t| \leq \mu F_n \quad (3.30)$$

where  $F_t$  is the tangential force and  $\mu$  is the friction coefficient. It is therefore necessary to constrain the tangential force to remain less than or equal to  $\mu F_n$ . To impose the condition in eq. 3.30, two-stages similar to the normal force computation is adopted. The first step is to evaluate the candidate force, and is then accepted if it obeys the condition in eq. 3.30.

$$\hat{F}_t = -k_t \delta_t - \gamma_t \frac{d\delta_t}{dt}, \quad F_t = \begin{cases} sgn(F_t), & |\hat{F}| \geq \mu F_n \\ \hat{F}_t, & |\hat{F}| < \mu F_n \end{cases} \quad (3.31)$$

where  $k_t$  is the stiffness of the tangential spring and  $\gamma_t$  is the damping constant. If  $|F_t| = \mu F_n$ , the contact is sliding, otherwise, it is non-sliding. It can be noted that the normal force ( eq. 3.26) and the tangential force ( eq. 3.31) are handled in the same way in Discrete Element Method. When the grains slide against each other, they do not retain any memory of their initial position, and hence do not return to its original position. In order to model this behaviour, a limiting value of  $\delta_t$  is imposed. When the contact slides  $\delta_t = \pm \mu F_n / k_t$  is imposed.

In addition to sliding, the grains can roll relative to one another about their centre of mass due to the tangential force acting at their contact surface. In this case,  $d\delta_t/dt = 0$ . It is important to assume that the grains touch at a single point instead of overlapping, i.e.  $\delta_n = 0$ . This point is located at  $x_i - r_i \mathbf{n} = x_j + r_j \mathbf{n}$ . If we consider that this point belongs to grain  $i$ , its velocity is  $v_i + r_i(\boldsymbol{\omega} \times \mathbf{n})$ . If it belongs to grain  $j$ , its velocity is  $v_j + r_j(\boldsymbol{\omega} \times \mathbf{n})$ . The relative velocity is the difference between these two velocities.

$$\frac{d\delta_t}{dt} = (\mathbf{v}_i - \mathbf{v}_j) \cdot \mathbf{t} - (r_i \boldsymbol{\omega}_i + r_j \boldsymbol{\omega}_j) \times \mathbf{n} \quad (3.32)$$

<sup>3</sup> It should be noted that the eq. 3.32 is only an approximation, as the grains in Molecular Dynamics do not touch at points, but overlap. It is therefore an approximation that produces

- <sup>5</sup> an error of order  $O(\delta_n/r)$  (Radjai and Dubois, 2011). It is assumed that the contact forces are  
<sup>6</sup> exerted at the point of contact. It implies that the tangential force is accompanied by torque  
 acting on two grains. If the overlap is zero, these torques are:

$$\tau_{ij} = -(a_i \mathbf{n}) \times (F_t \mathbf{t}), \tau_{ji} = -(a_j \mathbf{n}) \times (F_t \mathbf{t}), \quad (3.33) \quad \frac{2}{3}$$

The torques modify the angular velocities of the grains. It is therefore necessary to incorporate the equation for the angular coordinates of the grains in eq. 3.20:

$$I_j \frac{d\omega_i}{dt} = \sum_{j \neq i} \tau_{ij} \quad (3.34) \quad \frac{6}{6}$$

where  $I_j$  is the moment of inertia of grain j. The eq. 3.33 is only valid when  $\delta_n = 0$ . The torque is a vector product of the force and its lever arm. It is assumed that the lever arms have lengths equal to  $r_i$  and  $r_j$ , which is true only when the grains do not overlap, hence in this case they produce an error of order  $O(\delta_n/r)$ . It is nevertheless desirable to damp this type of motion (Radjai and Dubois, 2011). The interaction between two solid bodies is much more complex than that is described by the simple linear model. Nevertheless, the linear force law has several advantages. It is simple to implement, and its harmonic behaviour is well understood, which makes it easier to interpret the results. The most common non-linear interaction law is the Hertz law (Hertz, 1882). In certain situations, such as a quasi-static packing, a non-linear law can have significant influence on the acoustic properties (?), and on the global stiffness (?). However, in case of rapid granular flows, the interaction force between the particles has almost no effect on the phenomenon, and a linear law can be used to describe this kind of behaviour (Radjai and Dubois, 2011).

### <sup>1</sup> 3.5.2 Numerical algorithm and integration scheme

- <sup>2</sup> The efficiency of a Discrete Element Method program is mainly determined by its efficiency  
<sup>3</sup> to compute the interaction forces between particles. If we consider a model system with  
<sup>4</sup> pairwise interactions, we have to consider the contribution of the force on particle  $i$  due to all  
<sup>5</sup> its neighbours. If we consider only the interaction between a particle and the nearest image  
<sup>6</sup> of another particle, then for a system of  $N$  particles, we must evaluate  $N \times (N - 1)/2$  pair  
<sup>7</sup> distances. Consider a system of 1000 particles, at every time step all possible pairs of particles  
<sup>8</sup> have to be considered to compute the interaction forces, hence,  $N(N - 1)/2 \approx 500,000$  force  
<sup>9</sup> computations are required. For short-range particle interactions, the majority of these force  
<sup>10</sup> evaluations is unnecessary as the corresponding particles are located far apart and do not  
<sup>11</sup> necessarily touch each other. For a dense system of equally sized particles, the particles can

<sup>12</sup> have contacts with not more than 6 particles, this reduces the number of force computation  
<sup>13</sup> required to  $3N \approx 3000$ . In the preliminary force computation scheme, at least 166 times more  
<sup>14</sup> pair interactions are considered than necessary. Therefore, the numerical methods employed in  
<sup>15</sup> the Discrete Element Method program should try to minimize the computation of interaction  
<sup>16</sup> forces (?). There are three different methods for the efficient computation of the forces, the  
<sup>17</sup> *Verlet* algorithm, the *link-cell* algorithm, and a *lattice* algorithm. The *Verlet* algorithm described  
<sup>18</sup> in Grubmuller et al. (1991) is implemented in the present study.

<sup>19</sup> **Verlet list algorithm**

<sup>20</sup> The Verlet list algorithm assumes a cut-off value, so that only neighbouring particles that  
<sup>21</sup> contribute to the energy of a particle  $i$  are considered. It is advantageous to exclude the particles  
<sup>22</sup> that do not interact in the memory expensive energy computation. [Verlet \(1967\)](#) developed  
<sup>23</sup> a book-keeping technique, commonly referred to as the Verlet list or neighbour list, which  
<sup>24</sup> is illustrated in [3.6](#). In this method a second cut-off radius  $r_v > r_c$  is introduced, and before  
<sup>25</sup> we calculate the interactions, a list is made (the Verlet list) of all particles within a radius  
<sup>26</sup>  $r_v$  of the particle  $i$ . In the subsequent calculations of the interactions, only those particles in  
<sup>27</sup> this list will be considered. The idea of the Verlet algorithm is based on a simple property of  
<sup>28</sup> particle dynamics: neighbourhood relation between particles can only change slowly, i.e. two  
<sup>29</sup> particles which are close to each other at a given time step will remain as neighbours, at least  
<sup>30</sup> in the following few time steps. During initialization the neighbourhood relations between  
<sup>31</sup> the particles, i.e. the distance of all close pairs of particles are computed. Two particles are  
<sup>32</sup> considered as neighbours if the distance of their surface is smaller than a predefined distance  
*Verlet distance*:

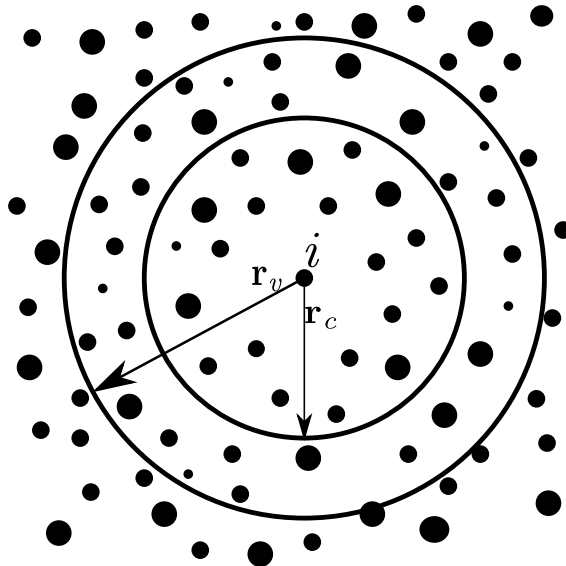


Figure 3.6 The Verlet list: a particle  $i$  interacts with those particles with the cut-off radius  $r_c$ , the Verlet list contains all the particles within a sphere with radius  $r_v > r_c$

<sup>33</sup>

<sup>34</sup>  $(|\vec{r}_i - \vec{r}_j| - R_i - R_j) < \text{Verlet distance}$  (3.35)

For each particle there is a *Verlet list* in which the close neighbours are saved. To initialise the Verlet lists efficiently, a grid that covers the simulation area is defined. Its mesh size is larger than the largest particle. For construction of the lists only pairs whose particles reside in the same or adjacent grids are considered. This procedure guarantees the detection of all close pairs

1  
2  
3  
4

of particles (?). Redundancy in Verlet lists, i.e. if particle  $i$  is a neighbour of  $j$ , then particle  $j$  is a neighbour of  $i$ , are avoided by imposing a restriction on the list of particle  $i$  contains, such that it contains only neighbours with index  $j < i$ . For the computation of interaction forces, the Verlet list of particle  $i$  is scanned and only pairs which are recorded in one of the Verlet lists are considered. Hence, the Verlet list of each particle  $i$  is scanned and the interaction force of  $i$  with each entry  $j$  in its list is computed. Initially to build the Verlet list, the particles are sorted into a grid of mesh size  $dx \times dy$ . For each grid there is a list of particles residing in the cell. During the simulation, the neighbourhood relation among the particles change, therefore, the Verlet lists have to be updated. The decision to update a Verlet list depends on how far the particles have travelled since the time when the present list was built. The Verlet list of a particle  $i$  must contain at any time all neighbours  $j$  with  $j < i$ . This assures that two particles  $i$  and  $j$  never touch and are not considered as neighbours, i.e.  $j$  is not in the list of  $i$  and  $i$  is not in the list of  $j$ . Hence,

$$|\vec{r}_i - \vec{r}_j| - R_i - R_j > 0 \quad (3.36)$$

The above condition is required for all pairs  $(i,j)$  of particles which are *not* known as neighbours. This condition is a criterion to update the Verlet lists (?). Assume at the instant when the

Verlet lists are constructed, the surfaces of the particles have the distance  $|\vec{r}_i - \vec{r}_j| - R_i - R_j >$  Verlet distance, i.e. they are not classified as neighbours. If the Verlet lists are updated before one of these particles has travelled the distance *verletdistance*/2 since the lists were constructed, they can never collide without being recognized as neighbours first. This is explained in figure 3.7. The impact of optimisation of the Verlet list algorithm has negligible effect on the computation time, as the algorithm is quite efficient already and only consumes a few percent of the total computation time in construction of the Verlet lists. The implementation of the Verlet list algorithm in force computation drastically reduces the computation time in comparison to the linear algorithm. The performance of the Verlet list algorithm is controlled by two crucial parameters: the number of cells  $N_c$ , for the construction of the Verlet lists and the Verlet distance  $r_v$  (?).

## 12 Leap frog or Verlet integration algorithm

Discrete Element Method involves numerically solving Newton's equation of motion eq. 3.20, which is an ordinary differential equation. Choosing an integration algorithm is important, as the forces are not always differentiable in time, and the temporary derivative of the force is discontinuous when the contact splits. It is also very essential to numerically integrate eq. 3.32 with the same precision as eq. 3.20. At first, computational speed seems important. It is usually not very relevant because the fraction of time spent on integrating the equation of motions

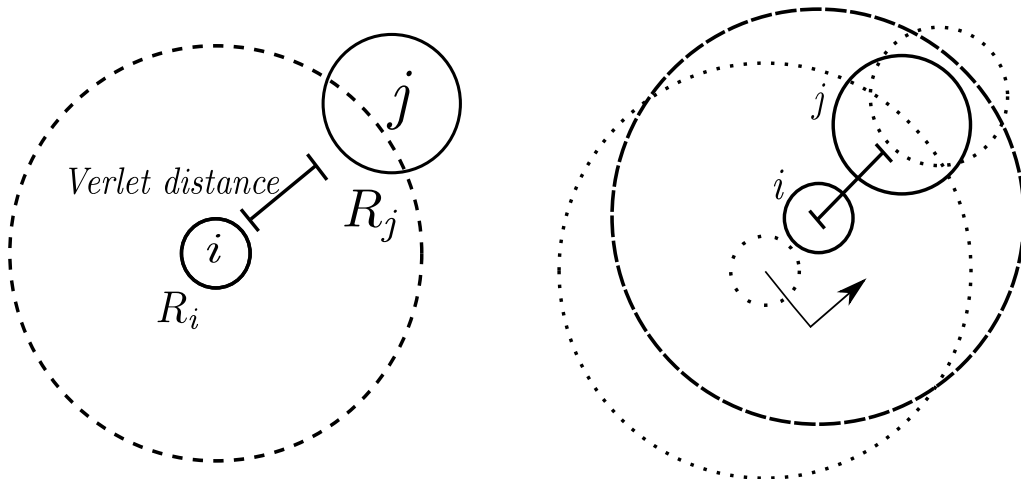


Figure 3.7 Checking the validity of Verlet lists. *Left:* the particles  $i$  and  $j$  are not recognized as neighbours since the distance of their surface is larger than the Verlet distance. The radius of the dashed circle is  $R_i + R_{max} + \text{Verlet distance}$ . *Right:* in the most unfortunate case the particles approach each other directly, travelling at the same velocity. As soon as one of the particles has travelled the distance  $\text{Verlet distance}/2$  (arrows), the Verlet lists have to be rebuilt. The particles  $i$  and  $j$  are now recognized as neighbours. Figure redrawn after ?.

(as opposed to computing the interactions) is small. Accuracy for large time steps is more important, because the larger the time step that we can use, the fewer evaluation of the forces are needed per unit of simulation time. Hence, this would suggest that it is advantageous to use a sophisticated algorithm that allows use of larger time step. Algorithms that allow the use of large time steps, achieve this by storing information on increasingly higher-order derivatives of the particle coordinates. Consequently, they tend to require more memory storage. However, the most important aspect to consider is the energy conservation. It is important to distinguish between two kinds of energy conservation: the short time and long time. The sophisticated higher-order algorithms tend to have very good energy conservation at short times. However, they often have undesirable feature that results in drifting of the overall energy for longer times. In contrast, the Verlet style algorithms tend to have only moderate short term energy conservation, but little long-term drift (?). In this case, such algorithms are not useful. They are more complicated to program, and do not yield a more precise solution (?). It might seem important to have an algorithm that accurately predicts the trajectories of all particles for both short and long durations, however no such algorithm exists. In certain cases, two trajectories that are initially very close may diverge exponentially as time progresses. Any integration error, however small it may be, would always diverge the predicted trajectory exponentially from the true trajectory. This phenomenon is called the Lyapunov instability, and it is devastating to the whole idea of Discrete Element Method simulation, but we have good reasons to assume that even this problem need not be serious (?). First of all, one should realize that the aim

of the Discrete Element Method simulation is not to predict precisely what will happen to a system, but to predict the average behaviour of the system that was prepared in an initial state about which we know something (initial position, velocity and energy), but not everything. Hence, Molecular Dynamics technique differs from other methods, which are used to predict the trajectories. However, considerable numerical evidence suggest that the shadow orbits exists, which is a true trajectory of a multi-body system that closely follows the numerical trajectory for a time that is longer in comparison with the time that is required for the Lyapunov instability to develop (?).

Newton's equations of motion are time reversible, and so should be the integration algorithm. The “leapfrog” algorithm or the Verlet integration algorithm is a numerical scheme used to integrate the Newton's equation of motion to calculate the trajectories of particles and was implemented in Discrete Element Method simulation by [Verlet \(1967\)](#). Verlet algorithm is fast and requires less storage memory, it is not particularly accurate for long time steps, and hence, we should expect to compute the forces on all particles rather frequently. Its short-term energy conservation is fair (in versions that use more accurate expression for velocity), but most importantly it exhibits little long-term energy drifts. This is related to the fact that the Verlet algorithm is time reversible and area preserving, however, it does not conserve the total energy of the system exactly (?). Verlet algorithm is simply based on a truncated Taylor expansion of particle co-ordinates.

$$t(t + \Delta t) = rt + \mathbf{v}(t)\Delta t + \frac{f(t)}{2m}\Delta t^2 + \dots \quad (3.37)$$

If we truncate this expansion beyond the term  $\Delta t^2$ , we obtain the Euler's algorithm, which looks similar to the Verlet Algorithm, but it does not preserve energy and have significant energy drifts. The simplest among the Verlet schemes is the *Leap frog algorithm*, which evaluates the velocities at half-integer time steps and uses these velocities to compute the new positions. The position of each grain is calculated at time  $t = 0, \Delta t, 2\Delta t, \dots$ , where  $\Delta t$  is the time step. On the other hand, their velocities are calculated at intermediate times, that is, at  $t = \Delta t/2, 3\Delta t/2, \dots$ . Let the position of a grain at time  $t = k\Delta t$  be written as  $x_k$ , and its velocity at time  $t = \Delta t(k + 1/2)$  be written  $\mathbf{v}_{k+1/2}$ , and its acceleration at  $t = k\Delta t$  be  $\mathbf{a}_k$ . Then the following equation is used to advance systematically:

$$\mathbf{v}_{k+1/2} = \mathbf{v}_{k-1/2} + \mathbf{a}_k \Delta t, \quad x_{k+1} = x_k + \mathbf{v}_{k+1/2} \Delta t \quad (3.38)$$

This algorithm determines the new grain position with an error of order  $O(\Delta t^4)$ . But [eq. 3.38](#) hides a difficulty in the application of this algorithm to granular materials ([Radjai and Dubois, 2011](#)). The problem is that the acceleration must be calculated at time  $t = k\Delta t$ . But the velocities are known at  $t = (k - 1/2)\Delta t$ , and not at  $t = k\Delta t$ . One way to get around this problem is to

<sup>13</sup> write:

<sup>14</sup>  $\mathbf{v}_k = \mathbf{v}_{k-1/2} + \mathbf{a}_{k-1}\Delta t/2$  (3.39)

<sup>15</sup> The equation uses the acceleration of the preceding time step to estimate the velocity. This  
<sup>16</sup> approximation does not diminish the order of the algorithm. eq. 3.39 estimates  $\mathbf{v}_k$  with an  
<sup>17</sup> error of order  $\mathbf{O}(\Delta t^2)$ , which produces an error of the same order in the calculation of the  
<sup>18</sup> force in eq. 3.38. But this causes only an error of order  $\mathbf{O}(\Delta t^3)$  in the velocity and an error  
<sup>19</sup> of order  $\mathbf{O}(\Delta t^4)$  in the position. However, this problem does not exist in energy conservation  
<sup>20</sup> systems, because the computed forces do not depend on the velocities of the grains. The  
<sup>21</sup> heaviest computational task is the evaluation of forces and not the integration of equations. The  
<sup>22</sup> Verlet integration scheme is summarized in eq. 3.40 and figure 3.8. To calculate the forces and  
<sup>23</sup> acceleration, it requires the positions and velocities at time t:

<sup>24</sup>  $\mathbf{v}(t + \Delta t/2) = \mathbf{v}(t - \Delta t/2) + \mathbf{a}(t)\Delta t$   
<sup>25</sup>  $x(t + \Delta t) = x(t) + \mathbf{v}(t + \Delta t/2)\Delta t$   
<sup>26</sup>  $\mathbf{v}(t) = \mathbf{v}(t - \Delta t/2) + \mathbf{a}(t - \Delta t)\Delta t/2$  (3.40)

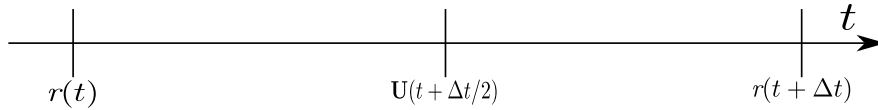


Figure 3.8 Verlet integration scheme

<sup>28</sup> The analysis of the Discrete Element Method formulation reveals that the linear force law  
<sup>29</sup> gives the model a harmonic character, showing that it is very closely related to simple models  
<sup>30</sup> widely used in physics and mechanics. The shortest time scales often arise from the oscillations  
<sup>31</sup> of one or two grains. The integration algorithm must resolve these movements with sufficient  
<sup>32</sup> precision. Thus, the time steps used must be smaller than these time scales, the most rapid  
<sup>33</sup> frequency is usually  $\omega_N$ , the characteristic oscillation frequency of very short waves. This  
<sup>34</sup> frequency is proportional to  $\omega_0$ , which is easier to estimate. Therefore, it is essential to choose  
 a time step  $\Delta t \approx \epsilon/\omega_0$ , where  $\epsilon$  is a constant that depends on the integration algorithm. Values  
 such as  $\epsilon \approx 0.01$  are often a reasonable choice (?). In the case of rapid granular flows, the time  
 step must be small enough so that the fastest grains move only by a small fraction of their size  
 during one time step. The grains must be stiff enough so that violent collisions do not lead to  
 large overlaps between particles.

1  
2  
3  
4  
5

### 3.5.3 Boundary conditions

6

In many cases, the dynamic and static properties of a granular system are substantially affected by the interaction of the granular material with the system boundaries, i.e. by the properties of the container or the surface on which the material is present. The effect of boundary conditions on the response of the granular assembly can be noticed in the convective motion of granular material in vibrating containers, the formation of density waves in pipes, the motion of granular material on conveyors, and the clogging of hoppers. In these and many other cases, careful definition of the interaction between the granular material and the contact surface is essential. Of particular importance is the realistic modelling of the wall surface roughness. Unfortunately the mechanical interaction of a granular materials with a rough wall is poorly understood (?). A simple way to define the wall property is to build up the wall from particles, which obey the same rules of interaction as the particles of granular material. By varying the size and position of the wall particles, system boundaries of adjustable roughness can be described. However, the surface roughness that characterizes the frictional properties of the wall has to be arrived iteratively, and may not represent the real conditions. In the present case, a solid wall with corresponding stiffness, damping and frictional characteristics is introduced to model the interaction between particles and the wall. The interaction force is computed in a similar fashion to that of a pair of particles in contact and is divided into the normal and tangential components. The compression of the particle upon collision with the wall is calculated along the normal direction to the wall and the particle contact.

7

8

9

10

11

12

13

14

15

16

17

18

19

20

21

22

23

#### **3 Periodic boundary**

The effect of a wall on the response of particles is very critical, especially in numerical simulation where the number of particles is relatively fewer in comparison to the experiments.

The undesired effect of a wall can be eliminated using periodic boundary conditions, i.e. a periodic extension of the simulation area in one or more dimensions. Any particle leaving the system at one side is reintroduced at the opposite side, and correspondingly the interaction forces between particles at opposite sides of the simulation area are taken into account. In this framework, the simulation domain becomes a unit area containing particles with periodic copies paving the whole system. The periodic boundary conditions extend the system boundaries to infinity, so that the simulation cell simply plays the role of a coordinate system to locate particle positions 3.9.

The external stresses or displacements are applied on the simulation box by constraining the degrees of freedom of the wall, which are alternatively kept free or fixed depending on whether a stress or a displacement is monitored in a system. With periodic boundary conditions, this role

is played by the collective degrees of freedom carried by the coordinate system, whose basis vectors become dynamic variables, and their conjugate stresses are expressed as a state function of the granular configuration (?). In the case of granular systems, there is dissipation of energy during particle interactions. The kinematics, equation of dynamics, and the time-stepping schemes for Discrete Element Method are discussed in detail in Radjai et al. (2011). The periodicity in position implemented in the present study is discussed below.

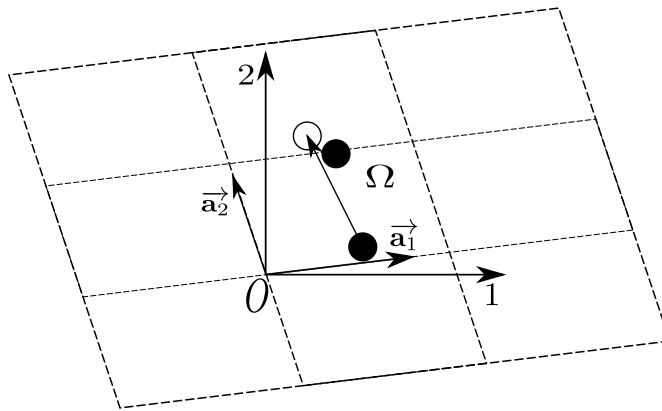


Figure 3.9 A 2D simulation cell  $\omega$  with its basis vectors in an absolute frame. A particle located at the right boundary interacts with the image of another particle located at the left boundary.

Let us consider a collection of  $N_p$  particles with their centres contained in a cell of volume  $V$ . The cell can have any shape allowing for a periodic tessellation of space. The simplest shape is a parallelepiped i.e. parallelogram in 2D. The cell and its replicas define a regular lattice characterized by its basis vectors ( $\vec{a}_1, \vec{a}_2$ ). In the case of a parallelogram, the basis vectors may simply be the two sides of the parallelogram; figure 3.9. The origin  $O$  of the simulation cell is a vertex of the cell of coordinates (0, 0) and its replicas are defined by two indices  $(i_1, i_2)$  corresponding to a translation of the origin by the vector  $i_1 \vec{a}_1 + i_2 \vec{a}_2$ . Then, the coordinates  $\vec{r}(i')$  of the image  $i'$  of a particle  $i \in \Omega$  of coordinates  $\vec{r}(i)$  are given by:

$$\vec{r}(i') = \vec{r}(i) + \sum_{k=1}^2 i_k \vec{a}_k \quad (3.41)$$

The particles belonging to the cell  $\Omega$ , characterized by  $i_1 = i_2 = 0$ , can interact with the particles of the same cell but also with image particles in the neighbouring cells characterized by  $i_k \in 1, 1$ . There are  $3^D - 1$  cells surrounding the simulation cell and they are involved in the search of contact partners for each particle. The distance between two particles  $i$  and  $j \in \Omega$  is the shortest distance separating  $i$  from  $j$  or from one of its images  $j'$ . As the system evolves in time, a particle  $i$  may leave but one of its images  $i'$  enters at the same moment. In order to keep all original particles in the cell, the status “original” should be reserved to the particles whose

centres belongs to  $\Omega$ . Hence, whenever a particle  $i$  leaves the simulation cell, it becomes an image of  $i'$ , which then becomes the original. This means that a particle crossing a border of the simulation cell, returns to the cell by crossing another border.

### 3.5.4 Particle Assembling Methods

In order to simulate a granular assembly, it is essential to assign an initial position and velocity to all the particles in the system. Particle positions should be chosen to be compatible to the structure (granular fabric) we are trying to simulate. In any event, the particles should not be positioned such that there is an appreciable overlap between particles. In order to achieve the initial position of the particles, various particle-assembling methods can be adopted. The particle assembling methods can be classified into two broad categories: dynamic methods and geometrical approaches. The dynamic approach involves packing of grains using laws of mechanics and contacts, while in the geometrical method the particles are packed considering their geometry, i.e. grain size, shape and its position. In general, the packing of particles can be categorized into two types: crystal/lattice packing, like hexagonal or square pattern of mono-disperse particles, and random packing with varying density employing mono-disperse or poly-disperse grains. The crystalline packing arrangements, such as hexagon and square lattices, are easier to generate, however they have non-trivial effects on the response of the granular system ([Staron et al., 2005](#)). Hexagonal packing is the densest possible arrangement for mono-dispersed spherical grains. In 2D, the packing of mono-dispersed circles on a hexagonal lattice yields a packing density of  $\eta_h = \frac{1}{6}\pi\sqrt{3} \approx 0.9068$

The rheology of a granular material is controlled by the geometry of the assembly, which includes the particle shape, size distribution, and their arrangement. This prevailing role of geometry sometimes permits to simplify the dynamics in favour of a better description of the geometry and/or higher numerical efficiency ([Radjai and Dubois, 2011](#)). For example, dense granular packing may be efficiently constructed by replacing the equations of dynamics by simple displacement rules satisfying the geometrical constraints. Purely geometrical procedures can be much simpler and numerically faster than dynamic or quasi-static methods. Contrary to dynamic simulation methods, the geometrical methods allow for quick assembling of a large number of particles. Such packing may then be used as the initial state for dynamic simulations. The issue of the assembling methods is to construct configurations of particles as close as possible to a state of mechanical equilibrium with built-in packing properties. This can be a target packing density for a given particle size distribution. In the same way, the average connectivity of the particles (coordination number) and the anisotropy of the contact network are basic geometrical properties. The coordination number represents the mechanical response of packing. The homogeneity of the particle assembly in terms of packing fraction

<sup>7</sup> and connectivity is another important property, which depends on the assembling rules. In the  
<sup>8</sup> present study, the initial grain packing is obtained using ballistic deposition technique.

### <sup>9</sup> **Ballistic deposition**

<sup>10</sup> Initially a random arrangement of particles which do not touch each other is generated ( ??).  
<sup>11</sup> The radii of the particles are chosen from the interval of  $(R_{min}, R_{max})$  in such a way that the  
<sup>12</sup> total mass of all particles from a certain size interval is the same for all sizes, thus ensuring that  
<sup>13</sup> neither larger nor smaller particles dominate the system. This distribution can be obtained, if  
<sup>14</sup> the radii are chosen according to the probability distribution:

$$\begin{aligned} \text{15} \quad p(R) &= \frac{R_{min}R_{max}}{R_{max}-R_{min}} \frac{1}{R^2} \\ \text{16} \end{aligned} \tag{3.42}$$

<sup>17</sup> Random numbers according to the above distribution can be generated from equi-distributed  
<sup>18</sup> random numbers  $z \in [0, 1]$  via the transformation

$$\begin{aligned} \text{19} \quad R &= \frac{R_{min}R_{max}}{R_{max}-z(R_{max}-R_{min})} \\ \text{20} \end{aligned} \tag{3.43}$$

<sup>21</sup> This transformation is applied to initialise the particle radii and the particles are arranged  
<sup>22</sup> randomly on a regular lattice. The configuration of particles obtained after this step is presented  
<sup>23</sup> in ???. In the second step, the particles arranged in a regular lattice are allowed to fall down  
<sup>1</sup> and are packed using the *random deposition with relaxation method*, a ballistic deposition  
<sup>2</sup> technique. The geometrical methods help in this way to improve numerical efficiency in the  
<sup>3</sup> preparation phase. For example, gravitational deposition of particles located initially on a  
<sup>4</sup> regular grid can require hours of computation whereas a nearly similar result may be obtained  
<sup>5</sup> by means of a geometrical method in only a few minutes. The drawback is that the resulting  
<sup>6</sup> sample will not be in mechanical equilibrium and no information is available on the contact  
<sup>7</sup> forces. Nevertheless, depending on the relaxation rule, the sample may still be sufficiently close  
<sup>8</sup> to equilibrium to be considered as a good starting point for mechanical simulations. Hence,  
<sup>9</sup> a combined approach of ballistic deposition and Discrete Element Method is adopted in the  
<sup>10</sup> present study to generate mechanically stable samples. The random deposition and relaxation  
<sup>11</sup> method, first proposed by [Vold \(1959\)](#); ? and developed by [Jullien et al. \(1992\)](#) and [Meakin and Jullien \(1985\)](#),  
<sup>12</sup> is adopted in the present study. The general principle of this method is quite  
<sup>13</sup> simple (see figure 3.10); it consists of placing the particles consecutively on a substrate or a  
<sup>14</sup> layer of already deposited particles. Each particle first touches the substrate or a deposited  
<sup>1</sup> particle, then undergoes a relaxation process (single-particle restructuring) along the steepest  
<sup>2</sup> descent (steepest-descent model) until a more stable position according to a stability criterion

is reached. The construction of the packing proceeds layer by layer from the substrate, hence this deposition model is also known as bottom-to-top restructuring model. The first step is to release a particle from a random position above the substrate. Upon contact with the first deposited particle, the particle rolls following the steepest descent until a new contact is formed with a second particle. In 2D, two contacts are sufficient to balance a particle if its centre of gravity lies between the two contacts. This corresponds to a position of local stable equilibrium. If this criterion is not met, the particle continues to roll and the procedure is iterated until a local stable position is reached. The wall effects are eliminated by adopting periodic boundaries (Sec 3.5.3) in the horizontal direction (perpendicular to that of deposition). figure 3.10 shows a small sample prepared by this method (the grey particles are periodic images of the black ones). In this method, the order of deposited particles is generally random and independent of their sizes. The mechanically stable sample obtained from equilibrating the random deposited and relaxed sample is presented in ??

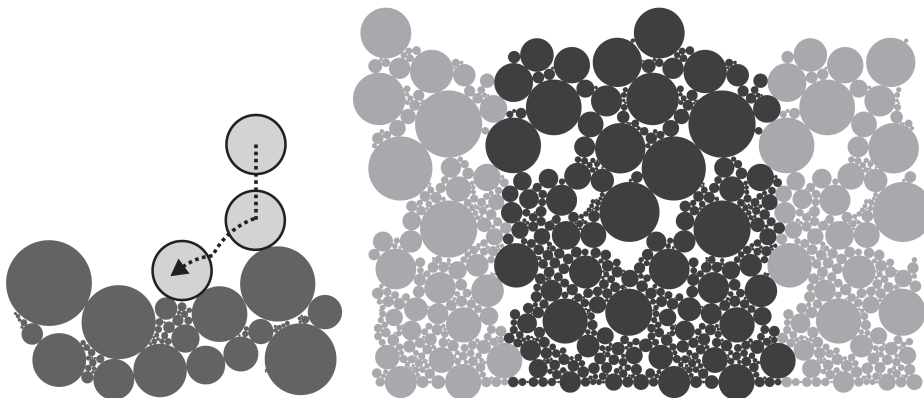


Figure 3.10 (a)Ballistic deposition: first contact followed by steepest descent; (b) small-scale periodic sample ([Radjai and Dubois, 2011](#))

### Statistical analysis of prepared sample

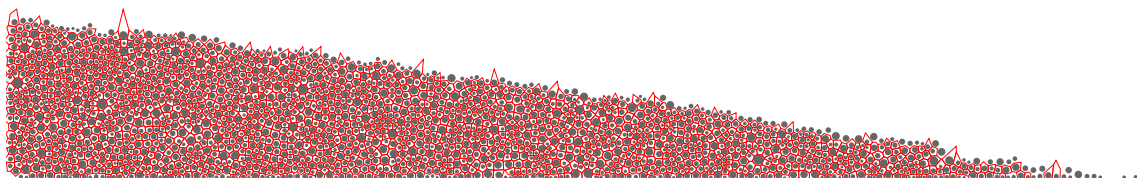
In order to ensure the homogeneity of the sample prepared using the above technique, a statistical analysis of the sample is performed. Various parameters such as particle size, coordination number, contact normal direction, contact normal force, etc., can be used in the statistical analysis to verify the homogeneity of the prepared sample. Of the various parameters available, the coordination number, i.e. the average number of contacts per particle is chosen to study the homogeneity of the sample, because of its simplicity and its physical significance in representing the density of the sample. With increase in the coordination number, the density of the granular assembly increases. The mechanically stable sample prepared by ballistic deposition technique presented in ?? is used for the statistical analysis. Representative elements

<sup>1</sup> deposition technique presented in ?? is used for the statistical analysis. Representative elements

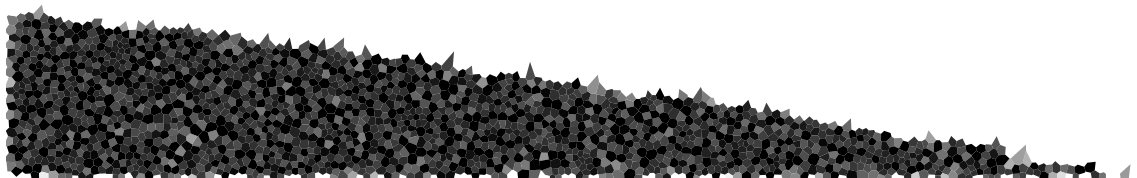
of size  $0.02 \text{ m} \times 0.01 \text{ m}$  (highlighted segments in ??) were considered. Each representative element has approximately 40 particles. A histogram is plotted showing the number of particles having a particular coordination number for all the representative elements ( ??). A normal distribution of the number of particles and the coordination number can be observed from ??.

Most particles are found to have 2 or 3 contacts with its neighbours. The number of particles with higher coordination number, i.e. coordination number greater than 3, is found to increase as we go down the sample. This is attributed to the effect of gravity, which increases linearly as we go down. Representative elements at the top are found to have a shift in their peak towards lower coordination number, as they are less restrained in comparison to their counterparts at the bottom of the sample. Overall, the sample is found to be homogeneous, with representative elements having similar normal distribution of the coordination number. Thus, the prepared sample is a good representation of the actual granular assembly and the simulations based on these samples are found to be more realistic in comparison to crystalline/lattice packing of granular particles.

### 3.5.5 Voronoi Tessellation



(a) Voronoi Tessellation



(b) Local packing density (dark - dense and light - loose)

Figure 3.11 Voronoi tessellation to average bulk properties



## <sup>17</sup> Chapter 4

# <sup>18</sup> Multi-scale modelling of dry granular <sup>19</sup> flows

### <sup>20</sup> 4.1 Introduction

<sup>21</sup> In nature, instabilities of slopes or cliffs are dramatic events involving sudden release of a  
<sup>22</sup> large mass of soil. The prediction of these catastrophic events represents several challenges,  
<sup>23</sup> one difficulty being our incomplete understanding of the granular flow dynamics ([Rondon et al., 2011](#)). Understanding the mechanics is of particular importance for risk assessment.  
<sup>24</sup> Small scale laboratory experiments are usually unable to properly capture the dynamics of  
<sup>25</sup> geophysical events. However, they can be useful to precisely study the physical mechanisms,  
<sup>26</sup> which may play a crucial role in real flows ([Iverson, 1997](#)).

<sup>28</sup> Conventionally, granular materials such as soils are modelled as a continuum. On a  
<sup>29</sup> macroscopic scale, granular materials exhibit many collective phenomena and the use of  
<sup>30</sup> continuum mechanics to describe the macroscopic behaviour can be justified. However on  
<sup>31</sup> a grain scale, the granular materials exhibit complex solid-like and/or fluid-like behaviour  
<sup>32</sup> depending on how the grains interact with each other. Numerical studies at grain scale allow a  
<sup>33</sup> precise understanding of the internal flow structure. However, even in simplified geometries  
<sup>34</sup> such as those investigated in the laboratory-scale experiments, DEM suffers from a serious  
1 short-coming in the number of grains that can be simulated in a reasonable time. This is a  
2 critical issue when more complex geometries or long-time granular processes are considered, or  
3 when particle size distributions are broad. For this reason, most numerical studies are performed  
4 in 2D or simple particles shapes and size distributions are considered.

<sup>5</sup> Classical modelling strategies based on the finite element method (FEM) cannot be used for  
6 the simulation of very large deformations due to mesh distortion effects. In various application

of FEM, this problem is treated by means of technical tools such as re-meshing. These methods are, however, not robust and lead to round-off errors and are sensitive to the mesh characteristics. Recent works on granular materials suggest that a continuum law may be incapable of revealing in-homogeneities at the grain-scale level, such as orientation of force chains, collapse of local voids and grain rearrangements, which are purely micro-structural effects (Rycroft et al., 2009). Discrete element approaches are capable of simulating the granular material as a discontinuous system allowing one to probe into local variables such as position, velocities, contact forces, etc. The fundamental question is how to model granular materials which exhibit complex phenomenon. It is important to understand the mechanics of granular flows and the ability and limitations of continuum methods in modelling the granular flow dynamics.

## 4.2 Granular column collapse

The collapse of a granular column, which mimics the collapse of a cliff, has been extensively studied in the case of dry granular material (Hogg, 2007; Kerswell, 2005; Lajeunesse et al., 2004; Lo et al., 2009; Lube et al., 2005; Staron and Hinch, 2007; Zenit, 2005). The granular column collapse experiment involves filling a rectangular channel of height  $H_0$  and width  $L_0$  with a granular material of mass ‘m’ (see figure 4.1). The granular column is then released *en masse* by quickly removing the gate, thus allowing the granular material to collapse onto the horizontal surface, forming a deposit having a final height  $H_f$  and length  $L_f$ . Despite the complexity of the intermediate flow dynamics, experimental investigations have shown that the flow evolution, the spreading velocity, the final extent of the deposit, and the energy dissipation can be scaled in a quantitative way independent of the substrate properties, grain size, density, the shape of the granular material and the released mass (Lajeunesse et al., 2005; Lube et al., 2005; Staron and Hinch, 2007). The granular collapse has also been studied using discrete element method, which allows precise measurement of the internal flow structure (Lo et al., 2009; Staron and Hinch, 2007; Staron et al., 2005; Utili et al., 2014). Power laws relating the final run-out and height to the initial aspect ratio ( $a = H_0/L_0$ ) of the column were observed. These findings immediately pose a question: are these simple scaling fortuitous, an oversimplification, or in fact indicative of a simple dynamical balance?

Granular flows are conventionally modelled as a frictional dissipation process in continuum mechanics but the lack of influence of inter-particle friction on the energy dissipation and spreading dynamics (Lube et al., 2005) is surprising. However, Kerswell (2005) showed the run-out behaviour has a clear material dependence. Although, the collapse of a granular column on a horizontal surface is a simple case of granular flow, a proper model that describes the flow dynamics is still lacking. Simple mathematical models based on conservation of

horizontal momentum capture the scaling laws of the final deposit, but fail to describe the initial transition regime. From a theoretical point of view, the spreading has been described using depth averaged equations (Kerswell, 2005; Larrieu et al., 2006). The depth-averaged and Saint-Venant equations, however, struggle to recover the precise dynamic behaviour of the system (Warnett et al., 2013) and only succeeds in predicting the scaling observed for aspect ratio less than one. Describing the behaviour of larger aspect ratio and capturing the initial stage of the collapse, when the grains experience a rapid change of direction from vertical to horizontal, remain an open challenge.

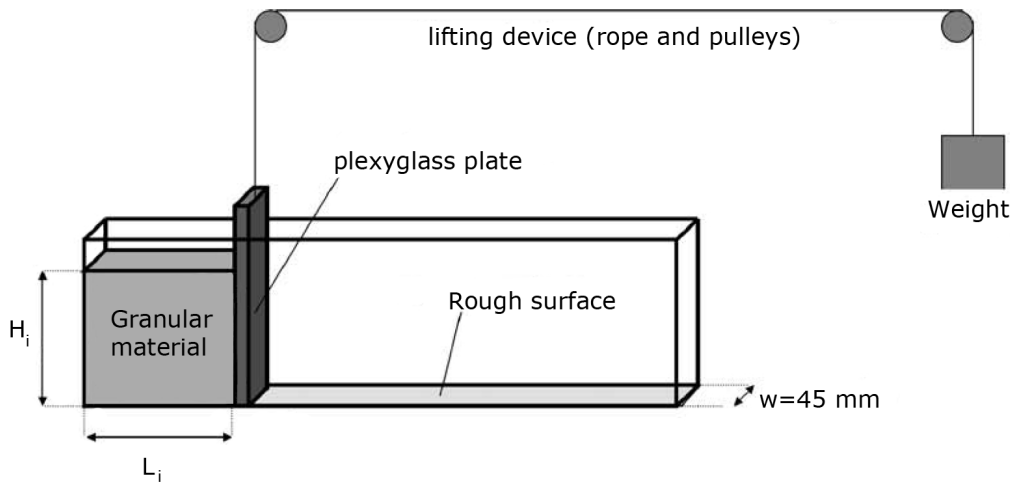


Figure 4.1 Schematic of experimental configuration for 2-D collapse in a rectangular channel, (Lajeunesse et al., 2004)

In the present study, multi-scale numerical modelling, i.e. grain-scale modelling and continuum analyses, of quasi-two dimensional collapse of granular columns are performed using two-dimensional Discrete Element Method (DEM) and Generalised Interpolation Material Point Method (GIMPM). GIMPM, a hybrid Eulerian – Lagrangian approach, with Mohr-Coulomb failure criterion is used to describe the continuum behaviour of the granular column collapse. Whereas, the micro-mechanics of the flow is captured using DEM simulations. Comparing the grain scale behaviour with the continuum simulations highlights the limitations of the continuum approach in modelling dense granular flows and their ability in capturing the complex flow kinematics which are due to micro-scale rheology.

### 4.2.1 Numerical set-up

In this study, the numerical set-up of granular columns are analogous to the experimental investigation performed by Lajeunesse et al. (2004). The experimental configuration of Lajeunesse et al. (2004) is shown in figure 4.1. Granular material of mass ‘m’ is poured into a container

17 to form a rectangular heap of length ‘ $L_0$ ’, height ‘ $H_0$ ’ and thickness ‘ $W$ ’. The internal friction  
 18 angle and the wall friction between the wall and the glass beads measured by [Lajeunesse et al.](#)  
 19 ([2004](#)) are listed in table 4.1. The gate is then quickly removed to release the granular mass that  
 20 spreads in the horizontal channel until it comes to rest. The final run-out distance ‘ $L_f$ ’ and the  
 21 collapsed height ‘ $H_f$ ’ are measured. The run-out distance and collapse height exhibit a power  
 22 law relation with the initial aspect ratio ‘ $a$ ’ ( $= H_0/L_0$ ) of the column.

Table 4.1 Material properties of glass ballotini ([Lajeunesse et al., 2004](#))

Parameter	Value
Mean grain diameter	1.15 mm
Repose angle	$22 \pm 0.5^\circ$
Avalanche angle	$27.4 \pm 0.5^\circ$
Wall friction angle	$24.8 \pm 0.2^\circ$

23 Granular materials when released suddenly on a horizontal surface exhibit transient flow.  
 24 In this study, the mechanism of flow initiation, spreading dynamics and energy dissipation are  
 studied for varying initial aspect ratios of the granular column. The soil grain characteristics  
 of the DEM sample match that of the experiment. The particle size distribution (PSD) is  
 one of the most important factors controlling landslide initiation and soil permeability ([Utili](#)  
[et al., 2014](#)). Cumulative  $\beta$  distribution (described in ??) is used to generate a graded sample  
 with a mean grain diameter of 1.15mm (see figure 4.2b). The DEM sample is composed  
 of  $\sim 3000$  disks with a uniform distribution of diameters by volume fractions in the range  
 $[d_{min}, d_{max}] = 0.92 - 1.38$  mm with polydispersity  $r = \frac{d_{max}}{d_{min}} = 1.5$ . The granular column is  
 prepared by allowing randomly placed grains to undergo ballistic deposition with a constant  
 potential head between layers of soil grains. A snapshot of the sample generated is shown  
 in figure 4.2a. A DEM sample with soil grains arranged in a regular hexagonal lattice is also  
 used to study the influence of crystallisation and jamming on the run-out behaviour.

The overlap between grains are determined by the stiffness  $k_n$  of the spring in the normal  
 direction. Typically, an average overlap in the range 0.1 to 1.0% is desirable ([Zenit, 2005](#)) and  
 the spring constant is chosen to produce grain overlaps in this range. The stiffness is determined  
 as

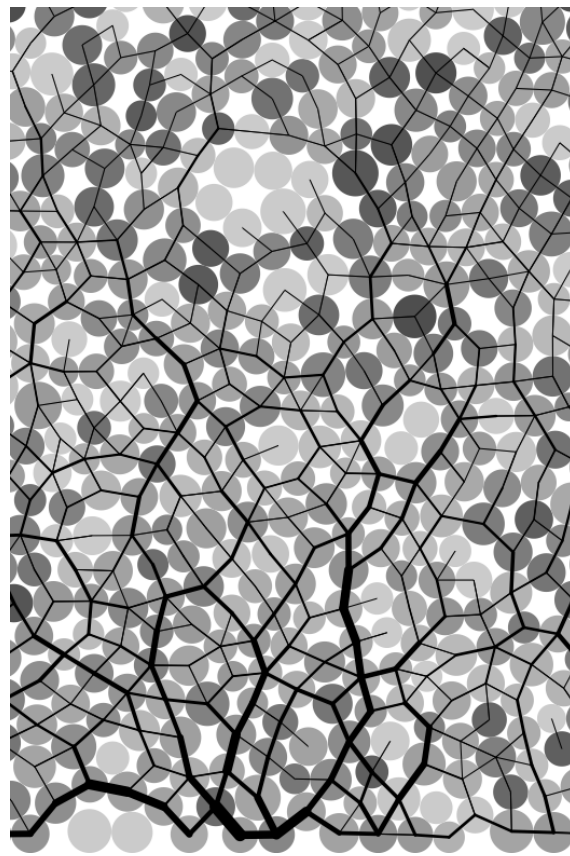
$$k_n = \frac{2\pi G}{(1-\nu)[2\ln(\frac{2r}{A}) - 1]} \quad (4.1) \quad 16$$

$$A = \left[ \frac{2r(1-\nu)f_n}{\pi G} \right]^{\frac{1}{2}}, \quad (4.2) \quad 17$$

18

## 4.2 Granular column collapse

85



(a) DEM sample prepared using ballistic deposition

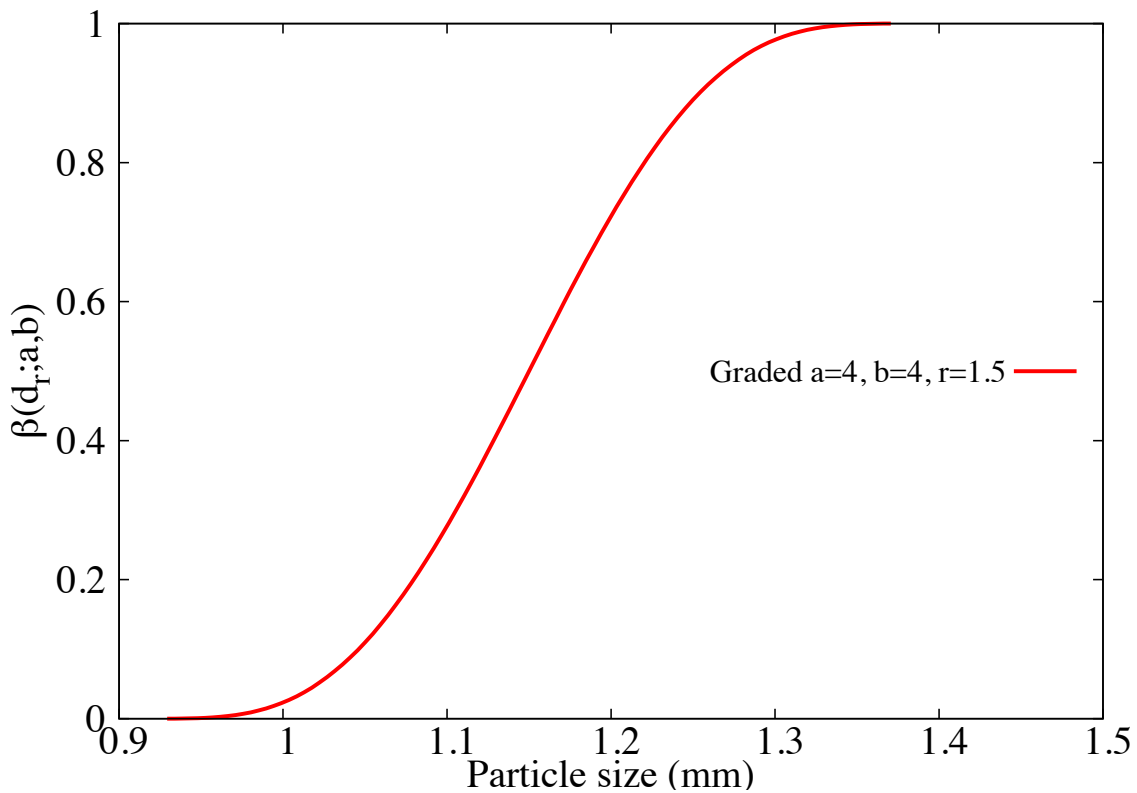
(b) DEM grains generated using the cumulative  $\beta$  distribution

Figure 4.2 DEM sample characteristics

where  $f_n$  is the normal contact force; G is the shear modulus; v is the Poisson's ratio and r is the radius of the grain. A simpler form of stiffness for a spherical grain is defined as

$$k_n = 4ER, \quad (4.3)$$

where E is the Young's modulus of the material and R is the radius of the grain. Cambou et al. (2009) observed that the contact model has negligible influence on the run-out behaviour of rapid granular flows. The granular collapse simulations performed using non-linear Hertz-Mindlin contact model and the linear-elastic contact model showed no significant difference in the granular flow behaviour (Utili et al., 2014). Linear-elastic contact model is used in the present study due to its simplicity and lower computation time requirement. The maximum tangential force is limited by the Mohr-Coloumb criterion.

Staron and Hinch (2007) observed that the coefficient of restitution  $\varepsilon$  dramatically changes the behaviour of the system for  $\varepsilon \rightarrow 1$ ; in particular, this dramatic change is expected to become more important for increasing values of a. On the contrary, for  $\varepsilon \leq 0.8$ , the influence of the coefficient of restitution becomes negligible. In the present study, a value of 0.75 is adopted as the coefficient of restitution, similar values of restitution coefficient was adopted by Girolami et al. (2012) and Zenit (2005). The normal damping coefficient  $C_n$  is appropriately chosen to achieve the required coefficient of restitution  $\varepsilon$ :

$$C_n = 2\gamma\sqrt{m_{ij}k_n} \quad (4.4)$$

$$\text{where } \gamma = -\frac{\ln(\varepsilon)}{\sqrt{\pi^2 + \ln^2(\varepsilon)}}, \quad \text{and} \quad m_{ij} = \frac{m_i m_j}{m_i + m_j}. \quad (4.5)$$

The micro-mechanical parameters used in this study are presented in table 4.2. Due to the unsteady nature of the flow, the grains get dispersed on the horizontal plane as discrete bodies start to separate from the main mass, hence the run-out distance is calculated as the position of the farthest grain which has at least one contact with the main mass.

GIMPM with Mohr-Coloumb constitutive model is used to simulate plane strain collapse of granular columns. Crosta et al. (2009) observed that the Mohr-Coloumb with non-associate flow rule is able to capture granular collapse dynamics and models the strong vertical motion. This method does not suffer the limitations of typical shallow water equation techniques. In order to understand the ability and limitations of continuum approaches in capturing the local rheology, it is important to scale the grain scale material properties, such as the inter-particle friction and stiffness, to the continuum scale (macroscopic friction and Young's modulus). Crosta et al. (2009) observed that the friction angle plays a significant role on the run-out behaviour.

Table 4.2 Micro-mechanical parameters used in DEM simulations

Parameter	Value
Young's modulus of glass bead	$70 \times 10^9 \text{ N m}^{-2}$
Poisson's ratio	0.22 - 0.24
Diameter of glass beads	0.92 to 1.38 mm
Normal and shear stiffness of grains	$1.6 \times 10^8 \text{ N m}^{-1}$
Normal and shear stiffness of wall	$4 \times 10^8 \text{ N m}^{-1}$
Inter-particle friction coefficient, $\mu$	0.53
Wall friction coefficient	0.466
Coefficient of restitution, $\epsilon$	0.755

In MPM simulations, the granular flow is assumed to be in critical state and the critical state friction angle is used in the Mohr-Coloumb model. In order to obtain the critical state friction angle of the granular sample, a shear test is performed using 1078 DEM grains. A bi-periodic boundary condition is adopted on the sides of the sample (see figure 4.3a). Two layers of fixed grains (shown in black) is placed at the top and the bottom of the shear sample. A normal pressure 'P' and a horizontal velocity  $v$  is applied to the fixed grains at the top of the shear sample. As the normal effective stress is varied, the average shear stress in the sample is measured. The sample is sheared until critical state is reached. The slope of shear stress versus normal effective stress gives the critical state friction angle. A critical state friction angle of  $22.2^\circ$  is obtained. The macroscopic friction angle is in the range observed by Estrada et al. (2008) and Mitchell and Soga (2005). The Young's modulus of the granular assembly is obtained as the initial slope of the stress-strain plot of a uni-axial compression of a granular column using DEM.

Guilkey et al. (2003) suggests using at least four material points per cell for large deformation problems. In the present study, 16 material points per cell is adopted. If the mesh is too fine and the number of particles is too large, the particle size  $2l/p$  decreases, and the GIMPM interpolation function tends to approach the original MPM function, as shown by ?. Hence, GIMPM loses the merit that it reduces the numerical noise due to material points crossing the background mesh. In addition, the probability of particles crossing the background mesh increases with decrease in the mesh size, hence, more noise may be produced (Abe et al., 2013). The effect of number of material points per cell on the run-out behaviour is discussed in section 4.3.5. In the present study, each material point represents one-fourth of a DEM soil grain. The parameters used for the continuum analyses are presented in table 4.3.

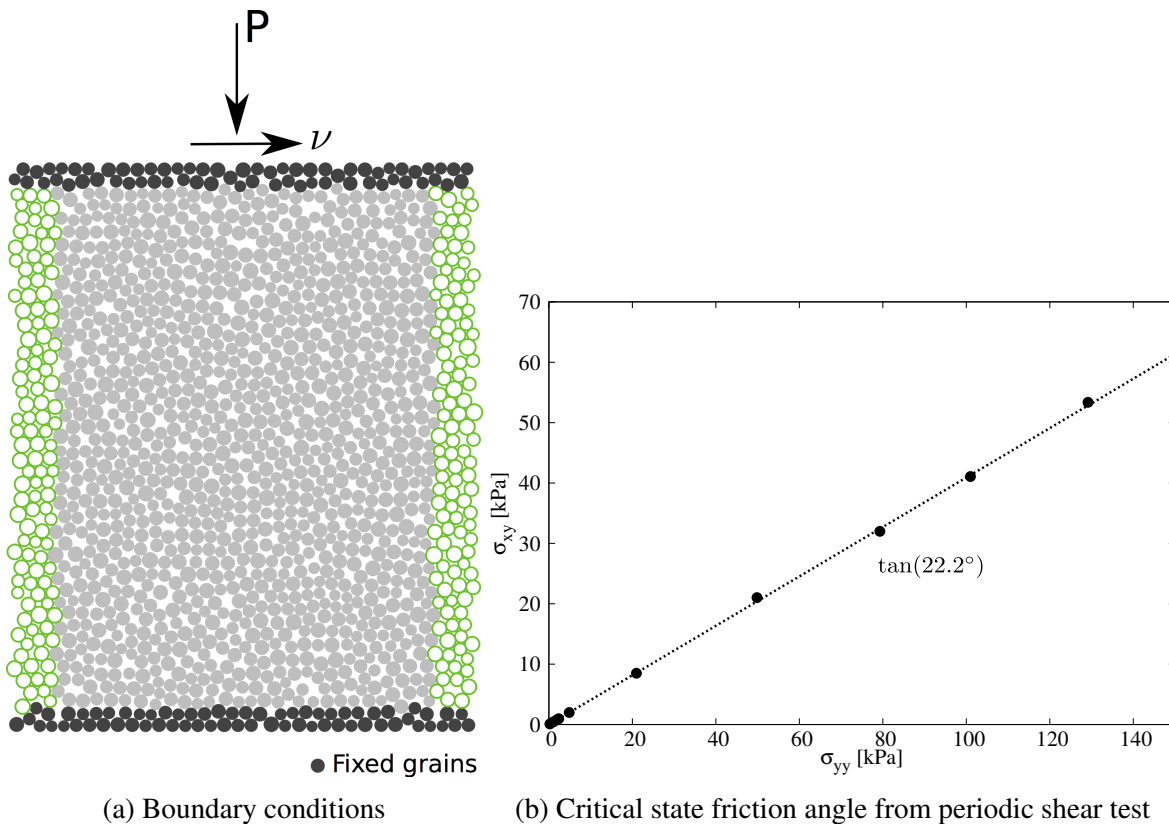


Figure 4.3 Periodic shear test

Table 4.3 Parameters used in continuum simulations

Parameter	Value
Material point spacing	0.575 mm
Number of material points per cell	16
Young's Modulus, E	$1.98 \times 10^6 \text{ N m}^{-2}$
Poisson's ratio, $\nu$	0.22 to 0.24
Friction angle, $\phi$	$23.2 \pm 0.2^\circ$
Dilatancy angle, $\Phi$	$0^\circ$
Density, $\rho$	$1800 \text{ kg m}^{-3}$
Wall friction	0.466
Time step increment	$1.0 \times 10^{-6} \text{ s}$

### 6 4.2.2 Deposit morphology

7 Two-dimensional plane-strain MPM and DEM simulations of granular column collapse are  
 8 performed by varying the initial aspect ratio of the column from 0.2 to 10. The normalized final  
 9 run-out distance,  $\Delta L = (L_f - L_0)/L_0$ , as a function of the initial aspect ratio ‘a’ of the column  
 10 is presented in figure 4.4. Similar to the experimental behaviour a power law relation between  
 11 the run-out and the initial aspect ratio of the column is observed. Two distinct flow regimes can  
 12 be seen: (a) for ‘a’ < 2.7 a linear relation between the spread and aspect ratio can be observed,  
 13 and (b) for ‘a’ > 2.7 a power-law relationship exists. In the present study, the following scaling  
 14 law for the run-out (using DEM) is observed:

$$\frac{L_f - L_0}{L_0} \approx \begin{cases} 1.67a, & a \lesssim 2.7 \\ 2.7a^{2/3}, & a \gtrsim 2.7 \end{cases} \quad (4.6)$$

Both, MPM and DEM simulations are able to capture the linear relationship for ‘a’ < 2.7,  
 and the simulation results agree with the experimental investigation ([Lajeunesse et al., 2005](#)).  
 This shows that a simple frictional dissipation model is able to capture the flow dynamics for  
 columns with small aspect ratios. For ‘a’ < 2.7, the normalised run-out distance predicted using  
 DEM simulations are very close to those observed in the experiment. DEM simulations with  
 hexagonal packing shows shorter run-out distances in comparison to randomly packed sample.  
 This difference in the run-out behaviour might be due to the crystallisation and jamming effects  
 in hexagonal packing. The small difference in the final run-out between the DEM and the  
 experimental results can be attributed to the variation in the packing of grains. Also, the  
 experimental data corresponds to granular column collapse in a rectangular channel, where the  
 collapse is not a pure two-dimensional collapse as in the case of numerical simulations.

Significant difference in the final run-out between MPM, which is based on a simple  
 frictional model for dissipation of potential energy, and DEM simulations indicates a change in  
 the mechanism of energy dissipation for columns with large aspect ratios (‘a’ > 2.7). [Staron and](#)  
[Hinch \(2005\)](#) observed that a constant frictional dissipation model cannot describe a power-law  
 relation observed at large aspect ratios. A transition in the run-out behaviour at an aspect ratio  
 of 2.7 indicates a change in the flow kinematics. Similar behaviour in the run-out distance was  
 observed by [Bandara \(2013\)](#) for columns with large aspect ratios ( $a \geq 2$ ).

The longer run-out distance in MPM simulations at large aspect ratios might be influenced  
 1 by the amount of material mobilised during the collapse. In tall columns, the entire column  
 2 participates in the flow, in contrast to short columns where the collapse is due to avalanching of  
 3 flanks ([Lajeunesse et al., 2004](#)). It is possible that MPM simulations collapse more resulting  
 4 in longer run-out distances. Figure 4.5 shows the normalized final height as a function of the

5 initial aspect ratio of the column. Similar to the run-out behaviour, the normalised-height also  
 6 shows two distinct regimes. The scaling of final height of the column with the initial aspect  
 7 ratio of the column can be written as

$$8 \quad \frac{H_f}{L_i} \propto \begin{cases} a, & a \lesssim 0.7 \\ a^{2/3}, & a \gtrsim 0.7 \end{cases} \quad (4.7)$$

10 The final height predicted by both DEM and MPM simulations match the experimental data  
 11 for columns with smaller aspect ratio ( $a \leq 0.7$ ). Linear relationship between the final height and  
 12 the aspect ratio indicates that only a part of the granular column is mobilised during the collapse.  
 13 For tall columns, both approaches predict similar normalised height. However, the normalised  
 14 height observed in MPM is higher than in DEM simulations, which is in contrast to the idea of  
 15 increase in the amount of material mobilised during the collapse in MPM simulations resulting  
 16 in longer run-out distance. Hence, the longer run-out observed in MPM simulations is due a  
 17 change in the flow dynamics at higher aspect ratios, which is not captured in MPM simulations.  
 18 The final height of a column is controlled by the amount of static region in the granular column  
 19 collapse, while the run-out distance is essentially a function of the flowing mass. Hence, it is  
 20 important to compare the evolution of flow and the internal flow structure in DEM and MPM  
 21 simulations.

### 22 4.2.3 Flow evolution and internal flow structure

23 The normalised run-out and height as a function of the aspect ratio indicates that, for a given  
 24 granular material and substrate properties, the flow dynamics and the final deposit morphology  
 25 are independent of the volume of granular material released, but depend only on the geometry  
 26 of the column. A power law relationship is observed between the run-out distance and the  
 27 initial aspect ratio of the column. A transition in the run-out behaviour at an aspect ratio of 2.7  
 28 indicates a change in the flow dynamics.

29 For short columns ('a' < 2.7), the flow is initiated by a failure at the edge of the pile along a  
 30 well-defined fracture surface. The granular mass fails through avalanching of flanks producing  
 31 a truncated cone-like deposit ('a' < 0.7) or conical deposit ('a' > 0.7). The grains located above  
 32 the failure surface move "*en masse*" leaving a static region underneath the failure surface.

33 Dimensional analysis of granular column collapse reveals an intrinsic time defined as  
 34  $\sqrt{H_0/g}$ . This intrinsic time is a transient time of order  $\tau_c$ , at which the flow is fully developed,  
 35 i.e., the potential energy available at the initial stage of collapse is now fully converted to  
 36 kinetic energy. Numerical simulation of the velocity profile of a granular column ('a'=0.4) at  
 critical time  $\tau_c$  is presented in figure 4.6. At critical time, the velocity field depends only on the

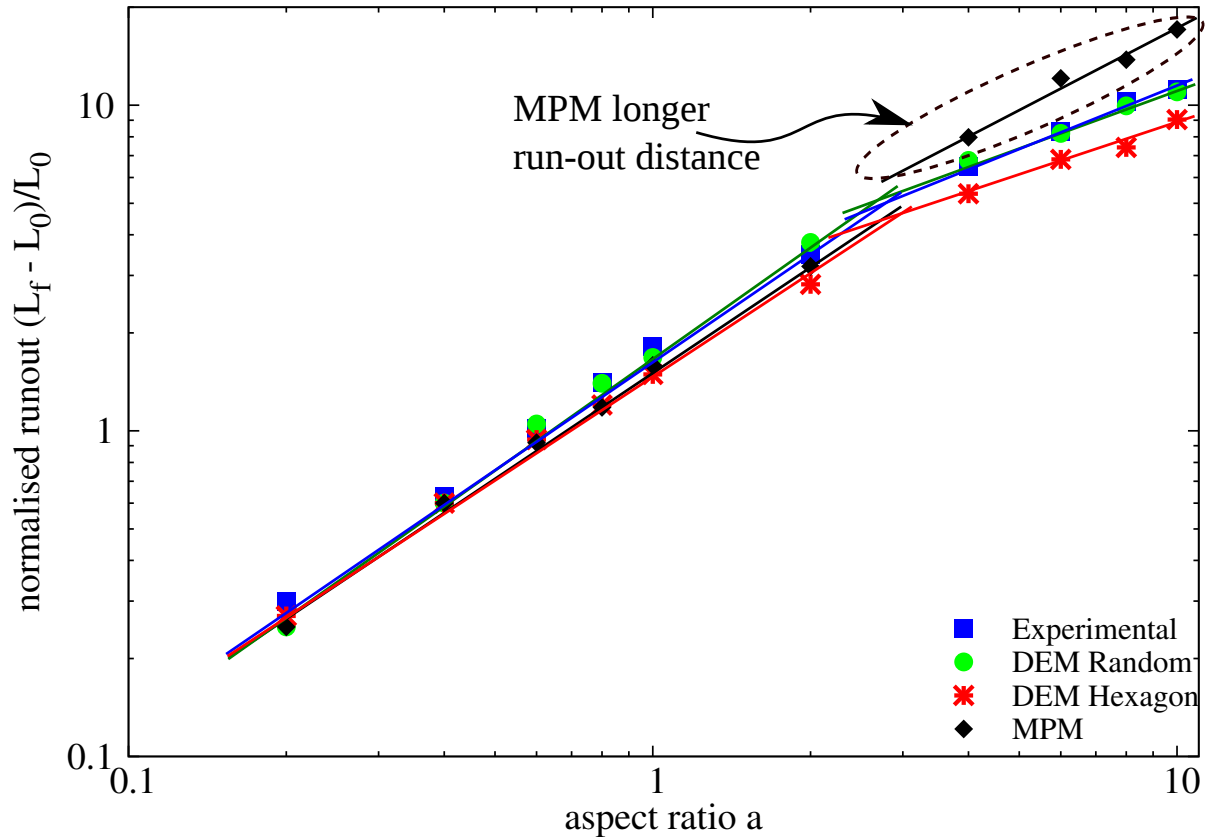


Figure 4.4 Normalised final run-out distance for columns with different initial aspect ratios

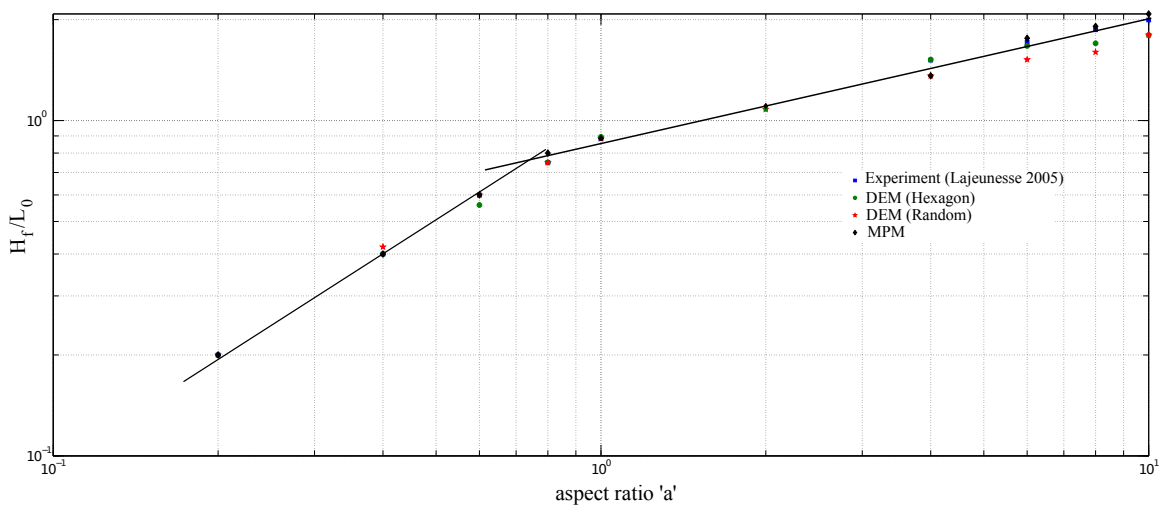


Figure 4.5 Normalised final collapse height for columns with different initial aspect ratios

position of the grain along the sliding mass. The maximum velocity is observed at the front of the flowing mass corresponding to that of a plug flow in horizontal direction. Particulate and continuum simulations show similar run-out distance at the critical time. Both approaches show similar quantity of material destabilised above the failure surface. However, the crystalline arrangement of soil grains in a hexagonal packing results in a different flow mechanics, which also shows the effect of jamming at the flow front. The continuum nature of MPM results in a slightly different geometry of the material destabilised above the failure surface in comparison to DEM simulations. The velocity profile is similar to a steady granular surface flow observed by [Lajeunesse et al. \(2004\)](#).

For columns with lower initial aspect ratios, the run-out distance is proportional to the mass flowing above the failure surface. The spreading results from a Coulomb-like failure of the edges and implies no free fall of the column. [Daerr and Douady \(1999\)](#) also observed active Coulomb yielding in transient granular surface flows. In this case, the effective friction properties of the flow can be simply predicted from the shape of the final deposit. The amount of mass mobilized during the collapse is significantly affected by the angle of the failure surface. Figure 4.6 shows that both numerical techniques predict a distinct failure surface when the flow is fully developed at critical time  $\tau_c$ . The angle of the failure surface is found to be about  $55^\circ$ . The failure surface begins from the toe of the column and propagates inwards at an angle of  $50$  to  $55^\circ$ . The formation of the “truncated conical deposit” or “conical deposit” depends only on the initial length of the column, as the angle of the failure surface is found to be independent of the aspect ratio. The failure angle is consistent with the interpretation in terms of *active Coulomb failure* ([Lajeunesse et al., 2004](#)), which leads to a predicted failure angle  $\theta_y = 45^\circ + \delta/2$ , where  $\delta$  is the friction angle of the granular material. In the present study, the macroscopic friction angle is  $22^\circ$ , which leads to  $\theta_y = 45^\circ + 22^\circ/2 = 56^\circ$ , which is in good agreement with the numerical simulations and experimental observations by [Lajeunesse et al. \(2004\)](#). The fracture angle has a direct effect on the transition between the truncated cone and the conical deposit occurring at an aspect ratio of 0.7. [Schaefer \(1990\)](#) observed the onset of instabilities in a narrow wedges of  $56$  to  $65^\circ$  for Cambridge-type constitutive models that describes granular flows, which is in-line with the failure angle observed in the present study.

The final profile of the granular column with an initial aspect ratio of 0.4 is shown in figure 4.7. Both MPM and DEM show similar run-out behaviour. The continuum approach is able to capture the flow dynamics of short columns, where the failure mechanism is active Coulomb failure. In dense hexagonal packing, the failure surface is steep due to crystallisation effect. The variation in the angle of the failure surface causes a difference in the amount of material destabilised, and in turn the run-out distance. This crystallisation phenomenon is found to have a significant influence on the final deposit of the granular column. [Lacaze and](#)

## 4.2 Granular column collapse

## 93

- <sup>2</sup> Kerswell (2009) observed that poly-disperse grains are less susceptible to crystallize especially  
<sup>3</sup> in the case of tall columns.

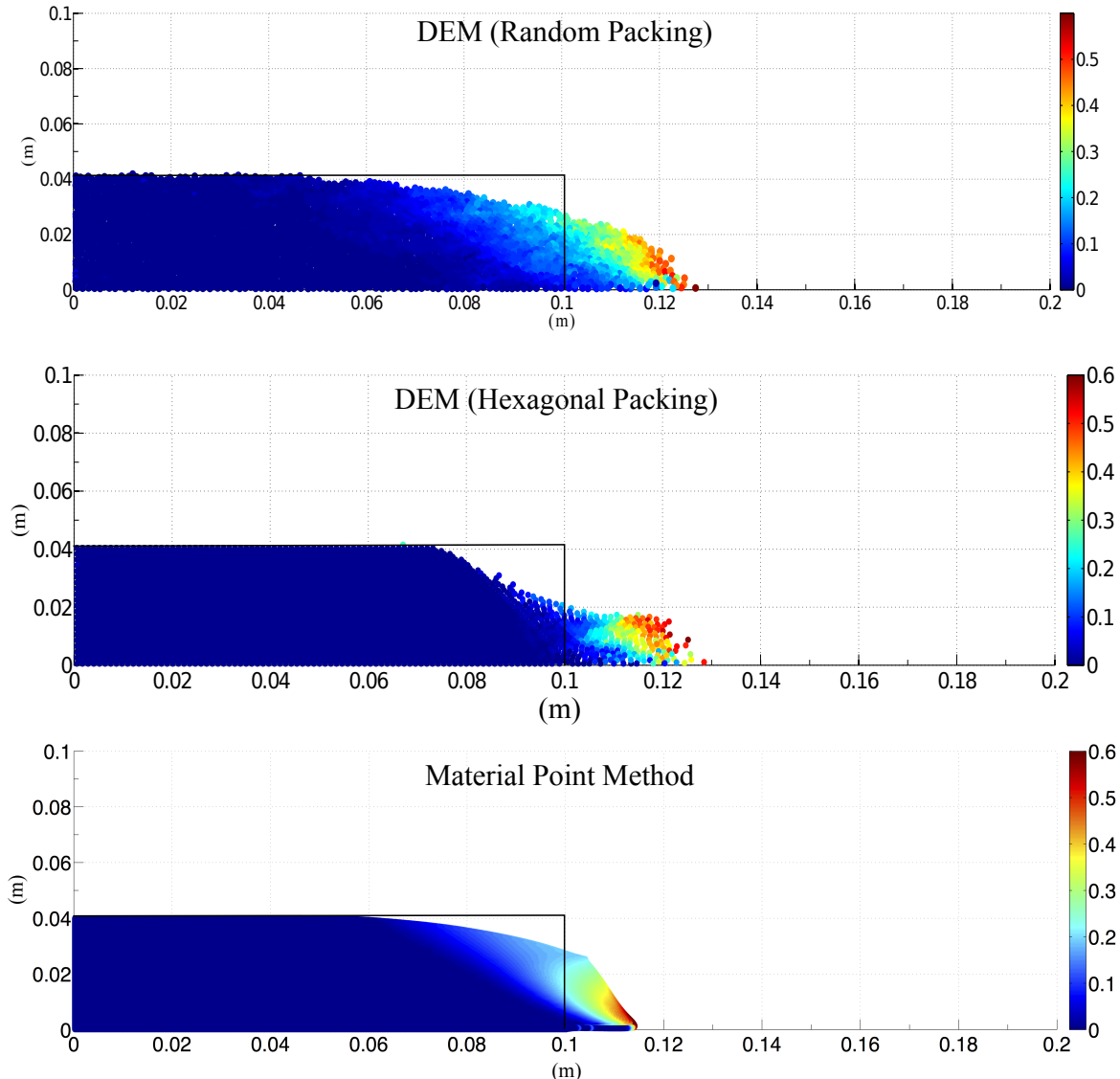


Figure 4.6 Velocity profile of a granular column collapse ( $a = 0.4$  &  $t = \tau_c$ )

- <sup>4</sup> For tall columns ('a' > 2.7), the flow is still initiated by a well defined failure surface as  
<sup>5</sup> can be seen in figure 4.8. However, in this case the initial granular column is much higher  
<sup>6</sup> than the top of the failure surface. Due to gravity most of the grains in the column experience  
<sup>7</sup> free-fall consuming the column along their way. When they reach the vicinity of the failure  
<sup>8</sup> surface, the flow gets deviated along the horizontal direction releasing a huge amount of kinetic  
<sup>9</sup> energy gained during the free fall. For larger aspect ratio ( $a > 0.7$ ), the resulting static region is

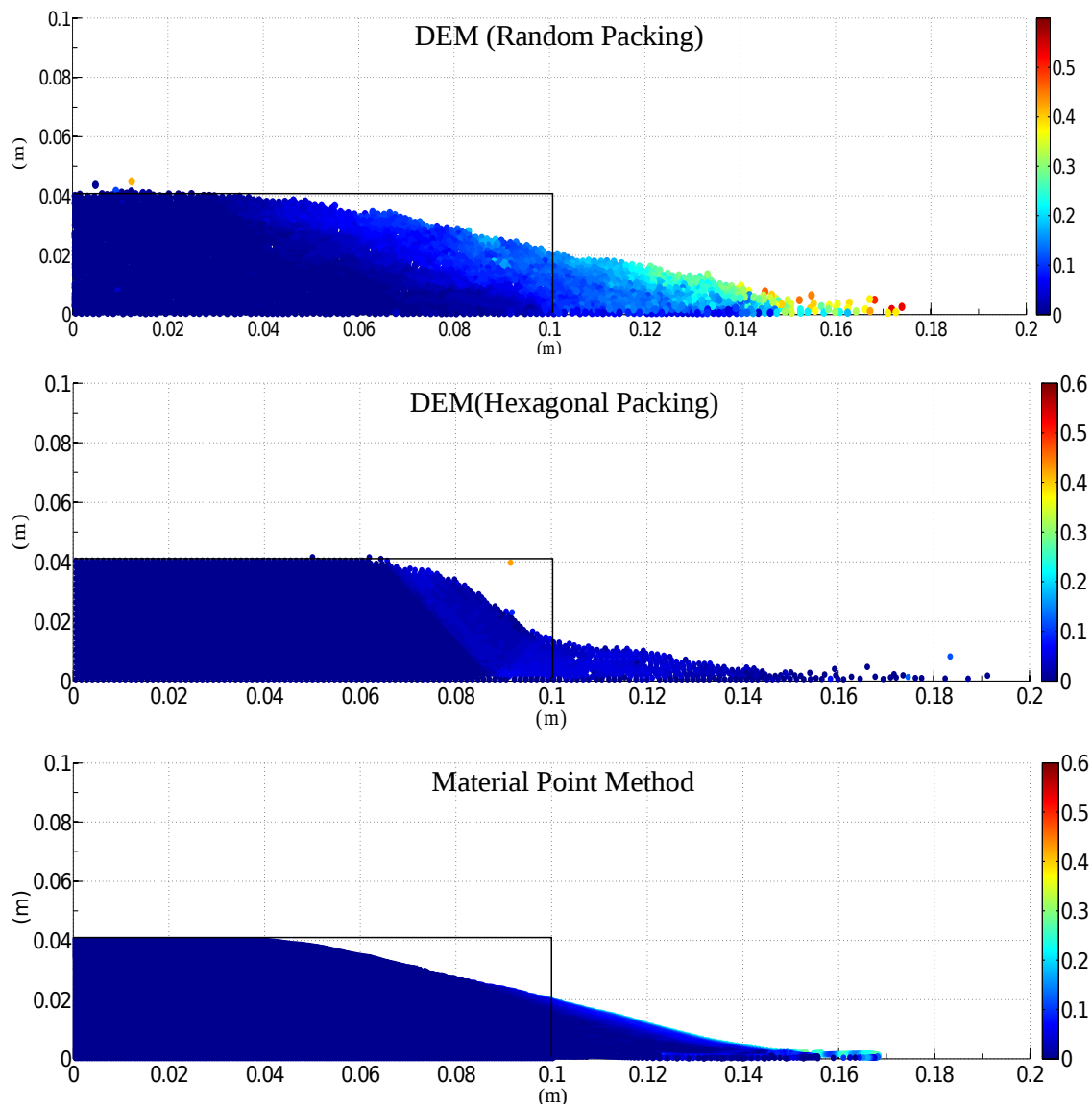


Figure 4.7 Velocity profile of a granular column collapse ( $a = 0.4$  &  $t = 3 \times \tau_c$ )

<sup>10</sup> a cone, the final height of the cone, i.e.,  $H_f$  lies above the summit of the failure surface. Hence,  
<sup>11</sup> a different evolution is observed from that of the axis-symmetric geometry ([Lube et al., 2005](#)),  
<sup>12</sup> where the final height coincides with the summit of the failure surface forming a truncated  
<sup>13</sup> conical deposit. [Lajeunesse et al. \(2004\)](#) observed that the variation in the deposit morphology  
<sup>14</sup> between the axis-symmetric case and the rectangular collapse to be a geometrical effect rather  
<sup>15</sup> than as an experimental artefact.

<sup>16</sup> An initial failure surface starting from the toe end of the column at an angle of about 55°  
<sup>17</sup> can be observed at the critical time  $\tau_c$ . As the collapse of the granular collapse progresses,  
<sup>18</sup> successive failure planes parallel to the initial failure surface are formed and shear failure occurs  
<sup>19</sup> along these planes. The presence of several shear bands in the final profile of the collapsed  
<sup>20</sup> granular column confirms this behaviour. Crystallisation in hexagonal packing has a significant  
<sup>21</sup> effect on the run-out distance by forming series of parallel shear bands, resulting in unnatural  
<sup>22</sup> flow kinematics. This observation throws light on the mechanics of propagation of shear bands  
<sup>23</sup> in massive landslides such as the Storegga submarine landslide. The flow behaviour becomes  
<sup>24</sup> similar to that of columns with lower aspect ratio as the flow starts descending along the  
<sup>25</sup> failure plane. The final profile of the collapsed granular column with an initial aspect ratio  
<sup>26</sup> of 6 is presented in figure [4.9](#). For tall columns, the dissipation process is more complex due  
<sup>27</sup> to the free-fall dynamics. The vertical acceleration of the grains induces a non-trivial mass  
<sup>28</sup> distribution in the flow during spreading. This mass distribution plays a dominant role in the  
<sup>29</sup> power-law scaling observed in the run-out ([Staron and Hinch, 2007](#)).

<sup>30</sup> Regardless of the experimental configuration and the initial aspect ratio of the columns, the  
<sup>31</sup> flow is initiated by a well-defined rupture surface, above which the material slides down leaving  
<sup>32</sup> a static region underneath the failure plane. Depending on the aspect ratio of the column, two  
<sup>33</sup> asymptotic behaviours are observed. For smaller aspect ratios, the flow is dominated by friction  
<sup>1</sup> where as the large aspect ratio columns are influenced by the pressure gradient.

<sup>2</sup> To study the influence of aspect ratio on the flow dynamics of granular columns, the flow  
<sup>3</sup> front  $L(t)$  and the maximum height of column  $H(t)$  are tracked. The evolution of scaled height  
<sup>4</sup> ( $H_f/L_0$ ) and the run-out distance ( $L_f - L_0$ )/ $L_0$  with time for granular columns with an initial  
<sup>5</sup> aspect ratio of 0.4 and 6 are presented in figure [4.10](#). Three distinct regions can be observed  
<sup>6</sup> in the flow evolution of a granular column collapse regardless of the initial aspect ratio of  
<sup>7</sup> the column. An initial transient acceleration phase is observed for a time  $0.8\tau_c$ . This phase  
<sup>8</sup> is followed by a heap movement of granular materials at the foot with a constant spreading  
<sup>9</sup> velocity  $V$  for about  $2\tau_c$ . When time ' $t$ ' >  $\tau_c$ , the velocity varies linearly with depth in the  
<sup>10</sup> flowing layer and decreases exponentially with depth near the static layer. This velocity profile  
<sup>11</sup> is similar to those observed in steady granular surface flows ([Lajeunesse et al., 2004](#)). Most  
<sup>12</sup> of the run-out happens during this phase. The final phase involves deceleration of the flow

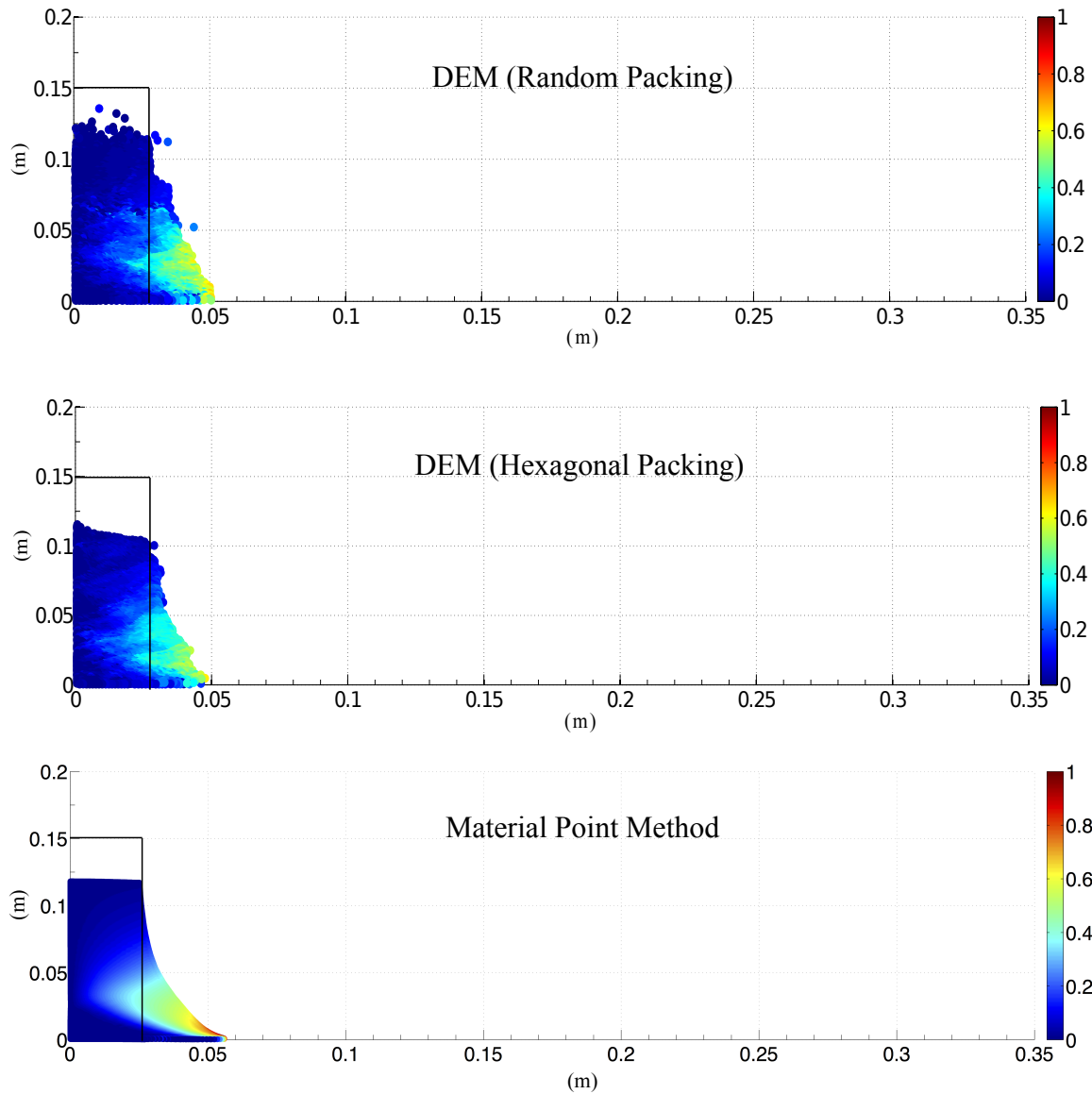


Figure 4.8 Velocity profile of a granular column collapse ( $a = 6$  &  $t = \tau_c$ )

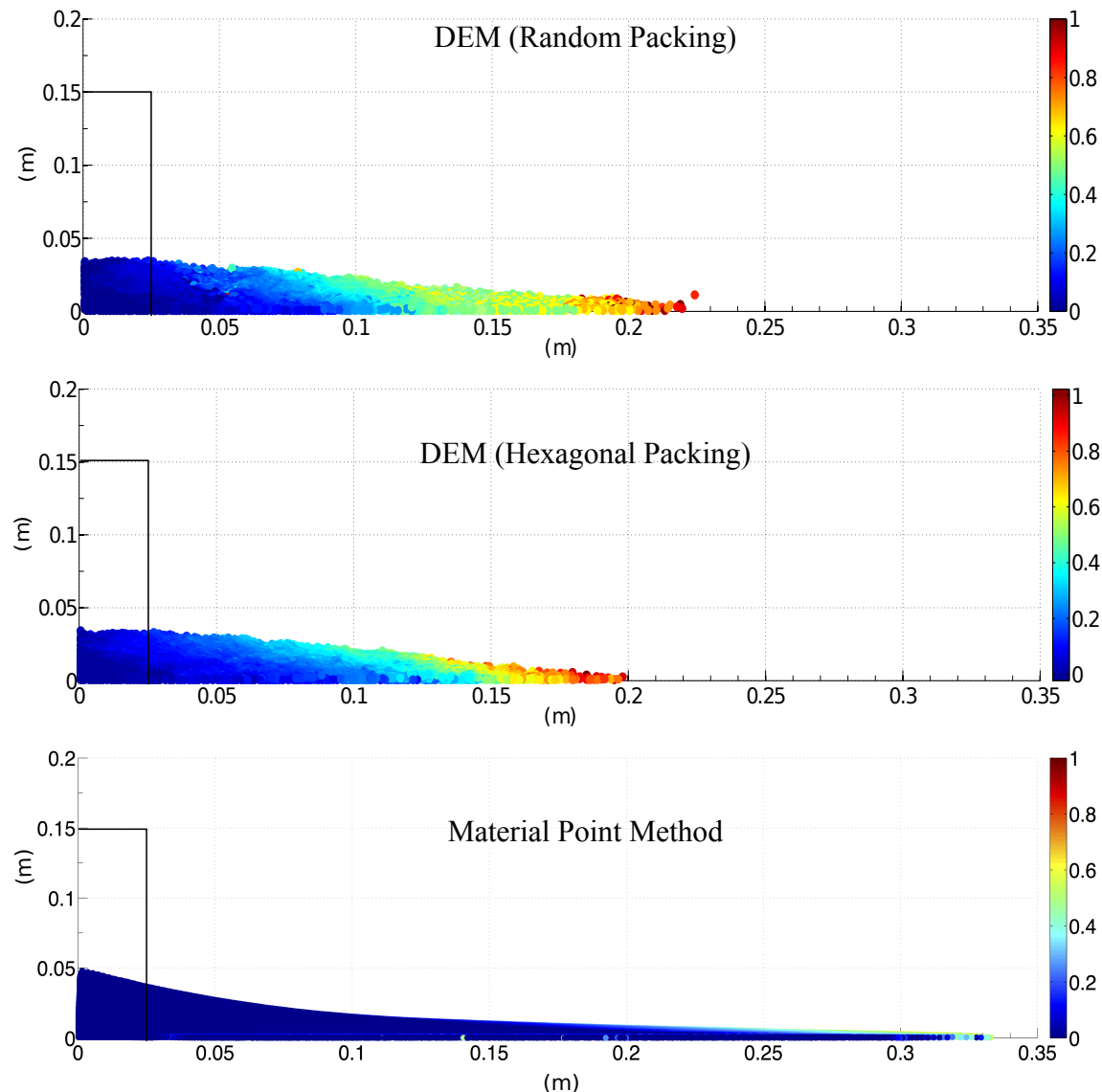


Figure 4.9 Velocity profile of a granular column collapse ( $a = 6$  &  $t = 3 \times \tau_c$ )

front and the flow comes to rest after about  $0.6\tau_c$ . The spreading of the granular column ceases after a time in the order of about  $3\tau_c$ , however some motion still persists along the free surface behind the flow front for a much longer time due to internal rearrangement, the duration of which can last up to  $t \approx 6\tau_c$ .

The critical time is evaluated as the time at which the potential energy available for the flow has been converted to the kinetic energy. In short columns, the critical time observed in both hexagonal and random packing of grains matches the experimental observations. However, the material point method overestimates the critical time by a factor of 0.75, which means that it takes longer for the flow to be fully mobilized. However, the actual run-out duration of the flow is short and the granular mass comes to rest at about  $t = 3\tau_c$ .

For columns with larger aspect ratios, the continuum and particulate approaches simulate similar flow evolution up to  $3\tau_c$ , beyond which particulate simulation decelerates and comes to rest, while the flow continues to evolve in MPM simulation resulting in longer run-out distance. The flow comes to rest at time  $t = 6\tau_c$ . The three phases in a granular flow can be distinctly observed in the flow evolution plot for a column with an initial aspect ratio of 6 (see figure 4.10b). The flow evolution behaviour observed in the case of DEM simulation matches the experimental observation by Lajeunesse et al. (2004). Hexagonal packing predicts longer time for the flow to evolve, which can be attributed to jamming of grains. In MPM simulations, the failure starts at the toe of the column and slowly propagates up to form the failure surface. This results in slower initiation of the flow. Whereas in DEM, the initial stage of collapse is characterised by free-fall under gravity. It can be observed that MPM overestimates the critical time by 50%. Although, MPM and DEM simulations show the same run-out at time  $t = 3\tau_c$ , the flow evolution between both the approaches is different. MPM simulations continue to accelerate beyond  $3\tau_c$  and ceases to flow at  $6\tau_c$ . In order to understand the difference in the flow dynamics in the case of material point method, it is important to study the mechanism of energy dissipation.

#### 4.2.4 Energy dissipation mechanism

The energy dissipation mechanism during the collapse provides useful insights into the flow dynamics. In the case of small aspect ratios, the columns undergo no free fall. The spreading mainly results from the failure of the edges, while the top of the column remains essentially undisturbed in the central area. Staron and Hinch (2007) showed that the amount of energy dissipated during the spreading  $\delta E$  can be easily recovered using the simple shape of the final

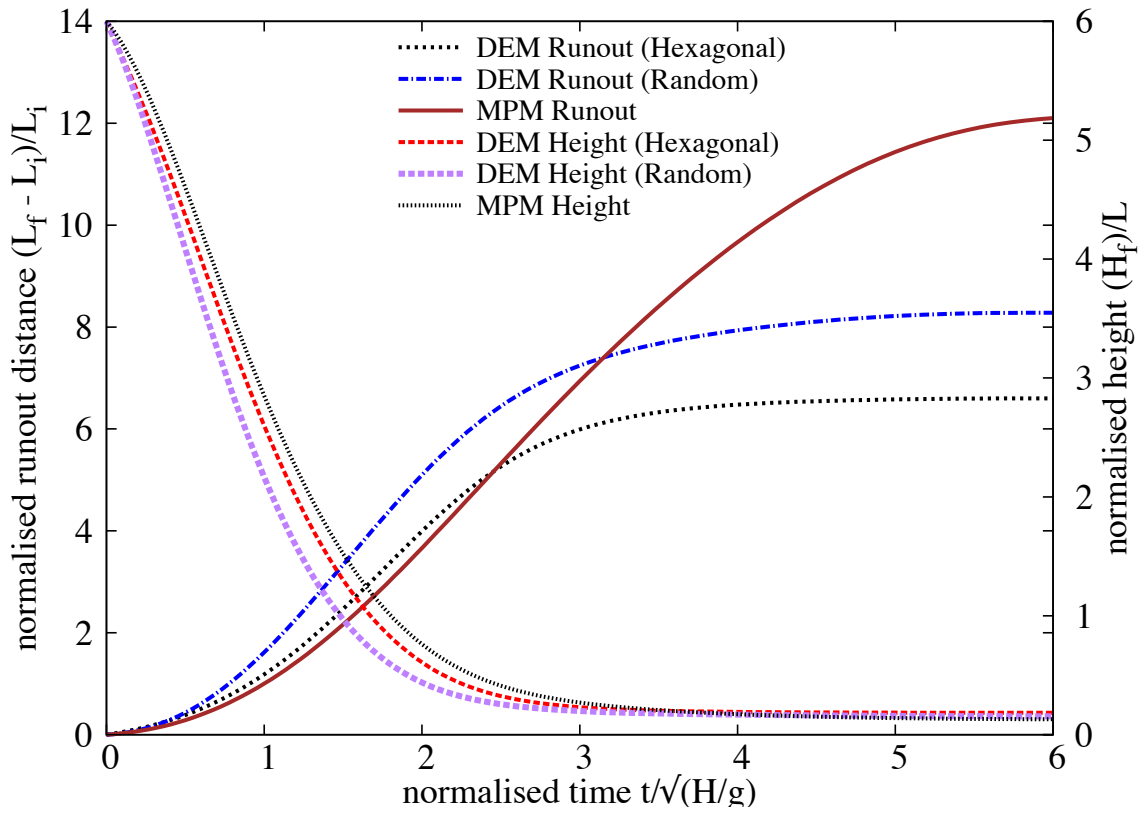
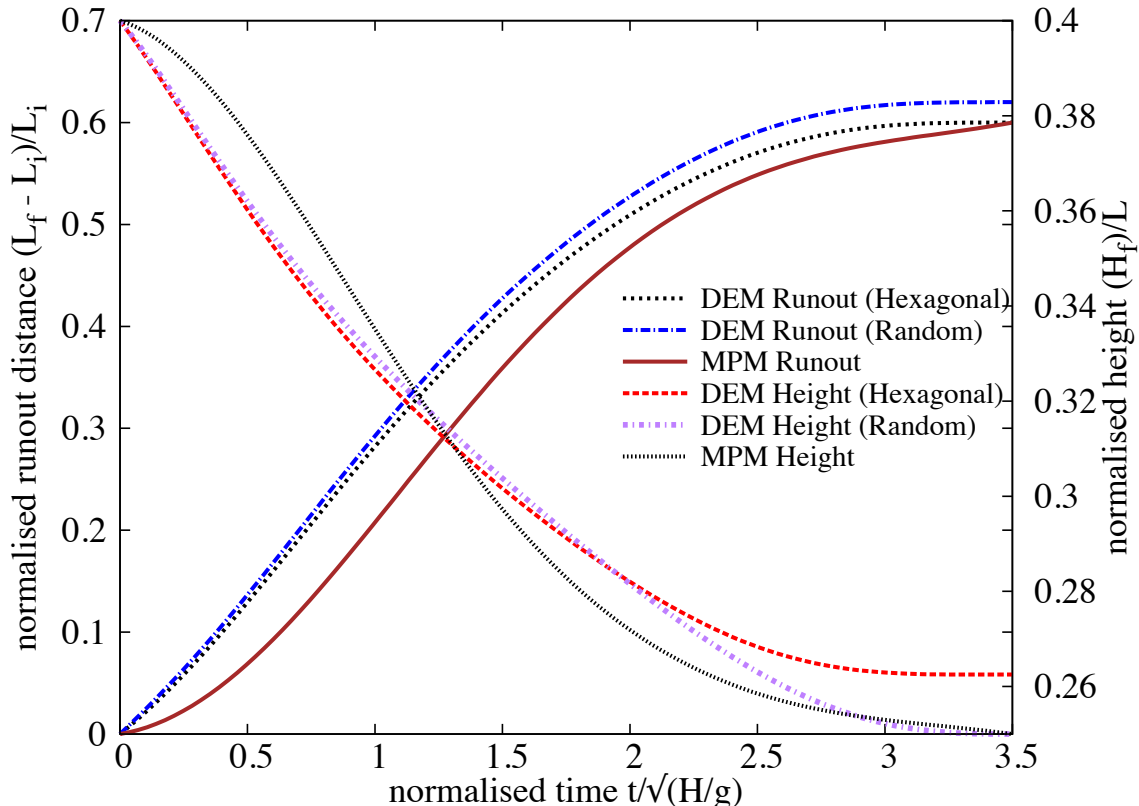


Figure 4.10 Flow evolution of granular column collapse

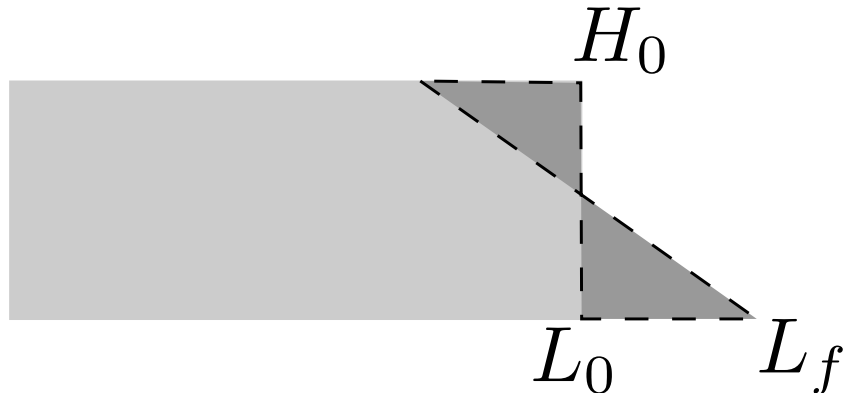


Figure 4.11 Scheme of collapse for small aspect ratio columns. The amount of energy  $\delta E$  lost in the process can be evaluated from the run-out distance  $L_f - L_0$  (after [Staron and Hinch \(2007\)](#)).

deposit and volume conservation (see figure 4.11). The difference of potential energy between the initial and the final states gives

$$\delta E = \frac{1}{6} g \rho (L_f - L_0) H_0^2, \quad (4.8)$$

where  $\rho$  is the density of the packing. It is assumed that this energy is dissipated by the work of frictional forces  $W_\mu$  over the total run-out distance by the center of mass G of the spreading material. [Staron et al. \(2006\)](#) considers two regions of dissipation: the amount of mass destabilised  $\frac{1}{4}(L_f - L_0)H_0$  over two thirds of the runout distance  $2(L_f - L_0)/3$  (considering the triangular shape of the final deposit and the initial and the final positions of the center of mass).  
1 The effective coefficient of friction  $\mu_e$  characterizes the mean dissipation in the flow. The work  
2 of friction forces is  
3

$$W_\mu = \frac{1}{6} \mu_e g \rho (L_f - L_0) H_0^2, \quad (4.9)$$

Equating  $\delta E$  and  $W_\mu$  gives  $\mu_e(L_f - L_0) = H_0$ . The scaling of the runout leads directly to the relation  $\mu_e = \lambda^{-1}$ , which is the numerical constant, which depends on the material properties ([Balmforth and Kerswell, 2005](#)), in the power-law relation between the run-out and the initial aspect ratio. The amount of energy  $\delta E$  dissipated during the spreading is compared with  $W = N_p g m_p r_p$ , where  $N_p$  is the total number of grains,  $m_p$  is their mass, and  $r_p$  is the total horizontal distance run by each of them. We observe that the dissipation energy  $\delta E$  is proportional to  $W$ . [Staron and Hinch \(2007\)](#) observed that the coefficient of proportionality gives a measure of the effective friction and observed a power law dependence between  $\mu_e$  and internal friction angle  $\mu$ :  $\mu_e = 0.425\mu^{0.2}$ . In this study, an effective friction angle  $\mu_e$  of  $21^\circ$  is observed, which is very close to the critical state friction angle of  $22^\circ$  used in MPM simulations. This proves that the energy dissipation mechanism modelled in a continuum

<sup>16</sup> sense as a frictional dissipation process captures the flow kinematics observed in DEM and  
<sup>17</sup> experiments, for short columns.

<sup>18</sup> Figure 4.12a shows the time evolution of the normalised potential energy ( $E_p/E_0$ ) and ki-  
<sup>19</sup> netic energy ( $E_k/E_0$ ) for granular columns with an initial aspect ratio ‘a’ = 0.4. The normalised  
<sup>20</sup> potential and kinetic energy are computed as

$$\text{21} \quad E_p = \sum_{p=1}^{N_p} m_p g h_p, \quad (4.10)$$

$$\text{22} \quad E_{ki} = \frac{1}{2} \sum_{p=1}^{N_p} m_p v_p^2, \quad (4.11)$$

<sup>24</sup> where  $N_p$  is the total number of grains,  $m_p$  is the mass of a grain ‘p’,  $h_p$  is the height and  $v_p$  is  
<sup>25</sup> the velocity of the grain ‘p’. The cumulative dissipation energy is computed as

$$\text{26} \quad \frac{E_d}{E_0} = 1 - \frac{E_k}{E_0} - \frac{E_p}{E_0}. \quad (4.12)$$

<sup>28</sup> It can be observed that both MPM and DEM show similar energy dissipation mechanism.  
<sup>29</sup> The DEM simulation shows 3% more potential energy dissipation in comparison with MPM  
<sup>30</sup> simulations. This small difference in the potential energy is due to grain rearrangements. This  
<sup>31</sup> shows the ability of continuum approach in capturing the flow kinematics of columns with  
<sup>32</sup> small aspect ratios ( $a \leq 2.7$ ).

<sup>33</sup> The evolution of normalised kinetic and potential energy of a tall column collapse (‘a’ of  
<sup>34</sup> 6) is shown in figure 4.12b. It can be observed that the initial potential energy stored in the  
<sup>1</sup> grains is converted to kinetic energy which is dissipated as the granular material flows down.  
<sup>2</sup> Three successive stages can be identified in the granular column collapse. In first stage, similar  
<sup>3</sup> to short columns, the flow is initiated by a well defined failure surface. However, the centre  
<sup>4</sup> of gravity of the granular column is much higher than the top of the failure surface, which  
<sup>5</sup> results in free fall of grains under gravity consuming the column along their way. In this stage  
<sup>6</sup> which lasts for ( $t < 0.8\tau_c$ ), the initial potential energy stored in the grains is converted into  
<sup>7</sup> vertical motion. In the second stage, when the grains reach the vicinity of the failure surface,  
<sup>8</sup> they undergo collisions with the bottom plane and the neighbouring grains, thus causing the  
<sup>9</sup> flow to deviate along the horizontal direction releasing a large amount of kinetic energy gained  
<sup>10</sup> during the free fall (see figure 4.9). In the third stage, the grains eventually leave the base area  
<sup>11</sup> of the column and flow sideways (Lajeunesse et al., 2004). As the process involves collective  
<sup>12</sup> dynamics of all the grains, it is difficult to predict the exact trajectory of a grain, however, the  
<sup>13</sup> overall dynamics can be explained.

<sup>14</sup> DEM simulations model both collisional and frictional dissipation process during the  
<sup>15</sup> collapse of tall columns. However, MPM simulations assume that the total initial potential  
<sup>16</sup> energy stored in the system is completely dissipated through friction over the entire run-out  
<sup>17</sup> distance, this results in longer run-out distance. Figure 4.12b shows the evolution of energy  
<sup>18</sup> with time. At the initial stage of collapse, characterised by free fall of grains under gravity,  
<sup>19</sup> DEM simulation due its particulate nature shows a rapid reduction in the potential energy in  
<sup>20</sup> comparison with MPM, where the failure begins from the toe of the column. The continuum  
<sup>21</sup> nature of MPM simulations results in slower initiation of collapse (see figure 4.10b). It can  
<sup>22</sup> be also observed from figure 4.12b that dissipation energy in MPM is 25% less than DEM  
<sup>23</sup> simulations. In order to understand the mechanism of energy dissipation, it is important to  
<sup>24</sup> separate the contribution from the cumulative frictional and collisional parts. The frictional  
<sup>25</sup> dissipation (basal and internal friction) observed in DEM is almost identical to the frictional  
<sup>26</sup> dissipation observed in MPM (figure 4.12b). The difference in the dissipation energy is due to  
<sup>27</sup> the collisional regime, which occurs at  $0.8\tau_c$ . The total dissipation and the frictional dissipation  
<sup>28</sup> curves diverge around  $0.8\tau_c$  where the grains near the vicinity of the failure surface undergo  
<sup>29</sup> collisions with the bottom plane and the neighbouring grains resulting in collisional dissipation  
<sup>30</sup> of the stored potential energy. DEM simulation show drop in the peak kinetic energy at  $\approx 0.8\tau_c$ ,  
<sup>31</sup> which is at the beginning collisional dissipation stage. MPM lacks this collision dissipation  
<sup>32</sup> mechanism, which results in longer run-out distances for columns with large aspect ratios.

<sup>33</sup>  $\mu(I)$  rheology, discussed in ??, describes the granular behaviour using a dimensionless  
<sup>34</sup> number, called the *inertial number I*, which is the ratio of inertia to the pressure forces. Small  
<sup>35</sup> values of I corresponds to critical state of soil mechanics and large values of I corresponds to  
<sup>36</sup> the fully collisional regime of kinetic theory.  $\mu(I)$  rheology is adopted in MPM simulations  
<sup>1</sup> to understand the characteristics of the flow regime. Mohr-Coulomb model was used along  
<sup>2</sup> with  $\mu(I)$  rheology. The friction angle is changed according to a friction law (Da Cruz et al.,  
<sup>3</sup> 2005) that is dependent on the inertial number I as  $\mu = \mu_{min} + bI$  where  $\mu_{min} = 0.22$  and  $b =$   
<sup>4</sup> 1. Figure 4.13 shows the flow evolution of granular column collapse for aspect ratio ‘a’ of 0.4  
<sup>5</sup> and 6 using  $\mu(I)$  rheology. For short columns, the evolution of flow based on  $\mu(I)$  rheology  
<sup>6</sup> is identical to the MPM simulation using Mohr-Coloumb model. However, for tall columns,  
<sup>7</sup>  $\mu(I)$  rheology evolves at the same rate as the DEM simulations up to  $t = 0.8\tau_c$ , after which  
<sup>8</sup> MPM simulation continues to accelerate due to lack of collisional dissipation, while the DEM  
<sup>9</sup> simulation decelerates with time.

<sup>10</sup> Figure 4.23b shows that the short column attains a maximum inertial number of 0.012,  
<sup>11</sup> which is in the dense granular flow regime, inertial number  $I \approx 10^{-3}$  to 0.1 (Da Cruz et al.,  
<sup>12</sup> 2005). However, the maximum inertial number  $I \approx 0.04$ , for tall is still within the dense  
<sup>13</sup> granular flow regime. DEM simulations, however, showed a collisional regime that has inertial

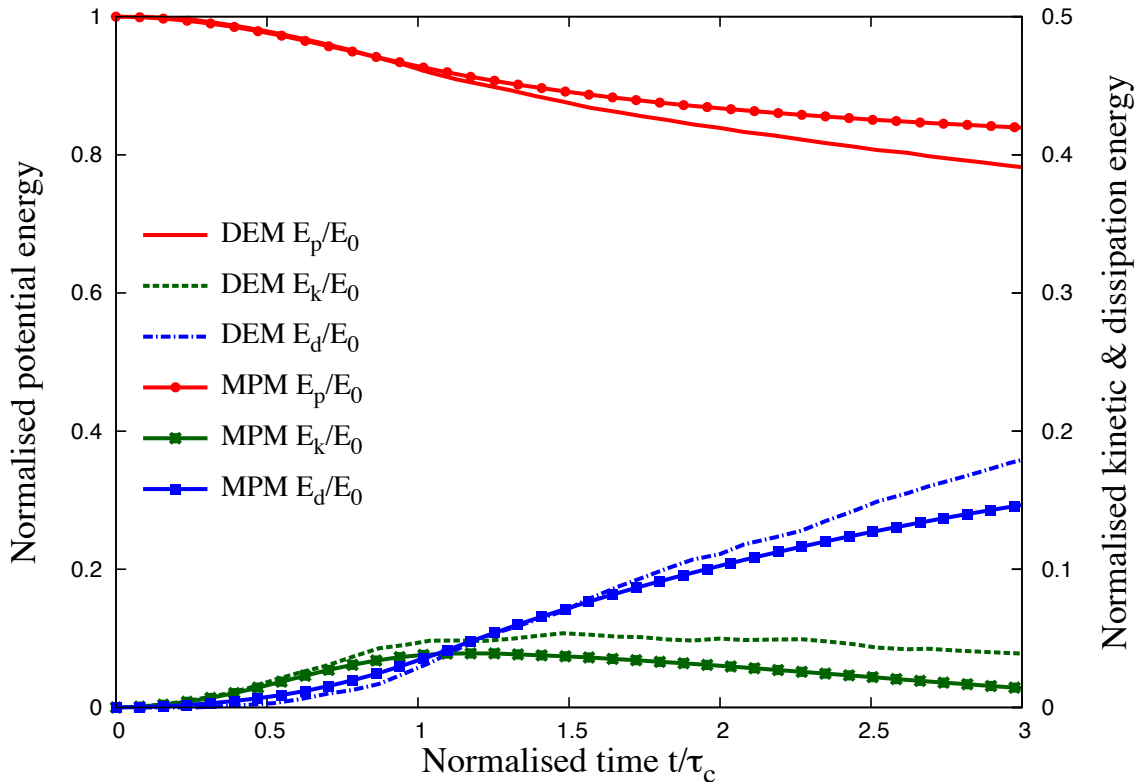
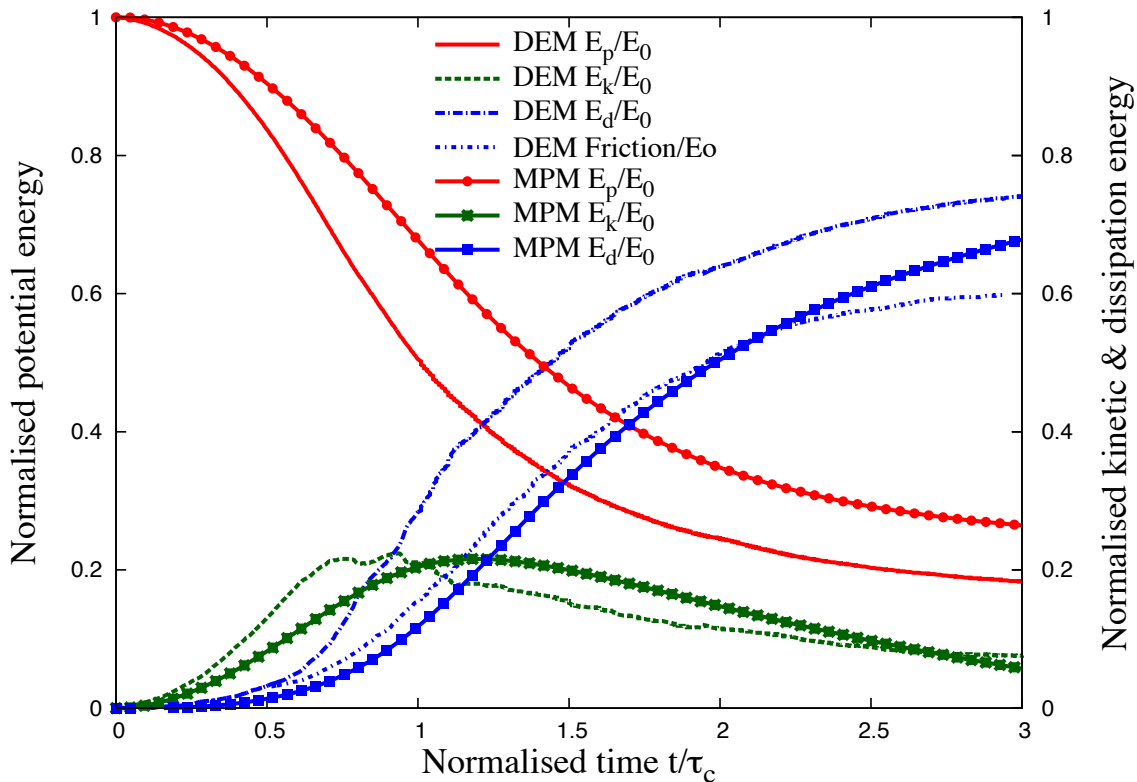
(a) Energy evolution of a column with  $a = 0.4$ (b) Energy evolution of a column with  $a = 6$ 

Figure 4.12 Energy evolution of granular column collapse

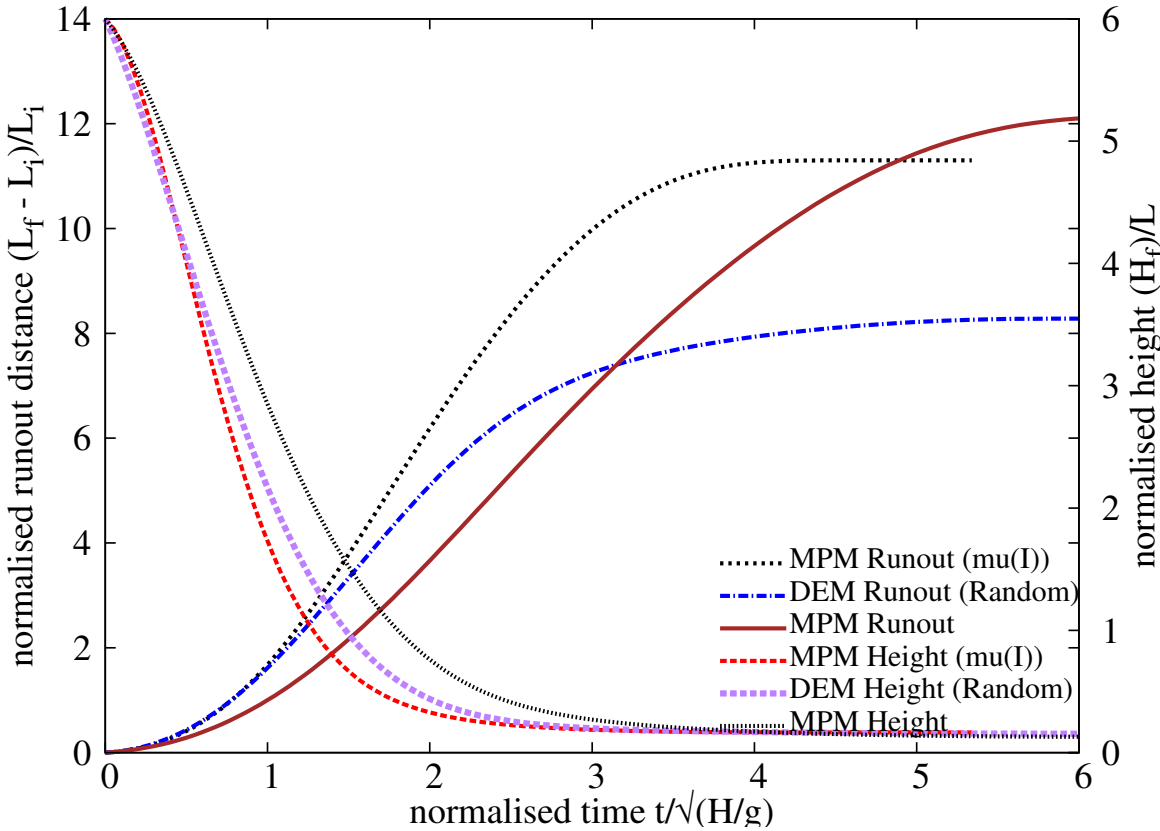
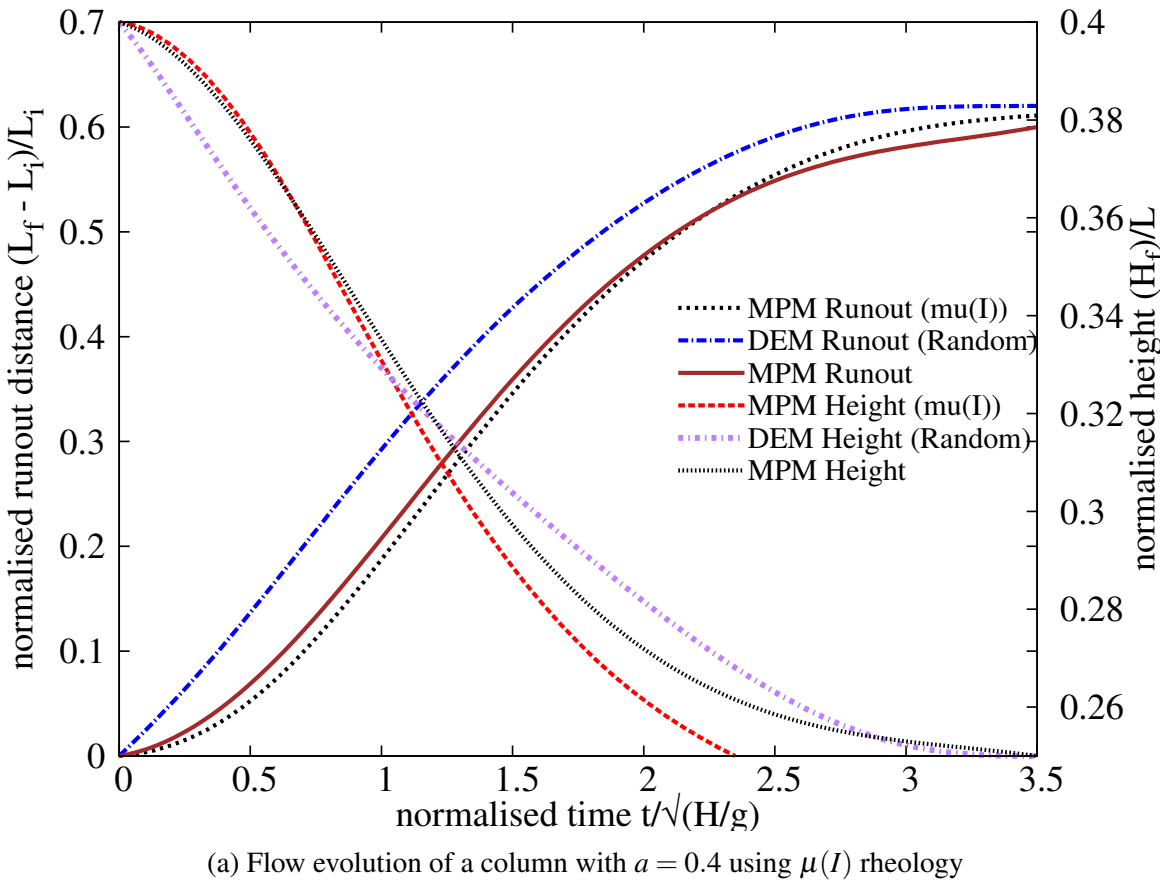


Figure 4.13 Flow evolution of granular column collapse using  $\mu(I)$  rheology

number higher than 0.1. This shows that continuum approach using frictional laws are able to capture the flow kinematics at small aspect ratios, however are unable to precisely describe the flow dynamics of tall columns, which is characterised by an initial collisional regime.

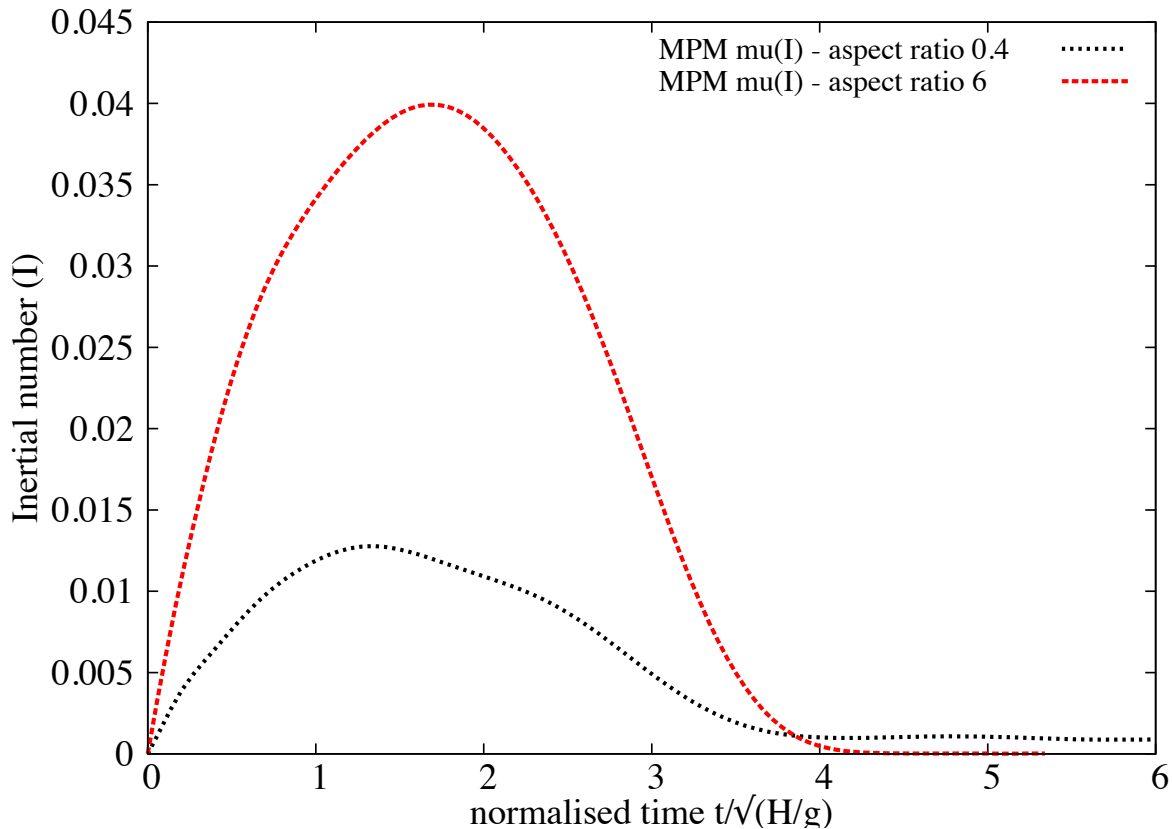


Figure 4.14 Evolution of inertial number with time for columns with  $a = 0.4$  and  $a = 6$

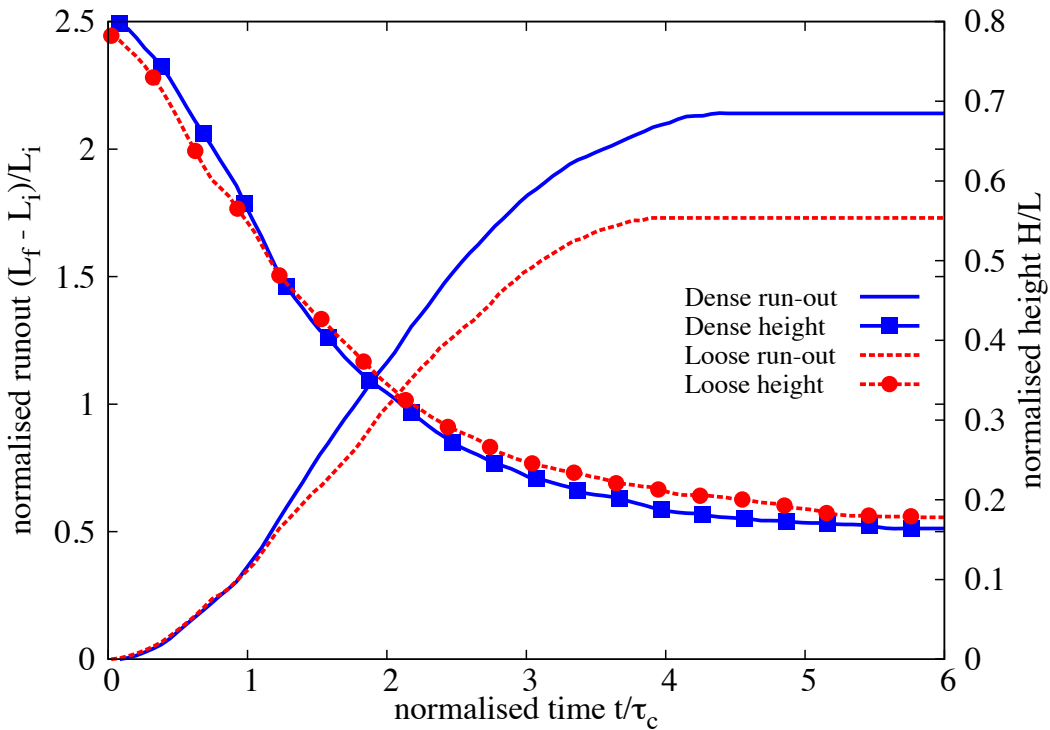
#### 4.2.5 Role of initial grain properties

Lube et al. (2005) observed that the run-out distance scales with the initial aspect ratio of the column, independent of the material properties. The run-out evolution after the initial transition regime is a frictional dissipation process, and the lack of influence of material properties on the run-out behaviour is inconsistent with frictional dissipation in continuum modelling of granular flow behaviour. Balmforth and Kerswell (2005) observed that the material properties have almost no influence on the exponent of the normalised run-out as a function of the initial aspect ratio. The numerical constant of proportionality, however, showed clear material dependence. This corroborates the conclusions of Lajeunesse et al. (2004) and softens that of Lube et al. (2005). Daerr and Douady (1999) also observed strong influence of initial packing density and the internal structure on the behaviour of granular flows.

10 It should be noted that the collapse experiment is highly transient and no clear stationary  
11 regime is observed. On the contrary, the acceleration and the deceleration phases cover nearly  
12 the whole duration of the spreading. This makes it difficult to analyse the flow structure and  
13 its relation with other characteristic of the system. The knowledge of the final run-out is not a  
14 sufficient characterization of the deposit: one also needs to know how the mass is distributed  
15 during the flow to understand the dynamics and the dissipation process. This is expected to be  
16 true in natural contexts as well as in experiments. While the inter-grain friction does not affect  
17 the early vertical dynamics, nor the power-law dependence, it controls the effective frictional  
18 properties of the flow, and its internal structure ([Staron and Hinch, 2007](#)). It is interesting to  
1 note that the details of the structure of the flow do not influence the final run-out dependence,  
2 and thus seem to play a marginal role in the overall behaviour of the spreading. This could  
3 explain why simple continuum model with a frictional dissipation could reproduce the run-out  
4 scaling for columns with small aspect ratios.

5 The run-out behaviour of a loose (79% packing density) and a dense (83% packing density)  
6 granular column ( $a = 0.8$ ) are studied to understand the influence of material properties.  
7 The evolution of normalised run-out with time for two different initial packing densities are  
8 presented in figure [4.15](#). At the initial stage of collapse  $t = \tau_c$ , the flow evolution is identical  
9 in both dense and loose conditions. However, the dense column flows 30% longer than the  
10 loose condition. Both the columns come to rest at around  $t = 4\tau_c$ . The columns, however,  
11 show similar evolution of the normalised height. This shows that only a part of the column is  
12 destabilised during the collapse.

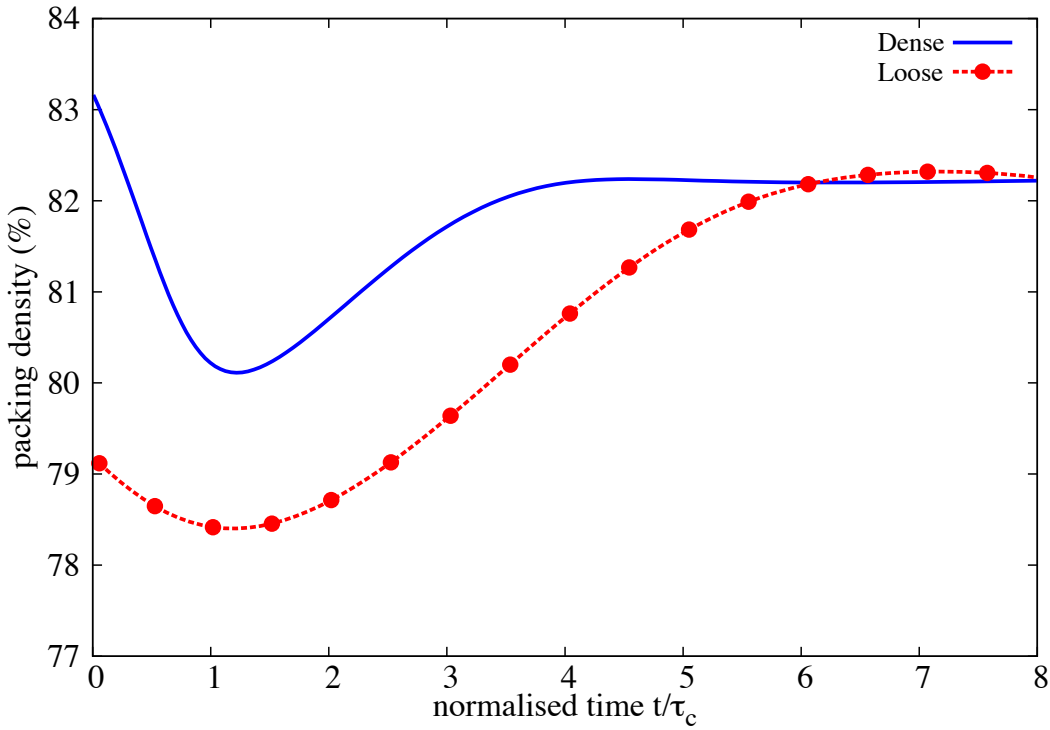
13 Figure [4.17](#) show the evolution of potential and kinetic energy with time. Similar potential  
14 energy evolution in both dense and loose conditions reveals that there is no change in the  
15 overall mechanism of collapse. The dense condition has slightly higher peak kinetic energy  
16 than the loose column. In the free-fall phase, the dense column shows a steeper increase in  
17 the horizontal kinetic energy in comparison to the loose column. This indicates that dense  
18 granular mass is pushed farther away more quickly than the loose column. Loose column  
19 exhibits higher vertical kinetic energy which may be due to particle rearrangement resulting in  
20 densification of the granular mass. Figure [4.16](#) shows that the loose sample densifies as the flow  
21 evolves. Both dense and loose granular columns dilate during the initial stage of collapse, this  
22 is due to grains experiencing shear along the fracture surface. In both cases, the granular mass  
23 attains similar packing density at the end of the flow. Dense granular column dilates, while the  
24 loose column compacts to achieve the same critical density. The dense condition has higher  
25 mobilised potential energy during the initial stage of collapse, which yields higher horizontal  
26 kinetic energy for the flow. However in loose condition, a higher proportion of the available  
27 energy is lost during compaction. This behaviour in addition to higher mobilised potential

Figure 4.15 Effect of density on run-out evolution  $a = 0.8$ 

28 energy results in longer run-out distance in dense granular column. [Lajeunesse et al. \(2004\)](#)  
 29 observed that the flow comes to rest at around  $3\tau_c$ , but the grains continue to re-arrange until  
 30  $6\tau_c$ , similar behaviour is observed in DEM simulations.

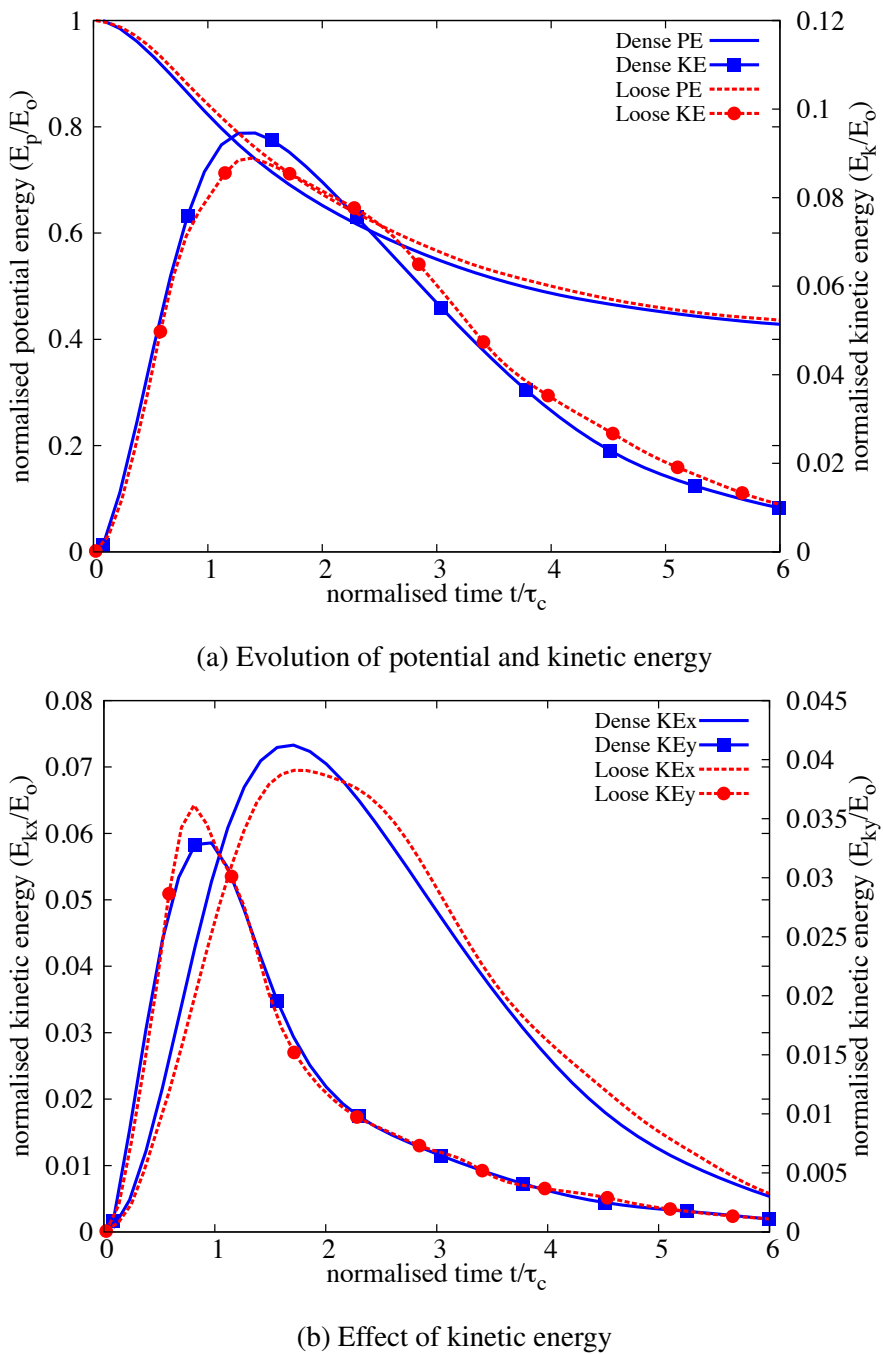
31 In order to remove the effect of crystallisation on the run-out behaviour, a highly poly-  
 32 disperse sample ( $r = d_{max}/d_{min} = 6$ ) is used. The flow kinematics of a dense (relative density  
<sub>1</sub>  $D_r = 74\%$ ) and a loose ( $D_r = 22\%$ ) granular column with aspect ratio of 0.8 is studied. Similar  
<sub>2</sub> to the previous case, the dense granular column exhibits longer run-out distance (see figure 4.18).  
<sub>3</sub> Due to compaction of grains in loose condition, almost 20% of the initial potential energy  
<sub>4</sub> available for collapse is lost in densification due to grain rearrangements in comparison to the  
<sub>5</sub> dense condition (see figure 4.20). The compaction of grains in loose column and the dilation  
<sub>6</sub> in dense column results in significantly different flow structure, especially at the flow front  
<sub>7</sub> (figure 4.19). As the loose column densifies, more granular mass is pushed to the flow front  
<sub>8</sub> resulting in higher vertical effective stress. The loose column exhibits a more parabolic final  
<sub>9</sub> deposit profile in comparison to the dense column, which shows a triangular deposit at the  
<sub>10</sub> front.

11 In short column, only a part of the granular column above the failure surface participates in  
 12 the flow. However, it appears that the collapse for large aspect ratios mixes two very different  
 13 dynamics: the first stage shows a large vertical acceleration, while the second stage consists

Figure 4.16 Evolution of local packing density  $a = 0.8$ 

14 of a “conventional” horizontal granular flows. The effect of density on the run-out behaviour  
 15 of tall columns is investigated. Similar to short columns, the dense granular column with an  
 16 aspect ratio of 6 shows higher run-out distance in comparison to the loose condition. The  
 17 dense granular column flows almost twice as much as that of the loose column. Unlike short  
 18 columns, the evolution of run-out is different even at the initial stage of the collapse. The dense  
 19 granular column, which has higher initial potential energy show a rapid increase in the run-out  
 20 due to free-fall and higher mobilised potential energy. During this stage of collapse, the dense  
 21 granular column has 15 % higher normalised kinetic energy available for the horizontal push.  
 22 This results in longer run-out distance for dense granular column in comparison to initially  
 23 loose granular column.

24 The initial packing fraction and the distribution of kinetic energy in the system has a  
 25 significant influence on the flow kinematics and the run-out behaviour, this suggests that  
 26 triggering mechanisms play a crucial role in the case of natural flows. This stresses the  
 necessity of accounting for initiation mechanisms while modelling the run-out behaviour using  
 continuum approaches to predict realistic granular flow behaviour.

Figure 4.17 Effect of density on energy evolution  $a = 0.8$

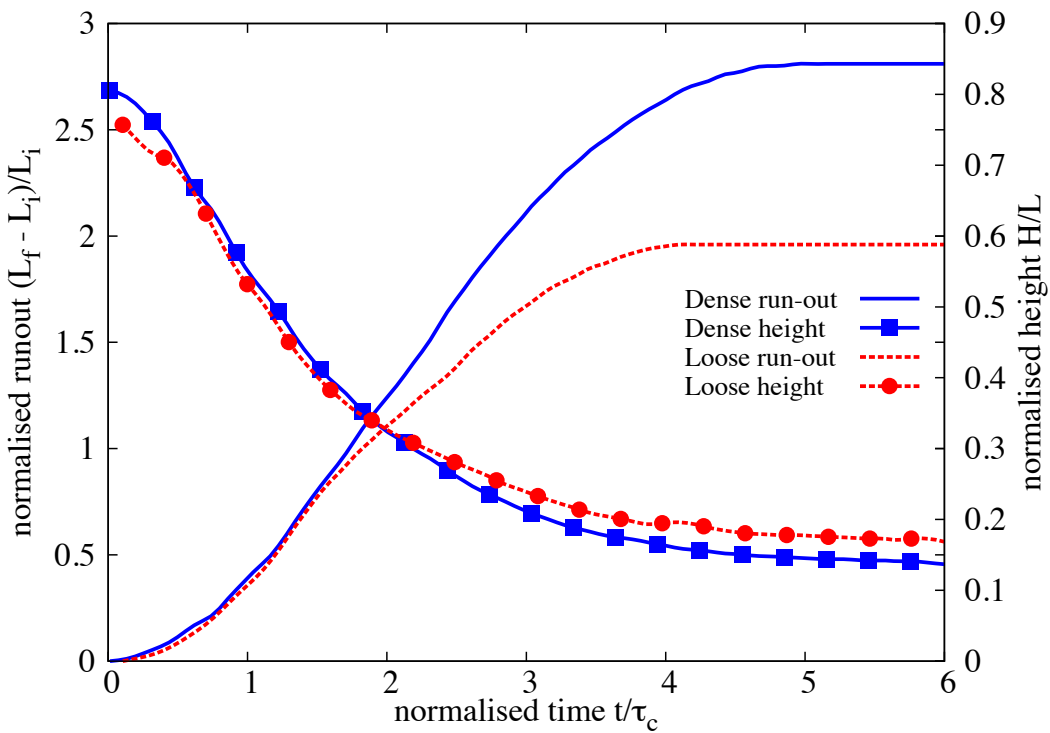
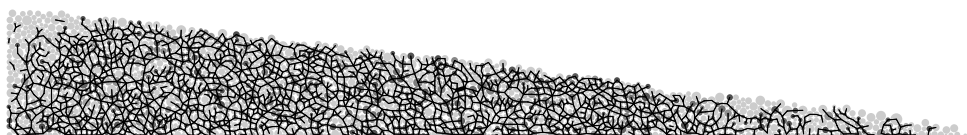
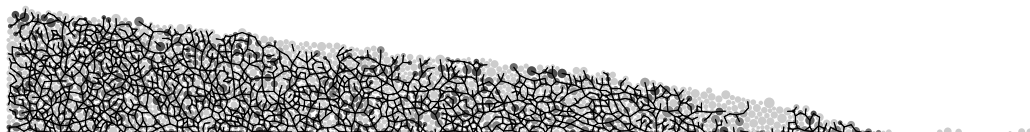


Figure 4.18 Effect of density on run-out evolution  $a = 0.8$  (poly-dispersity ‘r’ = 6)

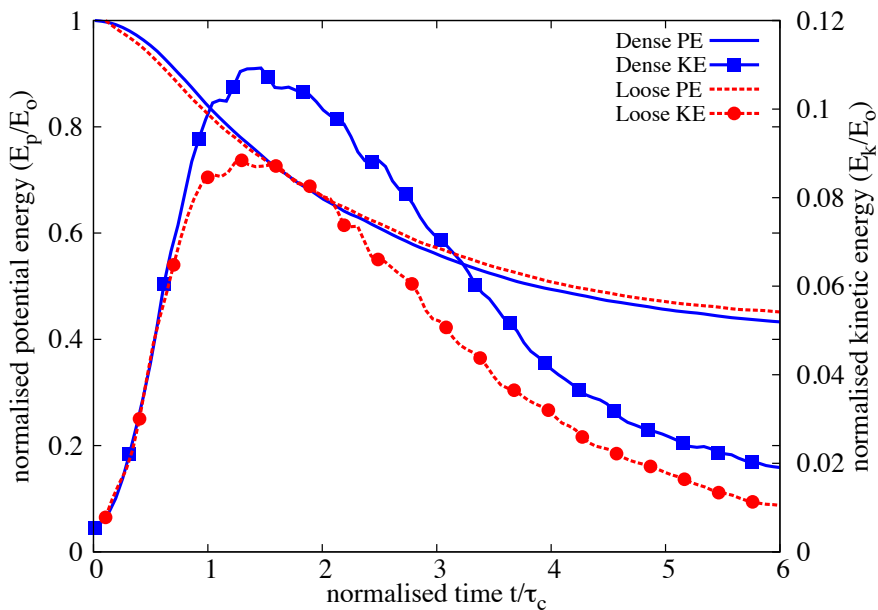


(a) Dense initial packing

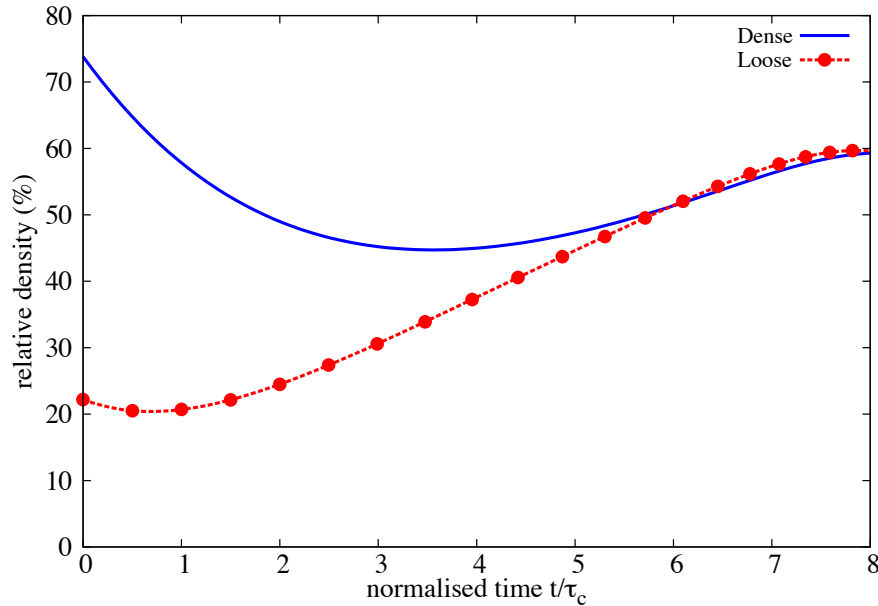


(b) Loose initial packing

Figure 4.19 Snapshots of granular column collapse  $t = 6\tau_c$

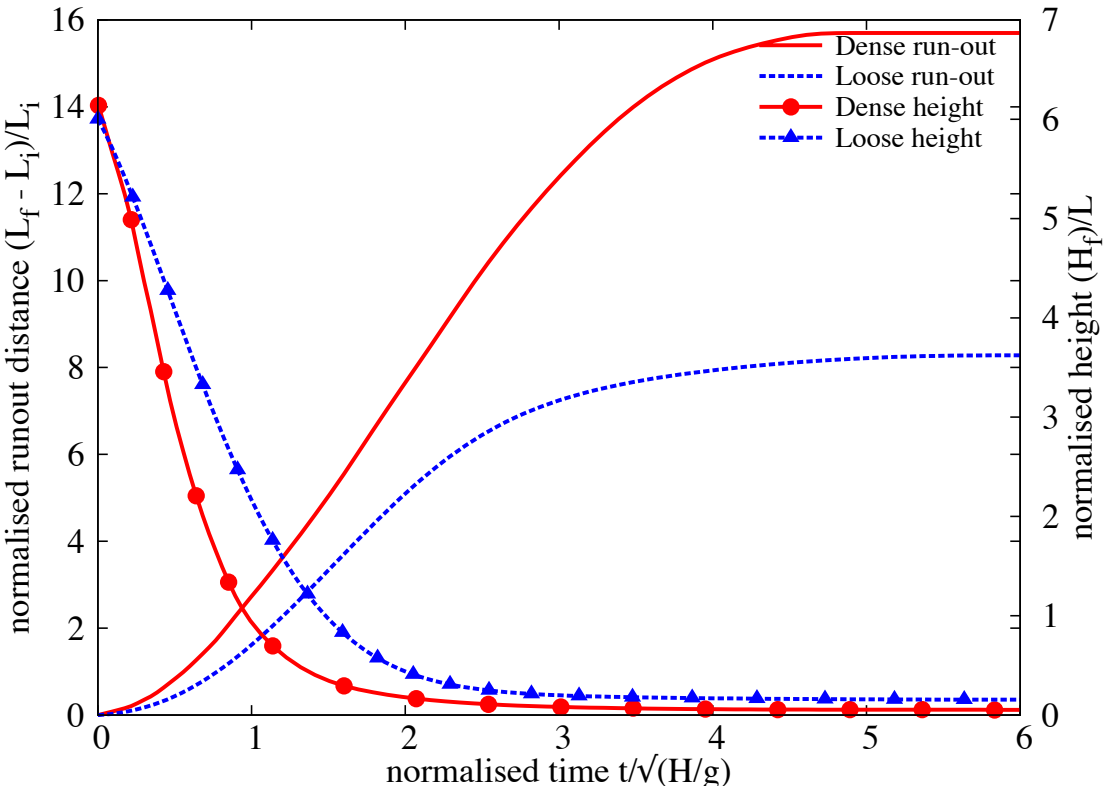


(a) Evolution of potential and kinetic energy

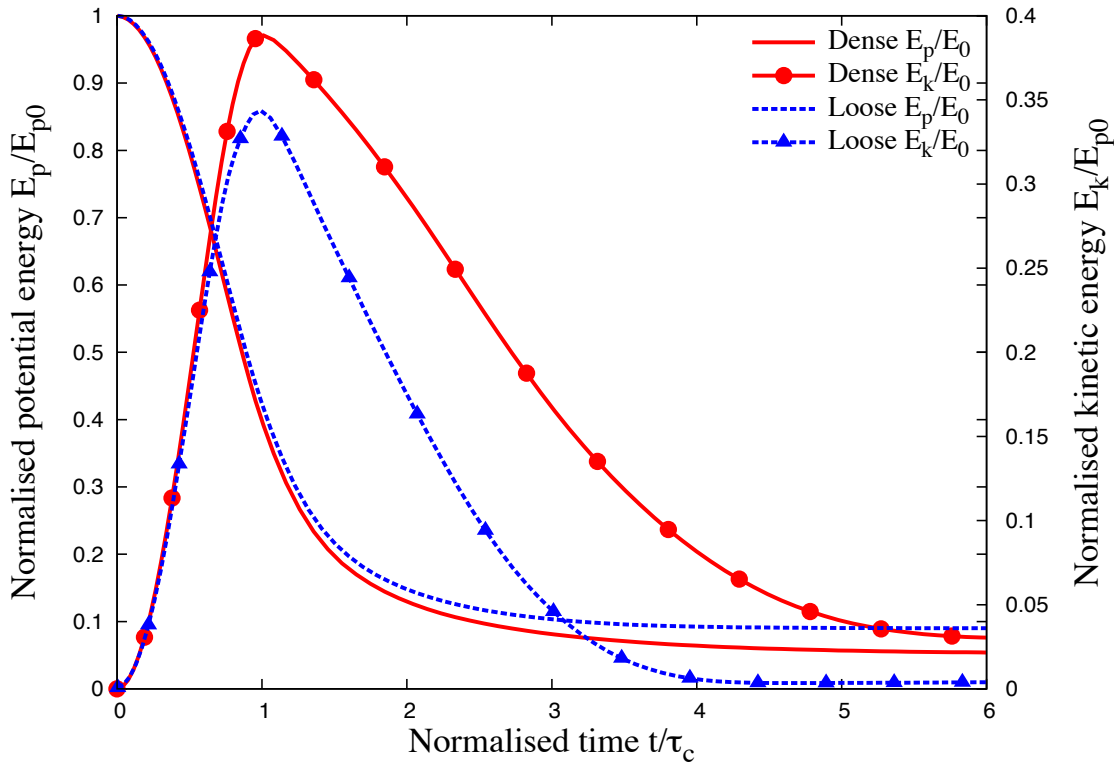


(b) Evolution of packing density

Figure 4.20 Effect of density on energy and packing fraction evolution  $a = 0.8$  (poly-dispersity ‘r’ = 6)



(a) Effect of density on run-out evolution



(b) Effect of density on energy evolution

Figure 4.21 Effect of density on run-out behaviour and energy evolution  $a = 0.6$

## 4.3 Slopes subjected to impact loading

Transient granular flows occur very often in nature. Well-known examples are rockfalls, debris flows, and aerial and submarine avalanches. In the geotechnical context, transient movements of large granular slopes is a substantial factor of risk due to their destructive force and the transformations they may produce in the landscape. Natural granular flows may be triggered as a result of different processes such as gradual degradation, induced by weathering or chemical reactions, liquefaction and external forces such as earthquakes. Most contemporary research on granular materials deals with the steady-state flow. Transients and inhomogeneous boundary conditions are much less amenable to observation and analysis, and have thus been less extensively studied despite their primary importance in engineering practice. In most cases of granular flow, an initially static pile of grains is disturbed by external forces, it then undergoes an abrupt accelerated motion and spreads over long distances before relaxing to a new equilibrium state. The kinetic energy acquired during destabilisation is dissipated by friction and inelastic collisions.

This section investigates the ability of MPM, a continuum approach, to reproduce the evolution of a granular pile destabilised by an external energy source. In particular, a central issue is whether power-law dependence of the run-out distance and time observed with respect to the initial geometry or energy can be reproduced by a simple Mohr-Coulomb plastic behaviour for granular slopes subjected an impact energy. Effect of different input parameters, such as the distribution of energy and base friction, on the run-out kinematics are studied by comparing the data obtained from DEM and MPM simulations.

### 4.3.1 Numerical set-up

The DEM sample is composed of  $\sim 13000$  disks with a uniform distribution of diameters by volume fractions ( $d_{max} = 1.5d_{min}$ ). The mean grain diameter and mass are  $d \simeq 2.455$  mm and  $m \simeq 0.0123$  kg, respectively. The grains are first poured uniformly into a rectangular box of given width and then the right-hand side wall is shifted further to the right to allow the grain to spread. A stable granular slope is obtained when all grains come to rest; see figure 4.22. This procedure leads to a mean packing fraction  $\simeq 0.82$ . Soil grains with mean density of  $2600$   $\text{kg m}^{-3}$  and internal friction coefficient of 0.4 between grains is adopted.

The initial static pile is set into motion by applying a constant horizontal gradient  $v_{0x}(y) = k(y_{max} - y)$  with  $k > 0$ . Such a configuration mimics the energy transfer mechanism of a horizontal quake along the bottom of the pile. The evolution of pile geometry and the total kinetic energy as a function of the initial input energy  $E_0$  is studied. The run-out distance  $L_f$  is the distance of the rightmost grain, which is still in contact with the main mass when the

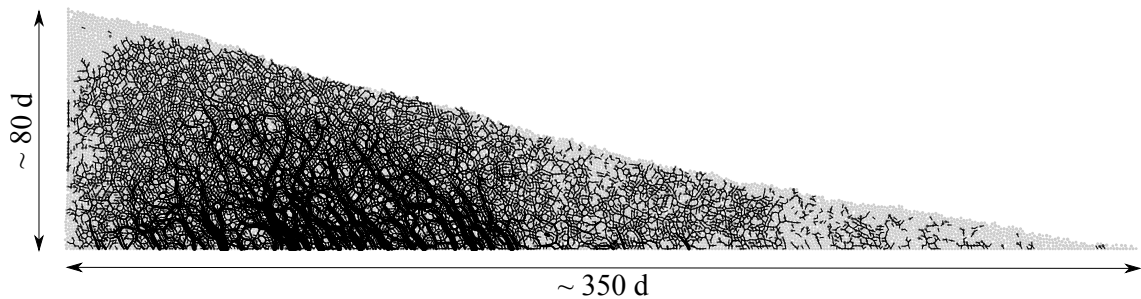
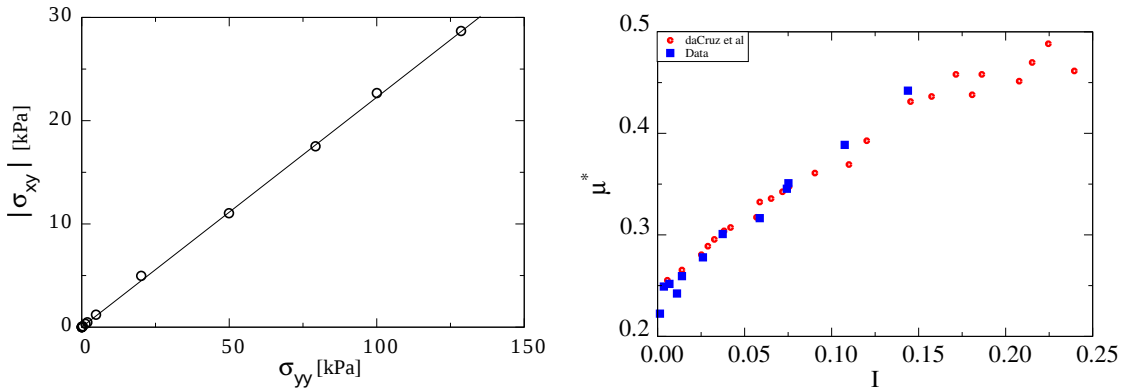


Figure 4.22 Initial geometry and dimensions of the pile

15 pile comes to rest. The run-out will be normalized by the initial length  $L_0$  of the pile, as in the  
 16 experiments of collapsing columns. The total run-out duration  $t_f$  is the time taken by the pile  
 17 to reach its final run-out distance  $L_f$ .

18 For grain scale simulations, classical DEM and Contact Dynamics approach are used. This  
 19 research is done in collaboration with Patrick Mutabaruka, University of Montpellier, who  
 20 performed Contact Dynamics (CD) simulations that are presented in this section. A detailed  
 21 description of the Contact Dynamics method can be found in Jean (1999); Moreau (1993);  
 22 Radjai and Dubois (2011); Radjai and Richefeu (2009). The CD method is based on implicit  
 23 time integration of the equations of motion and a nonsmooth formulation of mutual exclusion  
 24 and dry friction between particles. The CD method requires no elastic repulsive potential and  
 25 no smoothing of the Coulomb friction law for the determination of forces. For this reason, the  
 26 simulations can be performed with large time steps compared to discrete element simulations.  
 27 The unknown variables are particle velocities and contact forces, which are calculated at each  
 28 time step by taking into account the conservation of momenta and the constraints due to mutual  
 29 exclusion between particles and the Coulomb friction. An iterative research algorithm based on  
 30 a non-linear Gauss-Seidel scheme is used. The only contact parameters within the CD method  
 31 are the friction coefficient  $\mu$ , the normal restitution coefficient  $\epsilon_n$  and the tangential restitution  
 32 coefficient  $\epsilon_t$  between grains.

33 In MPM simulations the material point spacing is same as the mean grain diameter in DEM.  
 1 A mesh size of 0.0125m is adopted with 25 material points per cell. The effect of mesh size and  
 2 the number of material points per cell is investigated in section 4.3.5. A Mohr-Coulomb model  
 3 with no dilation is used to simulate the continuum behaviour of the granular pile. Periodic  
 4 shear tests using CD, see figure 4.23a, reveals a macroscopic friction coefficient of 0.22. The  
 5 evolution of inertial number with friction is presented in figure 4.23b. The natural units of the  
 6 system are the mean grain diameter  $d$ , the mean grain mass  $m$  and gravity  $g$ . For this reason,  
 7 the length scales are normalised by  $d$ , time by  $(d/g)^{1/2}$ , velocities by  $(gd)^{1/2}$  and energies by  
 8  $mgd$ .



(a) Evaluating the critical state friction angle from periodic shear test.  
 (b) Evolution of Inertial number with friction  $\mu$

Figure 4.23 Periodic shear test using CD ([Mutabaruka, 2013](#)).

### 4.3.2 Evolution of pile geometry and run-out

Figure 4.24 shows the initial evolution of granular slope subjected to an initial impact energy  $E_0 = 61$  (in dimensionless units) using MPM. As the granular slope is sheared along the bottom, the shear propagates to the top leaving a cavity in the vicinity of the left wall. This cavity gets partially filled as the granular mass at the top collapse behind the flowing mass due to inertia. Similar behaviour is observed during the initial stages of the flow evolution using DEM and CD techniques (see figure 4.25). Due to inertia, the grains at the top of the granular heap roll down to fill the cavity, while the pile continues to spread.

The flow involves a transient phase with a change in the geometry of the pile followed by continuous spreading. The gradient input energy applied to the granular slope mimics a horizontal quake. Despite the creation of a cavity behind the flowing mass, the granular heap remains in contact with the left wall irrespective of the input energy. Figure 4.26a shows the normalized run-out distance  $(L_f - L_0)/L_0$  and total run-out time  $t_f$  as a function of the input energy  $E_0$ . Two regimes characterized by a power-law relation between the run-out distance and time as a function of  $E_0$  can be observed. In the first regime, corresponding to the range of low input energies  $E_0 < 40 \text{ mgd}$ , the run-out distance observed varies as  $L_f \propto (E_0)^\alpha$  with  $\alpha \simeq 0.206 \pm 0.012$  over nearly one decade. Overall, the run-out distance predicted by the continuum approach matches the DEM simulations. At very low energies, DEM simulations show longer run-out distance due to local fluidisation. The difference in the run-out between DEM and CD arise mainly from the scales of description and the inelastic nature of Contact Dynamics. Similar behaviour between DEM and CD approaches was observed by [Radjai et al. \(1997\)](#).

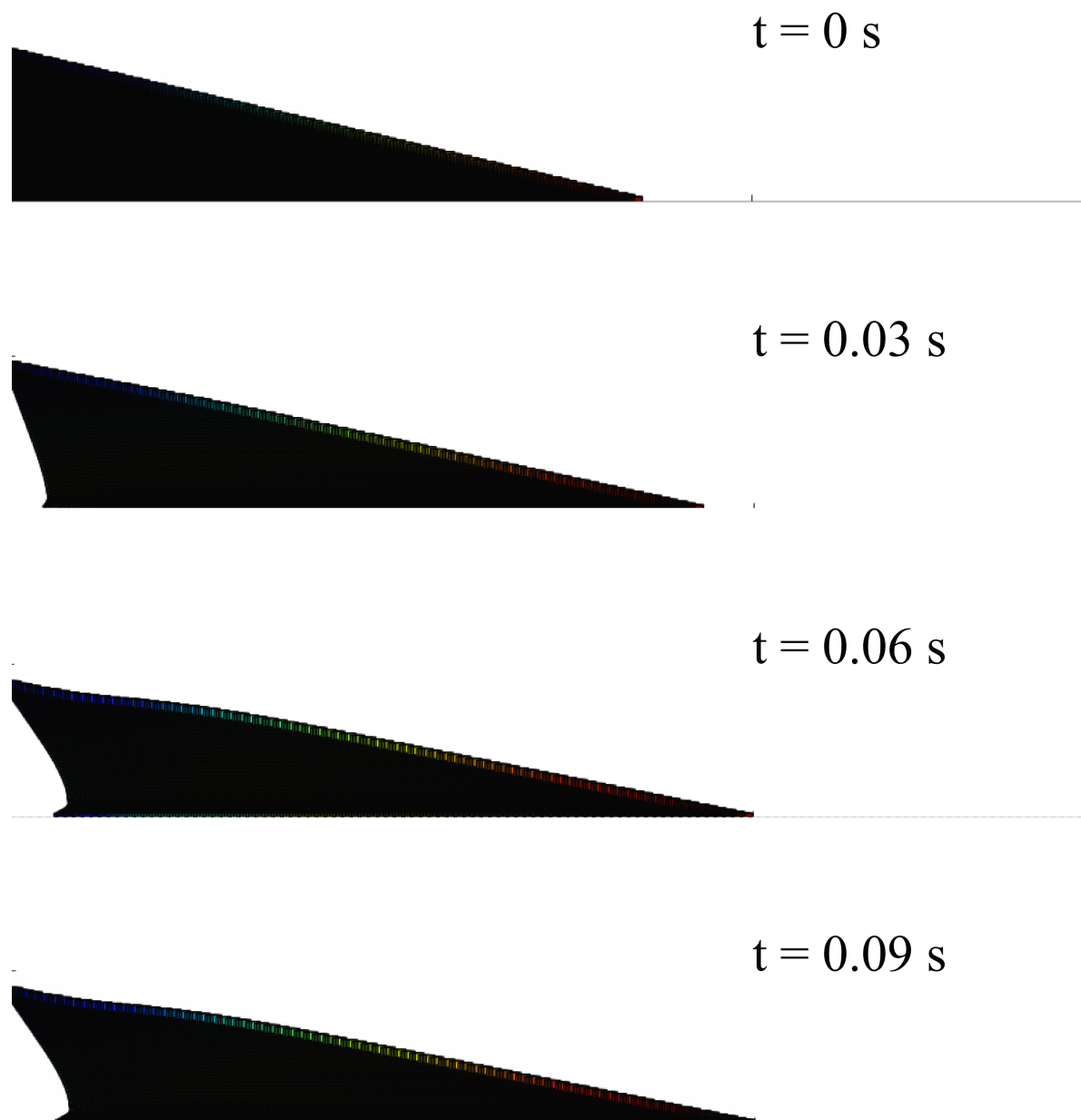


Figure 4.24 MPM simulation of the initial stages of granular pile subjected to a gradient impact energy.

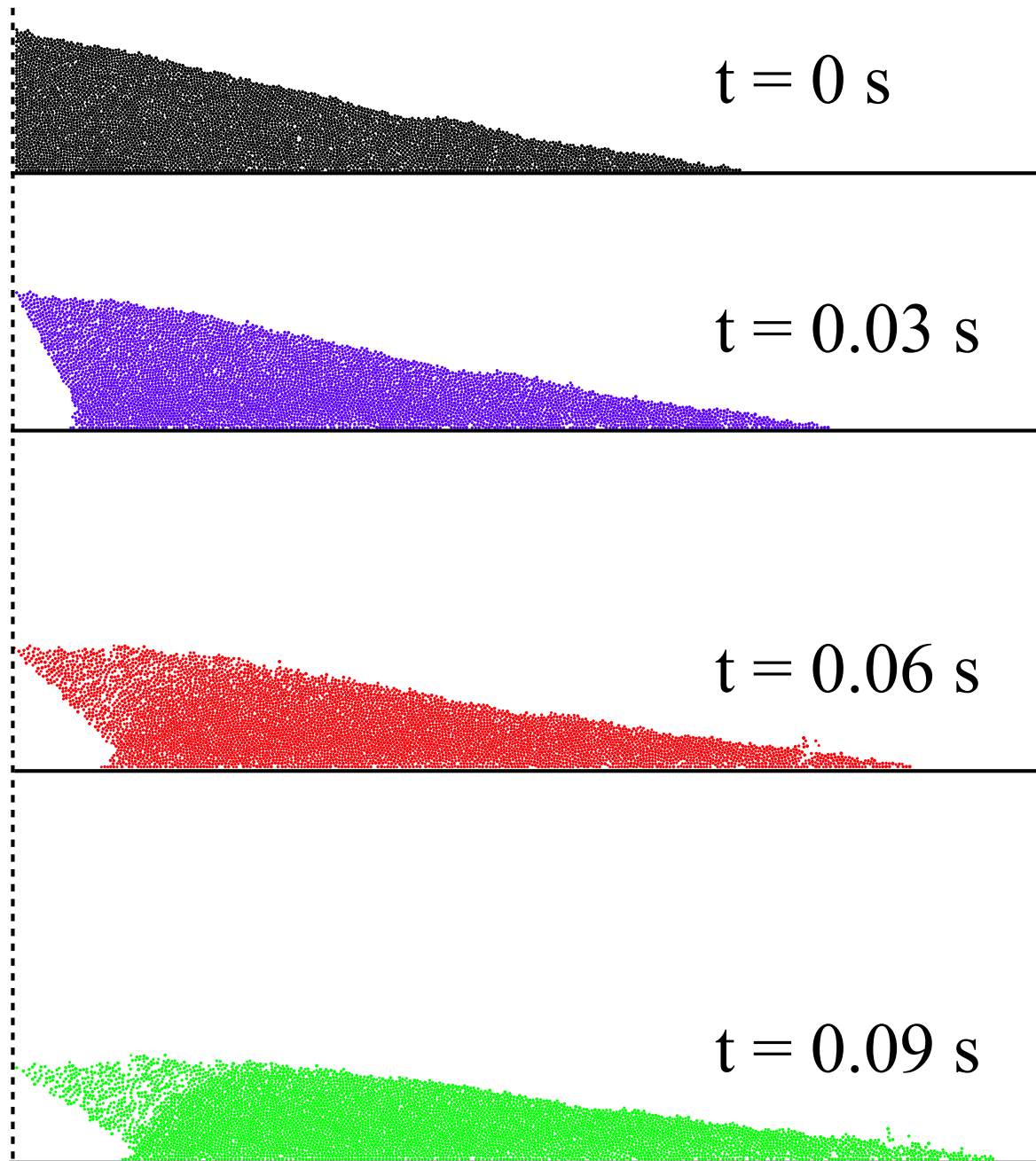


Figure 4.25 CD simulation of the initial stages of granular pile subjected to a gradient impact energy. ([Mutabaruka, 2013](#)).

While the run-out exhibits a power-law relation with the initial input energy, DEM simulations show that the flow duration remains constant at a value  $t_f \simeq 60 (d/g)^{0.5}$  irrespective of the value of  $E_0$ . The constant run-out time, in grain-scale simulations, indicates the collapse of grain into the cavity left behind the pile. An average run-out speed can be defined as  $v_s = (L_f - L_0)/t_f$ . According to the data,  $v_s \propto (E_0)^{0.52 \pm 0.012}$ . The error on the exponent represents the confidence interval of linear fits on the logarithmic scale. Since the initial average velocity varies as  $v_0 \propto (E_0)^{0.5}$ , this difference between the values of the exponents suggests that the mobilized mass during run-out declines when the input energy is increased.

In the second regime, corresponding to the range of high input energies  $E_0 > 40 \text{ mgd}$ , the run-out distance varies as  $L_f \propto (E_0)^{\alpha'}$  over one decade with  $\alpha' \simeq 0.56 \pm 0.04$  while the duration increases as  $t_f \propto (E_0)^{\beta'}$  with  $\beta' \simeq 0.33 \pm 0.02$ . Hence, in this regime the average run-out speed varies as  $v_s \propto (E_0)^{0.498 \pm 0.01}$ . This exponent is close to the value 0.5 in  $v_0 \propto (E_0)^{0.5}$ , and hence, within the confidence interval of the exponents. In the second regime, both DEM and MPM predict almost the same run-out behaviour. However, MPM predicts longer duration with increase in the input energy.

It is worth noting that a similar power-law dependence of the run-out distance and time were found in the case of granular column collapse with respect to the initial aspect ratio. In the column geometry, the grains spread away owing to the kinetic energy acquired during gravitational collapse of the column. [Topin et al. \(2012\)](#) found that the run-out distance varies as a power-law of the available peak kinetic energy at the end of the free-fall stage with an exponent  $\simeq 0.5$ . This value of exponent is lower than the run-out evolution observed in the second regime. This is, however, physically plausible since the distribution of kinetic energies at the end of the collapse is more chaotic than in this case where the energy is supplied from the very beginning in a well-defined shear mode. As pointed out by [Staron et al. \(2005\)](#), the distribution of kinetic energies is an essential factor for the run-out distance.

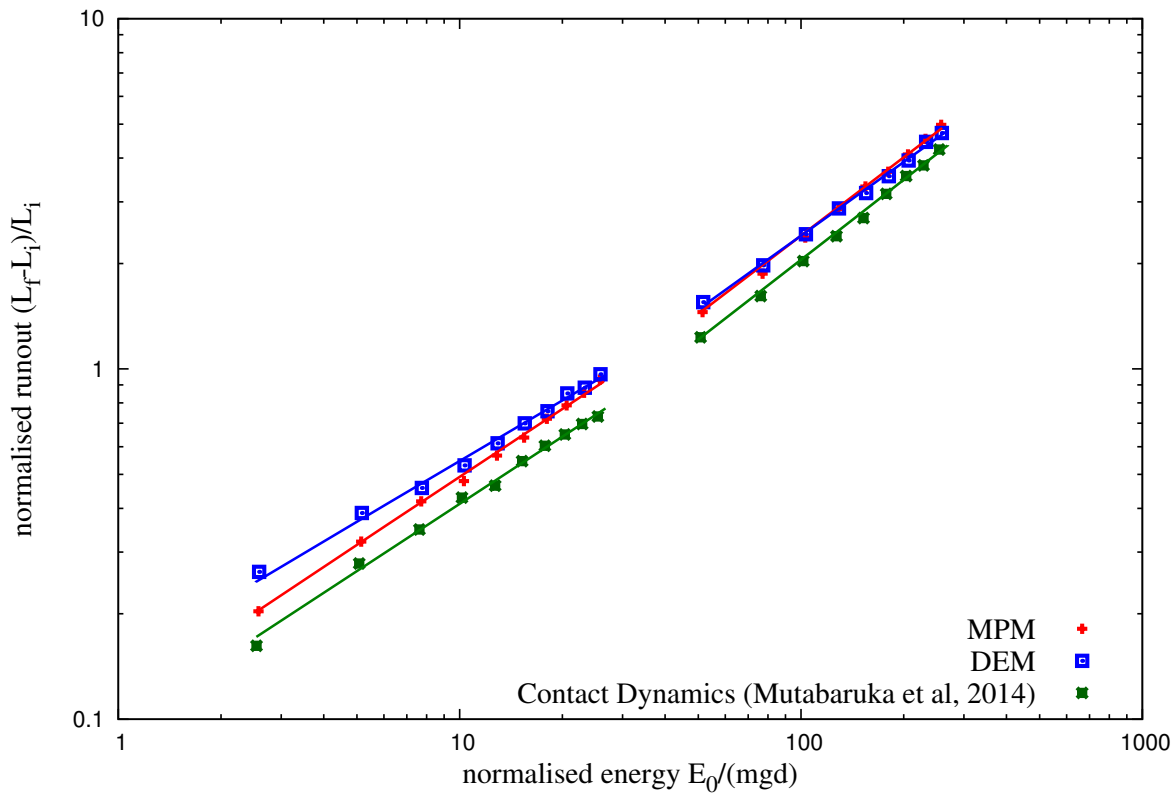
### 4.3.3 Decay of kinetic energy

The non-trivial evolution of the pile geometry in two regimes suggests that the energy supplied to the pile is not simply dissipated by shear and friction along the bottom plane. It is important to split the kinetic energy into vertical and horizontal components ( $K_{Ex}$  and  $K_{Ey}$ ) of the velocity field. Although, the input energy is in the  $x$  component, a fraction of energy is transferred to the vertical component of the velocity field and dissipated during the transient phase. The evolution of kinetic energy is studied to understand the behaviour of granular flow that is consistent with the evolution of the pile shape.

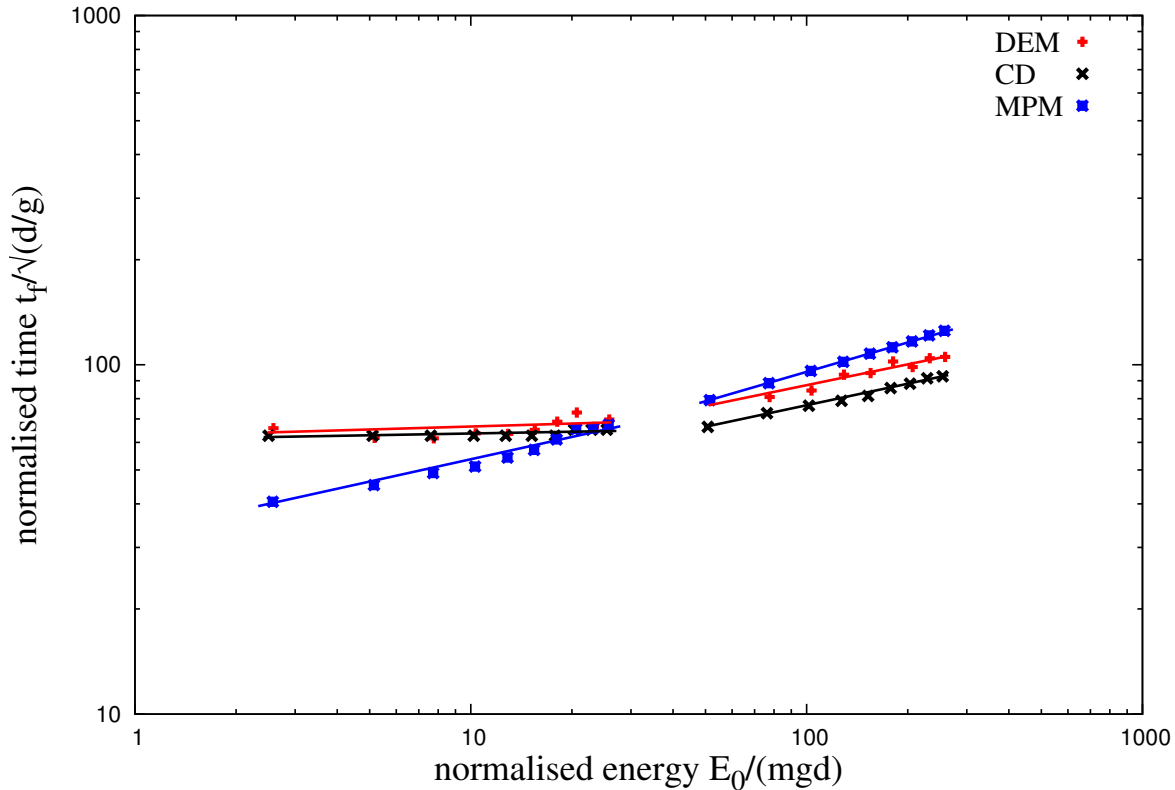
The evolution of total kinetic energies  $E_k$  with time for different values of the input energy  $E_{ki}$  based on MPM simulations are shown in figure 4.27. MPM simulations shows two distinct

## 4.3 Slopes subjected to impact loading

119



(a) Run-out distance as a function of normalised input kinetic energy



(b) Duration of run-out as a function of normalised input kinetic energy

Figure 4.26 Run-out behaviour of a pile subjected a gradient impact energy

regimes in the normalised kinetic energy plot as a function of normalised time in figure 4.27b.  
 However, DEM simulations (see figure 4.28) show that the energy evolution corresponding to  
 low energy regime nearly collapse on to a single time evolution. This is consistent with the  
 observation of run-out time  $t_f$  independent of the input energy. In contrast, MPM simulations  
 predict a power law relation between the run-out duration and input energy. However, the plots  
 corresponding to the high energy regime (figure 4.27), collapse only at the beginning of the  
 run-out i.e. for  $t < t_1 \simeq 7.5 (d/g)^{0.5}$ . Although MPM simulations show longer duration of  
 run-out (figure 4.27), the total kinetic energy is completely dissipated at  $t = 60\sqrt{d/g}$ . DEM  
 simulations predict  $t = 80\sqrt{d/g}$  for the kinetic energy to be completely dissipated. This is due  
 particle rearrangement at the free surface (figure 4.29). The granular mass densifies as the flow  
 progresses, after the initial dilation phase for  $t = 20\sqrt{d/g}$ .

Figure 4.30 displays the evolution of kinetic energy in the translational ( $E_x$  and  $E_y$ ) degrees  
 of freedom.  $E_x$  decays similar to the total energy dissipation, but  $E_y$  increases and passes  
 through a peak before decaying rapidly to a negligible level. The transient is best observed for  
 $E_y$ , which has significant values only for  $t < t_1$ . This energy represents the proportion of kinetic  
 energy transferred to the y component of the velocity field due to the destabilisation of the pile  
 and collapse of grains in the cavity behind the pile. Higher proportion of vertical acceleration  
 $E_{ky}/E_0$  is observed for lower values of input energy  $E_0$ . This means that, at lower input energies  
 a larger fraction of the energy is consumed in the destabilisation process. Whereas at a higher  
 input energies, most of the energy is dissipated in the spreading phase. For this reason, the  
 total duration  $t_1$  of this destabilisation phase is nearly the same in both regimes and its value is  
 controlled by the gravity rather than the input energy. The height of the pile being of the order  
 of  $80 d$ , the total free-fall time for a particle located at this height is  $\simeq 12 (d/g)^{0.5}$ , which is  
 of the same order as  $t_1$ . DEM simulations show that the contribution of the rotational energy  
 during the transient stage and the spreading stage is negligible.

To analyse the second phase for higher input energies, the kinetic energy  $E'_{kx0}$  available  
 at the end of the transient phase is considered. This energy is responsible for most of the  
 run-out and hence it is expected to control the run-out distance and time. Figure 4.31 shows the  
 evolution of  $E_{kx}$  normalized by  $E'_{kx0}$  as a function of time. The plots have seemingly the same  
 aspect but they show different decay times. A decay time  $\tau$  can be defined as the time required  
 for  $E_{kx}$  to decline by a factor 1/2. Figure 4.32 shows the same data in which the time  $t'$  elapsed  
 since  $t_1$ , normalized by  $\tau$ . Interestingly, now all the data nicely collapse on to a single curve.  
 However, this curve can not be fitted by simple functional forms such as variants of exponential  
 decay. This means that the spreading of the pile is not a self-similar process in agreement with  
 the fact that the energy fades away in a finite time  $t'_f$ .

## 4.3 Slopes subjected to impact loading

121

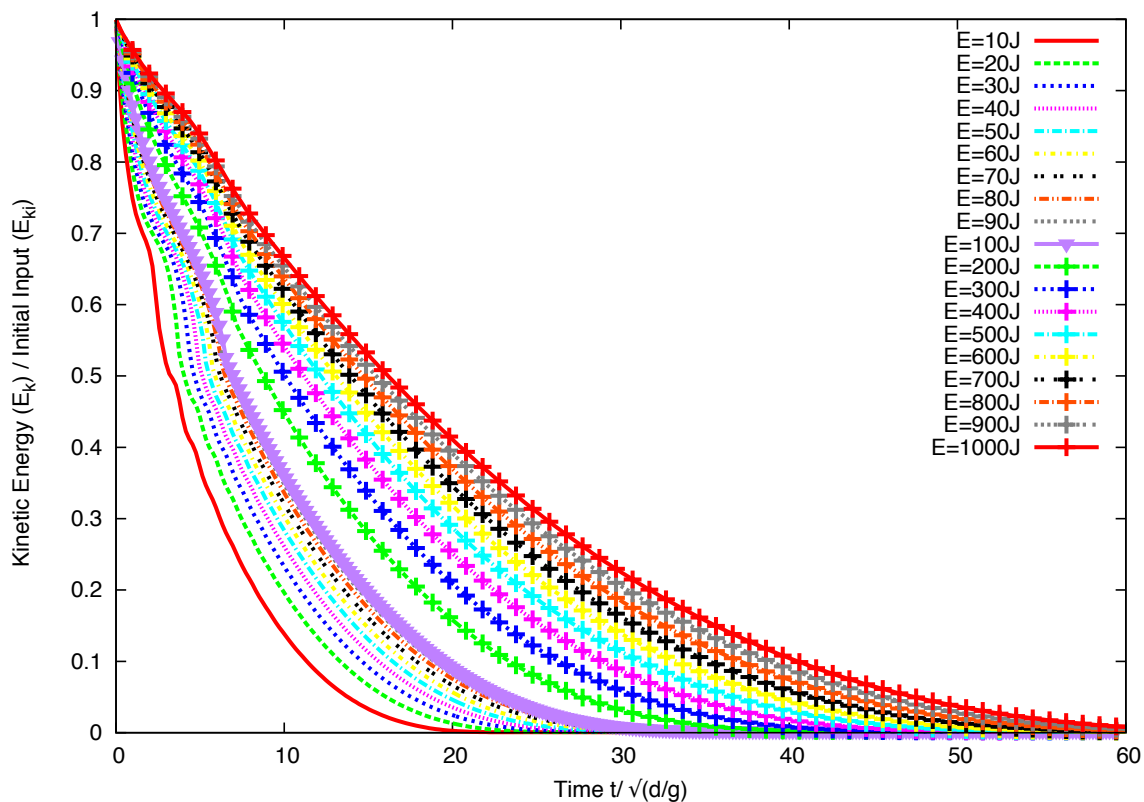
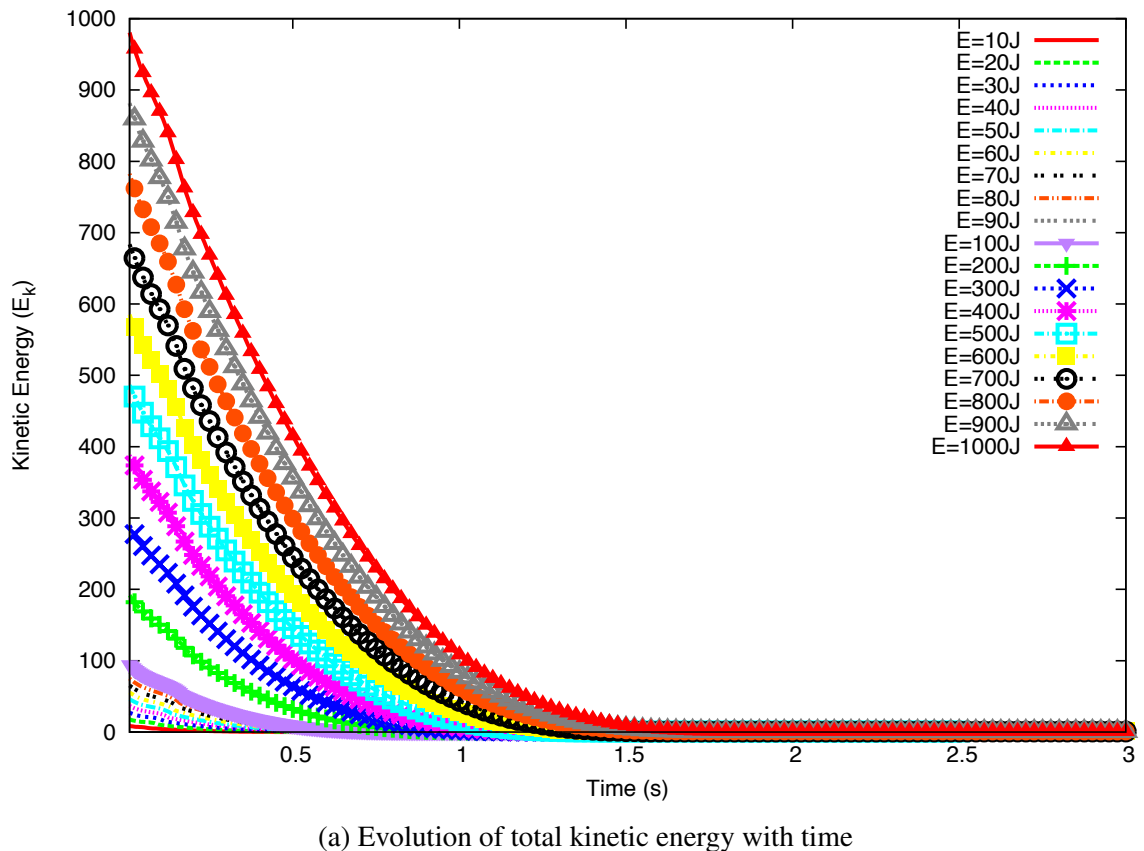


Figure 4.27 Evolution of kinetic energy with time (MPM)

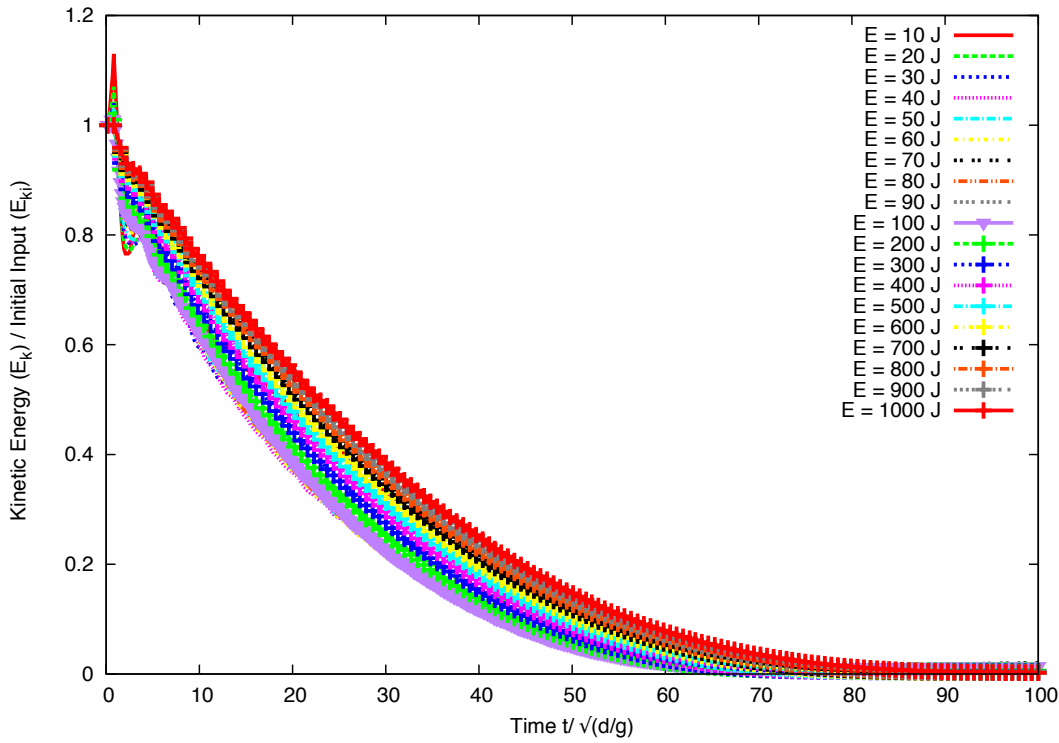


Figure 4.28 Evolution of normalised kinetic energy with normalised time

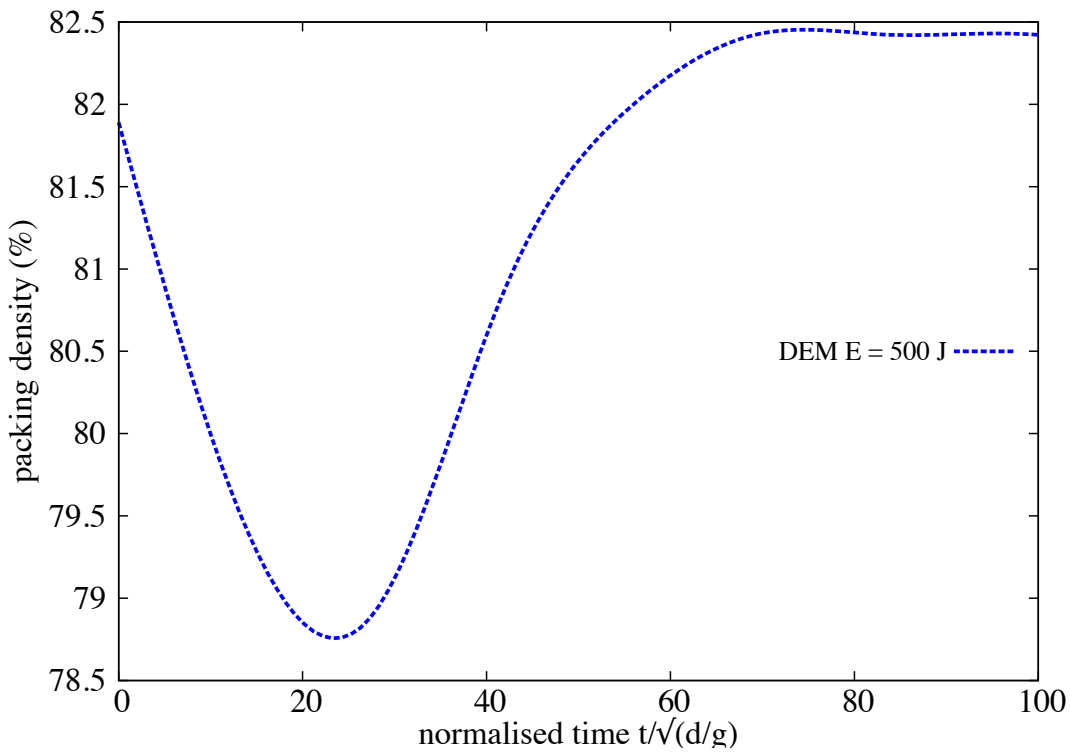
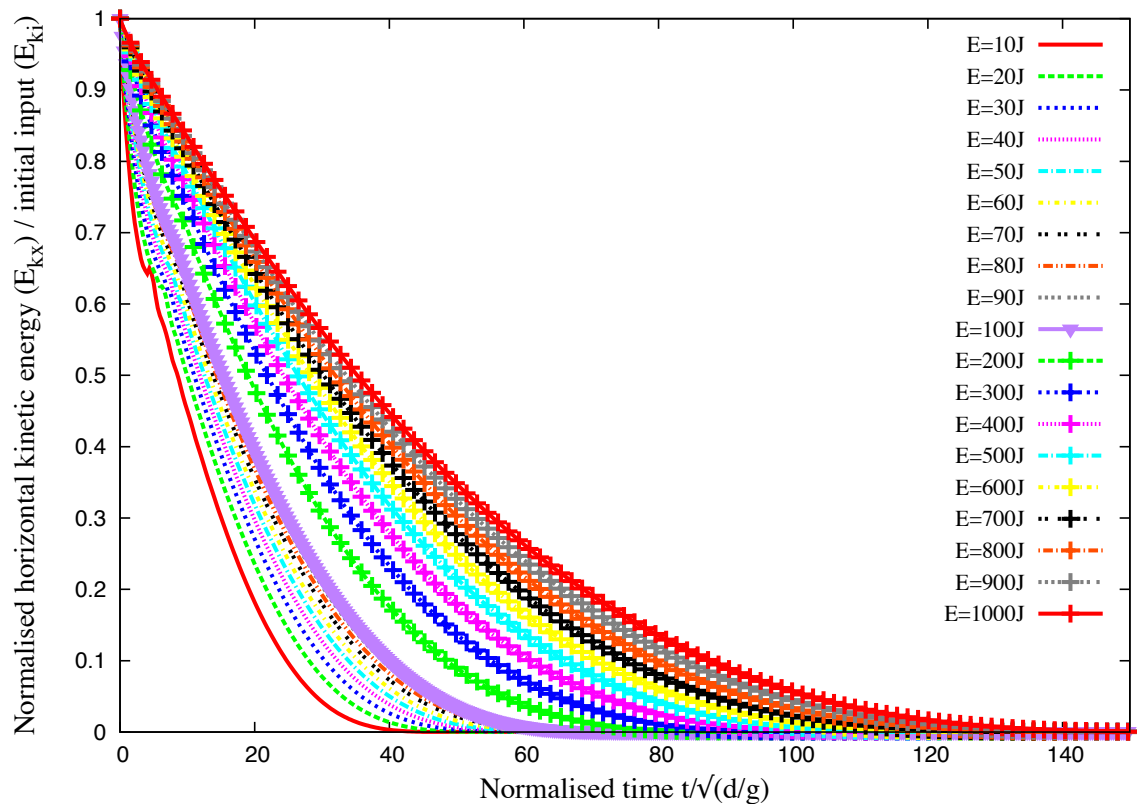
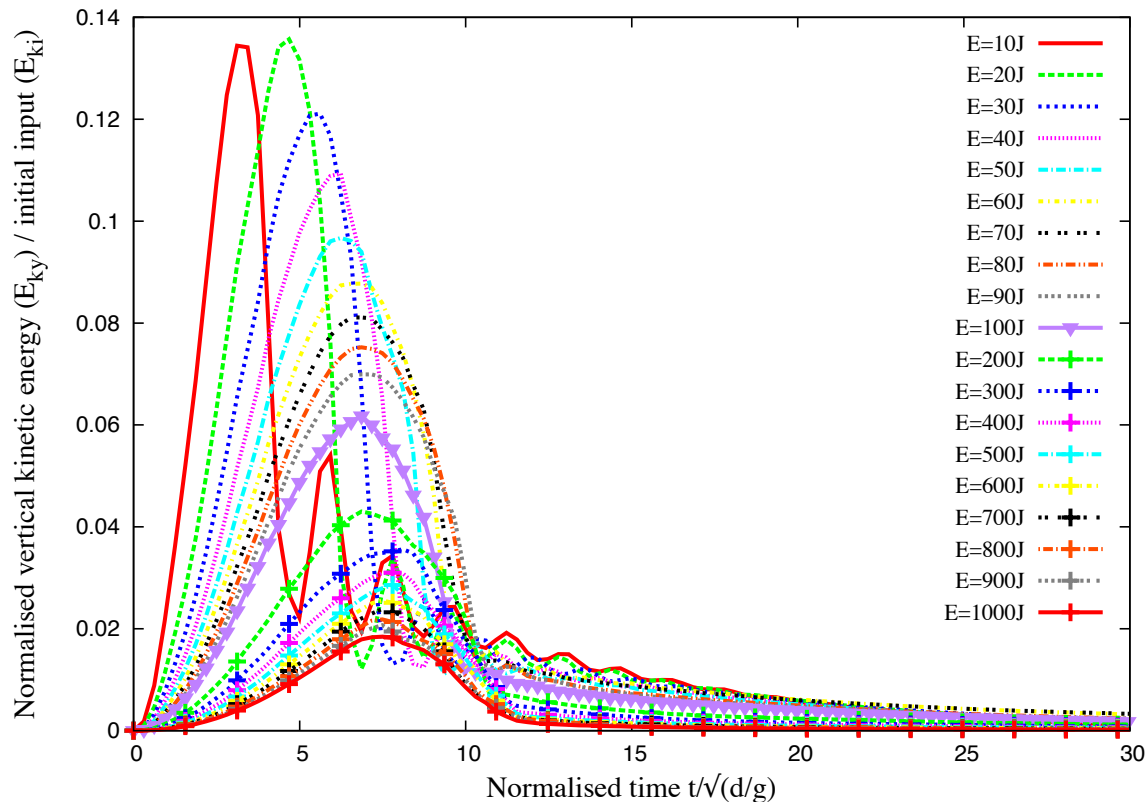


Figure 4.29 Evolution of packing density with time  $E_0 = 152\text{mgd}$  (DEM)

## 4.3 Slopes subjected to impact loading



(a) Evolution of normalised horizontal kinetic energy with time



(b) Evolution of normalised vertical kinetic energy with time

Figure 4.30 Evolution of vertical and horizontal kinetic energy with time (MPM)

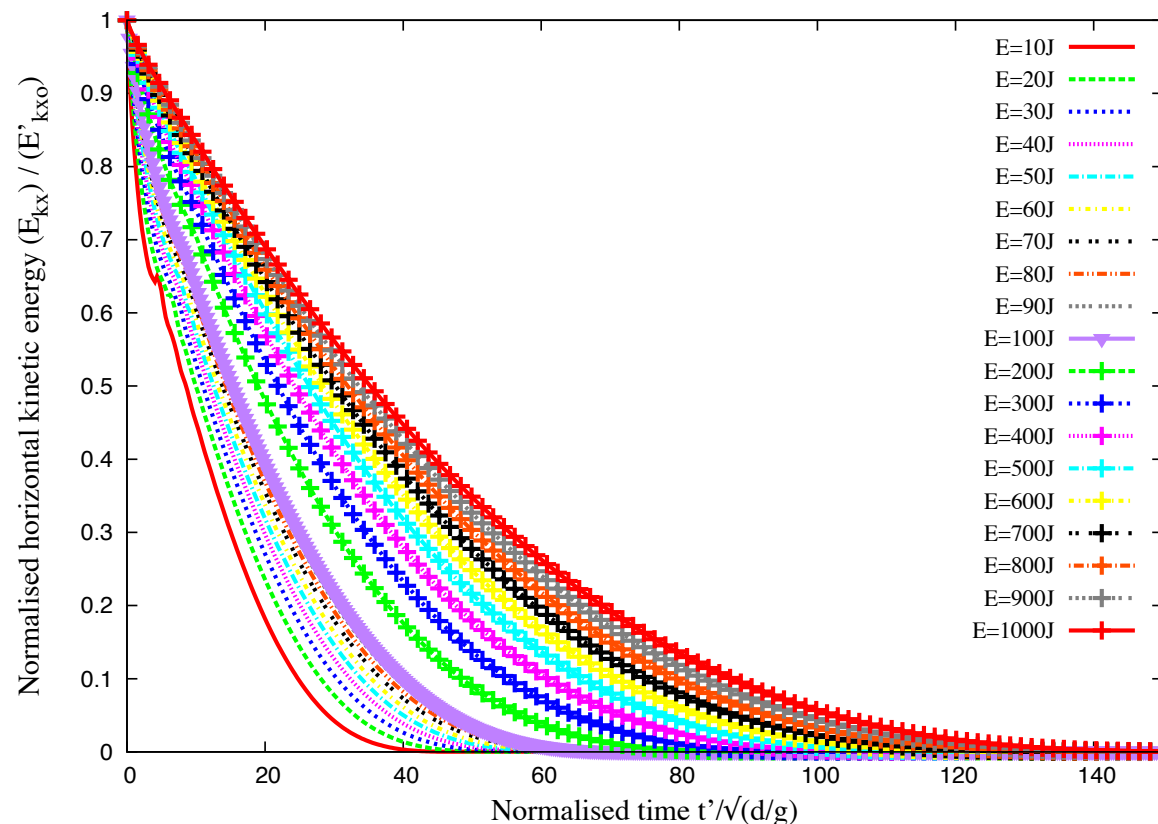


Figure 4.31 Evolution of kinetic energy in the  $x$  component of the velocity field normalized by the available kinetic energy at the end of the transient as a function of time elapsed since the same instant (MPM).

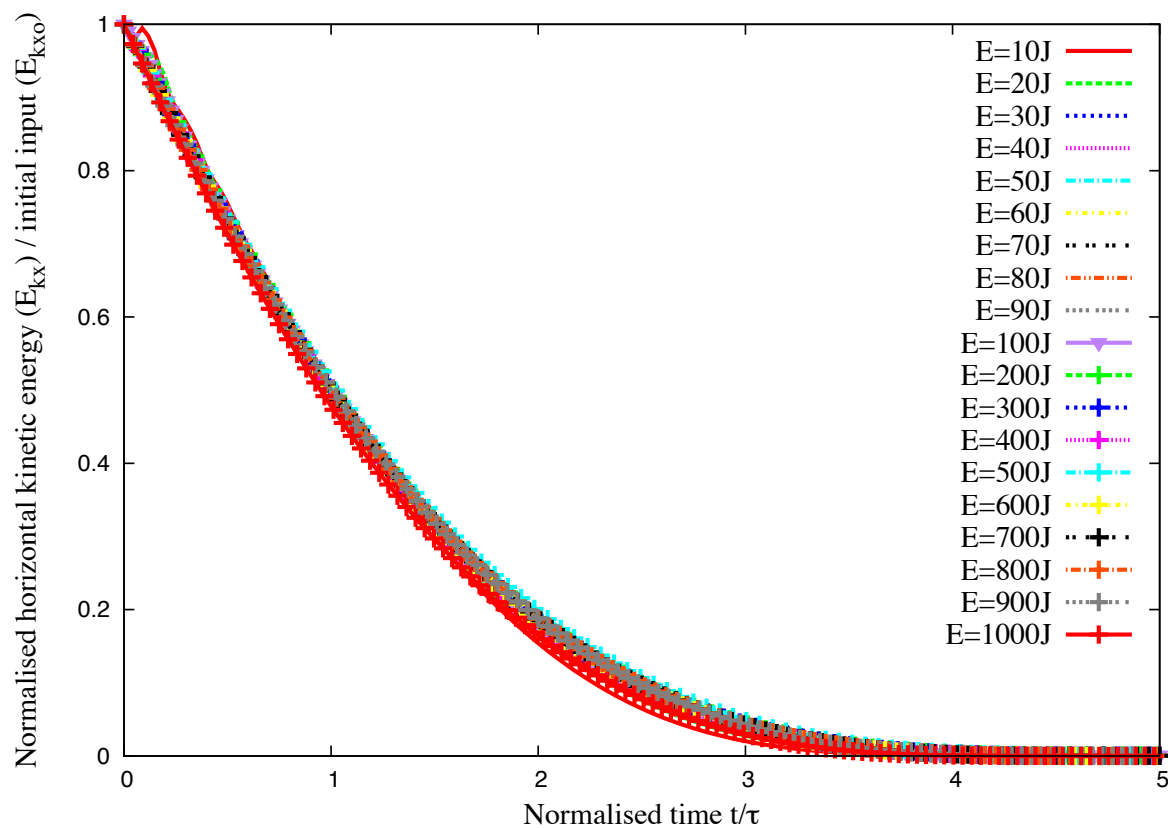


Figure 4.32 Evolution of kinetic energy in the  $x$  component of the velocity field normalized by the available kinetic energy at the end of the transient as a function of normalized time (MPM).

The scaling of the data with the decay time  $\tau$  suggests that the run-out time  $t'_f$ , since the beginning of the second phase, might be a simple function of  $\tau$ . Figure 4.33a shows both  $t'_f$  and  $\tau$  as a function of  $E'_{x0}$ , where a power-law relation can be observed for both time scales. The run-out time  $t'_f \propto (E'_{x0})^{\beta'}$  has the same exponent  $\beta' \simeq 0.33 \pm 0.02$  as  $t_f$  as a function of  $E_0$ . For the decay time we have  $\tau \propto (E'_{x0})^{\beta''}$  with  $\beta'' \simeq 0.38 \pm 0.03$ . The relation between the two times can thus be expressed as (see figure 4.33b)

$$t'_f = k \tau (E'_{x0})^{\beta'' - \beta'}, \quad (4.13)$$

where  $k \simeq 5 \pm 0.4$  and  $\beta'' - \beta' \simeq -0.06 \pm 0.05$ . This value is small enough to be neglected within the confidence interval of the data. It is therefore plausible to assume that the run-out time is a multiple of the decay time and the spreading process is controlled by a single time. A weak dependence on the energy  $E'_{kx0}$  is consistent with the fact that the energy available at the beginning of the second phase is not dissipated in the spreading process (calculated from the position of the tip of the pile) since the pile keeps deforming by the movements of the grains at the free surface even when the tip comes to rest. This can explain the small difference between the two exponents as observed here.

#### 4.3.4 Effect of friction

The run-out distance, duration of flow, and the dissipation of kinetic energy are controlled by the input energy and collective dynamics of the whole pile. However, the run-out behaviour is expected to depend also on the base friction. A series of simulations with different values of base friction was performed using MPM to analyse the influence of friction on the run-out behaviour. The influence of friction on the run-out behaviour is shown in figure 4.34a. The exponent of the power-law relation between the run-out and input energy has a weak dependence on the base friction, however, the proportionality constant is affected by the change in the base friction. This behaviour is similar to that observed in granular column collapse with varying initial properties (Balmforth and Kerswell, 2005; Lajeunesse et al., 2005).

CD simulations using different values of coefficient of restitution show no difference in the run-out behaviour. At large input energies, the pile remains in a dense state so that multiple collisions inside the pile occur at small time scales compared to the deformation time. When the restitution coefficients are increased, more collisions occur during a longer time interval but the overall energy dissipation rate by collisions remains the same. This effect is a seminal example of collective effects which erase the influence of local parameters at the macroscopic scale.

## 4.3 Slopes subjected to impact loading

127

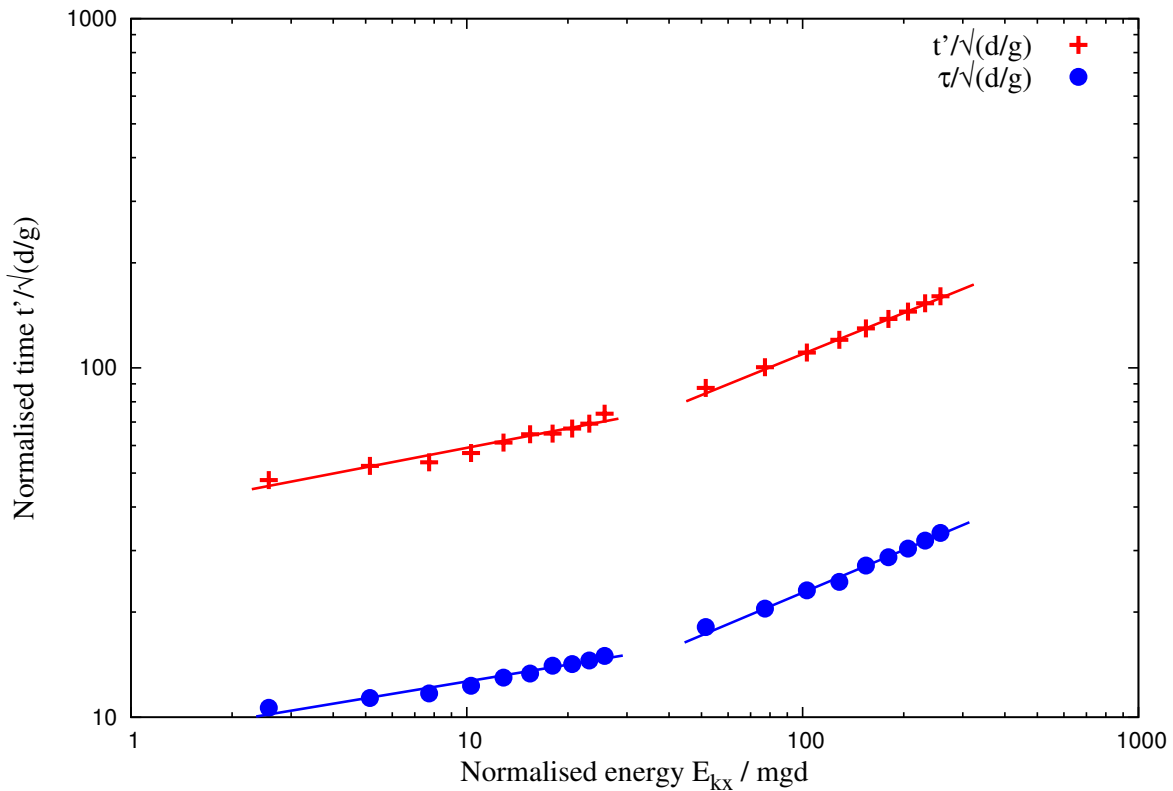
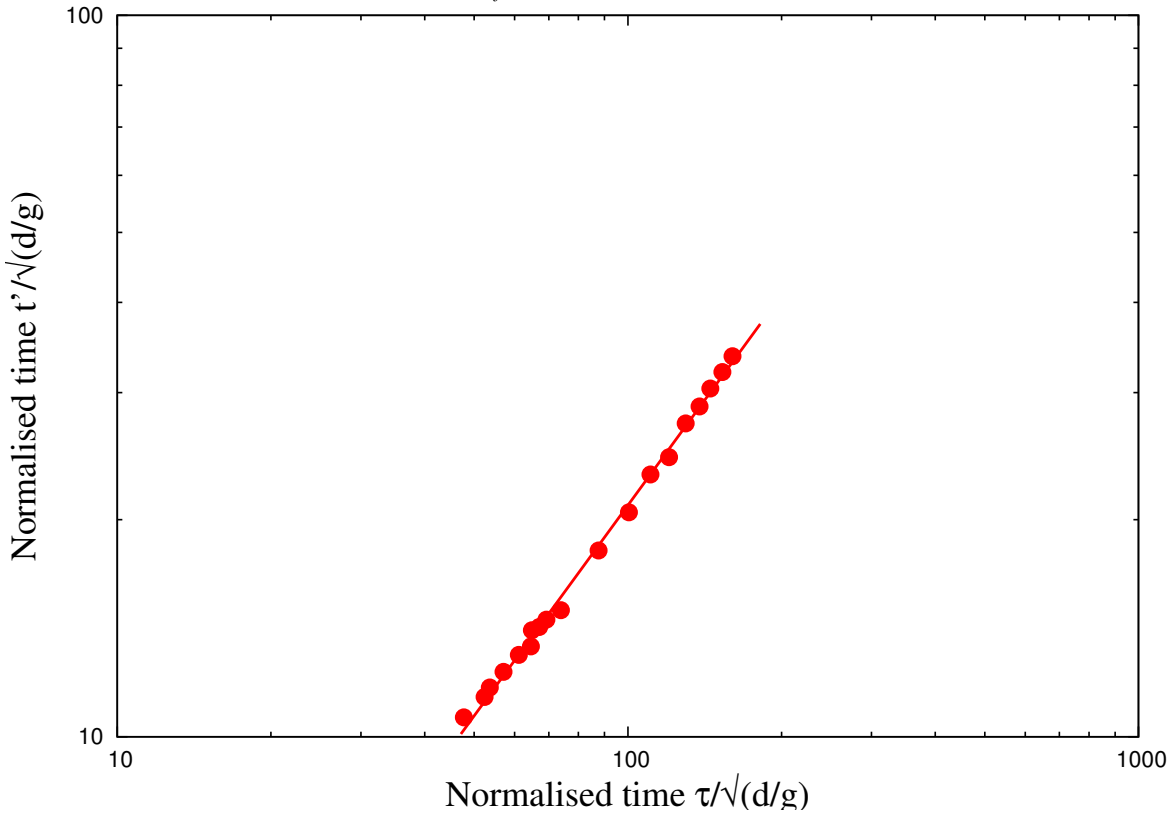
(a) Power law evolution of  $t'_f$  and  $\tau$  as a function of kinetic energy  $E'_{kx0}$ .(b) Linear relationship between decay time and run-out time after the transient as a function of the normalized kinetic energy  $E_{kx0}$ .

Figure 4.33 Decay time and run-out time as a function of the normalised kinetic energy  $E_{kx0}$ .

In contrast with the restitution coefficients, the effect of friction coefficient, however, is quite important for the run-out. MPM simulations with varying friction coefficient shows that, both the run-out distance and the decay time decrease as the friction coefficient is increased. This effect is much more pronounced at low values of the friction coefficient. The run-out time, for example, is reduced by a factor of  $\approx 4$  as  $\mu_s$  is increased from 0.1 to 0.2 while the change in the run-out and duration is less effected with increase in friction coefficient. This “saturation effect” can be observed in a systematic way in simple shear tests. The dissipation rate may reach a saturation point where the dilation of granular materials and rolling of the grains change in response to increase in friction coefficient (Estrada et al., 2008).

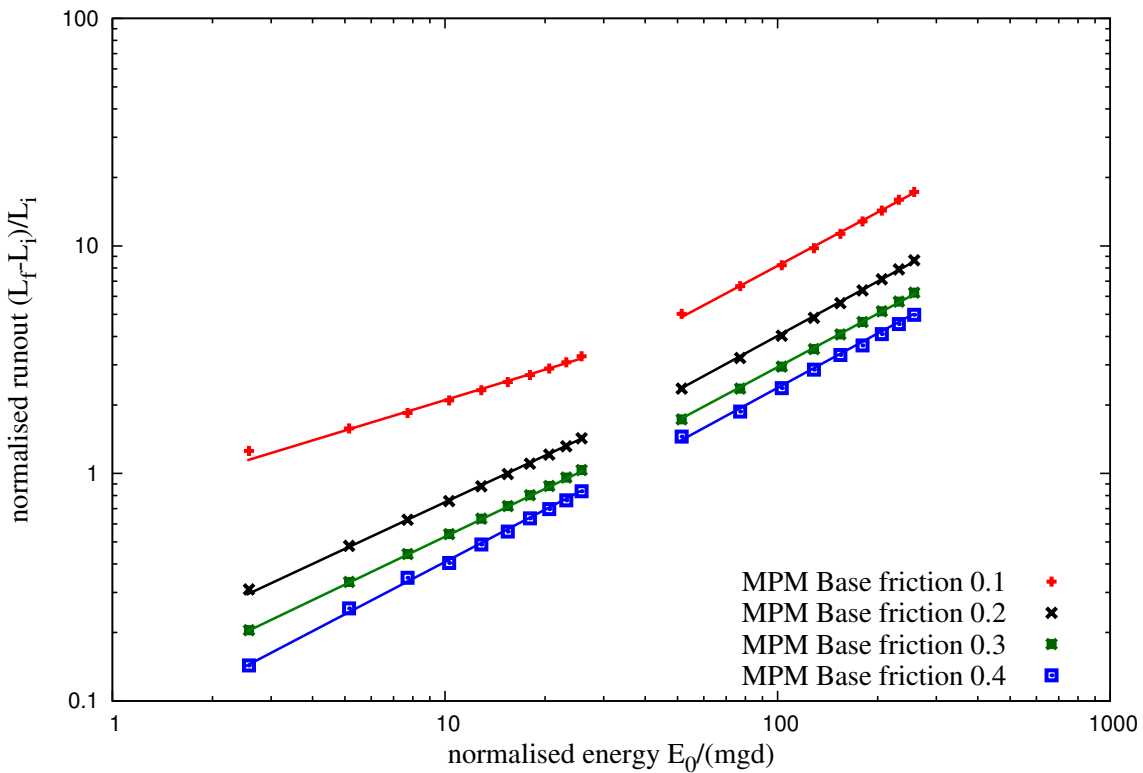
## Effect kinetic energy distribution

Staron et al. (2005) observed that the distribution of kinetic energy in the granular system is an essential factor for the run-out distance. In order to understand the influence of energy distribution on the run-out behaviour, granular pile subjected to two different velocity fields were studied. A uniform velocity  $V_{xo}(y) = V_0$  is applied to the entire pile, in contrast to the gradient impact velocity. Snapshots of flow kinematics at initial stages are shown in figure 4.35 (MPM simulations) and figure 4.36 (DEM). It can be observed from the figures that the continuum behaviour is identical to that of grain-scale simulations. As each grain experiences the same velocity, grains located at the top of the slope are pushed farther away and unlike the gradient input velocity, the cavity left behind the granular mass is not filled by the soil grains at the top.

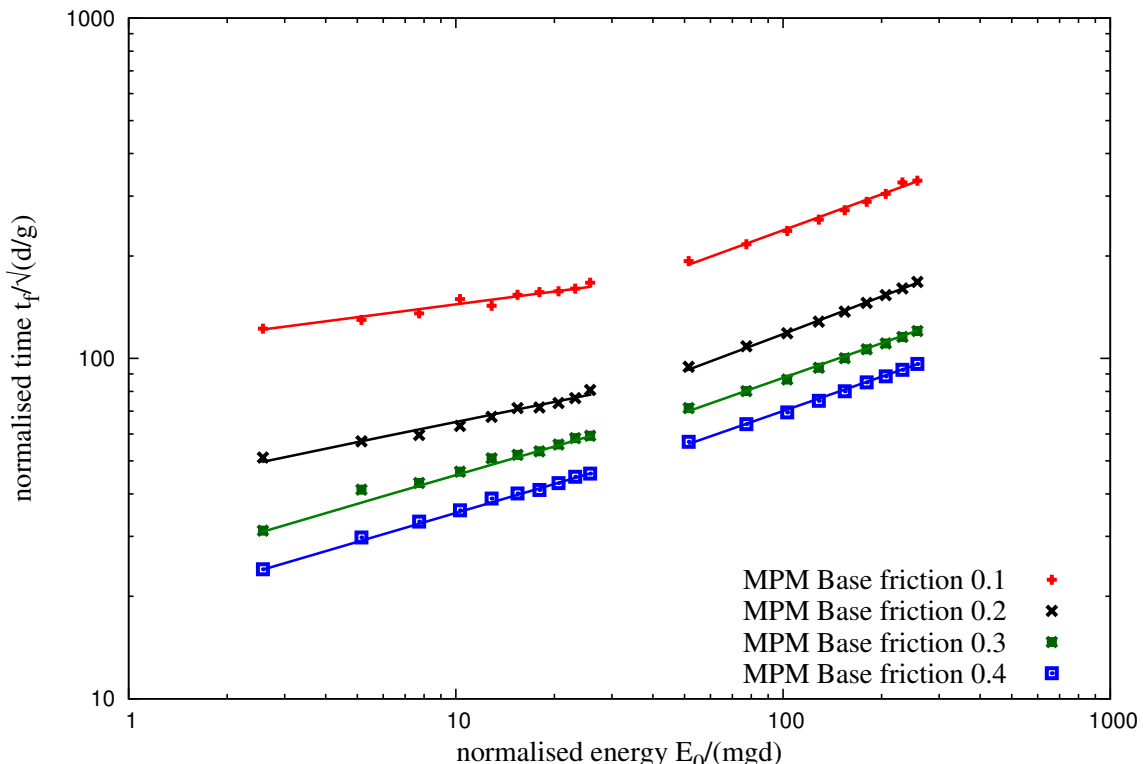
Figure 4.37a shows the influence of velocity distribution on the run-out behaviour. At low input energy, the gradient velocity distribution shows significantly longer run-out in comparison to uniform velocity distribution. Section 4.3.3 shows that at low input energies a larger fraction of the energy is consumed in the destabilisation process. Which means that the amount energy available for flow is less, in uniform velocity distribution, this energy is even smaller as the initial velocity is distributed uniformly throughout the granular mass. However at higher input energy, where most of the energy is dissipated during the spreading phase, the run-out distance has a weak dependence on the distribution of velocity in the granular mass. The duration of the flow shows similar behaviour to the run-out, however, a slope subjected to a gradient velocity flows quicker than a slope subjected to a uniform impact velocity. Gradient velocity distribution provides more input energy at the initial stage to overcome the frictional resistance at the base. This shows that the material property and the distribution of kinetic energy in the system has a non-trivial influence on the flow kinematics and the internal flow structure.

## 4.3 Slopes subjected to impact loading

129



(a) Effect of friction on the run-out distance



(b) Effect of friction on the duration of run-out.

Figure 4.34 Effect of friction on the run-out behaviour

$t = 0 \text{ s}$



$t = 0.03 \text{ s}$



$t = 0.06 \text{ s}$



$t = 0.09 \text{ s}$



Figure 4.35 Snapshots of MPM simulations of the evolution of granular pile subjected to a gradient impact energy  $E_0 = 61 \text{ mgd}$ .

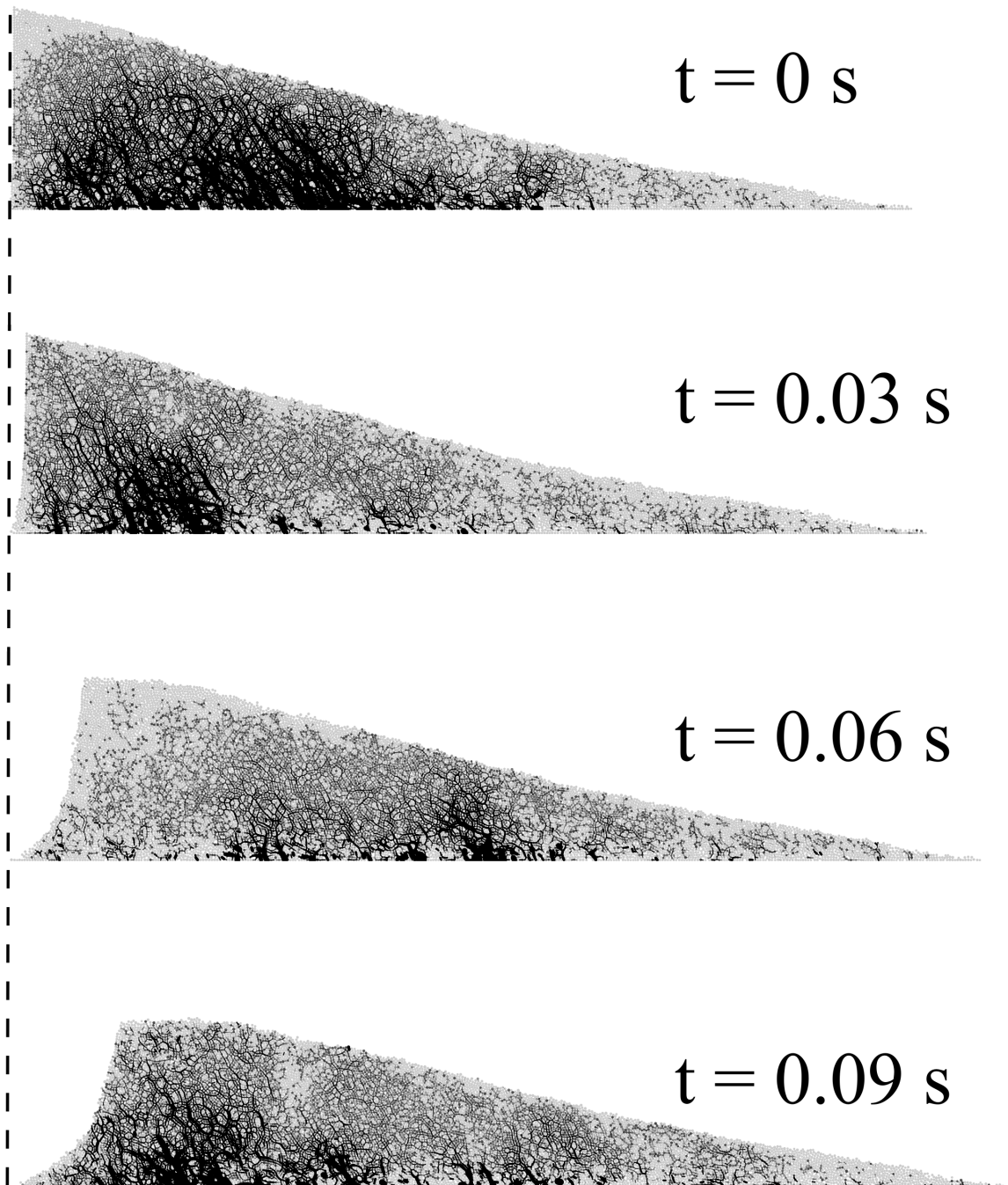
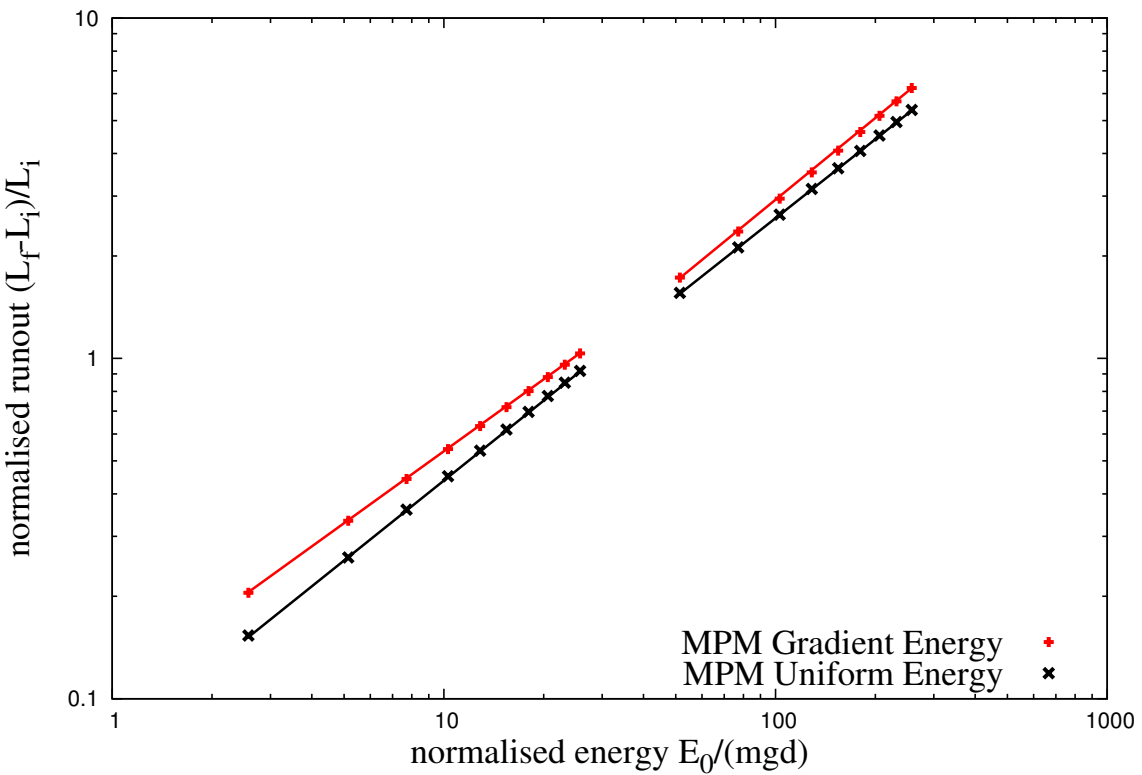
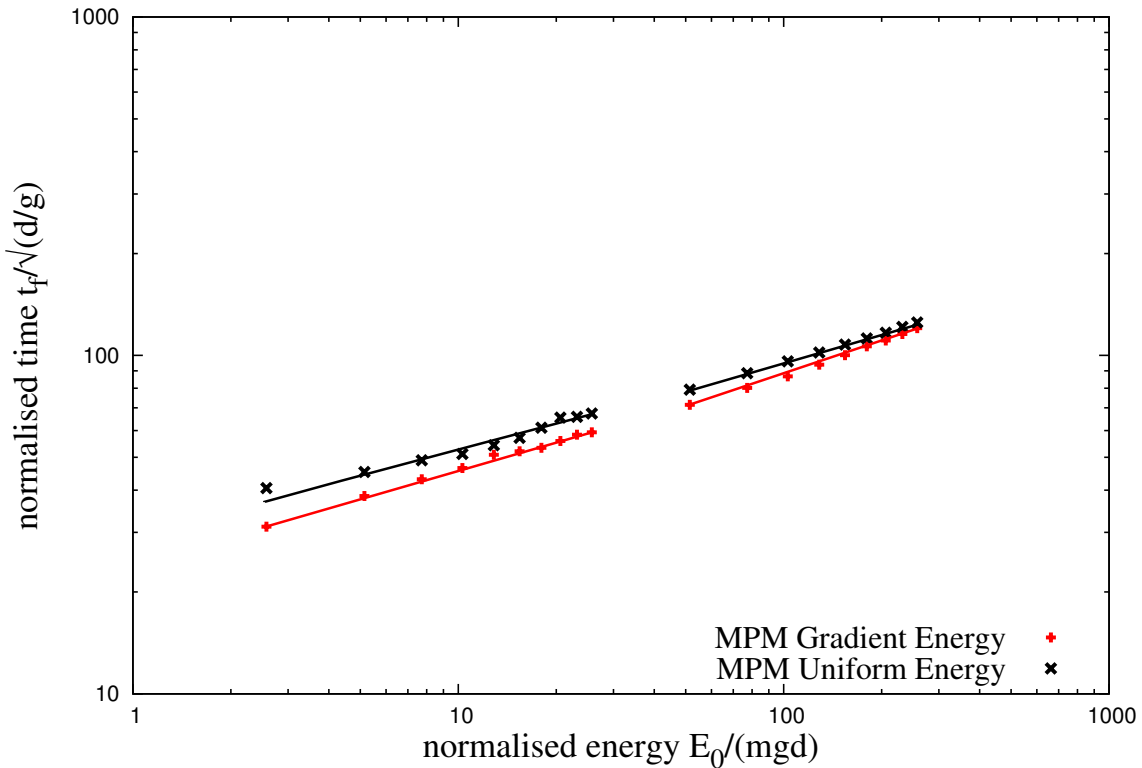


Figure 4.36 Snapshots of DEM simulations of the evolution of granular pile subjected to a gradient impact energy  $E_0 = 61 \text{ mgd}$ .



(a) Run-out distance as a function of normalised input kinetic energy



(b) Duration of run-out as a function of normalised input kinetic energy

Figure 4.37 Effect of input velocity distribution on the run-out behaviour

### 4.3.5 Effect of mesh size and number of material points per cell

Abe et al. (2013) observed that for a coarse mesh, the numerical error decreases with increase in the number of material points per cell. In contrast, they observed an opposite trend for the fine meshes (0.01 m). The influence of numerical noise due to particles crossing the background mesh was not observed when the mesh size is greater than 0.05 m. Coetzee et al. (2005) also found that the numerical error decreases with increase in mesh refinement.

In the present study, the effect of mesh size and the number of material points per cell on the run-out behaviour is investigated. For a mesh size of 0.0125 m, the number of material points per cell (PPC) is varied as 4, 16, 25, 36, 64, 81 and 100. The effect of number of material points on the run-out behaviour is presented in figure 4.38. At a low input energy of 50 J, 4 and 16 material points per cell result in longer run-out distance, where as the run-out distance converges when the number of PPC is more than 25. While at a high input energy of 500 J, both 4 and 16 PPC predict almost the same run-out distance, but is higher than the run-out predicted with more than 25 material points per cell.

The evolution of the granular pile during the initial stage of flow is show in figure 4.39 for different number of material points per cell. At low input energy, fewer material points per cell results in larger separation of the spreading mass from the left wall. Distinct shear bands can be observed for more than 16 PPC. The flow structure remains unchanged with increase in PPC of more than 25. At a higher input energy (see figure 4.40), almost all cases predict similar flow structure, except in the case of 4 PPC.

Figure 4.41 shows the evolution of kinetic energy with time for varying number of material points per cell. At low input energy, the horizontal kinetic energy evolution is identical for all cases. A slightly quicker run-out evolution during the spreading phase can be observed for the case of 4 PPC. However, increase in the number of material points per cell significantly affects the evolution of the vertical kinetic energy  $E_{ky}$ . At low energy, a large proportion of the input energy is dissipated in the destabilisation process. This results in material points falling behind the spreading mass to the fill the cavity. Fewer number of material points per cell results in cell crossing noise as the material points filling the cavity experience free-fall due to gravity. The effect of cell-crossing noise can be seen in the osciallation of vertical kinetic energy for fewer material points per cell. However, at high input energy, most of the input velocity is dissipated during the spreading process. This means that only a small fraction of energy is available in the vertical component resulting in almost similar behaviour for all cases. Four material points per cell predicts a higher peak vertical kinetic energy in comparison with other cases, unlike the low energy case, no oscillations were observed for the high input energy.

The effect of mesh size on the flow kinematics is studied by comparing two mesh sizes: 0.01 m and 0.0125 m (see figure 4.42). It can be observed that the run-out distance converges

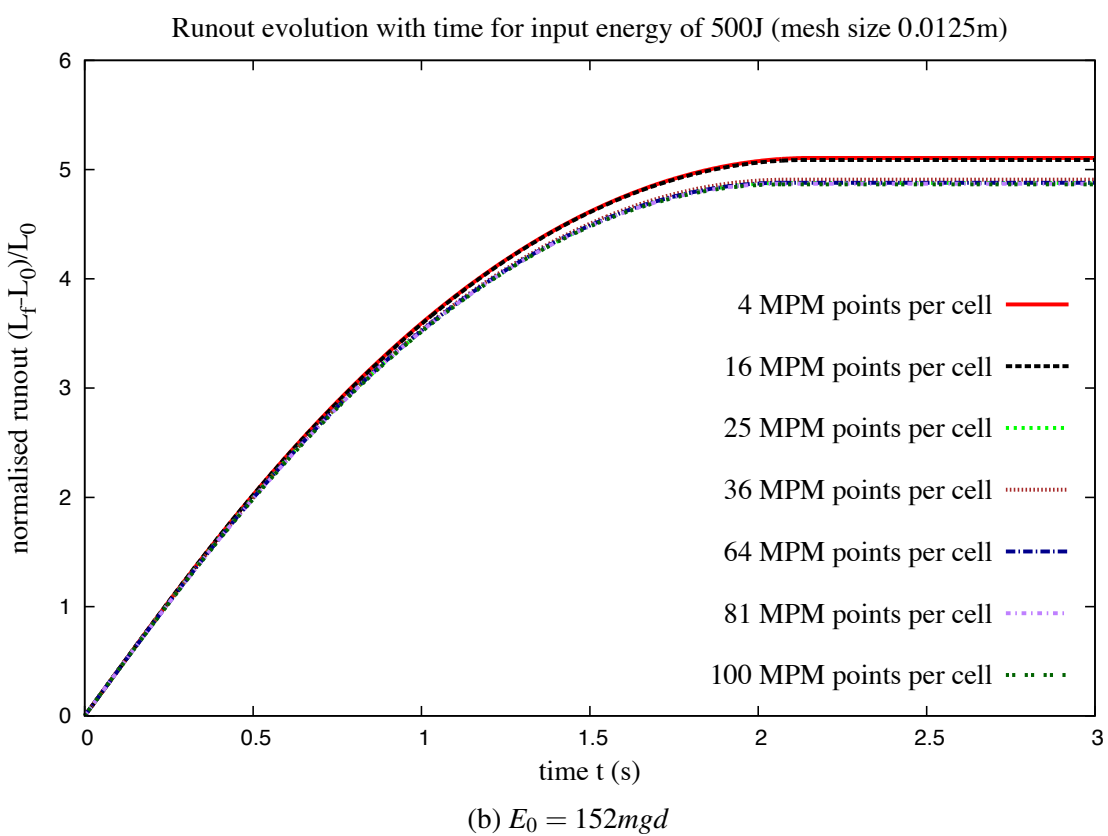
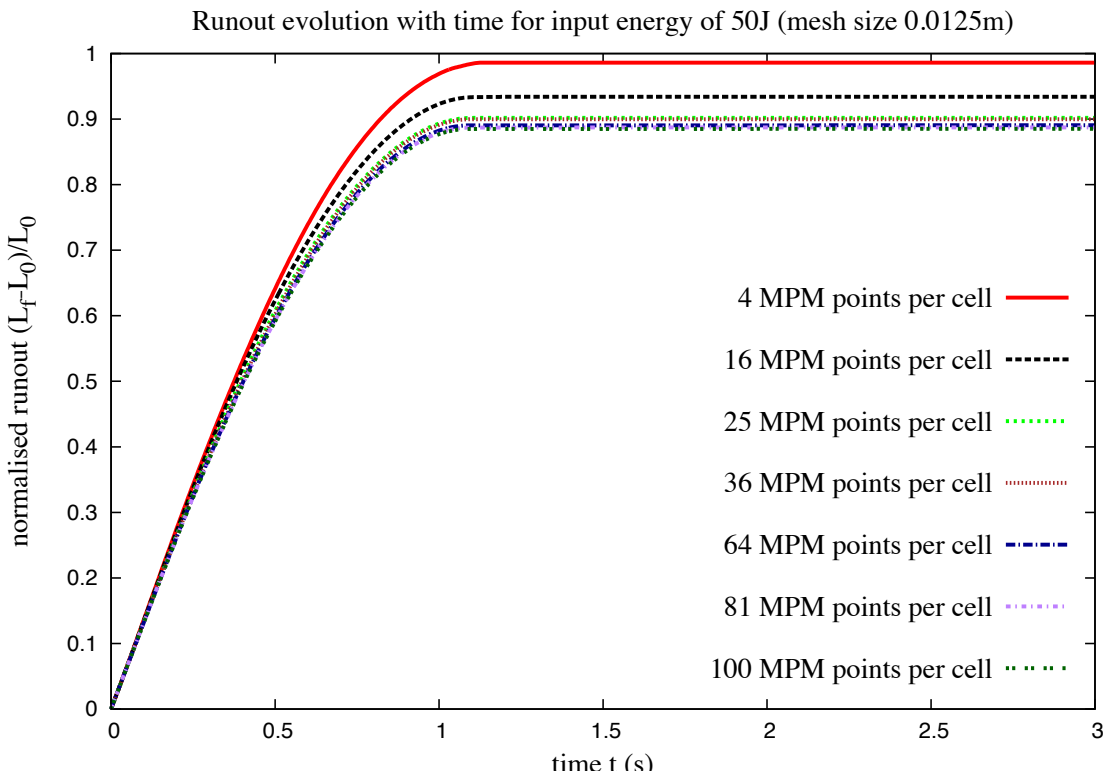


Figure 4.38 Evolution of run-out with time for varying material points per cell.

## 4.3 Slopes subjected to impact loading

135

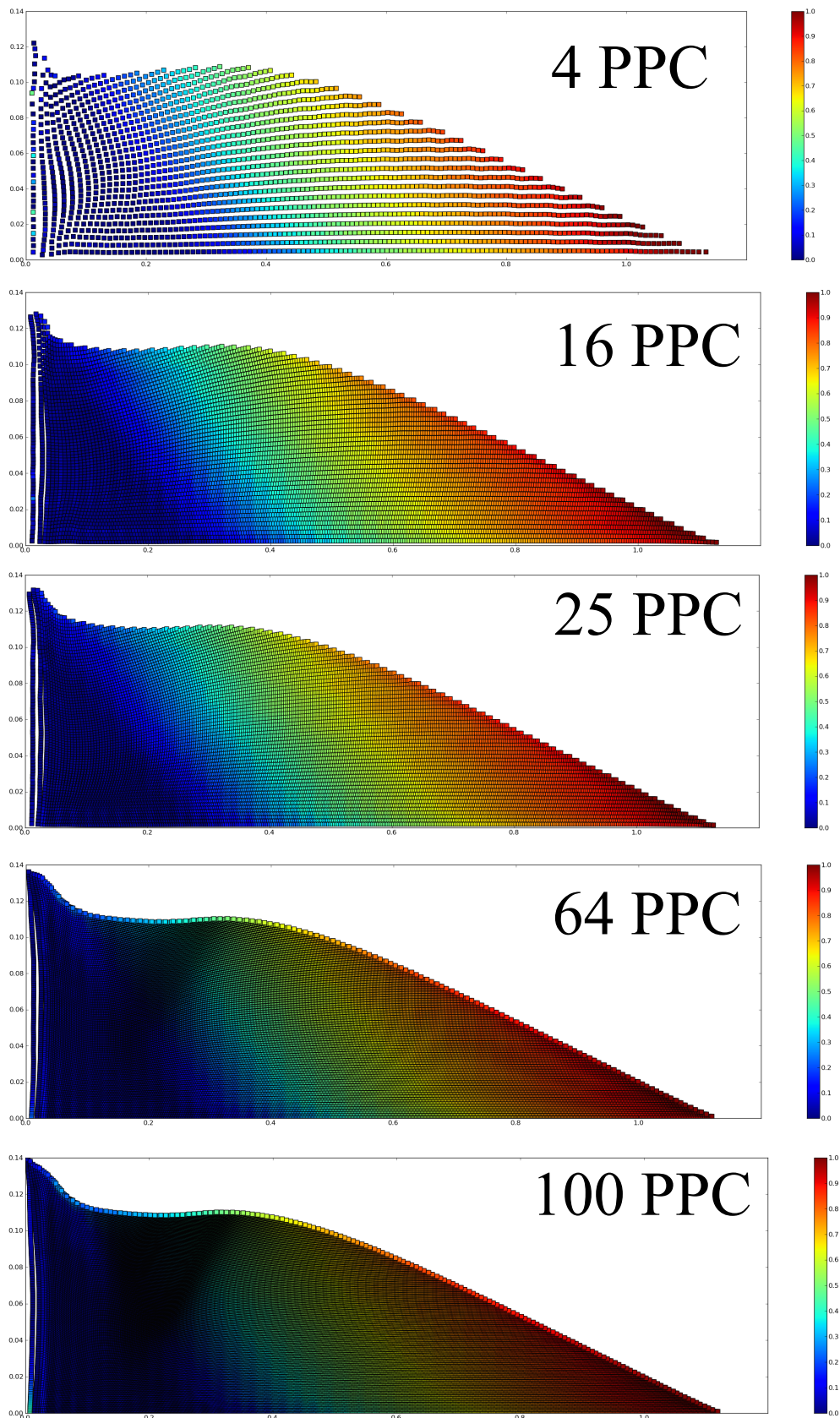


Figure 4.39 Effect of number of material points on cell on the run-out behaviour  $E_0 = 12.7mgd$ . Velocity profile (m/s) of granular pile subjected to gradient impact loading.

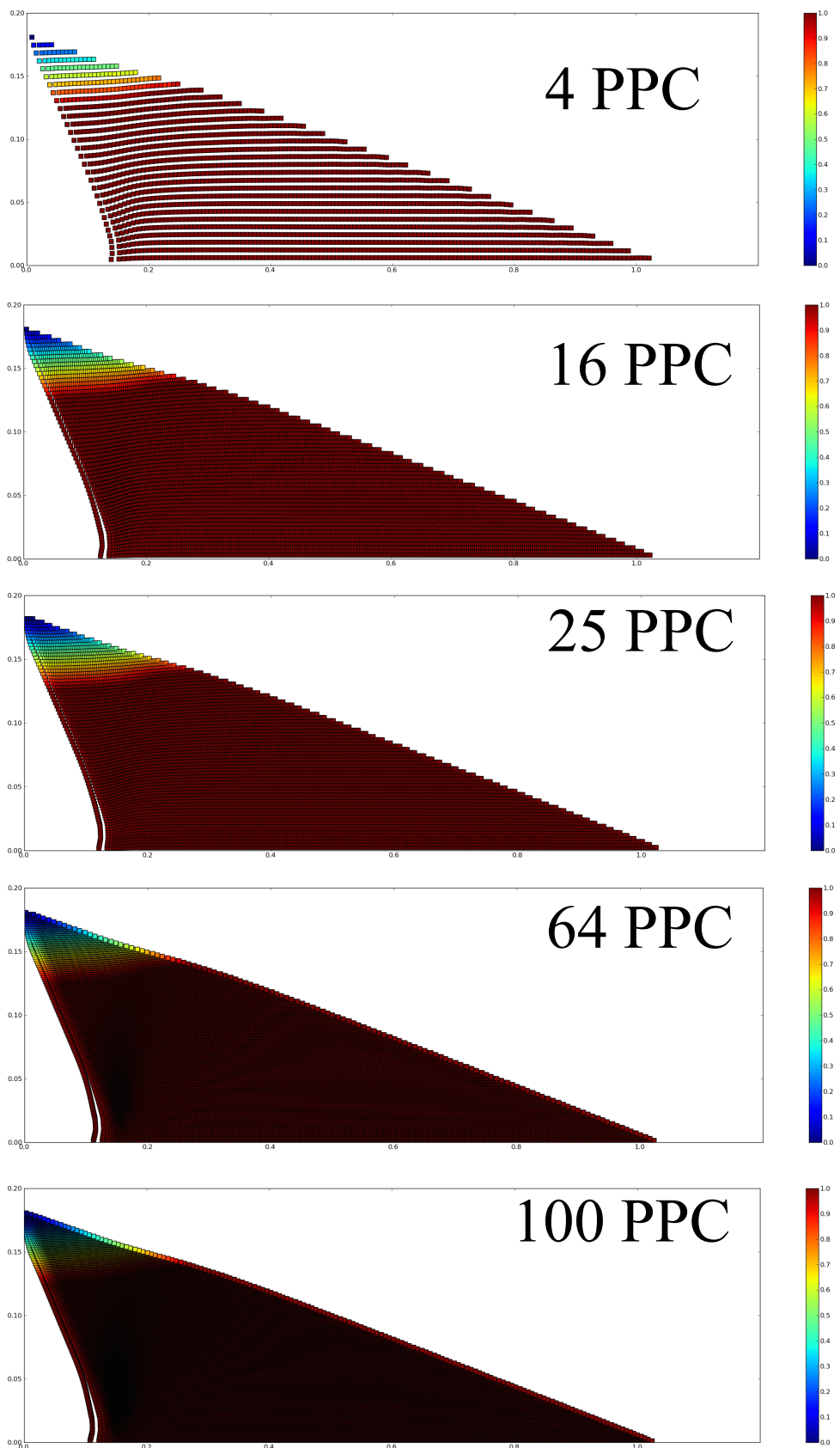


Figure 4.40 Effect of number of material points on cell on the run-out behaviour  $E_0 = 152mgd$ . Velocity profile (m/s) of granular pile subjected to gradient impact loading.

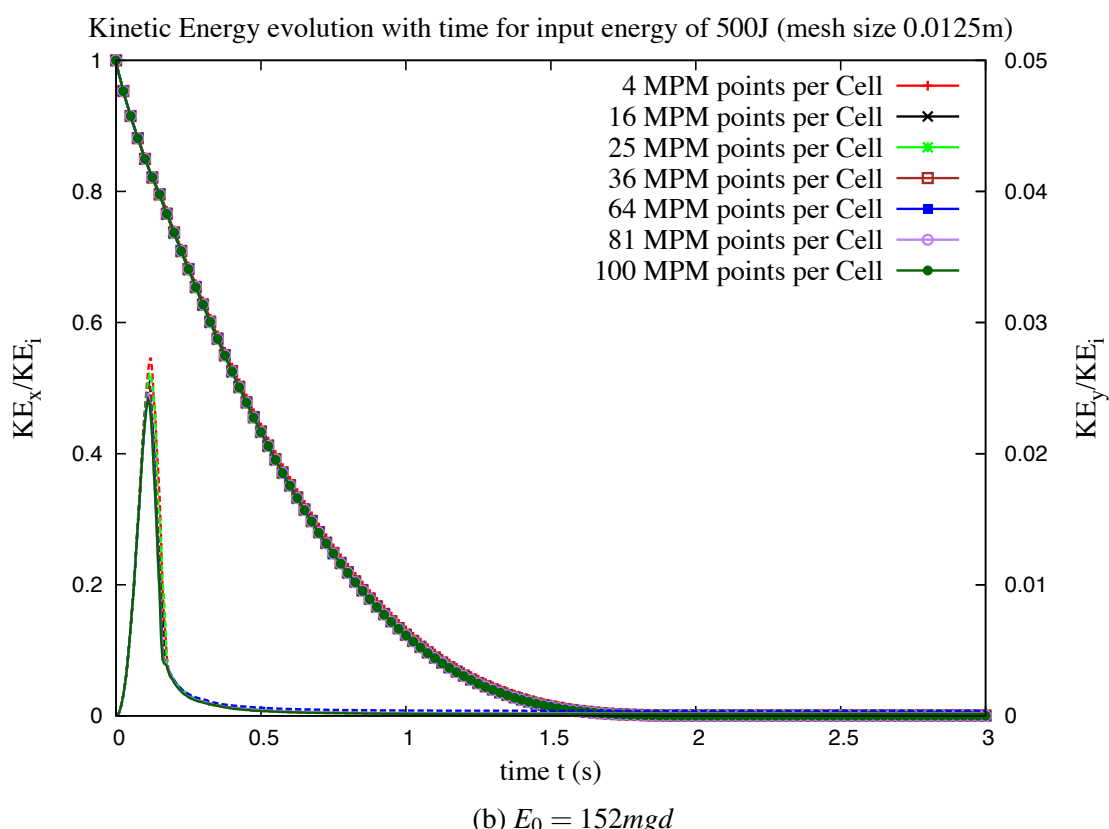
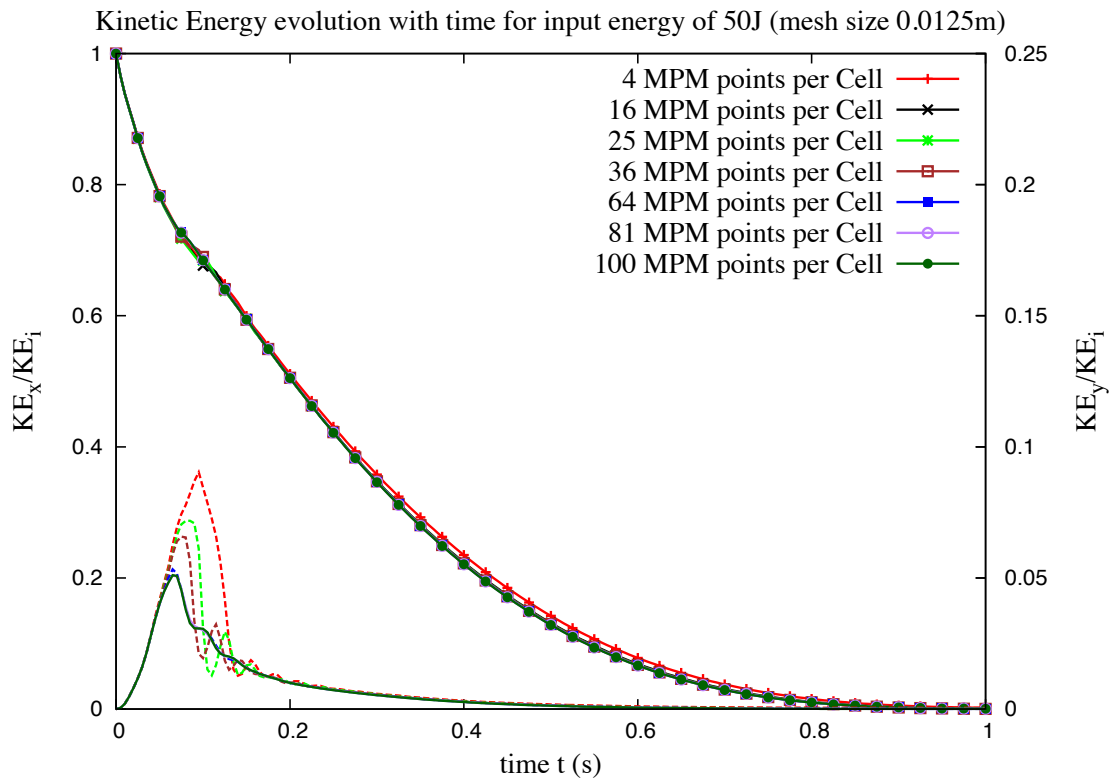


Figure 4.41 Evolution of kinetic with time for varying material points per cell

with increase in the number of material points per cell in both cases. Less than 1% difference in the run-out distance was observed between a mesh size of 0.0125 m and 0.01 m. The final run-out duration is almost unaffected by the increase in the number of material points per cell.

This shows that the run-out distance is affected by the number of material points per cell. However, the duration of the run-out is independent of the number of material points per cell. The computation time increases with increase in the number of material points per cell and decrease in the mesh size. However, the run-out distance converges with increase in number of material points per cell. Hence, an optimum number of 25 material points per cell was adopted in this case. In summary, for conducting a successful MPM analysis, a careful selection of the mesh size and the number of particles is necessary.

#### 4.3.6 Comparison with granular column collapse

Figure 4.43 shows the run-out behaviour of granular column collapse and the slope subjected to impact velocities as a function of normalised kinetic energy. In the case of column collapse, the peak energy at  $\tau_c$  is used as the energy available for the flow. It can be observed that MPM and DEM predict similar run-out behaviour for low energy regime (short columns), which undergo frictional failure along the flanks. However MPM predicts longer run-out for high energy regime (corresponding to a > 2.7), where the granular column experiences significant collisional dissipation. The lack of a collisional energy dissipation mechanism in MPM results in over prediction of run-out distances. In the case of granular column subjected to impact velocity, the dissipation is friction and MPM is able to predict the run-out response in good agreement with DEM simulations. At very low energy, DEM simulations show longer run-out in the case of slope subjected to impact due to local destabilisation at the flow front. Both granular flows, column collapse and slope subjected to impact, show power-law relation with the energy. This shows that the power-law behaviour is a granular flow characteristic.

### 4.4 Summary

Multi-scale simulation of dry granular flows were performed to capture the local rheology, and to understand the capability and limitations of continuum models in realistic simulation of granular flow dynamics. MPM with a simple frictional dissipation model is able to capture the flow kinematics of dry granular flows. However, the lack of collisional dissipation in MPM is a limitation in modelling the collapse of tall columns. Both DEM and MPM simulations show a power-law dependence of the run-out and time with the initial aspect ratio of the column.

## 4.4 Summary

## 139

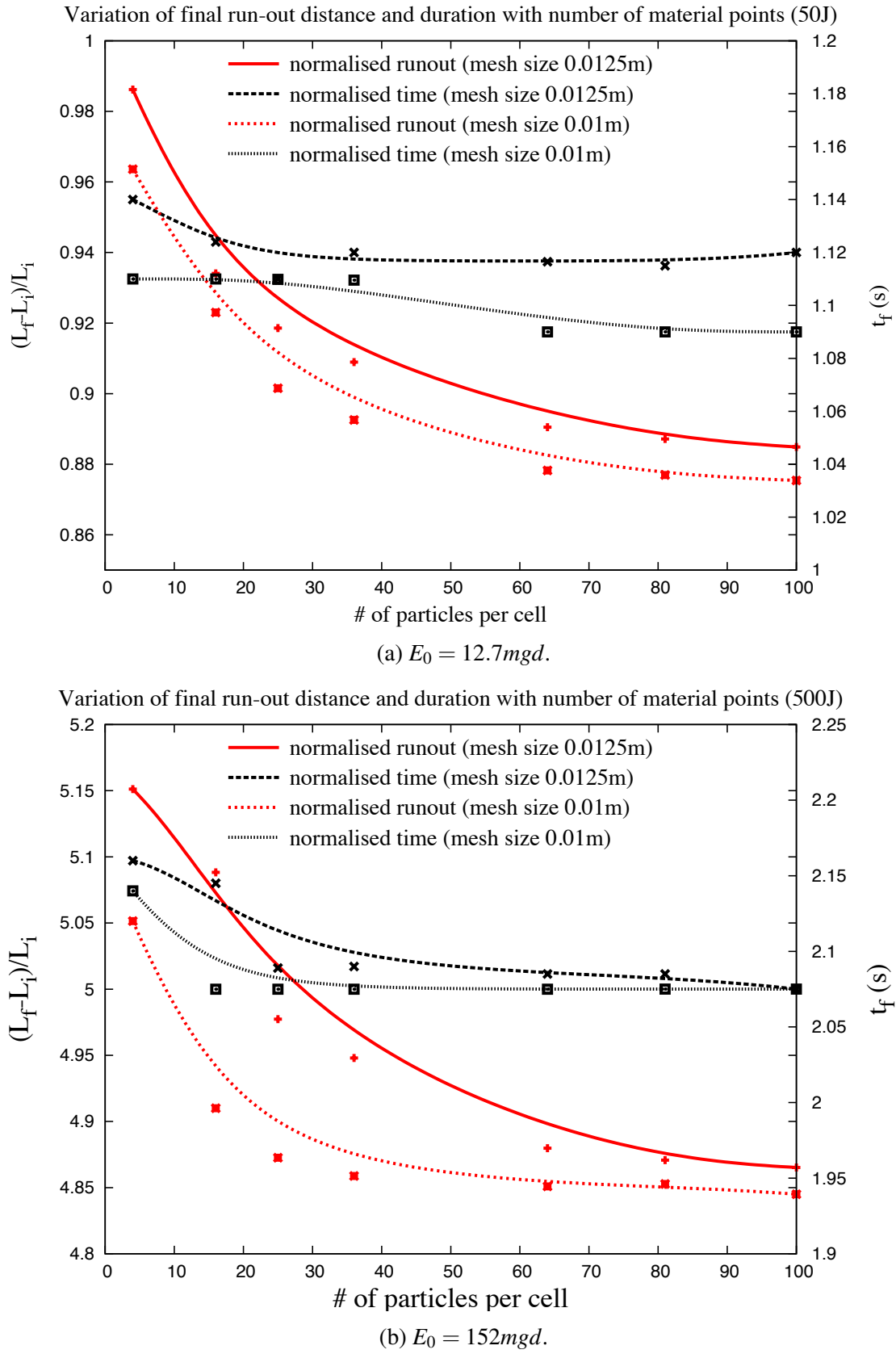


Figure 4.42 Evolution of run-out and duration of flow for varying material points per cell.

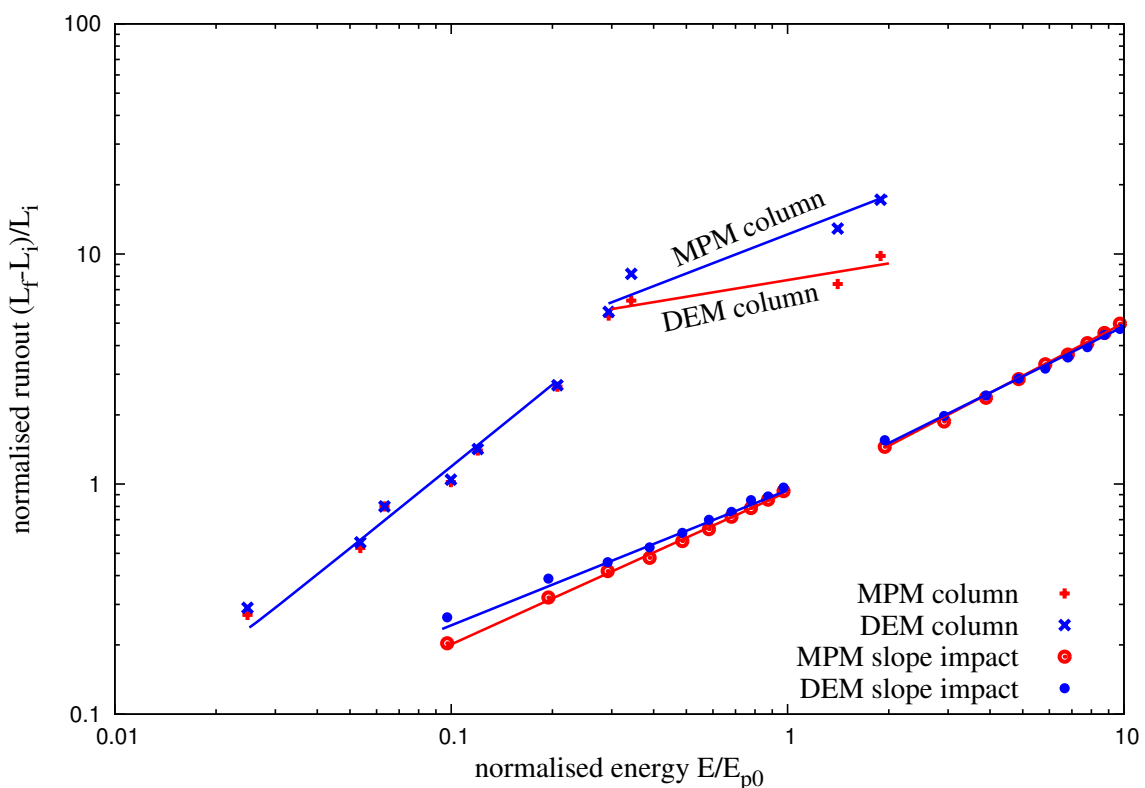


Figure 4.43 Comparison of column collapse with slope subjected to impact loading.

<sup>15</sup> The initial configuration and the material properties have a significant influence on the run-out  
<sup>16</sup> behaviour.

<sup>17</sup> Natural granular flows are triggered by different mechanisms. The distribution of kinetic  
<sup>18</sup> energy in the granular mass is found to have an effect on the flow kinematics. A multi-scale  
<sup>19</sup> analyses of granular slope subjected to impact velocity reveals a power-law dependence of the  
<sup>20</sup> run-out distance and time as a function of the input energy with non-trivial exponents. This  
<sup>21</sup> reveals that the power-law behaviour is a generic feature of granular dynamics. The values of  
<sup>22</sup> the exponents are not simple functions of the geometry.

<sup>23</sup> We also observe two regimes with different values of the exponents: a low-energy regime  
<sup>24</sup> and a high-energy regime. The low energy regime reflects mainly the destabilisation of the pile,  
<sup>25</sup> with a run-out time independent of the input energy. Whereas, the second regime is governed  
<sup>26</sup> by the spreading dynamics induced by higher input energy. The evolution of granular slope in  
<sup>27</sup> the high-energy regime can be described by a characteristic decay time and the energy available  
<sup>28</sup> at the end of the first stage, where the pile is destabilised. MPM is successfully able to simulate  
<sup>29</sup> the transient evolution with a single input parameter, the macroscopic friction angle. This study  
<sup>30</sup> exemplifies the ability of MPM, a continuum approach, in modelling complex granular flow  
<sup>31</sup> dynamics and opens the possibility of realistic simulation of geological-scale flows on complex  
<sup>32</sup> topographies.



## <sup>33</sup> Chapter 5

# Numerical modelling of fluid–grain interactions

## 5.1 Fluid simulation using lattice Boltzmann method

Grain–fluid systems can be found in many scientific and engineering applications, such as suspensions, fluidised beds, sediment transport, and geo-mechanical problems. In general, the fundamental physical phenomena in these systems are not well understood mainly due to the intricate complexity of grain–fluid interactions and the lack of powerful analysis tools (Han et al., 2007a). In addition to the interaction among soil grains, the motion of soil grains is mainly driven by gravity and the hydrodynamic force exerted by the fluid. The fluid flow pattern can be significantly affected by the presence of soil grains and this often results in a turbulent flow. Hence, the development of an effective numerical framework for modelling both the fluid flow patterns and the grain–fluid interactions is very challenging.

Development of a numerical framework depends crucially on the size of the soil grains relative to the domain/mesh size (Feng et al., 2007). Traditionally, the Navier-Stokes equation is solved by a grid-based Computational Fluid Dynamics (CFD) method, such as the Finite Volume Method, FVM, (Capelatro and Desjardins, 2013) or a mesh-free technique such as Smooth Particle Hydrodynamics (SPH) (Sun et al., 2013). The grid size in FVM or the smooth length in SPH for discretisation of the Navier-Stokes equation is at least an order of magnitude larger than the grain diameter (Xiong et al., 2014).

In situations where the average domain concentration phase is far from dilute, the computational effort is mostly devoted to the grain dynamics. The hydrodynamic forces on the soil grains are applied based on an empirical relation using the domain-averaged local porosity of the soil grains in the grid. As a result, developing a fast fluid hydrodynamics solver

is unimportant for dense flows. However, most geo-mechanical problems involve complex interactions between the solid and the fluid phase. This requires accurate modelling of the fluid flow pattern. Additionally, geophysical problems, such as submarine landslides and debris flow have a relatively large simulation domain, which requires parallel computation. Implementing traditional grid-based CFD methods face great challenges on multi-processor systems (Xiong et al., 2014). Although mesh-free approaches are free from the problem of parallel scalability, its modelling accuracy and speed are relatively low when compared to grid-based CFD methods. Therefore, an accurate, fast and a highly scalable scheme is required to model fluid - grain systems in geo-mechanics.

The Navier-Stokes equation describes the motion of a non-turbulent Newtonian fluid. The equation is obtained by applying Newton's second law to the fluid motion, together with an assumption that the fluid stress is the sum of the viscous term, proportional to the gradient of the velocity, and the pressure term. Conventional CFD methods compute pertinent flow fields, such as velocity  $u$  and pressure  $p$ , by numerically solving the Navier-Stokes equation in space  $x$  and time  $t$ . Alternatively, the transport equation or the Boltzmann equation, which deals with a single particle distribution function  $f(x, \xi, t)$  in phase space  $(x, \xi)$  and time  $t$ , can be used to solve various problems in fluid dynamics.

The Lattice Boltzmann Method (LBM) (Chen and Doolen, 1998; Han et al., 2007b; He and Luo, 1997a,b; Mei et al., 2000; Zhou et al., 2012) is an alternative approach to the classical Navier-Stokes solvers for fluid flows. LBM works on an equidistant grid of cells, called lattice cells, which interact only with their direct neighbours. In LBM, the discretisation of continuum equations is based on microscopic models and mesoscopic continuum theories. LBM is a special discretising scheme of the Boltzmann equation where the particle distribution functions (mass fractions) collide and propagate on a regular grid. The important aspect, however, is the *discretisation of the velocity*, which means that the particle velocities are restricted to a predefined set of orientations.

The theoretical premises of the LB equation are that (1) hydrodynamics is insensitive to the details of microscopic physics, and (2) hydrodynamics can be preserved so long as the conservation laws and associated symmetries are respected in the microscopic and mesoscopic level. Therefore, the computational advantages of LBM are achieved by drastically reducing the particle velocity space  $\xi$  to only a very few discrete points without seriously degrading the hydrodynamics (Mei et al., 2000). This is possible because LBM rigorously preserves the hydrodynamic moments of the distribution function, such as mass density and momentum fluxes, and the necessary symmetries (He and Luo, 1997a,b). LBM has evolved as a comprehensive fluid solver and its theoretical aspects link well with the conventional central finite difference scheme (Cook et al., 2004).

### 6 5.1.1 Formulation

7 LBM is a ‘micro-particle’ based numerical time-stepping procedure for the solution of incom-  
 8 pressible fluid flows. Consider a 2D incompressible fluid flow with density  $\rho$  and kinematic  
 9 viscosity  $\nu$ , in a rectangular domain  $D$ . The fluid domain is divided into rectangular grids or  
 10 lattices, with the same grid length ‘ $h$ ’ in both  $x$ - and  $y$ -directions (see figure 5.1).

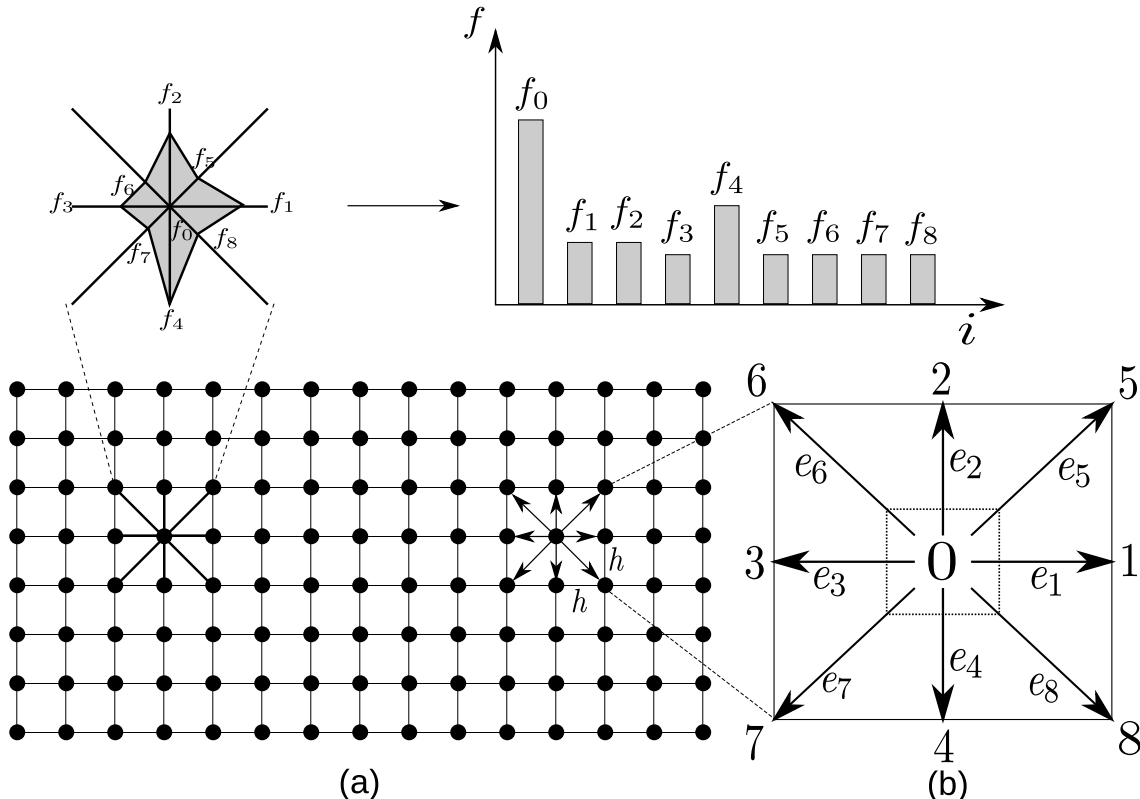


Figure 5.1 The Lattice Boltzmann discretisation and D2Q9 scheme: (a) a standard LB lattice and histogram views of the discrete single particle distribution function/direction-specific densities  $f_i$ ; (b) D2Q9 model.

11 These lattices are usually classified in the literature using the  $D\alpha Q\beta$ -notation, where  $\alpha$   
 12 denotes the space dimensionality and  $\beta$  is the number of discrete velocities (but also including  
 13 the possibility of having particles at rest) within the momentum discretisation. The most  
 14 common lattices are the  $D2Q9$  and the  $D3Q19$ -models, see He et al. (1997). The present study  
 15 focuses on two-dimensional problems, hence the  $D2Q9$  momentum discretisation is adopted.

16 LBM discretises the Boltzmann equation in space to a finite number of possible particle  
 spatial positions, microscopic momenta, and time. Particle positions are confined to the  
 lattice nodes. The fluid particles at each node are allowed to move to their eight intermediate  
 neighbours with eight different velocities  $e_i (i = 1, \dots, 8)$ . A particle can remain at its own node,

which is equivalent to moving with zero velocity  $e_o$ . The particle mass is uniform, hence these microscopic velocities and momentum are always effectively equivalent (Han et al., 2007b). Referring to the numbering system shown in figure 5.1, the nine discrete velocity vectors are defined as

$$\begin{cases} e_0 = (0, 0); \\ e_1 = C(1, 0); e_2 = C(0, 1); e_3 = C(-1, 0); e_4 = C(0, -1); \\ e_5 = C(1, 1); e_6 = C(-1, 1); e_7 = C(-1, -1); e_8 = C(1, -1), \end{cases} \quad (5.1)$$

where  $C$  is the lattice speed that is defined as  $C = h/\Delta t$ , and  $\Delta t$  is the discrete time step. The primary variables in LB formulation are called the *fluid density distribution functions*,  $f_i$ , each representing the probable amount of fluid particles moving with the velocity  $e_i$  along the direction  $i$  at each node. The macroscopic variables are defined as functions of the particle distribution function (see figure 5.1)

$$\begin{cases} \rho = \sum_{i=0}^{\beta-1} f_i & \text{(macroscopic fluid density)} \\ \text{and} \\ \overrightarrow{u} = \frac{1}{\rho} \sum_{i=0}^{\beta-1} f_i \overrightarrow{e}_i & \text{(macroscopic velocity)}, \end{cases} \quad (5.2)$$

where  $i \in [0, \beta - 1]$  is an index spanning the discretised momentum space. There are nine fluid density distribution functions,  $f_i (i = 0, \dots, 8)$ , associated with each node in the *D2Q9* model. The evolution of the density distribution function at each time step for every lattice point is governed by

$$f_i(\mathbf{x} + \mathbf{e}_i \Delta t, t + \Delta t) = f_i(\mathbf{x}, t) - \frac{1}{\tau} [f_i(\mathbf{x}, t) - f_i^{eq}(\mathbf{x}, t)] \quad (i = 0, \dots, 8), \quad (5.3)$$

where for any grid node  $\mathbf{x}$ ,  $\mathbf{x} + \mathbf{e}_i \Delta t$  is its nearest node along the direction  $i$ .  $\tau$  is a non-dimensional relaxation time parameter, which is related to the fluid viscosity; and  $f_i^{eq}$  is termed as the equilibrium distribution function that is defined as

$$\begin{cases} f_0^{eq} = w_0 \rho (1 - \frac{3}{2C^2} \mathbf{v} \cdot \mathbf{v}) \\ \text{and} \\ f_i^{eq} = w_i \rho (1 + \frac{3}{C^2} \mathbf{e}_i \cdot \mathbf{v} \frac{9}{2C^2} (\mathbf{e}_i \cdot \mathbf{v})^2 - \frac{3}{2C^2} \mathbf{v} \cdot \mathbf{v}) \quad (i = 0, \dots, 8), \end{cases} \quad (5.4)$$

## 5.1 Fluid simulation using lattice Boltzmann method

## 147

in which,  $w_i$  represents the fixed weighting values:

$$w_0 = \frac{4}{9}, \quad w_{1,2,3,4} = \frac{1}{9}, \quad \text{and} \quad w_{5,6,7,8} = \frac{1}{36}. \quad (5.5)$$

The right-hand side of [eq. 5.3](#) is often denoted as  $f_i(\mathbf{x}, t_+)$  and termed the post collision distribution. LBM ensures conservation of total mass and total momentum of the fluid particles

- <sup>1</sup> at each lattice node (see [eq. 5.3](#)). The lattice Boltzmann modelling consists of two phases:
- <sup>2</sup> *collision* and *streaming*. The collision phase computed in the right-hand side of [eq. 5.3](#) involves
- <sup>3</sup> only those variables that are associated with each node  $\mathbf{x}$ , and therefore is a local operation.
- <sup>4</sup> The streaming phase then explicitly propagates the updated distribution functions at each node
- <sup>5</sup> to its neighbours  $\mathbf{x} + e_i \Delta t$ , where no computations are required and only data exchange between
- <sup>6</sup> neighbouring nodes are necessary. These features, together with the explicit time-stepping
- <sup>7</sup> nature and the use of a regular grid, make LB computationally efficient, simple to implement
- <sup>8</sup> and easy to parallelise ([Han et al., 2007b](#)).

- <sup>9</sup> The streaming step involves the translation of the distribution functions to their neighbouring
- <sup>10</sup> sites according to the respective discrete velocity directions, as illustrated in figure [5.2](#) in
- <sup>11</sup> the *D2Q9* model. The collision step, (see figure [5.3](#)) consists of re-distribution the local
- <sup>12</sup> discretised Maxwellian equilibrium functions in such a way that local mass and momentum are
- <sup>13</sup> invariants. In incompressible flows, the energy conservation is equivalent to the momentum
- <sup>14</sup> conservation ([He et al., 1997](#)).

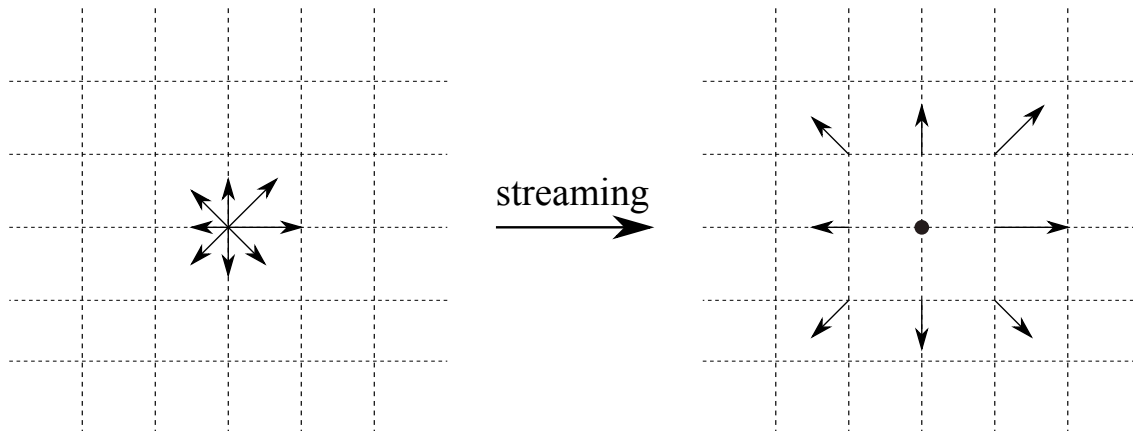


Figure 5.2 Illustration of the streaming process on a *D2Q9* lattice. The magnitude of the distribution functions remains unchanged, but they move to a neighbouring node according to their direction.

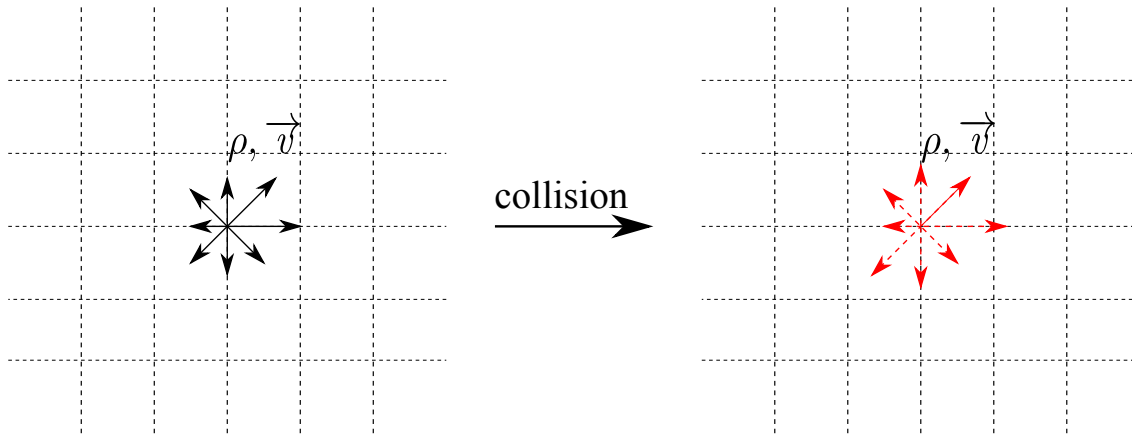


Figure 5.3 Illustration of the collision process on a  $D2Q9$  lattice. The local density  $\rho$  and velocity  $v$  are conserved, but the distribution functions change according to the relaxation to local Maxwellian rule.

<sub>15</sub> The standard macroscopic fluid variables, such as density  $\rho$  and velocity  $v$ , can be recovered  
<sub>16</sub> from the distribution functions as

$$\rho = \sum_{i=0}^8 f_i, \quad \text{and} \quad \rho \mathbf{v} = \sum_{i=0}^8 f_i e_i. \quad (5.6)$$

<sub>18</sub> The fluid pressure field ‘ $p$ ’ is determined by the equation of state

$$p = C_s^2 \rho, \quad (5.7)$$

<sub>20</sub> where  $C_s$  is termed the fluid speed of sound and is related to the lattice speed  $C$  as

$$C_s = C/\sqrt{3}. \quad (5.8)$$

<sub>22</sub> The kinematic viscosity of the fluid  $\nu$  is implicitly determined by the model parameters  $h$ ,  
<sub>23</sub>  $\Delta t$  and  $\tau$  as

$$\nu = \frac{1}{3}(\tau - \frac{1}{2}) \frac{h^2}{\Delta t} = \frac{1}{3}(\tau - \frac{1}{2}) Ch, \quad (5.9)$$

<sub>25</sub> which indicates that these three parameters are related to each other and have to be appropriately  
<sub>26</sub> selected to represent the correct fluid viscosity. An additional constraint to the parameter  
 selection is the lattice speed  $C$ , which must be sufficiently large in comparison to the maximum  
 fluid velocity  $v_{max}$ , to ensure accuracy of the solution. The ‘computational’ Mach number,  $M_a$ ,  
 defined as

$$M_a = \frac{v_{max}}{C}. \quad (5.10)$$

Theoretically, for an accurate solution, the Mach number is required to be  $<< 1$ . In practice,  $M_a$  should be at least smaller than 0.1 (He et al., 1997). From a computational point of view, it is more convenient to choose  $h$  and  $\tau$  as two independent parameters and  $\Delta t$  as the derived parameter

$$\Delta t = (\tau - \frac{1}{2}) \frac{h^2}{3v}. \quad (5.11)$$

It can be observed that  $\tau$  has to be greater than 0.5 (He et al., 1997). Since there is no a priori estimation available to determine appropriate values of  $h$  and  $\tau$ , for a given fluid flow problem and a known fluid viscosity  $v$ , a *trial and error* approach is employed to ensure a smaller *Mach Number*. This is similar to choosing an appropriate Finite Element mesh size, without using automatic adaptive mesh techniques.

### 5.1.2 Lattice Boltzmann - Multi-Relaxation Time (LBM-MRT)

The Lattice Boltzmann Bhatnagar-Gross-Krook (LGBK) method is capable of simulating various hydrodynamics, such as multiphase flows and suspensions in fluid (Succi, 2001; Succi et al., 1989). However, LBM suffers from numerical instability when the dimensionless relaxation time  $\tau$  is close to 0.5. The Lattice Boltzmann Method – Multi-Relaxation Time (LBM-MRT) overcomes the deficiencies of linearised single relaxation LBM-BGK approach, such as the fixed Prandtl number ( $Pr=v/\kappa$ ), where the thermal conductivity ‘ $\kappa$ ’ is unity (Liu et al., 2003). LBM-MRT offers better numerical stability and has more degrees of freedom. In LBM-MRT the advection is mapped onto the momentum space by a linear transformation and the flux is finished within the velocity space (Du et al., 2006).

The lattice Boltzmann equation with multiple relaxation time approximation is written as

$$f_\alpha(\mathbf{x} + \mathbf{e}_i \Delta_t, t + \Delta_t) - f_\alpha(\mathbf{x}, t) = -\mathbf{S}_{\alpha i}(f_i(\mathbf{x}, t) - f_i^{eq}(\mathbf{x}, t)), \quad (5.12)$$

where  $\mathbf{S}$  is the collision matrix. The nine eigen values of  $\mathbf{S}$  are all between 0 and 2 so as to maintain linear stability and separation of scales. This ensures that the relaxation times of non-conserved quantities are much faster than the hydrodynamic time scales. The LGBK model is a special case in which the nine relaxation times are all equal and the collision matrix  $\mathbf{S} = \frac{1}{\tau} \mathbf{I}$ , where  $\mathbf{I}$  is the identity matrix. The evolutionary progress involves two steps, advection and flux:

$$f_\alpha^+(\mathbf{x}, t) - f_\alpha(\mathbf{x}, t) = -\mathbf{S}_{\alpha i}(f_i(\mathbf{x}, t) - f_i^{eq}(\mathbf{x}, t)) \quad (5.13)$$

$$f_\alpha(\mathbf{x} + e_\alpha \Delta_t, t + \Delta_t) = f_\alpha^+(\mathbf{x}, t). \quad (5.14)$$

<sup>17</sup> The advection (eq. 5.13) can be mapped to the momentum space by multiplying with a  
<sup>18</sup> transformation matrix  $\mathbf{M}$ . The evolutionary equation of LBM–MRT is written as

$$\mathbf{f}(\mathbf{x} + \mathbf{e}_i \Delta_t, t + \Delta_t) - \mathbf{f}(\mathbf{x}, t) = -\mathbf{M}^{-1} \hat{\mathbf{S}}(\hat{\mathbf{f}}(\mathbf{x}, t) - \hat{\mathbf{f}}^{eq}(\mathbf{x}, t)), \quad (5.15)$$

<sup>20</sup> where  $\mathbf{M}$  is the transformation matrix mapping a vector  $\mathbf{f}$  in the discrete velocity space  $\mathbb{V} = \mathbb{R}^b$   
<sup>21</sup> to a vector  $\hat{\mathbf{f}}$  in the moment space  $\mathbb{V} = \mathbb{R}^b$ .

$$\hat{\mathbf{f}} = \mathbf{M}\mathbf{f}, \quad (5.16)$$

$$\mathbf{f}(\mathbf{x}, t) = [f_0(\mathbf{x}, t), f_1(\mathbf{x}, t), \dots, f_8(\mathbf{x}, t)]^T. \quad (5.17)$$

<sup>25</sup> The collision matrix  $\hat{\mathbf{S}} = \mathbf{M}\mathbf{S}\mathbf{M}^{-1}$  in moment space is a diagonal matrix:

$$\hat{\mathbf{S}} = \text{diag}[s_1, s_2, s_3, \dots, s_9].$$

<sup>27</sup> The transformation matrix  $\mathbf{M}$  can be constructed via Gram-Schmidt orthogonalisation procedure.

<sup>28</sup> The general form of the transformation matrix  $\mathbf{M}$  can be written as

$$\mathbf{M} = [|p\rangle, |e\rangle, |e^2\rangle, |u_x\rangle, |q_x\rangle, |u_y\rangle, |q_y\rangle, |p_{xx}\rangle, |p_{xy}\rangle]^T, \quad (5.18)$$

<sup>30</sup> whose elements are,

$$|p\rangle = |e_\alpha|^0 \quad (5.19a) \quad 1$$

$$|e\rangle_\alpha = Qe_\alpha^2 - b_2 \quad (5.19b) \quad 2$$

$$|e^2\rangle_\alpha = a_1(Qe_\alpha^4 - b_6) + a_2(Qe_\alpha^4 - b_6) \quad (5.19c) \quad 3$$

$$|u_x\rangle_\alpha = e_{\alpha,x} \quad (5.19d) \quad 4$$

$$|q_x\rangle_\alpha = (b_1 e_\alpha^2 - b_3) e_{\alpha,x} \quad (5.19e) \quad 5$$

$$|u_y\rangle_\alpha = e_{\alpha,y} \quad (5.19f) \quad 6$$

$$|q_y\rangle_\alpha = (b_1 e_\alpha^2 - b_3) e_{\alpha,y} \quad (5.19g) \quad 7$$

$$|p_{xx}\rangle_\alpha = d e_{\alpha,x}^2 - e_\alpha^2 \quad (5.19h) \quad 8$$

$$|p_{xy}\rangle_\alpha = e_{\alpha,x} e_{\alpha,y}, \quad (5.19i) \quad 9$$

where  $d = 2$  and  $Q = 9$ ,  $b_1 = \sum_{\alpha=1}^Q e_{\alpha,x}^2$ ,  $b_2 = \sum_{\alpha=1}^Q e_\alpha^2$ ,  $b_3 = \sum_{\alpha=1}^Q e_\alpha^2 e_{\alpha,x}^4$ ,  $a_1 = ||e^2||^2$ , and  
 $a_2 = \sum_{\alpha=0}^{Q-1} (Qc_\alpha^2 - b_2) \times (Qc_\alpha^4 - b_6)$ . 11  
12

## 5.1 Fluid simulation using lattice Boltzmann method

151

Explicitly, the transformation matrix can be written as

13

$$1 \quad \mathbf{M} = \begin{bmatrix} 1 & 1 & 1 & 1 & 1 & 1 & 1 & 1 & 1 \\ -4 & -1 & -1 & -1 & -1 & 2 & 2 & 2 & 2 \\ 4 & -2 & -2 & -2 & -2 & 1 & 1 & 1 & 1 \\ 0 & 1 & 0 & -1 & 0 & 1 & -1 & -1 & 1 \\ 0 & -2 & 0 & 2 & 0 & 1 & -1 & -1 & 1 \\ 0 & 0 & 1 & 0 & -1 & 1 & 1 & -1 & -1 \\ 0 & 0 & -2 & 0 & 2 & 1 & 1 & -1 & -1 \\ 0 & 1 & -1 & 1 & -1 & 0 & 0 & 0 & 0 \\ 0 & 0 & 0 & 0 & 0 & 1 & 1 & 1 & 1 \end{bmatrix}. \quad (5.20)$$
  
2

3 The corresponding equilibrium distribution functions in moment space  $\widehat{\mathbf{f}}^{eq}$  is given as

$$4 \quad \widehat{\mathbf{f}}^{eq} = [\rho_0, e^{eq}, e^{2eq}, u_x, q_x^{eq}, q_y^{eq}, p_{xx}^{eq}, p_{xy}^{eq}]^T, \quad (5.21)$$

5 where

$$6 \quad e^{eq} = \frac{1}{4}\alpha_2 p + \frac{1}{6}\gamma_2(u_x^2 + y_y^2) \quad (5.22a)$$

$$7 \quad e^{2eq} = \frac{1}{4}\alpha_3 p + \frac{1}{6}\gamma_4(u_x^2 + y_y^2) \quad (5.22b)$$

$$8 \quad q_x^{eq} = \frac{1}{2}c_1 u_x \quad (5.22c)$$

$$9 \quad q_y^{eq} = \frac{1}{2}c_2 u_y \quad (5.22d)$$

$$10 \quad p_{xx}^{eq} = \frac{3}{2}\gamma_1(u_x^2 - u_y^2) \quad (5.22e)$$

$$11 \quad p_{xy}^{eq} = \frac{3}{2}\gamma_3(u_x u_y). \quad (5.22f)$$
  
12

13 To get the correct hydrodynamic equation, the values of the co-efficients are chosen as  $\alpha_2 = 24$ ,  
 14  $\alpha_3 = -36$ ,  $c_1 = c_2 = -2$ ,  $\gamma_1 = \gamma_3 = 2/3$ ,  $\gamma_2 = 18$  and  $\gamma_4 = -18$ . The values of the elements in  
 15 the collision matrix are:  $s_8 = s_9 = \tau$  and  $s_1 = s_4 = s_6 = 1.0$  and the others vary between 1.0  
 16 and 2.0 for linear stability. Through the Chapman-Enskog expansion (Du et al., 2006), the  
 17 incompressible Navier-Stokes equation can be recovered and the viscosity is given as

$$18 \quad \nu = c_s^2 \Delta t (\tau - 0.5). \quad (5.23)$$

<sup>19</sup> **5.1.3 Boundary conditions**

<sup>20</sup> Boundary conditions (BC) form an important part of any numerical technique. In many cases,  
<sup>21</sup> the boundary conditions can strongly influence the accuracy of the algorithm. Velocity and  
<sup>22</sup> pressure are not the primary variables in LBM, hence the standard pressure, velocity, and  
<sup>23</sup> mixed boundary conditions cannot be imposed directly. Alternative conditions in terms of the  
<sup>24</sup> distribution functions are adopted to describe the boundary conditions.

<sup>25</sup> **Periodic boundary condition**

<sup>26</sup> The simplest type of boundary condition is the periodic boundary. In this case, the domain is  
<sup>27</sup> folded along the direction of the periodic boundary pair. For boundary nodes, the neighbouring  
<sup>28</sup> nodes are on the opposite boundary, using the normal referencing of neighbours (see figure 5.1a).  
<sup>1</sup> From the perspective of submarine landslide modelling, the periodic boundary conditions are  
<sup>2</sup> useful for preliminary analysis, as they imply a higher degree of symmetry of the fluid domain.  
<sup>3</sup> Further information on the periodic boundary condition can be found in Aidun et al. (1998).

**No-slip boundary condition**

The most commonly adopted BC in the lattice Boltzmann approach is the no-slip BC, especially  
<sup>5</sup> the simple bounce-back rule, which is quite elegant and surprisingly accurate. The basic idea is  
<sup>6</sup> that the incoming distribution functions at a wall node are reflected back to the original fluid  
<sup>7</sup> nodes, but with the direction rotated by  $\pi$  radians. The bounce-back boundary condition is one  
<sup>8</sup> of the benefits of LBM, as it is trivial to implement and it allows one to effortlessly introduce  
<sup>9</sup> obstacles into the fluid domain. However, the boundary conditions have been proven to be only  
<sup>10</sup> first-order accurate in time and space (Pan et al., 2006). A straightforward improvement is to  
<sup>11</sup> consider the wall-fluid interface to be situated halfway between the wall and the fluid lattice  
<sup>12</sup> nodes (Ziegler, 1993). It involves defining the *solid* nodes as those lying within the stationary  
<sup>13</sup> wall regions, and the *fluid* nodes otherwise. Then, if  $i$  is the direction between a fluid node  $n_1$   
<sup>14</sup> and a solid node  $n_2$ , the bounce-back rule requires that the incoming fluid particle from  $n_1$  to  
<sup>15</sup>  $n_2$  be reflected back along the direction it came from, i.e.,  
<sup>16</sup>

$$f_{-i}(\mathbf{x}, t + \Delta t) = f_i(\mathbf{x}, t_+), \quad (5.24)$$

where  $-i$  denotes the opposite direction of  $i$ . The bounce back rule is illustrated in figure 5.4.  
<sup>18</sup> This simple rule ensures that no tangential velocity exists along the fluid-wall interface, thereby  
<sup>19</sup> a non-slip condition is imposed, and can be extended to any shapes or objects in a fluid flow (Han  
<sup>20</sup> et al., 2007a; Zou and He, 1997). The slip boundary conditions have similar treatment to the  
<sup>21</sup>

## 5.1 Fluid simulation using lattice Boltzmann method

153

non-slip condition, except that the distribution functions are reflected in the boundary instead <sup>22</sup>  
<sub>1</sub> of bounce-back ([Succi, 2001](#)).

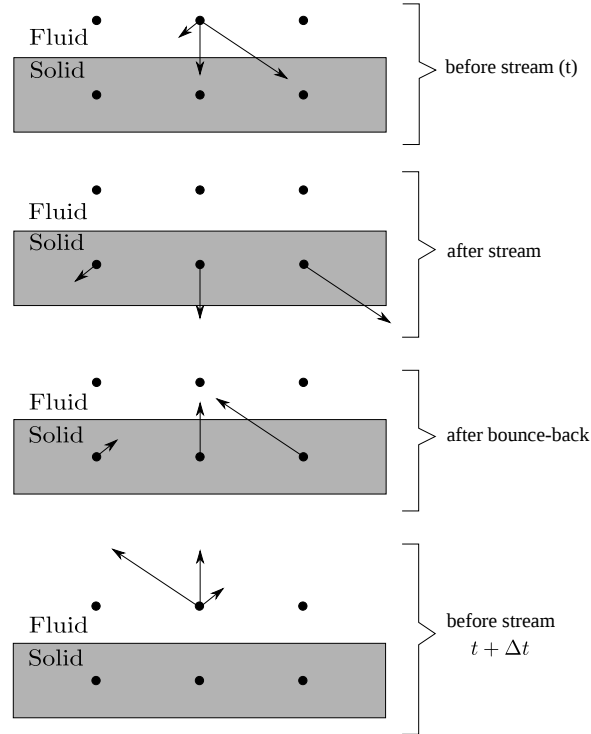


Figure 5.4 Half-way bounce back algorithm for the *D2Q9* model adopted after [Sukop and Thorne \(2006\)](#).

<sub>2</sub> **Pressure and velocity boundary condition**

<sub>3</sub> The pressure (Dirichlet) boundary condition can be imposed in lattice Boltzmann by specifying  
<sub>4</sub> a fluid density at the pressure boundary ([Zou and He, 1997](#)). To impose a pressure boundary  
<sub>5</sub> along the y-direction (for example, consider the left hand side inlet boundary in figure 5.5), a  
<sub>6</sub> density  $\rho = \rho_{in}$  is specified from which the velocity is computed. The vertical component of  
<sub>7</sub> the velocity on the boundary is set as zero,  $u_y = 0$ . After streaming,  $f_2, f_3, f_4, f_6$ , and  $f_7$  are  
<sub>8</sub> known,  $u_x$  and  $f_1, f_5, f_8$  are to be determined from [eq. 5.2](#) as

$$f_1 + f_5 + f_8 = \rho_{in} - (f_0 + f_2 + f_3 + f_4 + f_6 + f_7) \quad (5.25)$$

$$f_1 + f_5 + f_8 = \rho_{in} u_x + (f_3 + f_6 + f_7) \quad (5.26)$$

$$f_5 - f_8 = f_2 - f_4 + f_6 - f_7, \quad (5.27)$$

<sup>13</sup> Consistency of equations (5.25) and (5.26) gives

$$\text{14} \quad u_x = 1 - \frac{[f_0 + f_2 + f_4 + 2 * (f_3 + f_6 + f_7)]}{\rho_{in}}. \quad (5.28)$$

<sup>15</sup> The bounce-back rule for the non-equilibrium part of the particle distribution normal to the  
<sup>16</sup> inlet is used to find  $f_1 - f_1^{eq} = f_3 - f_3^{eq}$ . The values of  $f_5$  and  $f_8$  can be obtained from  $f_1$ :

$$\begin{aligned} \text{17} \quad f_1 &= f_3 + \frac{2}{3}\rho_{in}u_x \\ \text{18} \quad f_5 &= f_7 - \frac{1}{2}(f_2 - f_4) + \frac{1}{6}\rho_{in}u_x \\ f_8 &= f_6 + \frac{1}{2}(f_2 - f_4) + \frac{1}{6}\rho_{in}u_x. \end{aligned} \quad (5.29) \quad \begin{matrix} \frac{1}{2} \\ \frac{1}{2} \end{matrix}$$

The corner node at inlet needs some special treatment. Considering the bottom node at inlet as an example, after streaming,  $f_3, f_4, f_7$  are known;  $\rho$  is defined, and  $u_x = u_y = 0$ . The particle distribution functions  $f_1, f_2, f_5, f_6$ , and  $f_8$  are to be determined. The bounce-back rule for the non-equilibrium part of the particle distribution normal to the inlet and the boundary is used to find

$$f_1 = f_3 + (f_1^{eq} - f_3^{eq}) = f_3 \quad (5.30) \quad \begin{matrix} 3 \\ 4 \\ 5 \\ 6 \\ 7 \end{matrix}$$

$$f_2 = f_4 + (f_1^{eq} - f_3^{eq}) = f_4. \quad (5.31) \quad \begin{matrix} 8 \\ 9 \\ 10 \end{matrix}$$

Using these we can compute

$$f_5 = f_7 \quad (5.32) \quad \begin{matrix} 11 \\ 12 \end{matrix}$$

$$f_6 = f_8 = \frac{1}{2}[\rho_{in} - (f_1 + f_2 + f_3 + f_4 + f_5 + f_6 + f_7 + f_8)]. \quad (5.33) \quad \begin{matrix} 13 \\ 14 \end{matrix}$$

Similar procedure can be applied to the top inlet node and the outlet nodes. Von Neumann boundary conditions constrain the flux at the boundaries. A velocity vector  $u = [u_0 \ v_0]^T$  is specified, from which the density and pressure are computed based on the domain. The velocity boundary condition can be specified in a similar way (Zou and He, 1997). The pressure and velocity boundary conditions contribute additional equation(s) to determine the unknown distribution functions. In the case of velocity boundary, the boundary condition equation is sufficient to determine the unknown distribution functions in the D2Q9 model, however the pressure boundary conditions require additional constitutive laws to determine the unknown distribution functions.

Table 5.1 LBM parameters used in simulating laminar flow through a circular pipe.

Parameter	Value
Density $\rho$	1000 kg m <sup>-3</sup>
Relaxation parameter $\tau$	0.51
Kinematic viscosity	$1 \times 10^{-6}$ m <sup>2</sup> s <sup>-1</sup>
Grid resolution ‘h’	1 <sup>-2</sup> m
Number of steps	50,000
Error in predicting horizontal velocity	0.009 %

## 5.2 Validation of the lattice Boltzmann method

To verify the incompressible LBM model implemented in the above section, numerical simulation of a transient development of steady state Poiseuille flow in a straight channel is performed. At  $t = 0$ , the LBM water particles ( $\rho = 1000\text{kg/m}^3$ ) are simulated to flow through a channel of width ‘H’ (= 0.4 m) and simulation length ‘L’ (2.5H) under constant body force. Periodic boundary conditions are applied at either end of the channel and the pressure gradient is set to zero, which simulates the condition of a continuous flow of fluid in a closed circular pipe. The length ‘L’ has no effect on the simulation as no streamwise variation is detected in the solution. The parameters adopted in LBM simulation are presented in table 5.1. Sufficient time is allowed for the flow to travel beyond the required development length so that the flow is laminar (Durst et al., 2005). The development length  $X_D$  required for a flow to be fully laminar is

$$X_D/H = [(0.619)^{1.6} + (0.0567R_e)^{1.6}]^{1/1.6}, \quad (5.34)$$

where  $R_e$  is the Reynolds number. The velocity profile at steady state is presented in figure 5.5. A maximum horizontal velocity of 0.037863 m s<sup>-1</sup> is observed along the center-line of the channel. The maximum horizontal velocity is compared with the closed-form based on the Haygen-Poiseuille flow equation for no-slip boundary condition (Willis et al., 2008)

$$U_x = \frac{\Delta P}{2\mu L} \left[ \frac{H^2}{4} - y^2 \right], \quad (5.35)$$

where  $v_x$  is the horizontal velocity (m/s);  $\Delta P$  is the pressure gradient,  $\mu$  dynamic viscosity of the fluid. LBM predicts the maximum horizontal velocity within an error of 0.009 %.

In order to further validate the accuracy of the lattice Boltzmann code, the transient development of the Poiseuille’s flow is compared with the CFD simulation performed using ANSYS Fluent. Finite Volume Method is a common CFD technique, which involves solving

the governing partial differential equation (Navier-Stokes) over the discretised control volume. This guarantees the conservation of fluxes over a particular control volume. The finite volume equations yield governing equations of the form

$$\frac{\partial}{\partial t} \iiint Q dV + \iint F dA = 0, \quad (5.36)$$

where  $Q$  is the vector of conserved variables,  $F$  is the vector of fluxes in the Navier-Stokes equation,  $V$  is the volume of control volume element, and  $A$  is the surface area of the control volume element.

A 2D rectangular plane of length 1 m and height 0.04 m is discretised into 400 cells of size  $1^{-2}$  m (see figure 5.6). A constant velocity is applied at the inlet. Water ( $\rho = 998.2 \text{ kg/m}^3$ , viscosity ' $\eta'$  =  $1 \times 10^{-3} \text{ Ns/m}^2$ ) is allowed to flow through the channel and it develops into a fully laminar flow. The least squares approach was adopted to solve the gradient, and a maximum of 100 iteration steps were carried out until the solution converged.

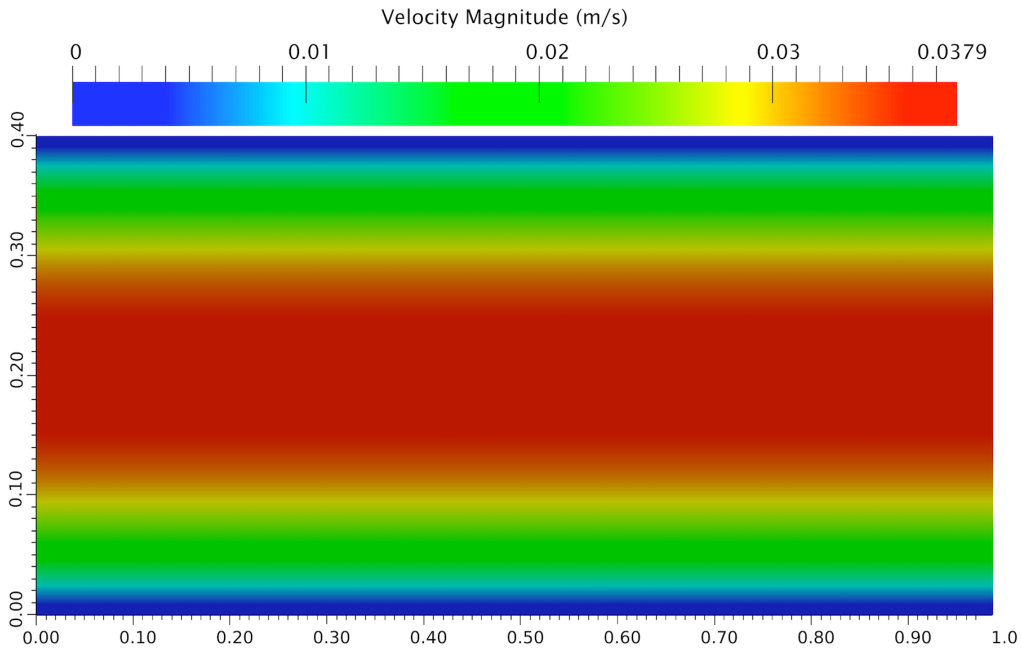


Figure 5.5 Velocity profile: LBM Simulation of a laminar flow through a channel.

The velocity profile obtained from the CFD simulation at cross-section ‘L/4’ is shown in figure 5.7. Figure 5.8 compares the development of computed velocity profiles with the analytical solution. At normalised time  $t = 1$ , the flow approaches steady state. It can be observed that LBM has excellent agreement with CFD and the analytical solution at various stages of flow evolution.

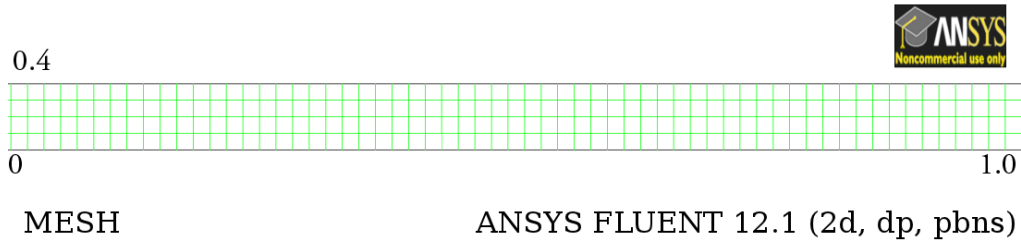


Figure 5.6 Finite Volume mesh used in the CFD analysis of laminar flow through a channel.

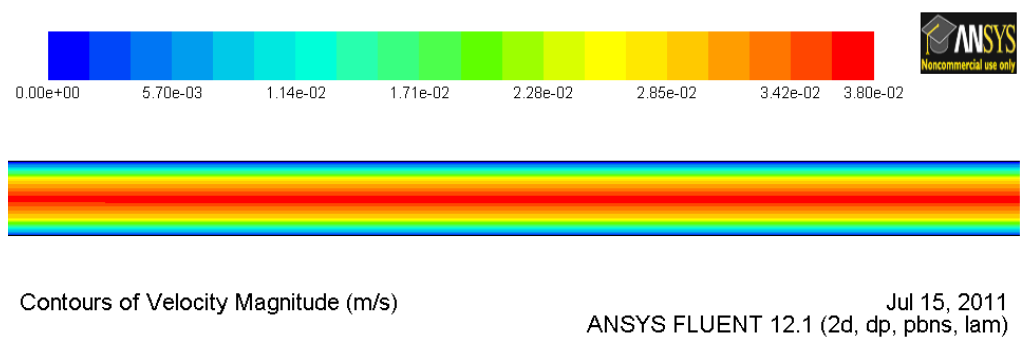


Figure 5.7 Velocity profile: CFD analysis of laminar flow through a channel.

12 In order to study the capability of the lattice Boltzmann technique to simulate fluid–solid  
 13 interaction, LB simulation of a fluid flow around a rectangular obstacle is compared with  
 14 the CFD technique. A solid wall of height ‘H/2’ is placed at length ‘L/4’ in the channel.  
 15 Bounce-back algorithm is employed to model the fluid-wall interaction in LBM. In the CFD  
 16 model, the control volume is discretised into 10,000 cells. A constant velocity is applied in the  
 17 inlet and the horizontal velocity profile is recorded. Both, CFD and LBM simulations were  
 18 performed to study the influence of a solid wall on the fluid flow behaviour.

19 The horizontal velocity profile obtained after 50,000 LBM iterations is presented in fig-  
 20 ure 5.9. LBM is able to capture the velocity shedding around the edges of the wall. The velocity  
 21 profile obtained from the CFD analysis is presented in figure 5.10. The horizontal velocity  
 22 profile at ‘L/4’ at  $t = 1$  is shown in figure 5.11. The maximum horizontal velocity from the  
 23 CFD analysis is 0.3% higher in comparison with the LBM simulation. The discrepancy in  
 24 the horizontal velocity profile (figure 5.11) can be attributed to the relaxation parameter used  
 25 in the LBM, which is obtained by a trial and error procedure. The velocity profile obtained  
 26 from the LBM simulation compares qualitatively with the FE analysis performed by [Zhong and](#)  
 27 [Olson \(1991\)](#). Thus, it can be concluded that the lattice Boltzmann method is a suitable form of  
 28 numerical representation of the Navier-Stokes equation to model fluid – solid interactions.

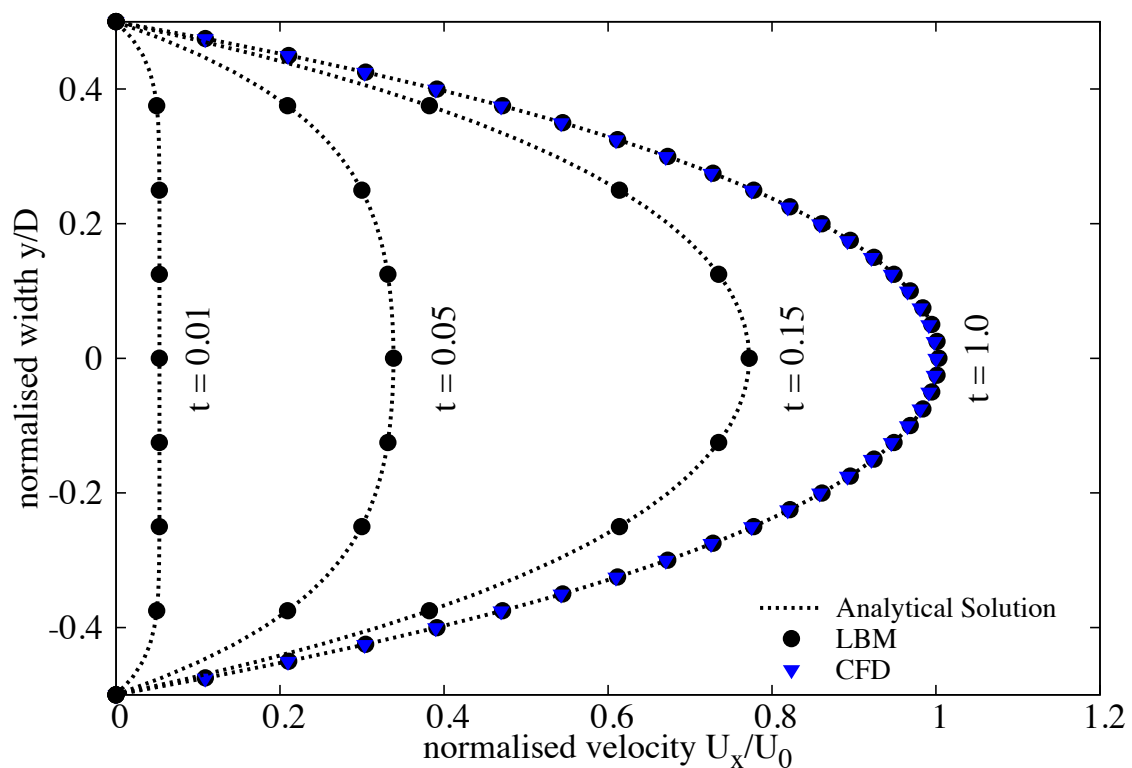


Figure 5.8 Development of the Poiseuille velocity profile in time: comparison between LBM simulation, CFD simulation and the analytical solution. Time is made dimensionless by  $H/U_0$ .

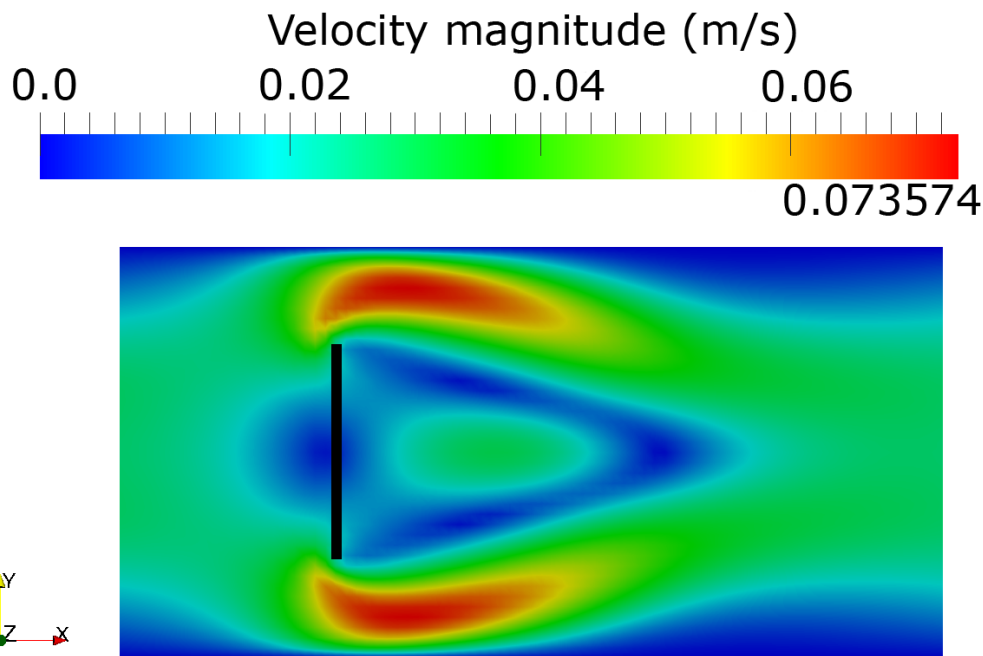


Figure 5.9 LBM simulation of velocity profile for a laminar flow through a pipe with an obstacle at L/4.

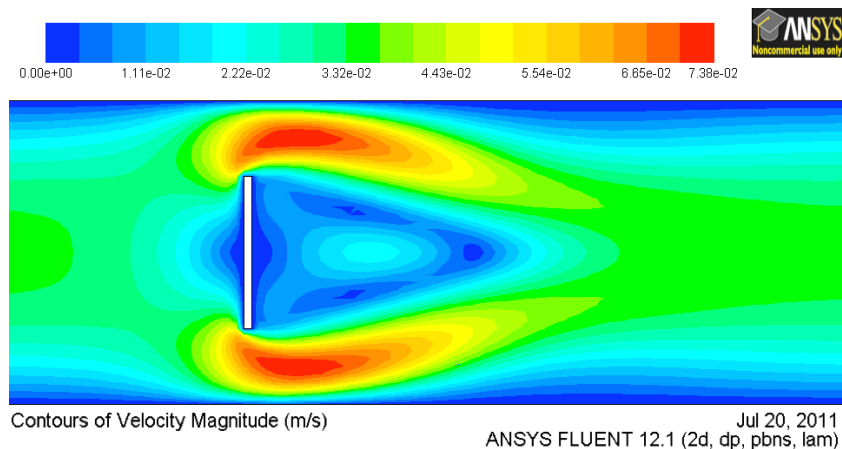


Figure 5.10 CFD simulation of velocity contour for a laminar flow through a pipe with an obstacle at L/4.

## **5.3 Turbulence in lattice Boltzmann method**

- The above formulation of lattice Boltzmann has been successfully applied to many fluid flow problems, however it is restricted to flows with low Reynolds number. Modelling fluids with low viscosity like water and air remains a challenge, necessitating very small values of  $h$ , and/or  $\tau$  very close to 0.5 (He et al., 1997). The standard lattice Boltzmann can deal with laminar

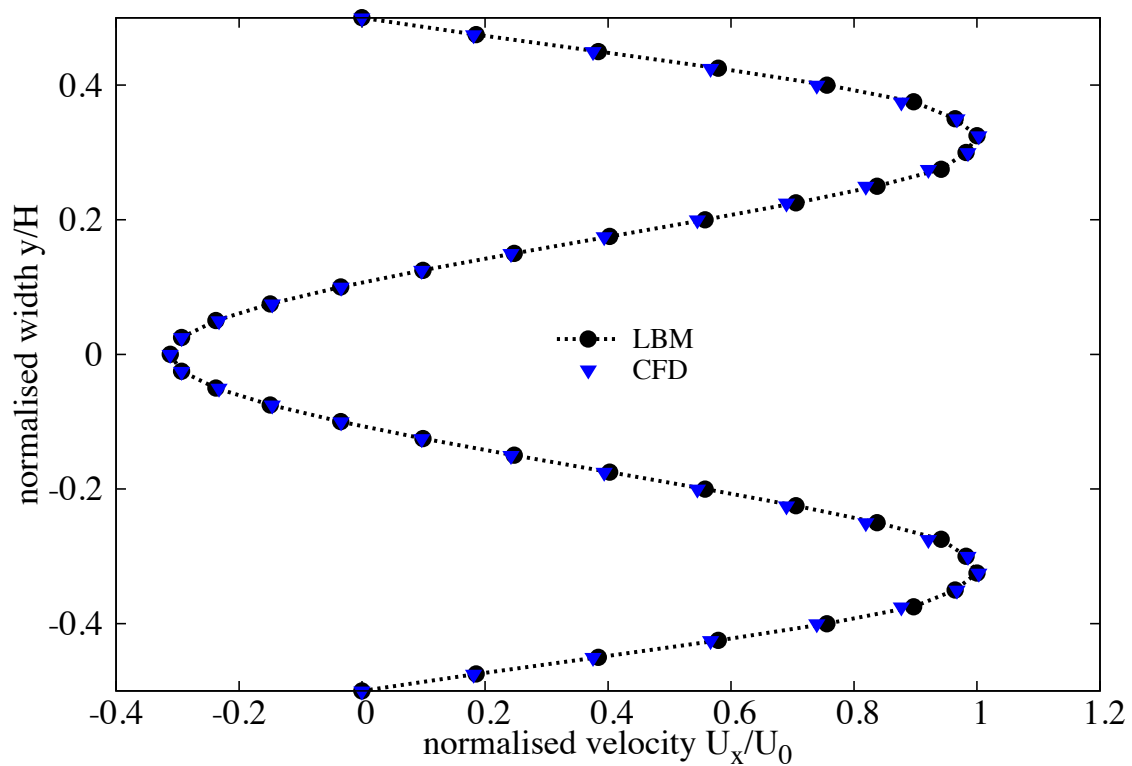


Figure 5.11 LBM and CFD simulation of a flow around an obstacle.

## 5.3 Turbulence in lattice Boltzmann method

161

flows, while practical problems with small kinematic viscosity are often associated with flows having large Reynolds numbers, i.e. flows which are unsteady or turbulent in nature. The turbulent flows are characterised by the occurrence of eddies with multiple scales in space, time and energy.

The large eddy simulation (LES) is the most widely adopted approach to solve turbulent flow problems. It directly solves the large scale eddies, which carry the predominant portion of the energy, and the smaller eddies are modelled using a sub-grid approach. The separation of scales is achieved by filtering of the Navier-Stokes equations, from which the resolved scales are directly obtained. The unresolved scales are modelled by a one-parameter Smagorinski sub-grid methodology, which assumes that the Reynolds stress tensor is dependent only on the local strain rate (Smagorinsky, 1963). It involves parametrising the turbulent energy dissipation in the flows, where the larger eddies extract energy from the mean flow and ultimately transfer some of it to the smaller eddies which, in turn, pass the energy to even smaller eddies, and so on up to the smallest scales. At the smallest scale, the eddies convert the kinetic energy into the internal energy of the fluid. At this scale, the viscous friction dominates the flow (Frisch and Kolmogorov, 1995).

In the Smargonisky model, the turbulent viscosity  $\nu$  is related to the strain rate  $S_{ij}$  and a filtered length scale ‘h’ as follows

$$S_{ij} = \frac{1}{2}(\partial_i u_j + \partial_j u_i) \quad (5.37)$$

$$\nu_t = (S_c h)^2 \bar{S} \quad (5.38)$$

$$\bar{S} = \sqrt{\sum_{i,j} \tilde{S}_{i,j} \tilde{S}_{i,j}}, \quad (5.39)$$

where  $S_c$  is the Smagorinski constant, which is close to 0.03 (Yu et al., 2005). The effect of the unresolved scale motion is taken into account by introducing an effective collision relaxation time scale  $\tau_t$ , so that the total relaxation time  $\tau_*$  is written as

$$\tau_* = \tau + \tau_t, \quad (5.40)$$

where  $\tau$  and  $\tau_t$  are respectively the standard relaxation times corresponding to the true fluid viscosity  $\nu$  and the turbulence viscosity  $\nu_t$ , defined by a sub-grid turbulence model. The new

viscosity  $\nu_*$  corresponding to  $\tau_*$  is defined as

$$\nu_* = \nu + \nu_t = \frac{1}{3}(\tau_* - \frac{1}{2})C^2\Delta t = \frac{1}{3}(\tau + \tau_t - \frac{1}{2})C^2\Delta t \quad (5.41)$$

$$\nu_t = \frac{1}{3}\tau_t C^2\Delta t. \quad (5.42)$$

The Smagorinski model is easy to implement and the lattice Boltzmann formulation remains unchanged, except for the use of a new turbulence-related viscosity  $\tau_*$ . The component  $s_1$  of the collision matrix becomes  $s_1 = \frac{1}{\tau + \tau_t}$ .

The effectiveness of LBM-LES model in simulating unsteady flows is verified by modelling the Kármán vortex street. In fluid dynamics, a Kármán vortex street is a repeating pattern of vortices caused by unsteady separation of fluid flow around circular obstacles. A vortex street will only be observed above a limiting value of Reynolds number of 90. The Reynolds number is computed based on the cylinder diameter ‘D’ and the mean flow velocity  $U$  of the parabolic inflow profile:

$$Re = \frac{UD}{\nu}. \quad (5.43)$$

LBM particles are simulated to flow through a 2D rectangular channel with an aspect ratio ‘L/H’ of 2.5. A cylinder of diameter ‘d’ = 0.27H is placed at H/2. The pressure gradient at the inlet and the outlet is varied to create flows with different mean velocities. Numerical simulations of vortex shedding behind a circular obstacle are carried out for three different fluid flow regimes (Reynolds number of 55, 75, and 112). The fully developed fluid flows for different Reynolds numbers are shown in figure 5.12. It can be observed from figure 5.12 that the von Kármán vortex street can only be observed at high a Reynolds number of 112 ( $Re > 90$ ), which shows the ability of the LBM turbulence model to capture instabilities in fluid flow.

One important quantity taken into account in the present analysis is the Strouhal number  $St$ , a dimensionless number describing oscillating unsteady flow dynamics. The Strouhal number is computed from the cylinder diameter D, the measured frequency of the vortex shedding f, and the maximum velocity  $U_{max}$  at the inflow plane:

$$St = \frac{fD}{U_{max}}. \quad (5.44)$$

The characteristic frequency  $f$  is determined by a spectral analysis (Fast Fourier Transform - FFT) of time series of the fluid pressure. Table 5.2 shows that the Strouhal numbers computed from LBM simulations have a very good agreement with FVM results obtained by Breuer et al. (2000). This shows the ability of LBM-LES in capturing unsteady flow dynamics.

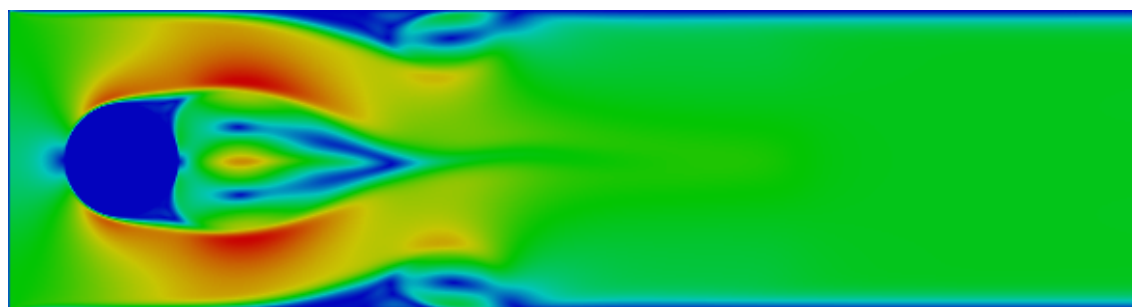
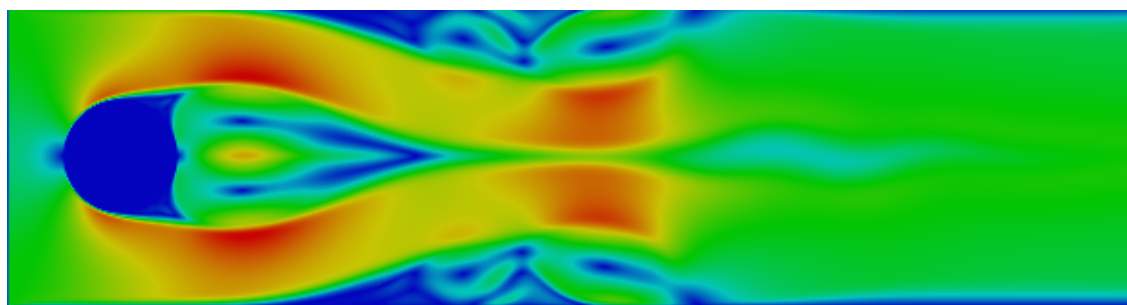
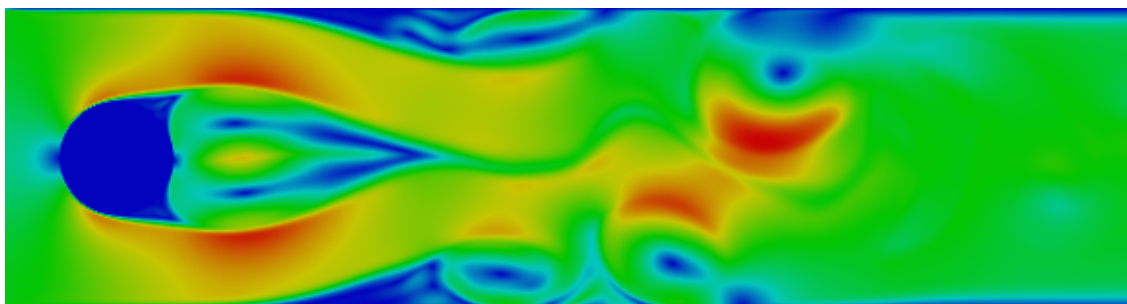
(a)  $\text{Re} = 55$ (b)  $\text{Re} = 75$ (c)  $\text{Re} = 112$ 

Figure 5.12 Kármán vortex street

Table 5.2 Computed Strouhal number for fluid flows with different Reynolds number

Reynolds number	Strouhal number	
	LBM	FVM
55	0.117	0.117
75	0.128	0.129
112	0.141	0.141

\* FVM results are from [Breuer et al. \(2000\)](#)

## 11 5.4 Coupled LBM and DEM for fluid-grain interactions

12 Modelling fluid–grain interactions in submarine landslides requires the ability to simulate  
 13 the interactions at the dynamic fluid – solid boundaries. In principle, the conventional FE  
 14 and FVM based approaches for solving the Navier-Stokes equations with moving boundaries  
 15 and/or structural interaction ([Bathe and Zhang, 2004](#)) can be applied to particle fluid interaction  
 16 problems. The common feature of these approaches is to model the interaction between the  
 17 fluid and the solid to a high degree of accuracy. However, the main computational challenge  
 18 is the need to continuously generate new geometrically adapted meshes to circumvent severe  
 19 mesh distortion, which is computationally very intensive ([Han et al., 2007b](#)).

20 The lattice Boltzmann approach has the advantage of accommodating large particle sizes  
 21 and the interaction between the fluid and the moving grains can be modelled through relatively  
 22 simple fluid - grain interface treatments. Further, employing DEM to account for the grain/grain  
 23 interaction naturally leads to a combined LB – DEM solution procedure. The Eulerian nature  
 24 of the lattice Boltzmann formulation, together with the common explicit time step scheme of  
 25 both LBM and DEM makes this coupling strategy an efficient numerical procedure for the  
 26 simulation of fluid – grain systems.

27 LBM – DEM technique is a powerful predictive tool for gaining insights into many fun-  
 28 damental physical phenomena in fluid-solid systems. Such a coupled methodology was first  
 29 proposed by ([Cook et al., 2004](#)) for simulating fluid-grain systems dominated by fluid-grain  
 1 and grain-grain interactions. To capture the actual physical behaviour of the fluid-grain system,  
 2 it is essential to model the boundary condition between the fluid and the grain as a non-slip  
 3 boundary condition, i.e. the fluid velocity near the grain should be similar to the velocity of  
 4 the grain boundary. The soil grains in the fluid domain are represented by lattice nodes. The  
 5 discrete nature of the lattice will result in stepwise representations of the surfaces, which are  
 6 otherwise circular, this is neither accurate nor smooth, unless sufficiently small lattice spacing  
 7 is adopted.

## 8 Modified bounce back rule

9 To accommodate the movement of solid particles in the commonly adopted bounce-back rule  
 10 (see section 5.1.3), Ladd (1994) modified the ‘no-slip’ rule for a given boundary link  $i$  to be

$$11 \quad f_i(\mathbf{x}, t + \Delta t) = f_i(\mathbf{x}, t_+) - \alpha_i e_i \cdot v_b \quad (\alpha_i = 6w_i \rho / C_s^2), \quad (5.45)$$

12 where  $f_i(\mathbf{x}, t_+)$  is the post collision distribution at the fluid or solid boundary node  $\mathbf{x}$ , and  $v_b$  is  
 13 the velocity at the nominal boundary point at the middle of the boundary link  $i$

$$14 \quad \mathbf{v}_b = \mathbf{v}_c + \boldsymbol{\omega} \times (\mathbf{x} + e_i \Delta t / 2 - \mathbf{x}_c), \quad (5.46)$$

15 in which  $v_c$  and  $\boldsymbol{\omega}$  are the translational and angular velocities at the mass centre of the solid  
 16 particle, respectively.  $\mathbf{x}_c$  and  $\mathbf{x} + e_i \Delta t / 2$  are the coordinates of the centre and the nominal  
 17 boundary point, respectively. The impact force on the soil grain from the link is defined as

$$18 \quad \mathbf{F}_i = 2[f_i(\mathbf{x}, t_+) - \alpha_i e_i \cdot v_b] / \Delta t. \quad (5.47)$$

19 The corresponding torque  $\mathbf{T}_i$ , produced by the force with respect to the centre of the particle is  
 20 computed as

$$21 \quad \mathbf{T}_i = \mathbf{r}_c \times \mathbf{F}_i (\mathbf{r}_c = \mathbf{x} + \mathbf{e}_i \Delta t / 2 - \mathbf{x}_c). \quad (5.48)$$

22 Then the total hydrodynamic force and torque exerted on the particle can be calculated by  
 23 summing up the forces and torques from all the related boundary links:

$$24 \quad \begin{aligned} \mathbf{F} &= \sum_i \mathbf{F}_i \\ \mathbf{T} &= \sum_i \mathbf{T}_i. \end{aligned} \quad (5.49)$$

25 Ladd and Verberg (2001) described a methodology that minimises the oscillations resulting  
 26 from soil grains crossing lattices at a very high speed. The methodology involves combining  
 27 several extensions for the fluid simulation like the treatment of moving curved boundaries with  
 28 the scheme of Yu et al. (2003) and a fluid/grain force interaction method with the momentum  
 exchange method of Ladd and Verberg (2001). The simulation of the moving curved grain  
 surfaces results in the intersection of links between two nodes at arbitrary distances (Iglberger  
 et al., 2008). These distance values are referred to as delta values:  
 1  
 2  
 3

$$26 \quad \delta = \frac{\text{Distance between fluid node and soil surface}}{\text{Distance between fluid node and soil node}} \in [0, 1]. \quad (5.50) \quad 4$$

For each pair of a fluid and grain node, a delta value has to be calculated. Delta values of zero are not possible as the nodes on the surface are considered as solid nodes. The algorithm for computation of the  $\delta$  value is presented in Iglberger et al. (2008). Figure 5.13 shows the three possible situations for delta values between 0 and 1. The fluid particles in LBM are always considered to be moving at the rate of one lattice per time step ( $\delta\mathbf{x}/\delta t$ ), for delta values smaller than 0.5. For  $\delta$  values larger than 0.5, the fluid particles would come to rest at an intermediate node  $\mathbf{x}_i$ . In order to calculate the reflected distribution function in node  $\mathbf{x}_f$ , an interpolation scheme has to be applied. The linear interpolation scheme of Yu et al. (2003) is used in the present study, which uses a single equation, irrespective of the value of  $\delta$  being smaller or larger than 0.5, to the reflected distribution function that is computed as

$$\begin{aligned} f_{\bar{\alpha}}(\mathbf{x}_f, t + \delta t) = & \frac{1}{1 + \delta} \cdot [(1 - \delta) \cdot f_{\alpha}(\mathbf{x}_f, t + \delta t) + \delta \cdot f_{\alpha}(\mathbf{x}_b, t + \delta t) \\ & + \delta \cdot f_{\bar{\alpha}}(\mathbf{x}_{f2}, t + \delta t) - 2w_a \rho_w \frac{3}{c^2} e_a \cdot \mathbf{u}_w], \end{aligned} \quad (5.51)$$

where  $w_{\alpha}$  is the weighting factor,  $\rho_w$  is the fluid density in node  $\mathbf{x}_f$ , and  $\mathbf{u}_w$  is the velocity at the bounce-back wall. In order to couple the fluid-grain interaction, the LBM approach is extended by adopting a force integration scheme, to calculate the fluid force acting on the grain surface, and the momentum exchanged method described earlier. The physical force acting on grain agglomerates is calculated as the sum over all fluid/grain node pairs, resulting in

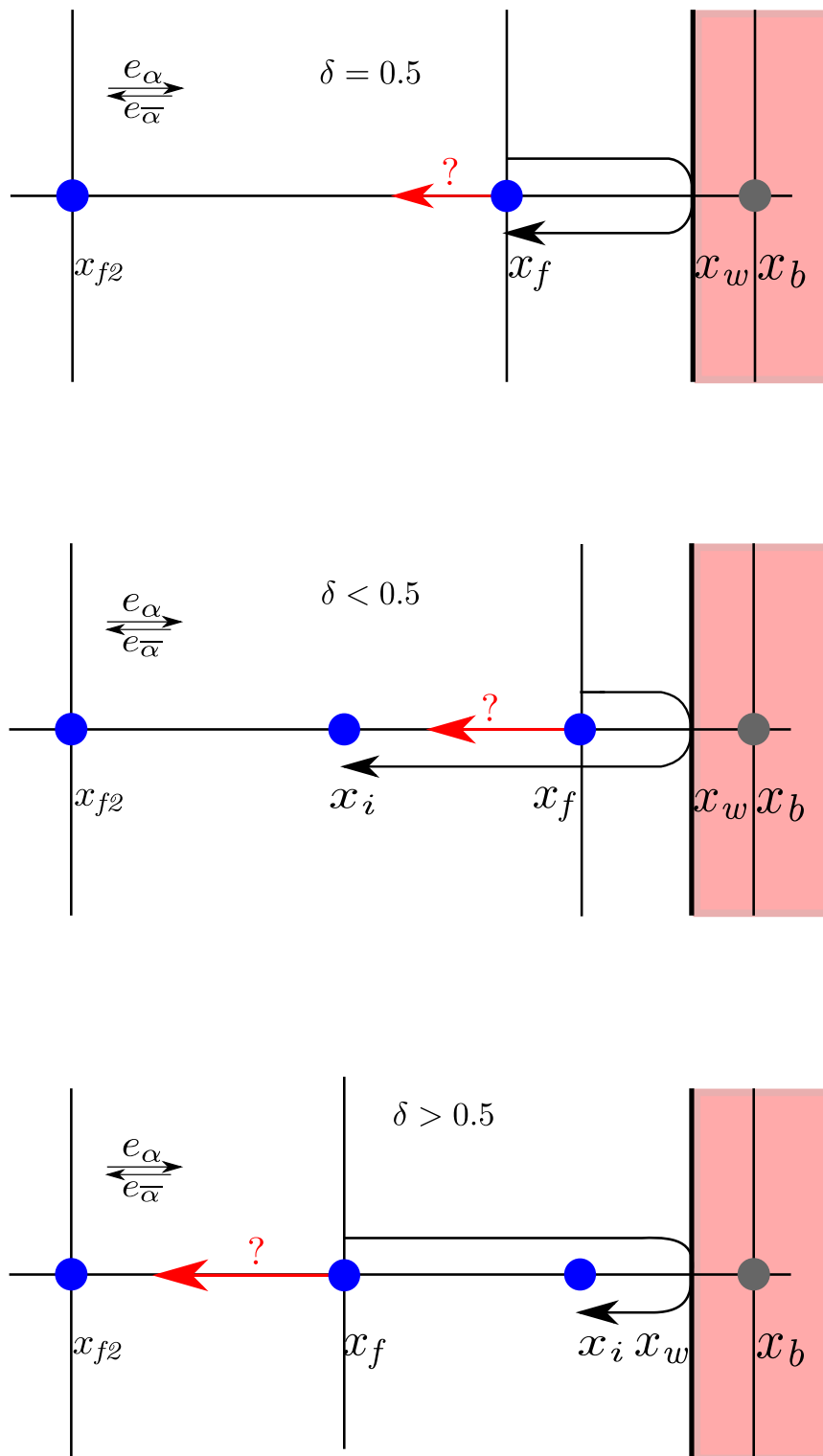
$$F = \sum_{\mathbf{x}_b} \sum_{\alpha=1}^{19} \mathbf{e}_{\alpha} [f_{\alpha}(\mathbf{x}_b, t) + f_{\bar{\alpha}}(\mathbf{x}_f, t)] \delta\mathbf{x}/\delta t. \quad (5.52)$$

After the force calculations, the coupled rigid body physics can be simulated in order to move the grains / grain-agglomerates according to the applied forces. The total hydrodynamic forces and torque exerted on a grain can be computed as (Cook et al., 2004; Noble and Torczynski, 1998)

$$\mathbf{F}_f = Ch \left[ \sum_n \left( \beta_n \sum_i f_i^m e_i \right) \right] \quad (5.53)$$

$$\mathbf{T}_f = Ch \left[ \sum_n (\mathbf{x}_n - \mathbf{x}_c) \times \left( \beta_n \sum_i f_i^m e_i \right) \right]. \quad (5.54)$$

The summation is over all lattice nodes covered by the soil grain, and  $\mathbf{x}_n$  represents the coordinate of the lattice node  $n$ .

Figure 5.13 Bounce back boundaries for different values of  $\delta$

When grains are not in direct contact among themselves, but are driven by the fluid flow and body force, i.e. gravity, their motion can be determined by Newton's equation of motion

$$m\mathbf{a} = \mathbf{F}_f + m\mathbf{g} \quad (5.55)$$

$$J\ddot{\theta} = \mathbf{T}_f, \quad (5.56)$$

where  $m$  and  $J$  are respectively the mass and the moment of inertia of a grain,  $\ddot{\theta}$  is the angular acceleration,  $\mathbf{g}$  is the gravitational acceleration,  $\mathbf{F}_f$  and  $\mathbf{T}_f$  are respectively the hydrodynamic forces and torque. The equation can be solved numerically by an explicit numerical integration, such as the central difference scheme.

The interaction between the soil grains, and the soil grains with the walls are modelled using the DEM technique. To solve the coupled DEM–LBM formulation, the hydrodynamic force exerted on soil grains and the static buoyancy force are considered by reducing the gravitational acceleration to  $(1 - \rho/\rho_s)\mathbf{g}$ , where  $\rho_s$  is the density of the grains. When taking into account all forces acting on an element, the dynamic equations of DEM can be expressed as

$$m\mathbf{a} + c\mathbf{v} = \mathbf{F}_c + \mathbf{F}_f + m\mathbf{g}, \quad (5.57)$$

where  $\mathbf{F}_c$  denotes the total contact forces from other elements and/or the walls, and  $c$  is a damping coefficient. The term  $c\mathbf{v}$  represents a viscous force that accounts for the effect of all possible dissipation forces in the system including energy lost during the collision between grains. Considering a linear contact model

$$\mathbf{F}_c = k_n\delta, \quad (5.58)$$

where  $k_n$  is the normal stiffness and  $\delta$  is the overlap, the critical time step associated with the explicit integration is determined as (He et al., 1997)

$$\Delta t_{cr} = 2(\sqrt{1 + \xi^2} - \xi)/\omega, \quad (5.59)$$

where  $\omega = \sqrt{k_n/m}$  is the local contact natural frequency and  $\xi = c/2m\omega$  is the critical damping ratio. The actual time step used for the integration of the Discrete Element equations is

$$\Delta t_D = \lambda \Delta t_{cr}. \quad (5.60)$$

The time step factor  $\lambda$  is chosen to be around 0.1 to ensure both stability and accuracy (He et al., 1997).

When combining the Discrete Element modelling of the grain interactions with the LB formulation, an issue arises. There are now two time steps:  $\Delta t$  for the fluid flow and  $\Delta t_D$  for the particles. Since  $\Delta t_D$  is normally smaller than  $\Delta t$ ,  $\Delta t_D$  is slightly reduced to a new value  $\Delta t_s$  so that  $\Delta t$  and  $\Delta t_s$  have an integer ratio  $n_s$

$$\Delta t_s = \frac{\Delta t}{n_s} \quad (n_s = [\Delta t / \Delta t_D] + 1). \quad (5.61)$$

This results in a sub-cycling time integration for the Discrete Element part. At every step of the fluid computation,  $n_s$  sub-steps of integration are performed for the Discrete Element Method (5.57) using the time step  $\Delta t_s$ . The hydrodynamic force  $\mathbf{F}_f$  is unchanged during the sub-cycling.

#### 5.4.1 Draft, kiss and tumbling: Sedimentation of two grains

In multiphase flows, fundamental mechanisms of fluid – grain and grain – grain interactions are very important for accurately predicting the flow behaviours. The sedimentation of two circular grains in a viscous fluid serves as the simplest problem to study these two types of interactions, and many experimental and numerical studies have been carried out to investigate this behaviour (Komiwas et al., 2005; Wang et al., 2014). Fortes (1987) observed experimentally that in the sedimentation of two grains under gravity in a Newtonian fluid, the two grains would undergo the draft, kiss and tumbling (DKT) phenomenon.

The *draft*: grain 2 is first placed within the hydrodynamic drag above grain 1. As the hydrodynamic drag of grain 1 is a depression zone, grain 2 is attracted inside. The *kiss*: grain 2 increases its vertical velocity until it touches grain 1. The horizontal velocity of grain 1 increases and its vertical velocity decreases below that of grain 2. *Tumbling*: grain 2 having the same horizontal velocity and higher vertical velocity than grain 1, overtakes grain 1.

LBM-DEM simulation of two grains under gravity in a viscous Newtonian fluid reproduces the draft, kiss and tumble effect (see figure 5.14). They are in agreement with the experimental description of the DKT effect. For better understanding of the DKT effect, the time history of three distances between the grains (normalised to the diameter of the grain D) are tracked i.e., the difference in the transverse coordinates  $\delta_x/D$  and longitudinal coordinates  $\delta_y/D$  of the two grain centres, and the gap between the two surfaces  $\delta = \sqrt{\delta_x^2 + \delta_y^2} - 1$  (see figure 5.15c).

As shown in figure 5.14, grain 1 trails grain 2. As grain 2 approaches the depression zone, corresponding to negative fluid pressure behind grain 1, the velocity of the trailing grain increases as the grains approach closer, this is in agreement with the experimental description of the draft. Grain 2 increases its vertical velocity more than grain 1 until it touches grain 1. The kiss happens at a normalised time  $(t / \sqrt{(D/g)}) = 25$ . At this stage, the gap  $\delta$  between the

13 grains is zero, but the actual gap is about one lattice spacing for the LBM collision model. After  
14 this time, the vertical velocity of grain 1 decreases and its horizontal velocity increases as the  
15 grains tumble. At this stage, the grains still remain in contact, i.e., the gap remains unchanged  
16  $\delta = 0$ . Subsequently, the two grains separate and move away from each other. Figure 5.15b  
17 shows that the terminal velocities of the two grains are in good agreement with the terminal  
18 velocity of a single grain found by an independent simulation and calculated using the empirical  
19 Schiller and Nauman formula (Komiwas et al., 2005).

20 **5.5 GP-GPU Implementation**

21 Graphics Processing Unit (GPU) is a massively multi-threaded architecture that is widely  
22 used for graphical and now non-graphical computations. Today's GPUs are general purpose  
23 processors with support for an accessible programming interface. The main advantage of GPUs  
24 is their ability to perform significantly more floating point operations (FLOPs) per unit time  
25 than a CPU. General Purpose computations on GPUs (GPGPUs) often achieve speedups of  
26 orders of magnitude in comparison with optimised CPU implementations.

27 A GPU consists of several *Streaming Multiprocessors* (SMs). Each SM contains 32 CUDA  
28 processors. Each CUDA processor has a fully pipelined integer arithmetic logic unit (ALU)  
29 and a floating point unit (FPU). The FPU complies with the IEEE 754-2008 industry standard  
30 for floating-point arithmetic, capable of double precision computations. The SM schedules  
31 work in groups of 32 threads called warps. Each SM features two warp schedulers and two  
32 instruction dispatch units, allowing two warps to be issued and executed concurrently. Each  
33 thread has access to both L1 and L2 caches, which improves the performance for programs  
34 with random memory access.

The occupancy rate of the SPs, i.e. the ratio between the number of threads run and the  
maximum number of executable threads, is an important aspect to take into consideration for  
the optimisation of a CUDA kernel. Even though a block may only be run on a single SM, it is  
possible to execute several blocks concurrently on the same SM. Hence, tuning the execution  
grid layout allows one to increase the occupancy rate. Nevertheless, reaching the maximum  
occupancy is usually not possible, as the threads executed in parallel on one SM have to share  
the available registers (Obrecht and Kuznik, 2011).

Many-core processors are promising platforms for intrinsically parallel algorithms such as  
the lattice Boltzmann method. Since the global memory for GPU devices shows high latency  
and LBM is data intensive, the memory access pattern is an important issue for achieving good  
performances. Whenever possible, global memory loads and stores should be coalescent and  
aligned, but the propagation phase in LBM can lead to frequent misaligned memory accesses.

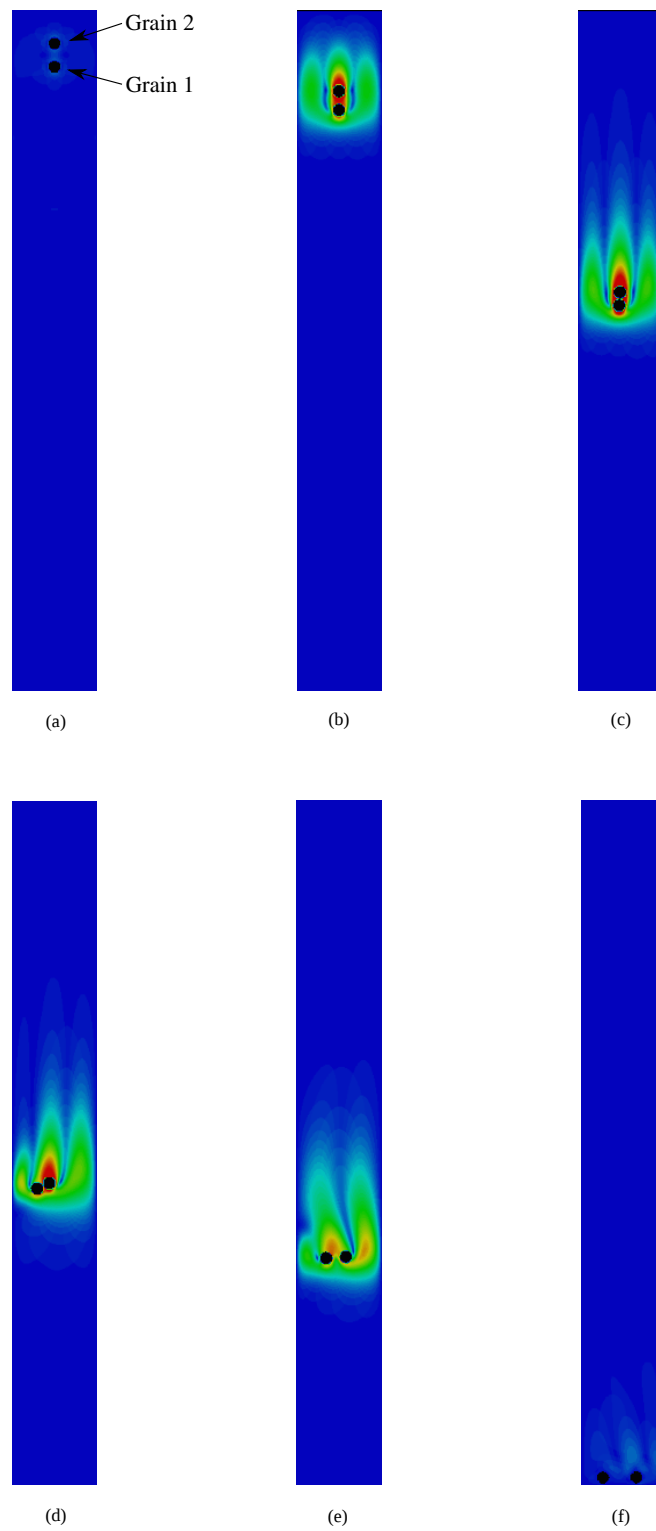


Figure 5.14 Time series of draft, kiss and tumble of two grains during sedimentation in a viscous fluid.

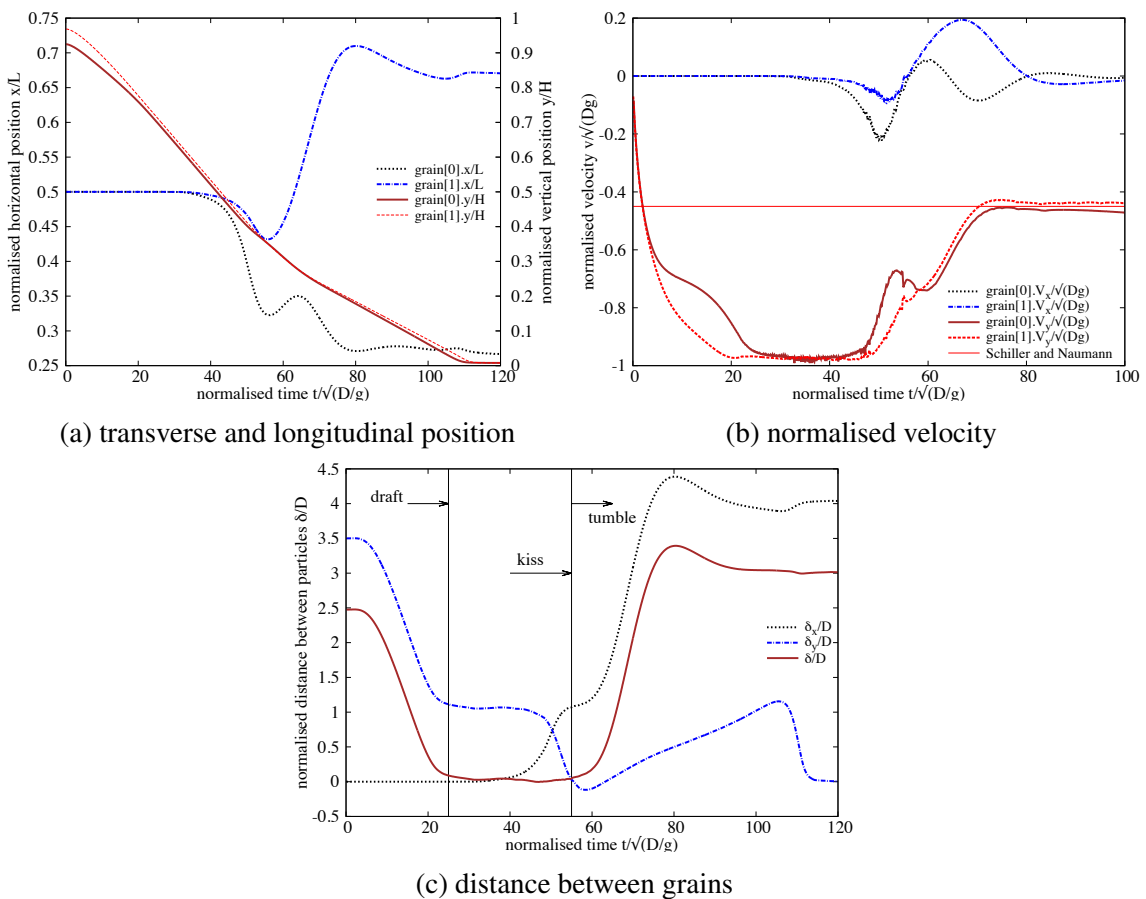


Figure 5.15 Time history of two circular grains during sedimentation.

Also, the data transfer between the host and the device is very expensive. In the present study,  
the LBM implementation follows carefully chosen data transfer schemes in global memory.

There are three ways to accelerate GPGPU applications: (a) Using ‘drop-in’ libraries,  
(b) using directives by exposing parallelism, and (c) using dedicated GPGPU programming  
languages. OpenACC (Open Accelerators) is an open GPU directives programming standard  
for parallel computing on heterogeneous CPU/GPU systems. Unlike conventional GPU pro-  
gramming languages, such as CUDA, OpenACC uses directives to specify parallel regions in  
the code and performance tuning works on exposing parallelism. OpenACC targets a host-  
directed execution model where the sequential code runs on a conventional processor and  
computationally intensive parallel pieces of code (kernels) run on an accelerator such as a GPU  
(see figure 5.16).

The original GPGPU LBM – DEM code was implemented in C using OpenACC API v1.0,  
which was released in November 2011. The current implementation in C++ uses OpenACC API  
v2.0a ([OpenACC-Members, 2013](#)) and has two compute constructs, the kernels construct and  
the parallel construct. LBM – DEM implementation predominantly uses the OpenACC gang and  
vector parallelism. The LBM – DEM code runs sequential and computationally less intensive  
functions on the CPU, OpenMP multi-threading is used when possible. Computationally  
intensive functions are converted to a target accelerator specific GPU parallel code. Schematics  
of a heterogeneous CPU/GPU system is shown in figure 5.16.

OpenACC offers kernel and parallel constructs to parallelise algorithms on CUDA kernels.  
The loop nests in a kernel construct are converted by the compiler into parallel kernels that  
run efficiently on a GPU. There are three steps to this process. The first is to identify the  
loops that can be executed in parallel. The second is to map that abstract loop parallelism  
onto a concrete hardware parallelism. In OpenACC terms, gang parallelism maps to grid-level  
parallelism (equivalent to a CUDA blockIdx), and vector parallelism maps to thread-level  
parallelism (equivalent to a CUDA threadIdx). The compiler normally maps a single loop  
across multiple levels of parallelism using strip-mining. Finally, in step three the compiler  
generates and optimizes the actual code to implement the selected parallelism mapping.

An OpenACC parallel construct creates a number of parallel threads that immediately begin  
executing the body of the parallel construct redundantly. When a thread reaches a work-sharing  
loop, that thread will execute some subset of the loop iterations, depending on the scheduling  
policy as specified by the program or at the runtime. The code generation and optimization  
for a parallel construct is essentially the same as for the kernel construct. A key difference  
is that unlike a kernel construct, the entire parallel construct becomes a single target parallel  
operation, aka a single CUDA kernel. Both constructs allow for automatic vectorization within  
the loops ([Wolfe, 2012](#)).

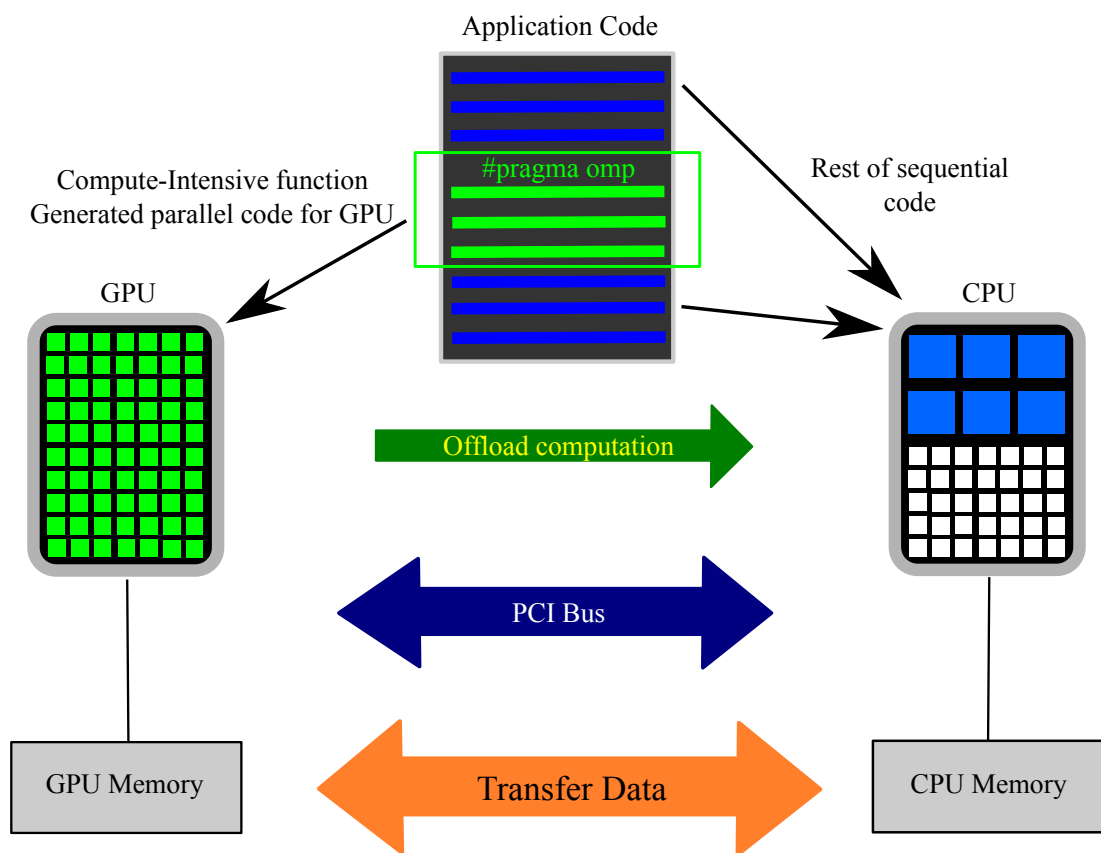


Figure 5.16 Schematics of a heterogeneous CPU/GPU system.

13 An excerpt from the LBM-DEM code showing the OpenACC GPU implementation of  
 14 the hydrodynamic force computation is presented in Listing 5.1. The kernels loop construct  
 15 tells the compiler to map the body of the following loop into an accelerator kernel. The GPU  
 16 implementation uses a two-dimensional grid splitting the iterations across both the vector and  
 17 gang modes. The kernel is mapped to a vector mode mapped (aligned with CUDA threadidx% $x$ )  
 18 with a vector length (thread block size) of 128. The kernel is also mapped to gang parallelism,  
 19 aligned to CUDA blockidx% $x$ , to avoid partition camping by mapping the stride-1 loop to  
 20 the  $x$  dimension. The compiler strip-mines the loop into chunks of 256 iterations, mapping  
 21 the 256 iterations of a chunk in vector mode across the threads of a CUDA thread block,  
 22 and maps the  $n/256$  chunks in gang mode across the thread blocks of the CUDA grid. The  
 23 consecutive iterations ( $i$  and  $i+1$ ), which refer to contiguous array elements ( $f_{hf}[i]$  and  $f_{hf}[i+1]$ ),  
 24 are mapped to adjacent CUDA threads in the same thread block, to optimize for coalesced  
 memory accesses.

Listing 5.1 OpenACC GPU implementation of the hydrodynamic force computation.

```

1 //OpenACC Kernels copy data between the host and the device
2 #pragma acc kernels
3 copyout(fhf1 [0: nbgrains ], f hf2 [0: nbgrains ], f hf3 [0: nbgrains ])
4 copyin(obst [0:][0:], g [0: nbgrains ], ey [0:], f [0:][0:][0:], ex [0:])
5 //Create individual threads for each DEM grain
6 #pragma acc parallel for
7 for ( i=0; i<nbgrains ;i++) {
8   // Reset hydrodynamic forces to zero at the start of time step
9   f hf1 [ i]=f hf2 [ i]=f hf3 [ i ]=0. ;
10  // Iterate through all lattice nodes
11  for ( y=0; y<ly;y++) {
12    for ( x=0; x<lx;x++) {
13      if (obst [x ][y]==i) {
14        // generate code to execute the iterations in parallel with
15        // no synchronization
16        #pragma acc for independent
17        for ( iLB=1; iLB<Q; iLB++) {
18          next_x=x+ex[iLB];
19          next_y=y+ey[iLB];
20          if (iLB<=half) halfq=half ;
21          else halfq= -half;
```

```

12      if (obst[next_x][next_y]!=i) {
13          fnx=(f[x][y][iLB+halfq]+f[next_x][next_y][iLB])*ex[iLB+halfq];
14          fny=(f[x][y][iLB+halfq]+f[next_x][next_y][iLB])*ey[iLB+halfq];
15          fhf1[i]=fhf1[i]+fnx;
16          fhf2[i]=fhf2[i]+fny;
17          fhf3[i]=fhf3[i]-fnx*(y-(g[i].x2-wall_bottom_y)/dx)
18              +fny*(x-(g[i].x1-wall_left_x)/dx);
19      }
20  }
21  }
22  }
23  }
24  }
25  }
26  }
27  }
28  }
29  }
30  }
31  }
32  }
33  }
34  }

```

Memory transaction optimisation is more important than computation optimisation. Registers do not give rise to any specific problem apart from their limited amount. Global memory, being the only one accessible by both the CPU and the GPU, is the critical path as it suffers from high latency. However, this latency is mostly hidden by the scheduler which stalls inactive warps until data are available. For data intensive LBM, this aspect is generally the limiting factor ([Obrecht and Kuznik, 2011](#)). To optimise the global memory transactions, the memory access is coalesced and aligned, as explained above. The memory transactions between the host and the target through a PCI bus are kept to a minimum.

A two-dimensional fluid – grain system, which consists of 7.2 million LBM nodes and 2500 DEM grains is used to demonstrate the ability of the GPGPU LBM – DEM code. The wall time required to compute 100 iterations of the given LBM – DEM problem is compared for executions running on a single CPU thread, multi-threaded CPU (using OpenMP) and the GPGPU implementations (see table 5.3). The speed-up of parallel implementations are measured against the single CPU thread execution time. OpenMP parallelised multi-threaded CPU execution running on 12 cores achieved a speed-up of 13.5x in comparison to a serial implementation. GPGPU implementation using OpenACC delivered an impressive 126x speed-up in comparison to a single thread CPU execution and about 10 times quicker than a CPU parallel code. In other words, a simulation that would have ordinarily taken 126 days to compute, could now be finished in a day using a GPU.

Scalability is an important criterion when developing high-performance computing codes. Scalability in GPUs is measured in terms of SM utilisation. It is important to distribute sufficient work to all SMs such that on every cycle the warp scheduler has at least one warp eligible to issue instructions. In general, sufficient warps on each SM should be available to

Table 5.3 GPU vs CPU parallelisation

Execution	Computational Time (s)	Speedup
CPU 1 OpenMP thread	2016	–
CPU 2 OpenMP threads	1035	1.5 x
CPU 4 OpenMP threads	660	3.0 x
CPU 12 OpenMP threads	150	13.5 x
GPU OpenACC	16	126.0 x

# Wall time for 100 iteration for 7.2 Million LBM nodes and 2500 DEM grains.

\* CPU OpenMP threads - 6 core Intel Xeon @ 3.3GHz

† GPU threads - GeForce GTX 580 - 512 CUDA cores

31 hide instruction and memory latency and to provide a variety of instruction types to fill the  
 32 execution pipeline. Figure 5.17 shows the scalability of GP-GPU implementation as the LBM  
 domain size is increased from 500,000 to 9 million nodes. With increase in LBM nodes the  
 computation time increases linearly with a slope of about 2, which shows that the LBM-DEM  
 implementation algorithm scales with the domain size.

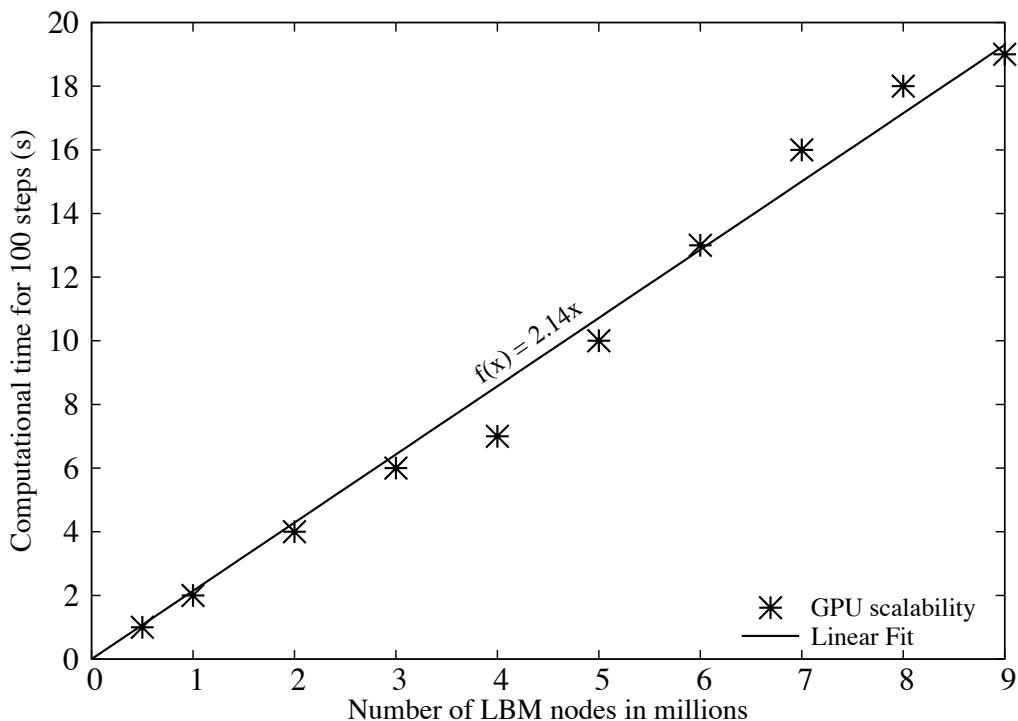


Figure 5.17 GPU scalability with increase in LBM nodes

A two-dimensional coupled LBM-DEM technique is developed to understand the local rheology of granular flows in fluid. The coupled LBM-DEM technique offers the possibility to

capture the intricate microscale effects such as the hydrodynamic instabilities. The Smagorinsky turbulence model is implement in LBM to capture the unsteady flow dynamics in underwater granular avalanches. The GPGPU implementation of the coupled LBM – DEM technique offers the capability to model large scale fluid – grain systems, which are otherwise impossible to model using conventional computation techniques. Efficient data transfer mechanisms that achieves coalesced global memory ensures that the GPGPU implementation scales linearly with the domain size.

6  
7  
8  
9  
10  
11  
12

# Chapter 6

13

## Underwater granular flows

14

### 6.1 Introduction

15

Avalanches, landslides, and debris flows are geophysical hazards, which involve rapid mass movement of granular solids, water, and air as a single phase system. Globally, landslides cause billions of pounds in damage, and thousands of deaths and injuries each year. Hence, it is important to understand the triggering mechanism and the flow evolution. The momentum transfer between the discrete and continuous phases significantly affects the dynamics of the flow as a whole (Topin et al., 2012). Although certain macroscopic models are able to capture simple mechanical behaviours (Peker and Helvacı, 2007), the complex physical mechanisms occurring at the grain scale, such as hydrodynamic instabilities, formation of clusters, collapse, and transport, (Topin et al., 2011) have largely been ignored. In particular, when the solid phase

1 reaches a high volume fraction, the strong heterogeneity arising from the contact forces between  
2 the grains, and the hydrodynamic forces, are difficult to integrate into the homogenization  
3 process involving global averages.

4 In order to describe the mechanism of immersed granular flows, it is important to consider  
5 both the dynamics of the solid phase and the role of the ambient fluid (Denlinger and Iverson,  
6 2001). The dynamics of the solid phase alone is insufficient to describe the mechanism of  
7 granular flow in a fluid. It is important to consider the effect of hydrodynamic forces that  
8 reduce the weight of the solids inducing a transition from dense-compacted to dense-suspended  
9 flows, and the drag interactions which counteract the movement of the solids (Meruane et al.,  
10 2010). Transient regimes characterized by change in the solid fraction, dilation at the onset of  
11 flow and development of excess pore pressure, result in altering the balance between the stress  
12 carried by the fluid and that carried by the grains, thereby changing the overall behaviour of the  
13 flow.

The presence of a fluid phase in a granular medium has profound effects on its mechanical behaviour. In dry granular media the rheology is governed by grain inertia and static stresses sustained by the contact network depending on the shear-rate and confining pressure, respectively (Midi, 2004). As the fluid inertia and viscosity come into play, complications arise as a result of contradictory effects. On one hand, the fluid may delay the onset of granular flow or prevent the dispersion of the grains by developing negative pore pressures (Pailha et al., 2008; Topin et al., 2011). On the other hand, the fluid lubricates the contacts between grains, enhancing in this way the granular flow, and it has a retarding effect at the same time by inducing drag forces on the grains. The objective of the present study is to understand the differences in the mechanism of flow initiation and kinematics between dry and submerged granular flow. In the present study, 2D Lattice-Boltzmann and Discrete Element Method is used to model the fluid-soil interactions in underwater granular flows.

## 6.2 Granular collapse in fluid

The collapse of a granular column, which mimics the collapse of a cliff, has been extensively studied in the case of dry granular material, when the interstitial fluid plays no role (see section 4.2). The problem of the granular collapse in a liquid, which is of importance for submarine landslides, has to our knowledge attracted less attention (Rondon et al., 2011). Thompson and Hupper (2007) observed that the presence of liquid dramatically changes the way a granular column collapses compared to the dry case. The destabilization of a granular pile strongly depends on the initial volume fraction of the packing. For dense packings the granular flow is localized at the free surface of the pile, whereas for loose packings the destabilization occurs in the bulk of the material and has a parabolic profile (Bonnet et al., 2010; Iverson, 2000; Topin et al., 2011). In the present study, the collapse of a granular column in fluid is studied using 2D LBM - DEM and the flow kinematics is compared with dry granular collapse. The role of permeability and initial volume fraction on the run-out behaviour is also investigated.

### 6.2.1 LBM-DEM Coupling

Lattice Boltzmann approach can accommodate large grain sizes and the interaction between the fluid and the moving grains can be modelled through a relatively simple fluid – grain interface treatment. Further, employing the Discrete Element Method (DEM) to account for the grain – grain interaction naturally leads to a combined LB – DEM procedure (Mansouri et al., 2009).

In this study, a 2D poly-disperse system ( $d_{max}/d_{min} = 1.8$ ) of circular discs in fluid is used to simulate the behaviour of granular collapse in fluid (see Figure 6.1). A cumulative  $\beta$  distribution

is adopted to generate grains with  $d_{max}$  and  $d_{min}$  as 1.25 mm and 2.2 mm, respectively. The soil column is modelled using  $\approx 2000$  discs of density  $2650 \text{ kg m}^{-3}$  and a contact friction angle of  $26^\circ$ . A linear-elastic contact model is used in DEM simulations. The collapse of the column was simulated inside a fluid with a density of  $1000 \text{ kg m}^{-3}$  and a kinematic viscosity of  $1 \times 10^{-6} \text{ m}^2 \text{ s}^{-1}$ . The gravity angle  $\theta$  is set to zero to simulate collapse onto a horizontal surface. The choice of a 2D geometry has the advantage of cheaper computational effort than a 3D case, making it feasible to simulate very large systems.

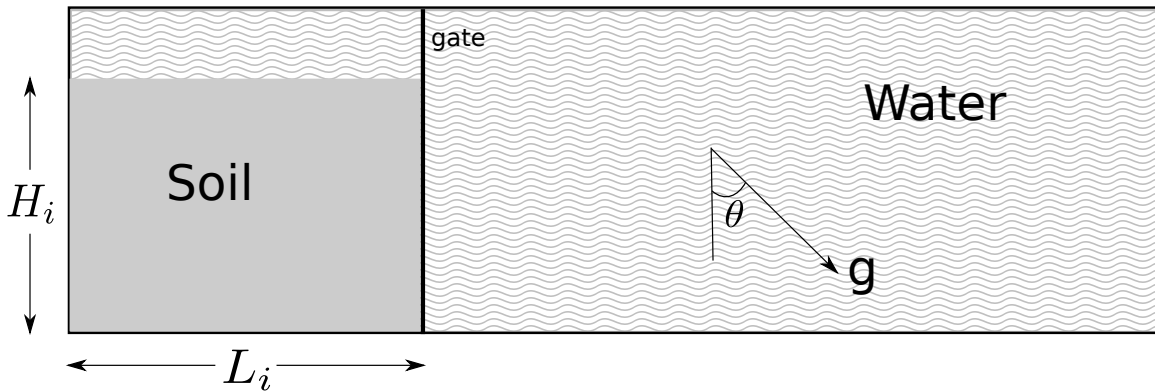


Figure 6.1 Underwater granular collapse set-up.

The Eulerian nature of the LBM formulation, together with the common explicit time step scheme of both LBM and DEM makes this coupling strategy an efficient numerical procedure for the simulation of grain – fluid systems. The critical time step for DEM is computed based on the local contact natural frequency and damping ratio. A sub-cycling time integration is adopted in DEM (see section 5.4). A fluid flow (LBM) time step,  $\Delta t = 2.0E^{-5}\text{s}$  is determined based on the viscosity and relaxation parameter  $\tau = 0.506$ . An integer ratio  $n_s$ , between the fluid flow time step  $\Delta t$  and DEM time step  $\Delta t_D$  is determined as 15, i.e., every LBM iteration involves a sub-cycle of 15 DEM iterations.

In order to capture realistic physical behaviour of the fluid – grain system, it is essential to model the boundary condition between the fluid and the grain as a non-slip boundary condition, i.e. the fluid near the grain should have similar velocity as the grain boundary. The solid grains inside the fluid are represented by lattice nodes. The discrete nature of lattice, results in a stepwise representation of the surfaces (see figure 6.2), which are circular, hence sufficiently small lattice spacing  $h$  is required. The smallest DEM grain in the system controls the length of the lattice spacing. In the present study, a very fine discretisation of  $d_{min}/h = 10$  is adopted, i.e., the smallest grain with a diameter  $d_{min}$  in the system is discretised into 100 lattice nodes ( $10h \times 10h$ ). This represents a very accurate representation of the interaction between the solid and the fluid nodes.

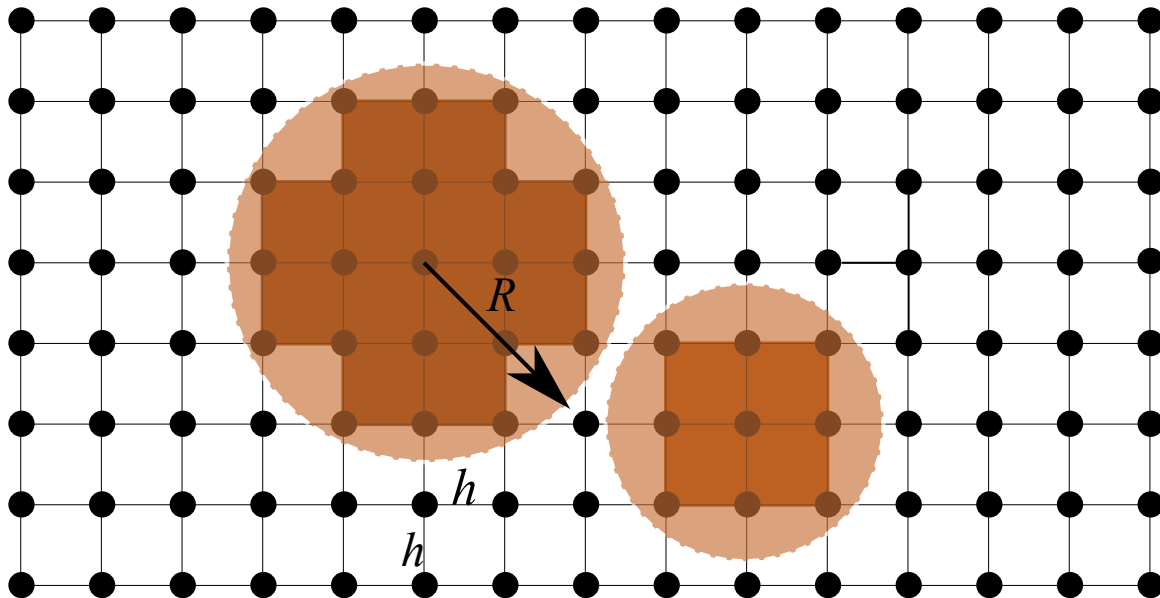


Figure 6.2 Discretisation of solid grains in LBM grid. Shows the step-wise representation of circular disks in the lattice.

### 6.2.2 Permeability

30

In DEM, the grain – grain interaction is described based on the contact interactions. In a 3D granular assembly, the pore spaces between grains are interconnected, whereas in a 2-D assembly, the grains are in contact with each other and this results in a non-interconnected pore-fluid space. Which means that the pore-fluid enclosed between the grains cannot flow to neighbouring pore-space. This results in an unnatural no flow condition in a 2-D case (see figure 6.3). In order to overcome this difficulty, a reduction in radius is assumed only during LBM computations (fluid and fluid – solid interaction). The reduced radius of the soil grain, i.e., the *hydrodynamic radius* ‘ $r$ ’, allows for interconnected pore space through which the pore-fluid can flow similar to 3D behaviour. The reduction in radius is assumed only during LBM computations, hence this technique has no effect on the grain – grain interactions computed using DEM.

1  
2  
3  
4  
5  
6  
7  
8  
9  
10  
11

Realistically, the hydrodynamic radius can be varied from  $r = 0.7R$  to  $0.95R$ , where ‘ $R$ ’ is the grain radius. Different permeability can be obtained, for any given initial packing, by varying the hydrodynamic radius of the grains, without changing the actual granular packing. Hence, the hydrodynamic radius represents the permeability of the granular assembly. In another sense, the hydrodynamic radius can be assumed to represent the irregularities on the granular surface. Reducing the hydrodynamic radius represents wider channel and more flow between the grains.

12  
13  
14  
15  
16  
17  
18

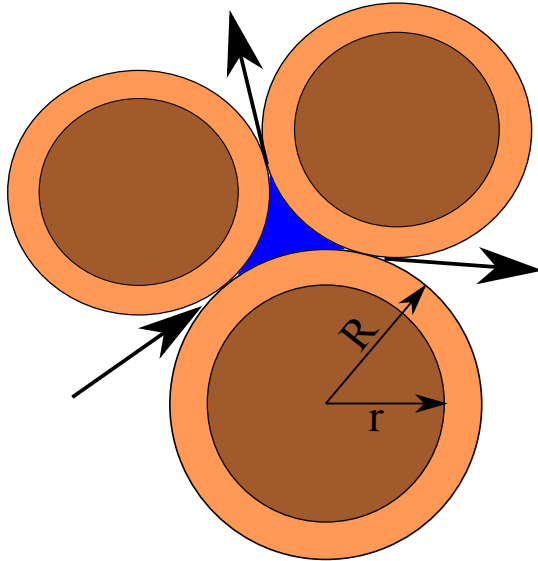


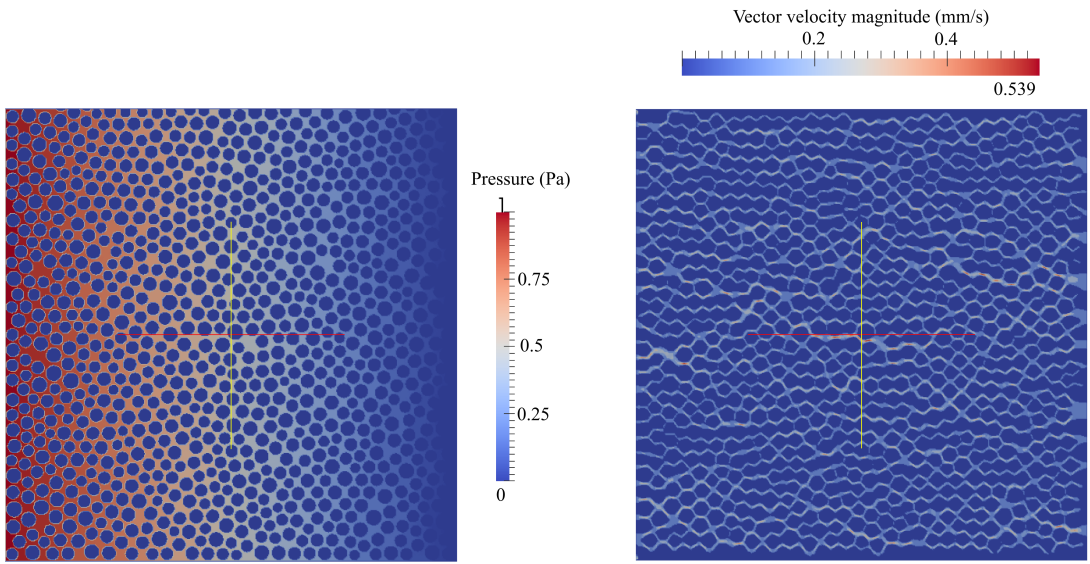
Figure 6.3 Schematic representation of the hydrodynamic radius in LBM-DEM computation

In order to understand the relation between the hydrodynamic radius and the permeability of the granular assembly, horizontal permeability tests are performed by varying the hydrodynamic radius as  $0.7R$ ,  $0.75R$ ,  $0.8R$ ,  $0.85R$ ,  $0.9$  and  $0.95R$ . A square sample of  $50\text{ mm} \times 50\text{ mm}$  is used to determine the transverse permeability. Dirichlet boundary condition (discussed in section 5.1.3), i.e., pressure/density constrain is applied along the left and the right boundaries. The density on the left boundary is increased in small increments ( $10^{-4}\Delta P$ ), which a constant density is maintained on the right boundary. This results in a pressure gradient causing the fluid to flow (see figure 6.4).

The mean velocity of flow ( $v$ ) is determined and the permeability of the sample ( $k$ ) is computed as:

$$k = v \cdot \mu \cdot \frac{\Delta x}{\Delta P}, \quad (6.1)$$

where  $\mu$  is the dynamic viscosity of the fluid (Pa s),  $\Delta x$  is the thickness of the bed of porous medium  $m$ , and  $\Delta P$  is the applied pressure difference Pa. For a given hydrodynamic radius, the pressure gradient  $\Delta P$  is varied to obtain different flow rates. Probing the fluid space showed a Poiseuille flow behaviour between grains. The flow is still within the Darcy's laminar flow regime, which is verified by the linear slope between the pressure gradient and mean flow velocity (see figure 6.5). It can be observed that with increase in the hydrodynamic radius the permeability decreases, i.e., the slope of the mean flow velocity to the pressure gradient decreases. At very low pressure gradient ( $\Delta P \leq 0.1$ ), both  $0.9R$  and  $0.95r$  has a no flow condition. A hydrodynamic radius of  $r = 0.95R$  shows almost no flow behaviour, even at higher pressure gradients. A high value of hydrodynamic radius  $r > 0.95R$  results in unnatural flow



(a) Pressure gradient in the granular assembly      (b) Horizontal flow due to pressure gradient

Figure 6.4 Evaluation of the horizontal permeability for a hydrodynamic radius of 0.7R.

4 behaviour. Hence, hydrodynamic radii in the range of 0.7 to 0.95R are adopted in the present  
 5 study.

6 Increase in the hydrodynamic radius from 0.7 to 0.95 reduces the porosity from 0.60 to  
 7 0.27. The permeability computed from LB – DEM method is verified by comparing it with the  
 8 analytical solution. One of the widely used analytical solution for permeability is the Carman  
  – Kozeny equation (CK Model), which is based on the Poiseuille flow through a pipe and is    1  
  mainly used for 3D, homogeneous, isotropic, granular porous media at moderate porosities.    2  
  In the present study, a modified Carman – Kozeny equation that takes into account the micro-    3  
  structure of the fibres and that is valid in a wide range of porosities is adopted ([Yazdchi et al.,    4  
  2011](#)). The normalized permeability is defined as    5

$$\frac{k}{d^2} = \frac{\varepsilon}{\psi_{CK}(1-\varepsilon)^2}. \quad (6.2) \quad 6$$

In the CK model, the hydraulic diameter  $D_h$ , is expressed as a function of measurable quantities:  
 7 porosity and specific surface area    8

$$D_h = \frac{4\varepsilon V}{S_v} = \frac{\varepsilon d}{(1-\varepsilon)}, \quad (6.3) \quad 9$$

$$a_v = \frac{\text{grain surface}}{\text{grain volume}} = \frac{S_v}{(1-\varepsilon V)} = \frac{4}{d}, \quad (6.4) \quad 10$$

11

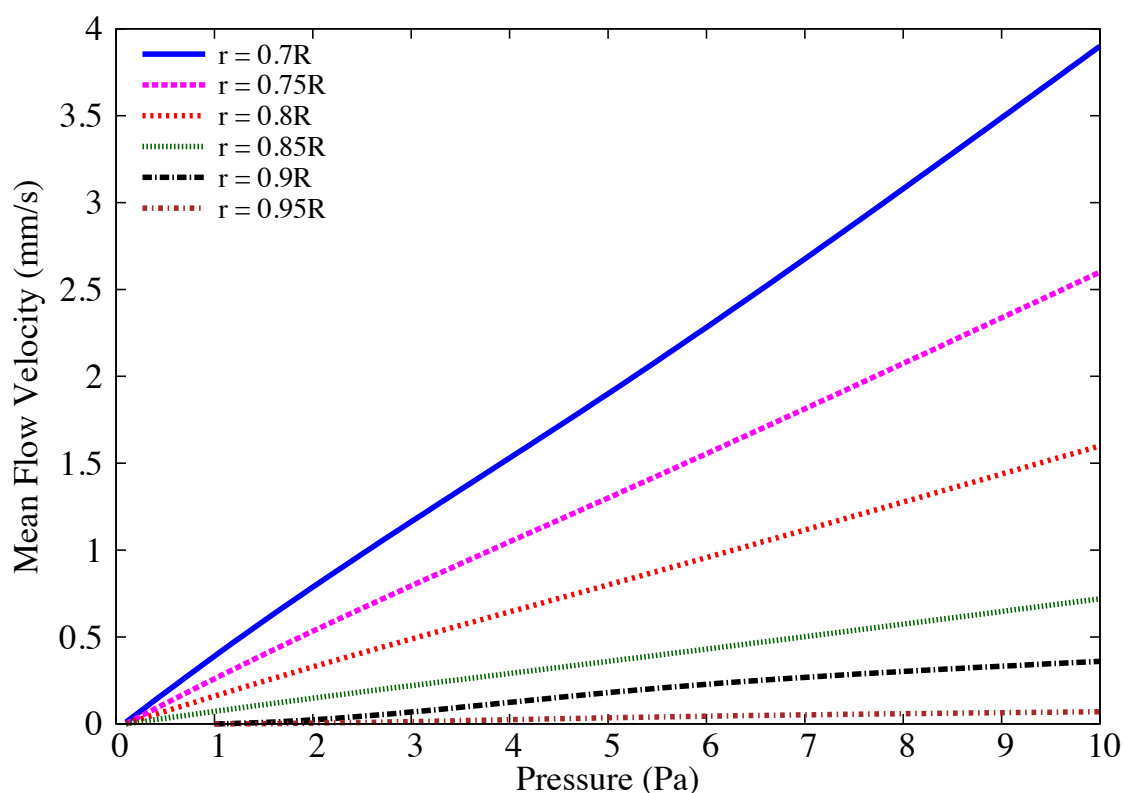


Figure 6.5 Variation of the mean flow velocity with pressure gradient for different hydrodynamic radius.

where  $S_v$  is the total wetted surface, and  $a_v$  is the specific surface area. The above value of  $a_v$  is for circles (cylinders) - for spheres  $a_v = 6/d$ .  $\psi_{CK}$  is the empirically measured CK factor, which represents both the shape factor and the deviation of flow direction from that in a duct. It is approximated for randomly packed beds of spherical grains. The normalized permeability for different porosity obtained by varying the radius from 0.7 to 0.95 is presented in figure 6.6.

The normalized permeability is found to match the qualitative trend of the Carman-Kozeny equations. The LB – DEM permeability curve lies between the permeability curves for spherical and cylindrical grain arrangements implying a better approximation of permeability in 2D granular assembly by reducing the radius during LBM computations.

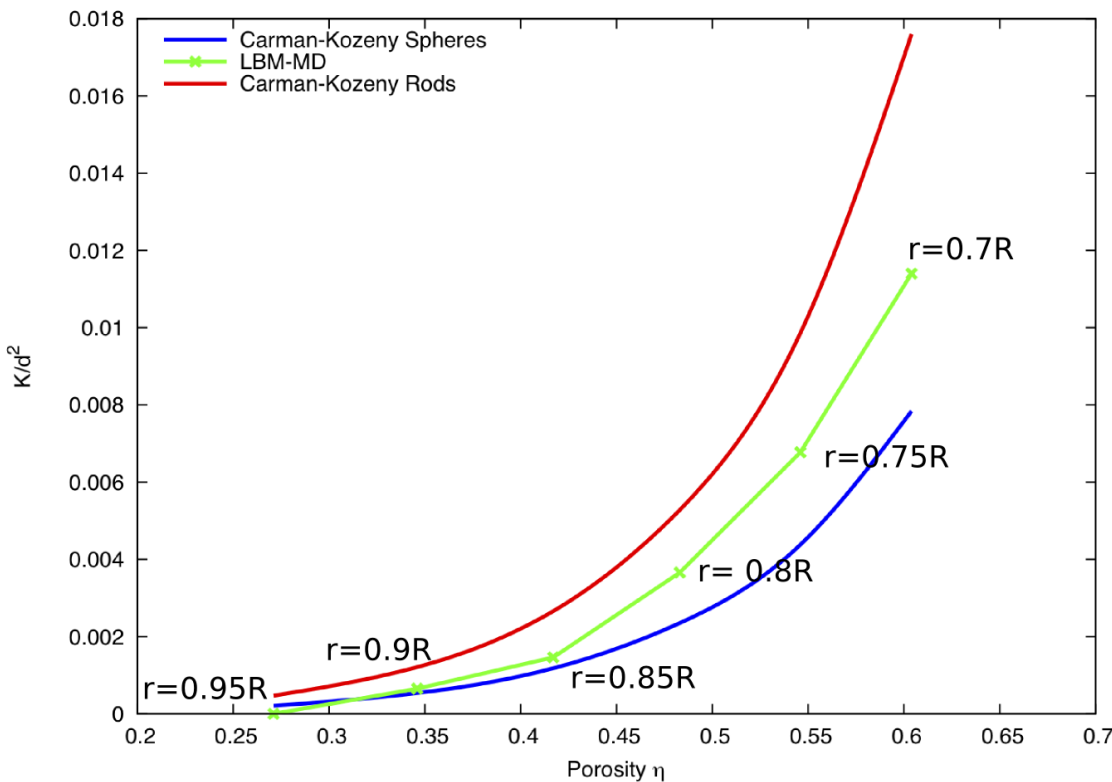


Figure 6.6 Relation between permeability and porosity for different hydrodynamic radius and comparison with the analytical solution.

### 6.2.3 Collapse in fluid: Flow evolution

Two-dimensional plane-strain LBM-DEM simulations of granular column collapse are performed by varying the initial aspect ratio of the column from 0.2 to 6. A hydrodynamic radius of 0.7R is adopted during LBM computations. The granular assemble has a packing fraction of 83%. The normalized final run-out distance is computed as  $\Delta L = (L_f - L_0)/L_0$ . Similar to

11 dry granular collapse, the duration of collapse is normalised with a critical time  $\tau_c = \sqrt{H/g}$ .  
12 Where,  $H$  is the initial height of the granular column and  $g$  is the acceleration due to gravity.  
13 Dry and buoyant analyses of granular column collapse are also performed to understand the  
14 effect of hydrodynamic forces on the run-out distance.

15 Snapshots of flow evolution of a granular column collapse with an initial aspect ratio of  
16 0.4 is shown in figure 6.7. The failure begins at the toe end of the column, and the fracture  
17 surface propagates into the column at an angle of about  $50^\circ$ , similar to dry column. For the  
18 short column, the failure is due to collapse of the flanks. Once the material is destabilised, the  
19 granular mass interacts with the surrounding fluid resulting in formation of turbulent vortices.  
20 These vortices interact with the grains at the surface, resulting in irregularities on the free  
21 surface. Force chains can be observed in the static region of collapse, which indicates the flow  
22 can be described using a continuum theory. As the granular material ceases to flow, force chains  
23 develop at the flow front, revealing consolidation of the granular mass resulting in increase in  
24 strength.

25 The evolution of run-out with time for a short column ( $a = 0.4$ ) is presented in figure 6.8.  
26 The dry column exhibits longer run-out distance in comparison to the submerged column. The  
27 collapse of a dry column using DEM represents a collapse in vacuum, without any influence of  
28 drag forces or viscosity of air. A LBM-DEM simulation of a granular column collapse using  
29 the kinematic viscosity of air is performed to compare the dry column with the collapse in air.  
30 It can be observed that both the “dry” condition and the collapse in air show almost the same  
31 run-out behaviour. However, the collapse in fluid (water) results in a much shorter run-out  
32 distance. The granular mass in fluid has the buoyant mass, in contrast to the dry density. A  
33 dry granular collapse with the buoyant unit weight is performed to understand the effect of  
34 buoyancy on the run-out behaviour. The dry column with buoyant unit weight also exhibits  
35 longer run-out behaviour than the collapse in fluid. However, due to decrease in the initial  
1 potential energy, the run-out observed in the buoyant condition is shorter than the dry condition.  
2 The column collapse in fluid takes longer to evolve when submerged in water, which might  
3 be due to the development of large negative porewater pressure that is generated during the  
4 shear failure along the fracture surface. The large negative pore pressure has to be dissipated  
5 before the granular mass above the fracture surface can collapse and flow. The shorter run-out  
6 distance in the fluid case, in comparison with the dry and buoyant conditions, shows that the  
7 collapse in fluid is significantly affected by the hydrodynamic drag force acting on the soil  
8 grains. The evolution of height  $H/L$  is presented in ???. Since the failure of the column is only  
9 at the flank, the central static region remains unaffected. Hence, the final height of the column  
10 is the same in dry and submerged conditions.

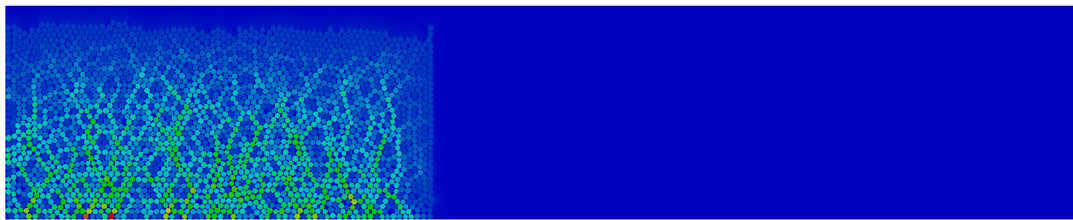
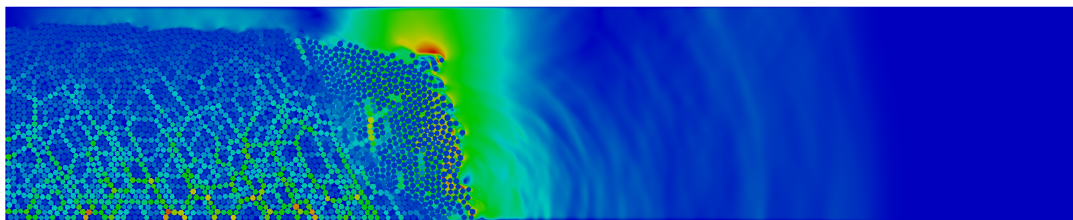
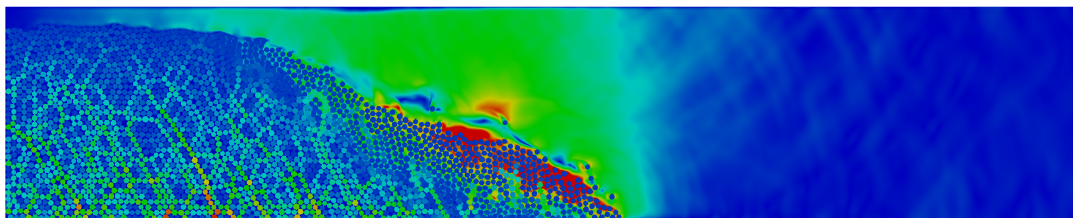
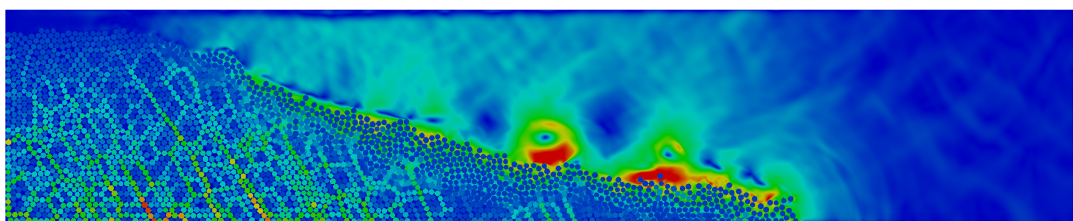
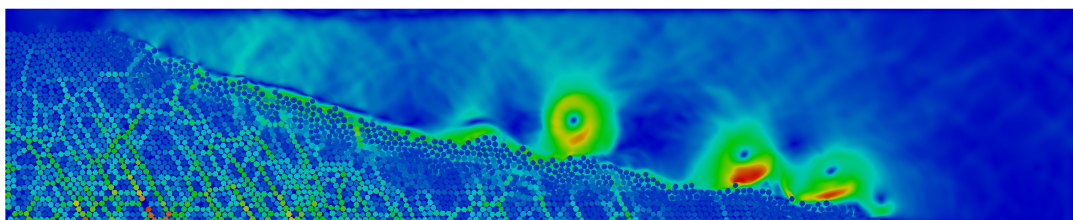
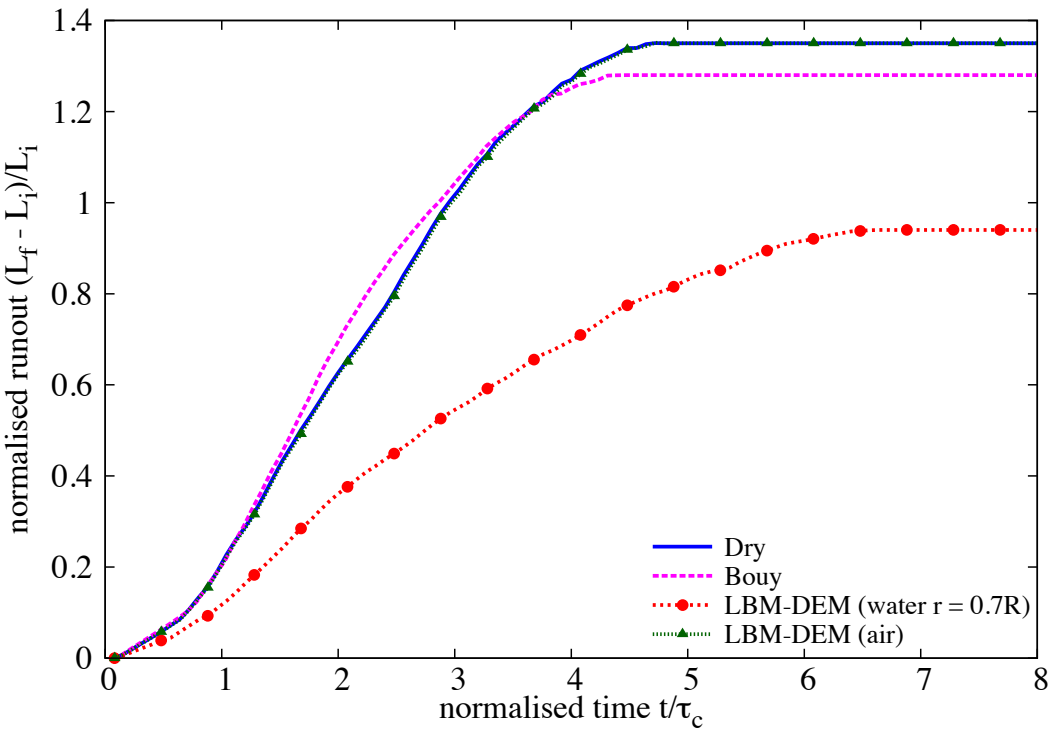
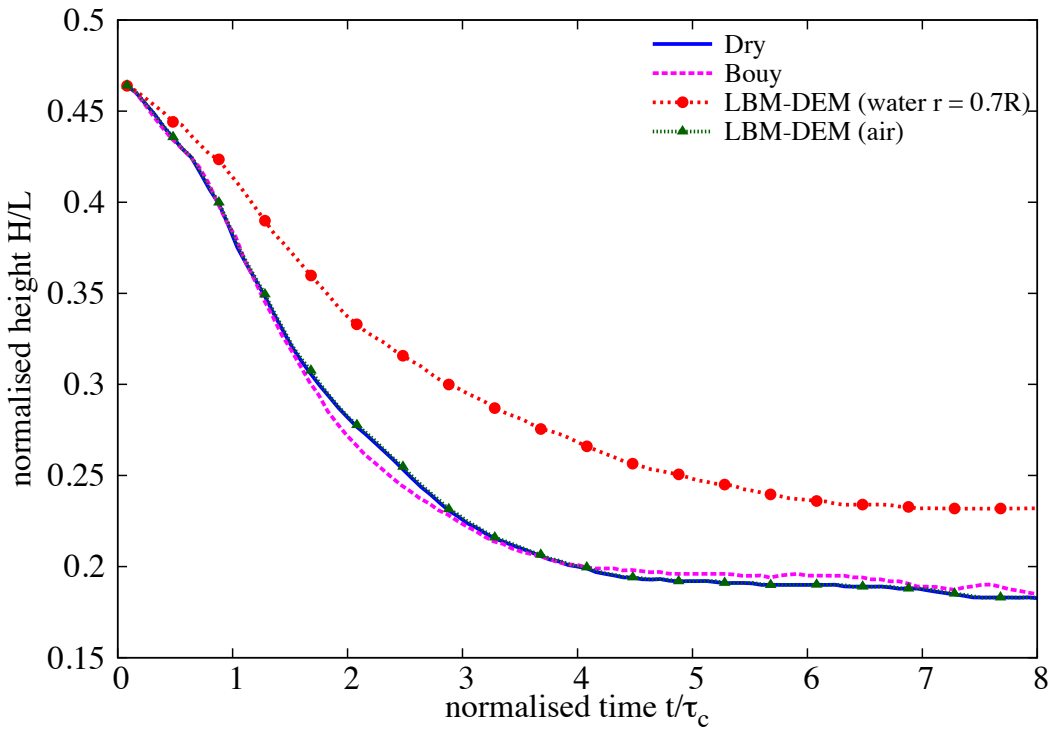
(a)  $t = 0\tau_c$ (b)  $t = 1\tau_c$ (c)  $t = 3\tau_c$ (d)  $t = 6\tau_c$ (e)  $t = 8\tau_c$ 

Figure 6.7 Flow evolution of a granular column collapse in fluid ( $a = 0.4$ ). Shows the velocity profile of fluid due to interaction with the grains (red - higher velocity).

Figure 6.8 Evolution of run-out for a column collapse in fluid ( $a = 0.4$ )Figure 6.9 Evolution of height with time for a column collapse in fluid ( $a = 0.4$ )

11 The evolution of normalised kinetic energy with time for a column with an initial aspect  
12 ratio of 0.4 is shown in figure 6.10. It can be observed that the peak kinetic energy is attained  
13 later in the submerged condition than the dry collapse. This can be attributed to the time  
14 required to overcome the negative pore pressure generated during the shear along the fracture  
1 surface. For short columns the critical time  $\tau_c$  is controlled by the vertical kinetic energy.  
2 The amount of kinetic energy in submerged case is significantly lower than the dry condition.  
3 Also, the potential energy evolution (see figure 6.11) shows a significant influence of the  
4 hydrodynamic forces on the amount of material destabilised during the collapse. The drag  
5 forces reduces and slows down the amount of material that undergo collapse resulting in shorter  
6 run-out distance for short columns.

7 Snapshots of flow evolution of a granular column collapse with an initial aspect ratio of 4 is  
8 shown in figure 6.11.

9 **6.2.4 Effect of permeability**

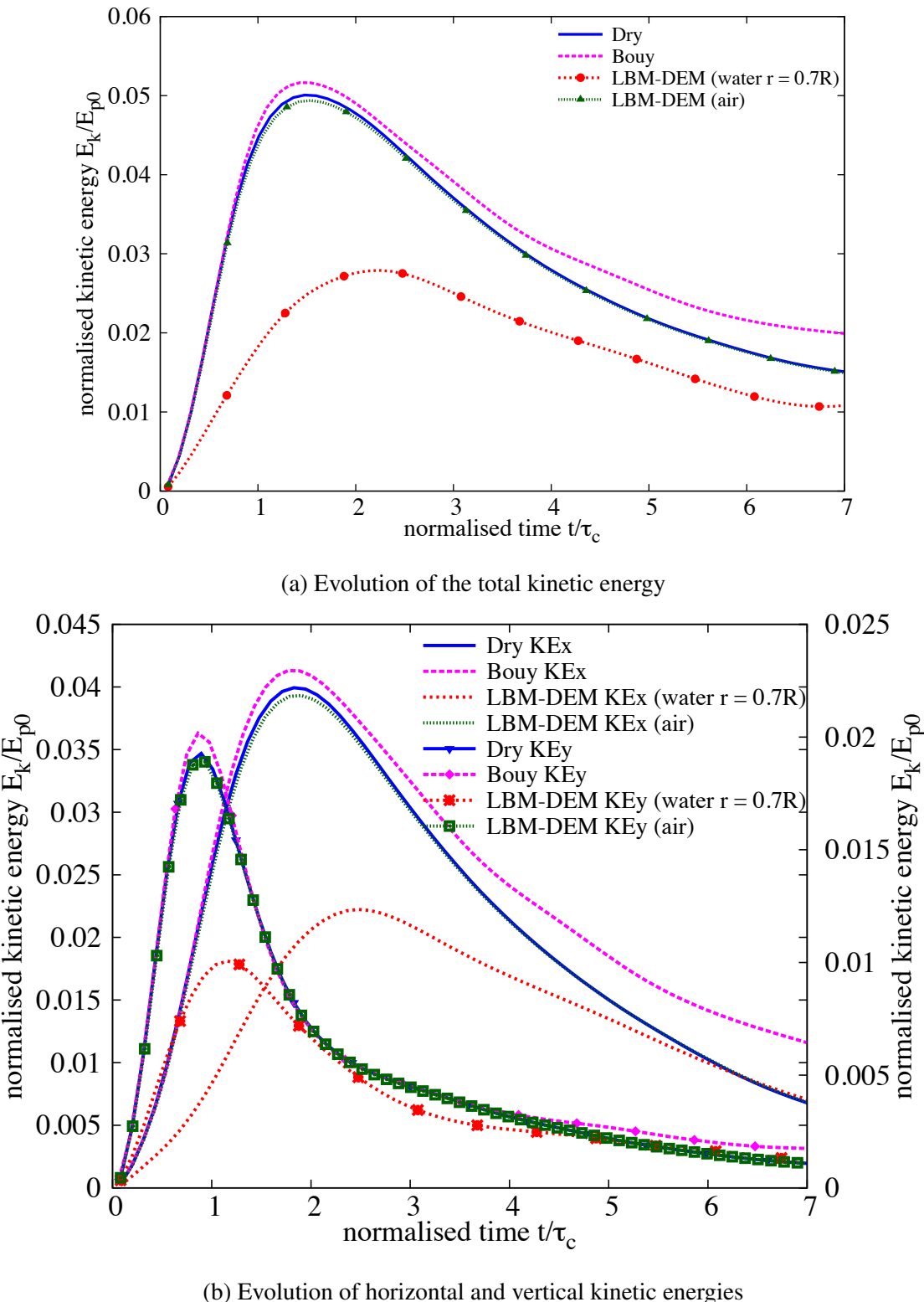


Figure 6.10 Evolution of kinetic energies with time for a granular column collapse in fluid ( $a = 0.4$ )

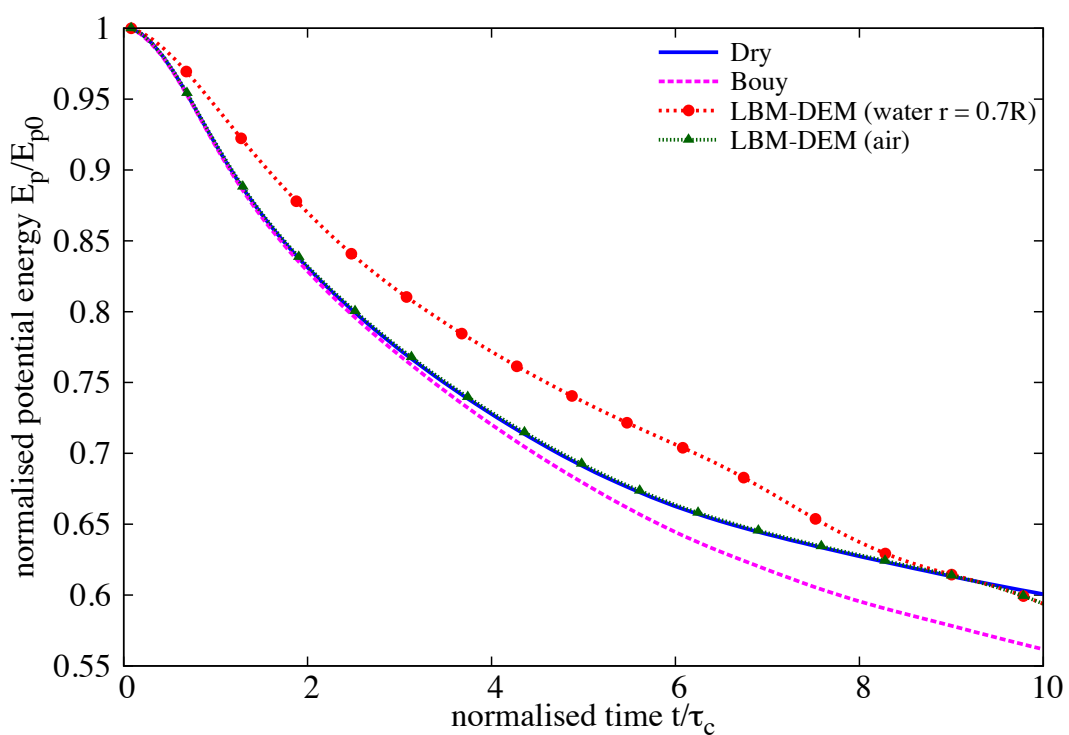
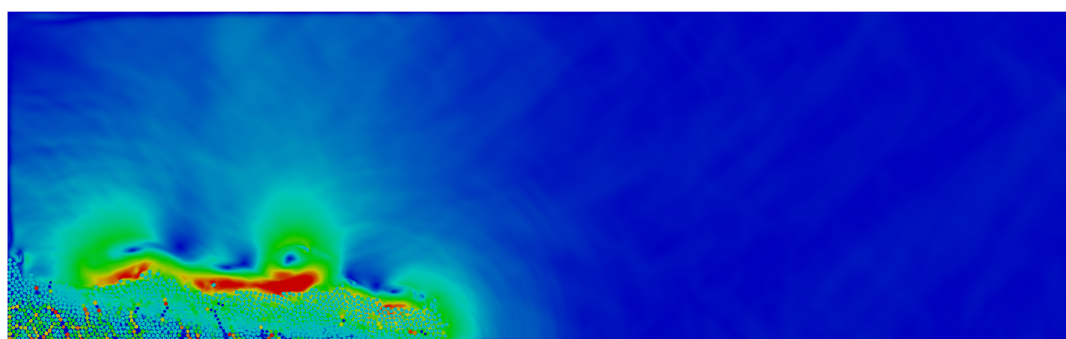


Figure 6.11 Evolution of the potential energy with time for a granular column collapse in fluid ( $a = 0.4$ )

 $t = 0\tau_c$  $t = 1\tau_c$  $t = 3\tau_c$

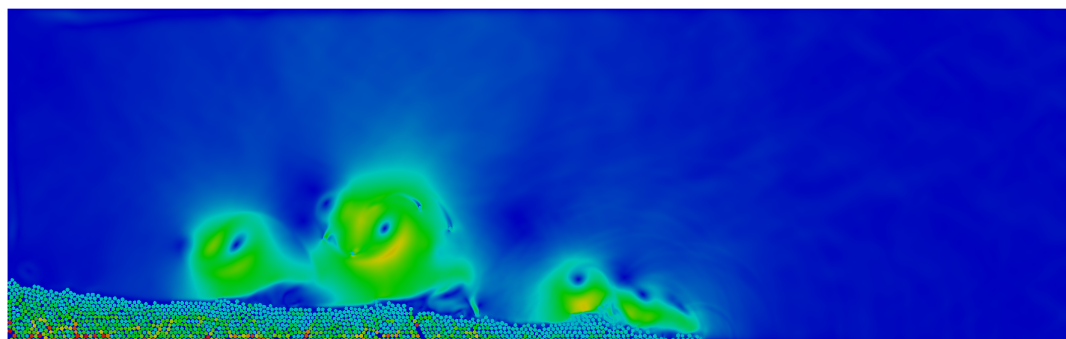
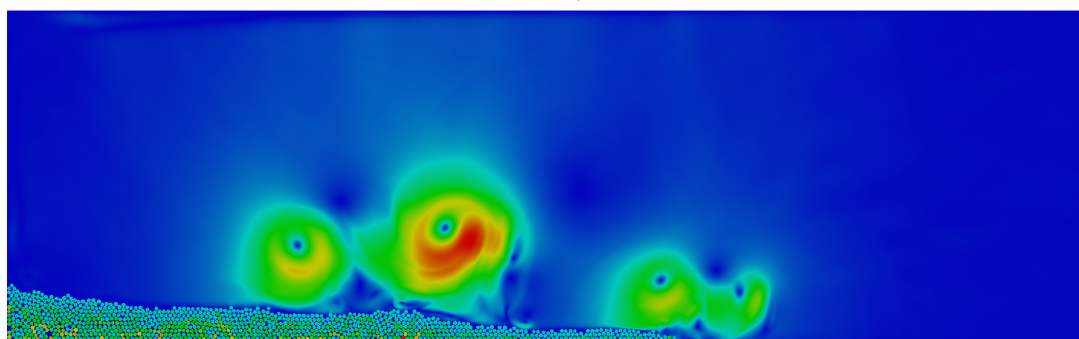
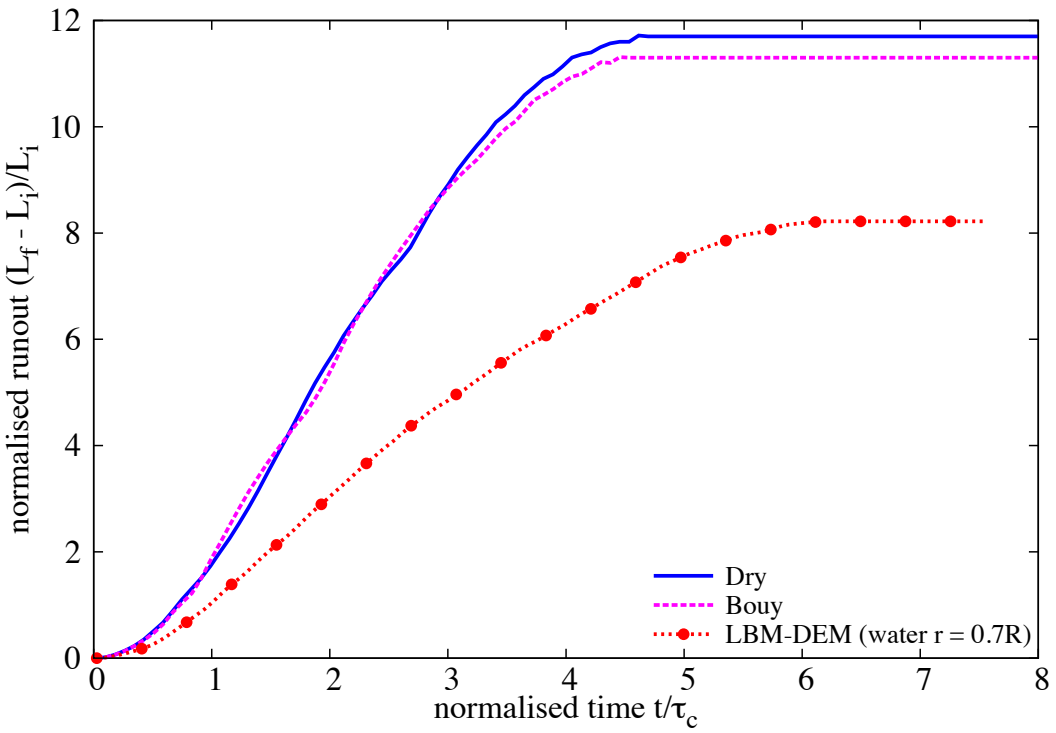
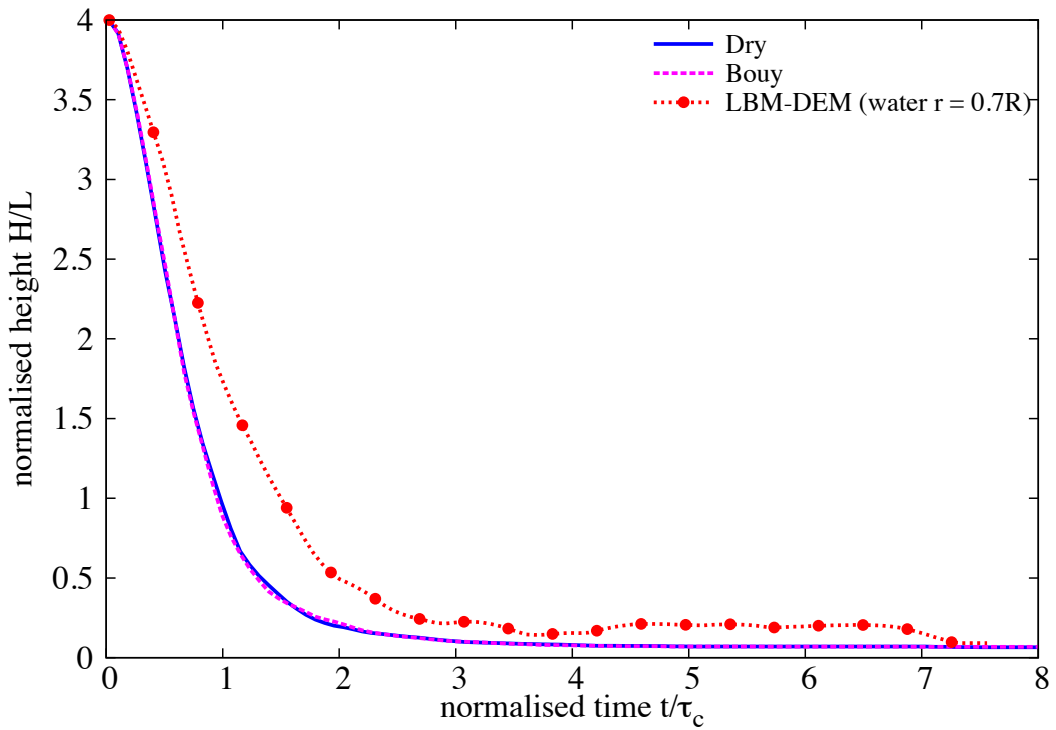
 $t = 6\tau_c$  $t = 8\tau_c$ 

Figure 6.11 Flow evolution of a granular column collapse in fluid ( $a = 4$ ). Shows the velocity profile of fluid due to interaction with the grains (red - higher velocity).

Figure 6.12 Evolution of run-out for a column collapse in fluid ( $a = 4$ )Figure 6.13 Evolution of height with time for a column collapse in fluid ( $a = 4$ )

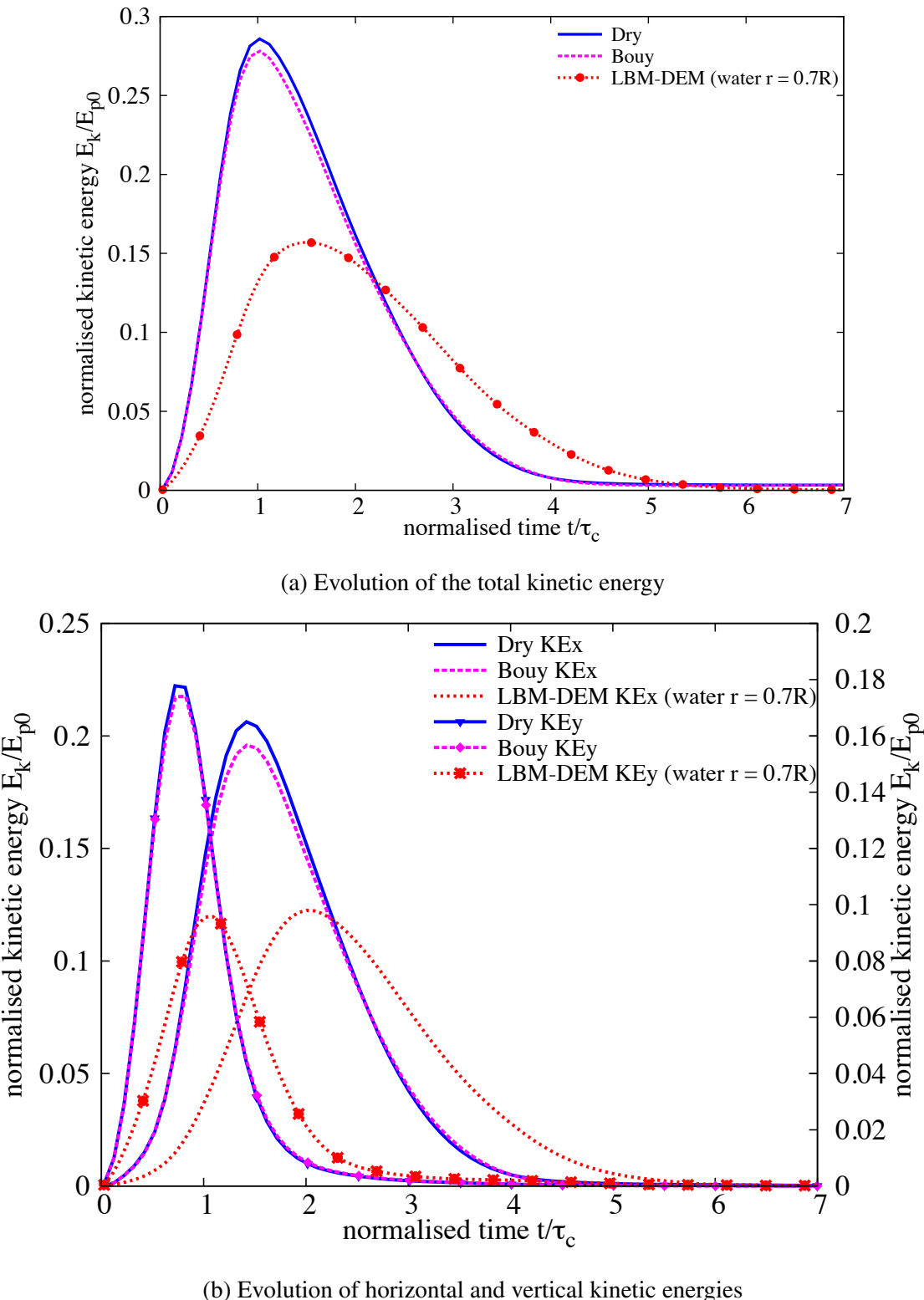


Figure 6.14 Evolution of kinetic energies with time for a granular column collapse in fluid ( $a = 4$ )

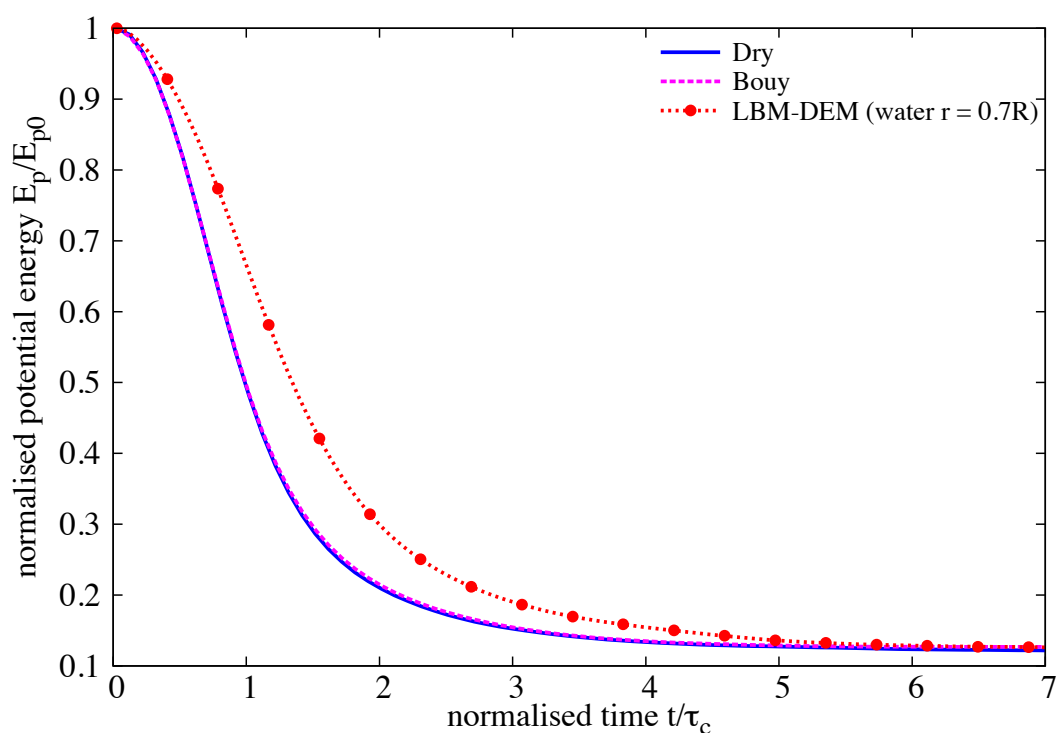


Figure 6.15 Evolution of the potential energy with time for a granular column collapse in fluid ( $a = 4$ )

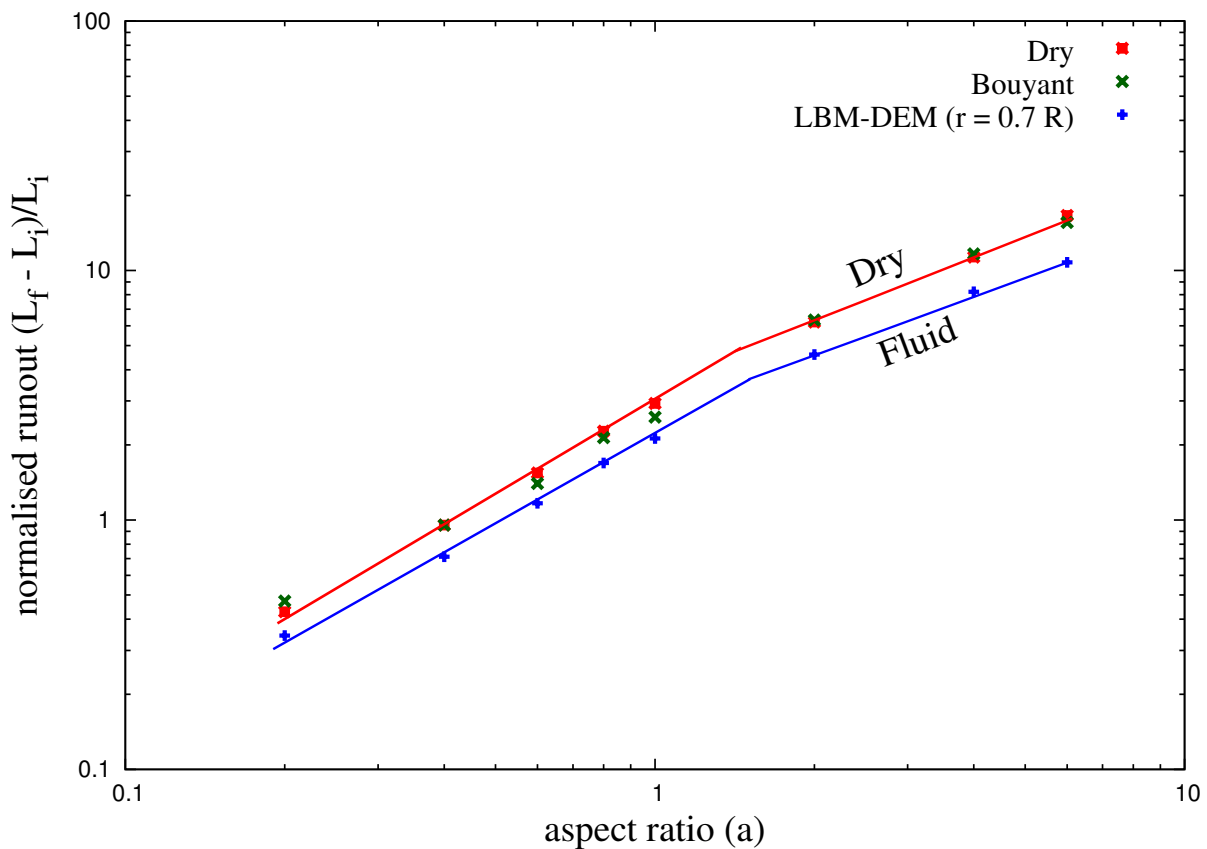


Figure 6.16 Normalised final run-out distance for columns with different initial aspect ratios. Comparison of dry and submerged granular column collapse.

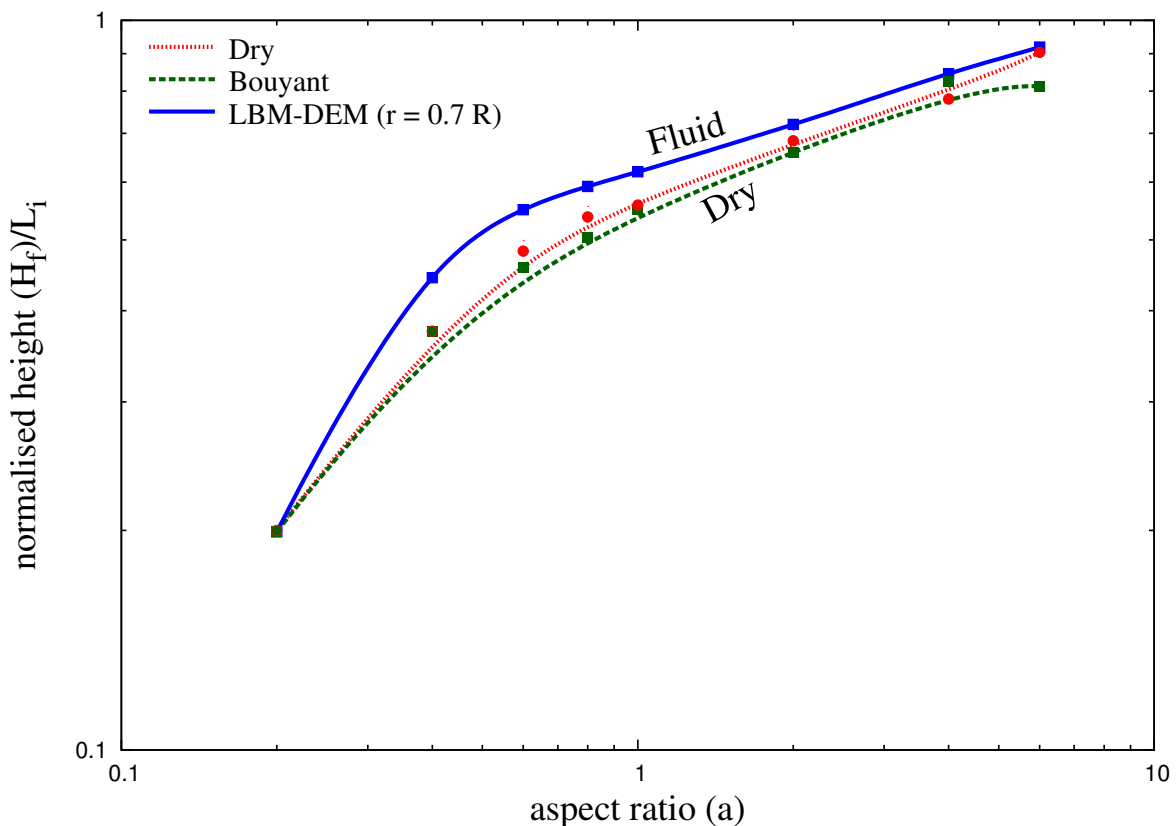


Figure 6.17 Normalised final collapse height for columns with different initial aspect ratios. Comparison of dry and submerged granular column collapse.

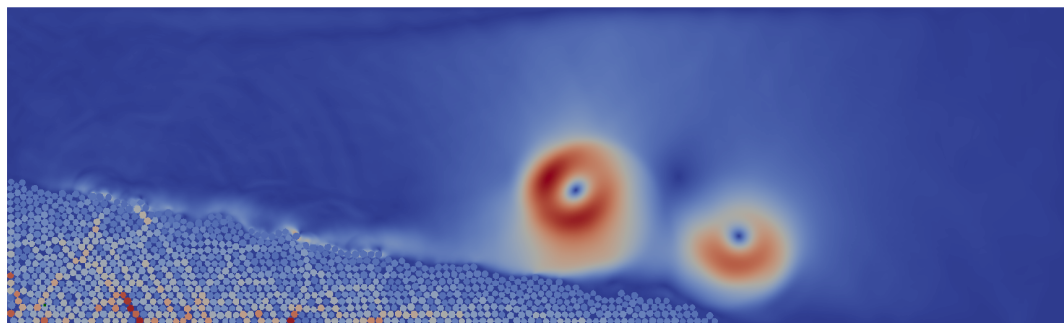
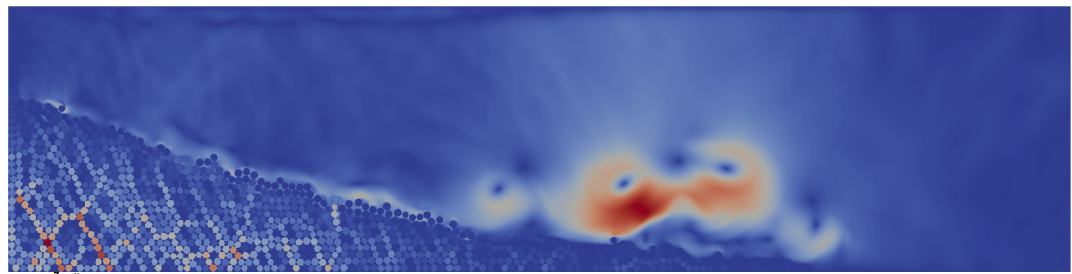
(a) High permeability ( $r = 0.7 R$ )(b) Low permeability ( $r = 0.95 R$ )

Figure 6.18 Effect of permeability on the deposit morphology of a granular column collapse in fluid ( $a = 0.8$ )

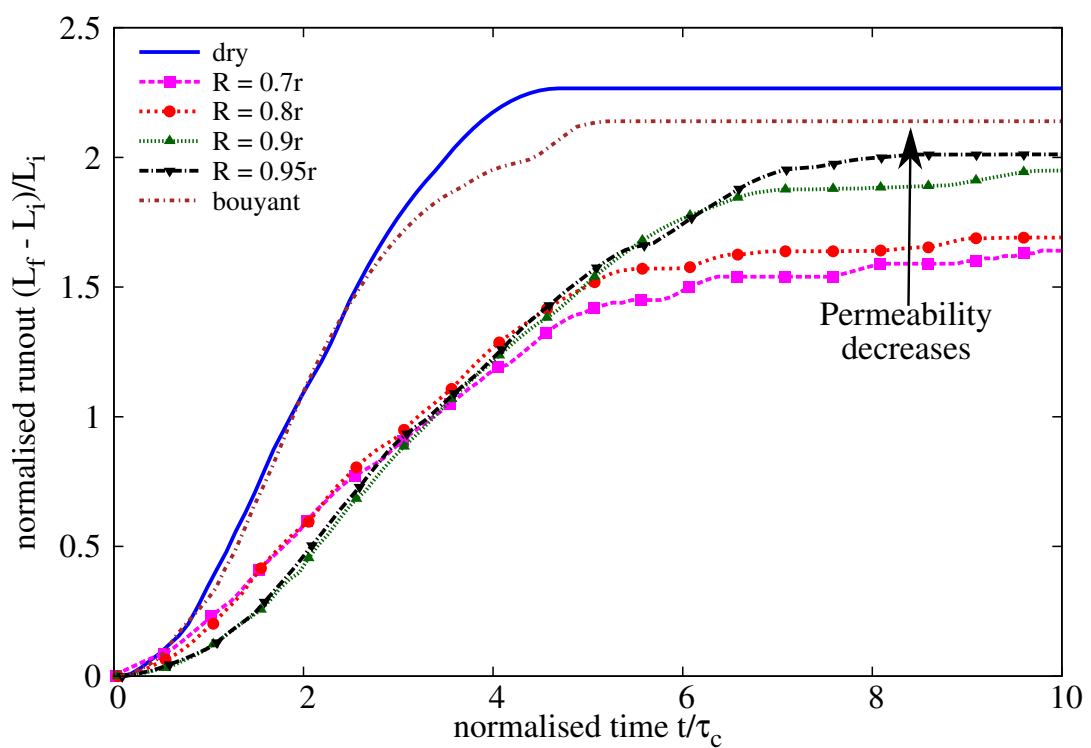
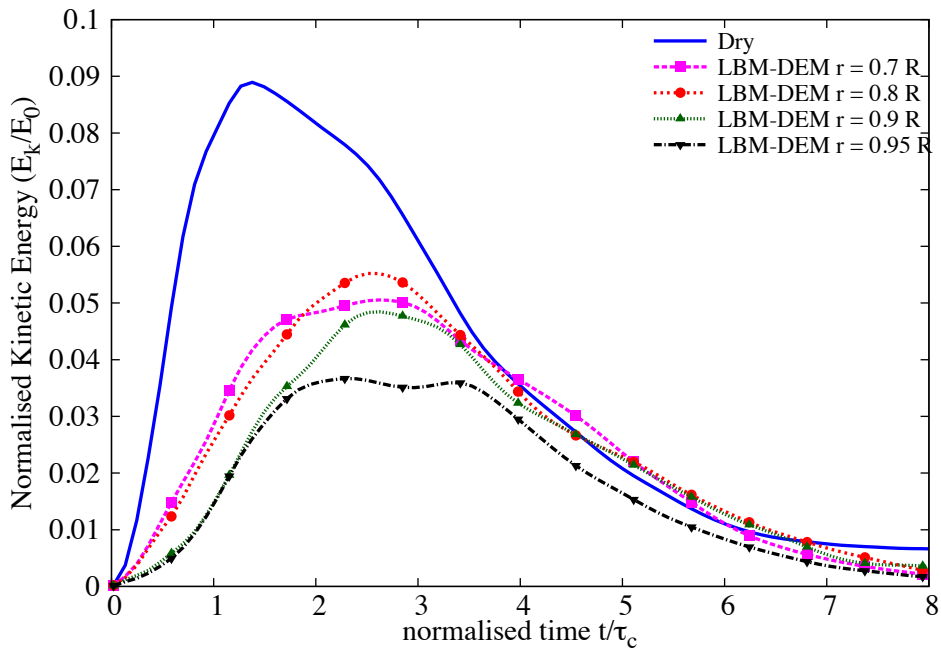
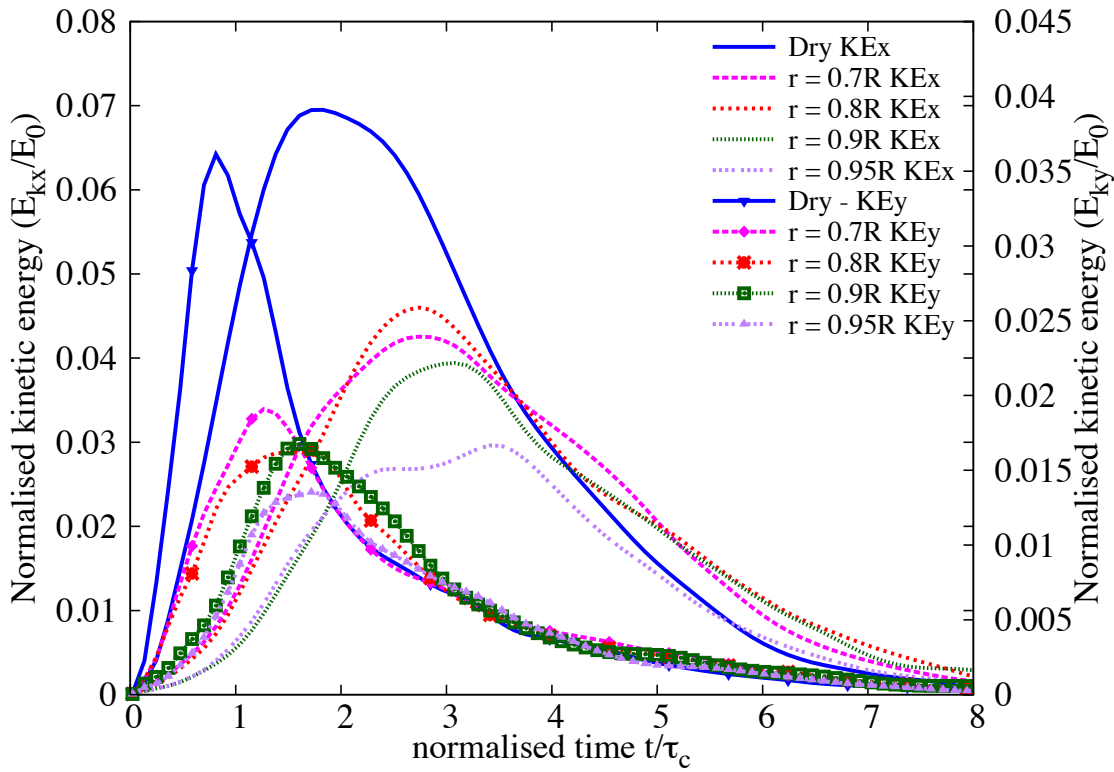


Figure 6.19 Effect of permeability on the evolution of run-out for a column collapse in fluid ( $a = 0.8$ )



(a) Evolution of the total kinetic energy



(b) Evolution of horizontal and vertical kinetic energies

Figure 6.20 Effect of permeability on the evolution of kinetic energies with time for a granular column collapse in fluid ( $a = 0.8$ )

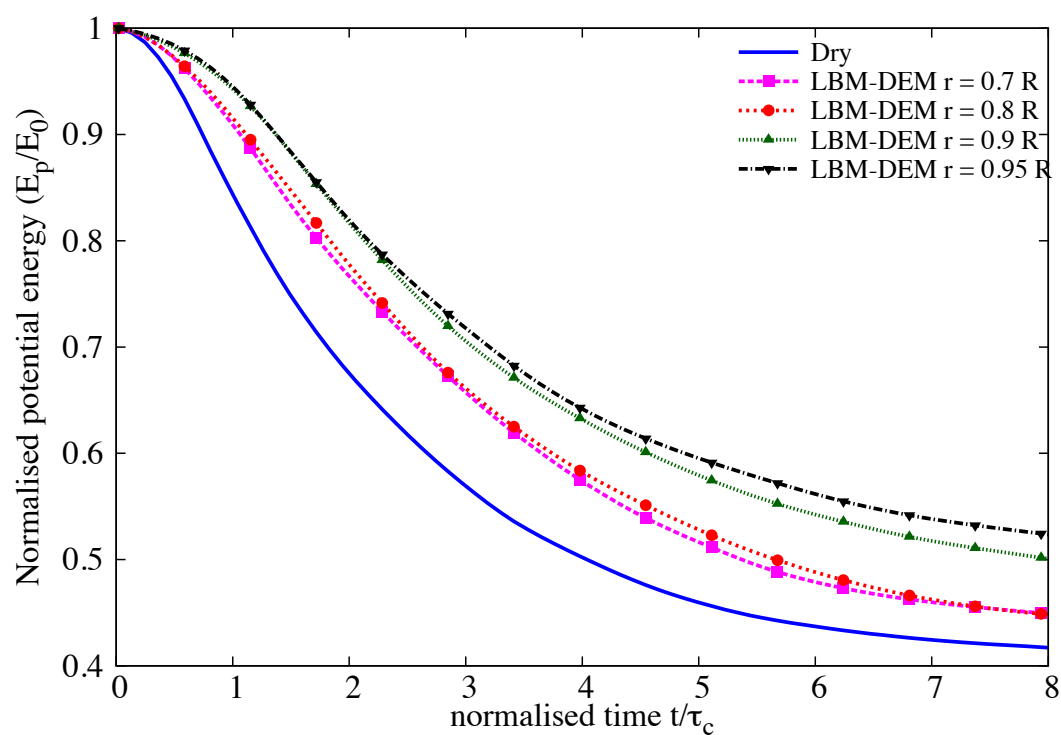


Figure 6.21 Effect of permeability on the evolution of the potential energy with time for a granular column collapse in fluid ( $a = 0.8$ )

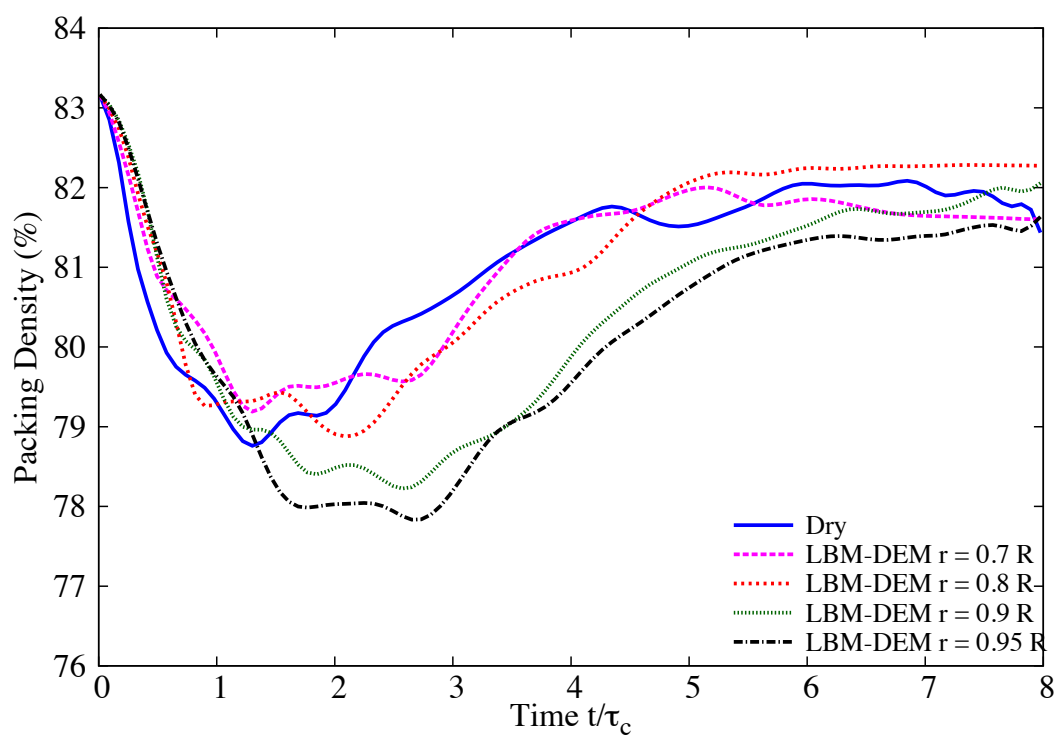


Figure 6.22 Effect of permeability on the evolution of packing density for a granular column collapse in fluid ( $a = 0.8$  & dense initial packing)

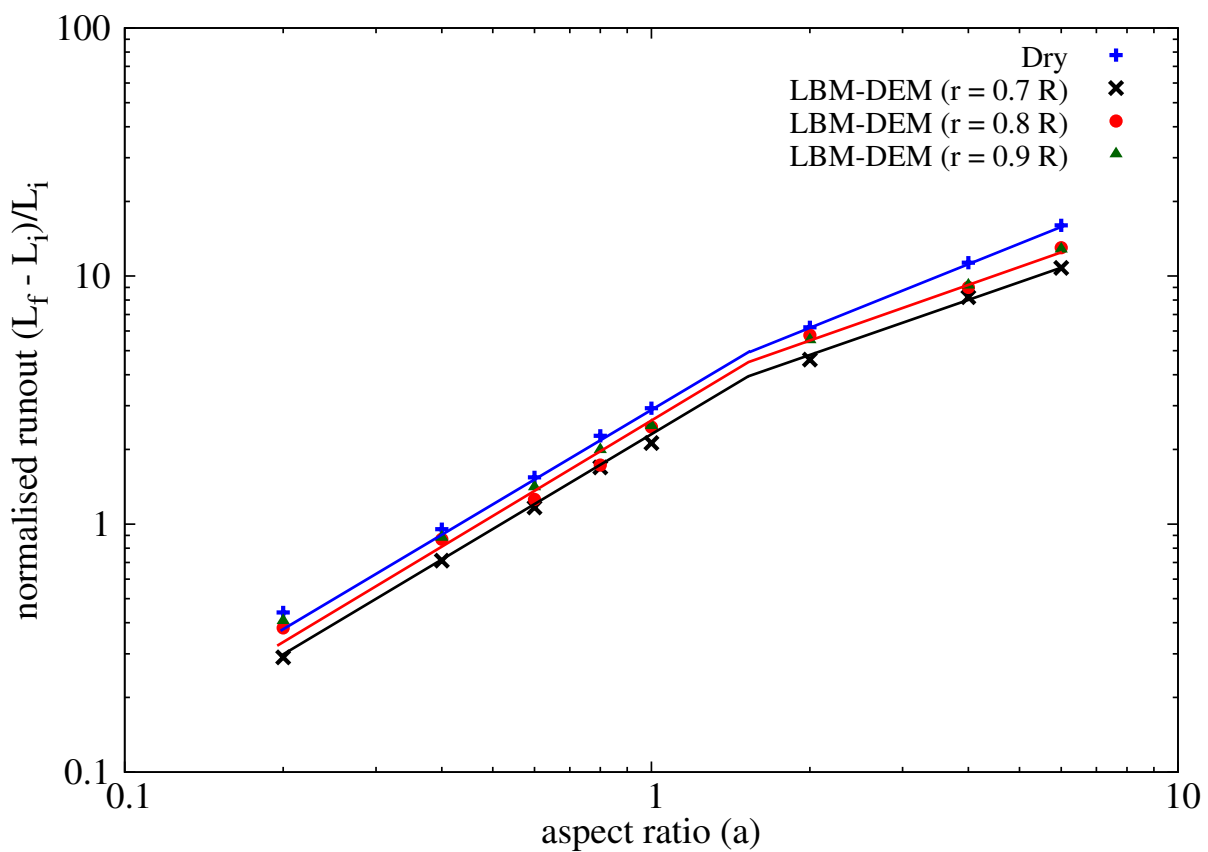


Figure 6.23 Normalised final run-out distance for columns with different initial aspect ratios. Comparison of dry and submerged granular column collapse for different hydrodynamic radius ( $0.7R$ ,  $0.8R$  and  $0.9R$ ).

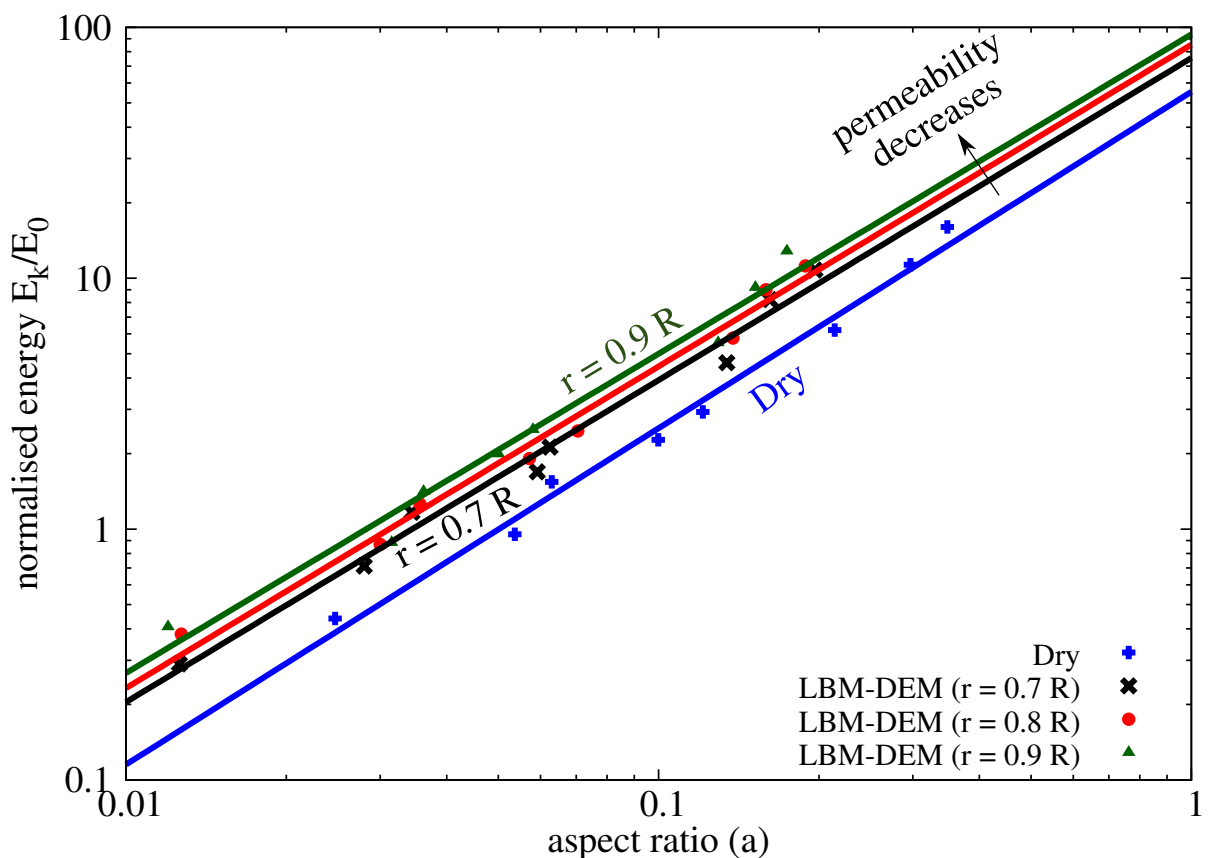


Figure 6.24 Normalised final run-out distance for columns as a function of peak kinetic energy. Comparison of dry and submerged granular column collapse for different hydrodynamic radius ( $0.7R$ ,  $0.8R$  and  $0.9R$ ).

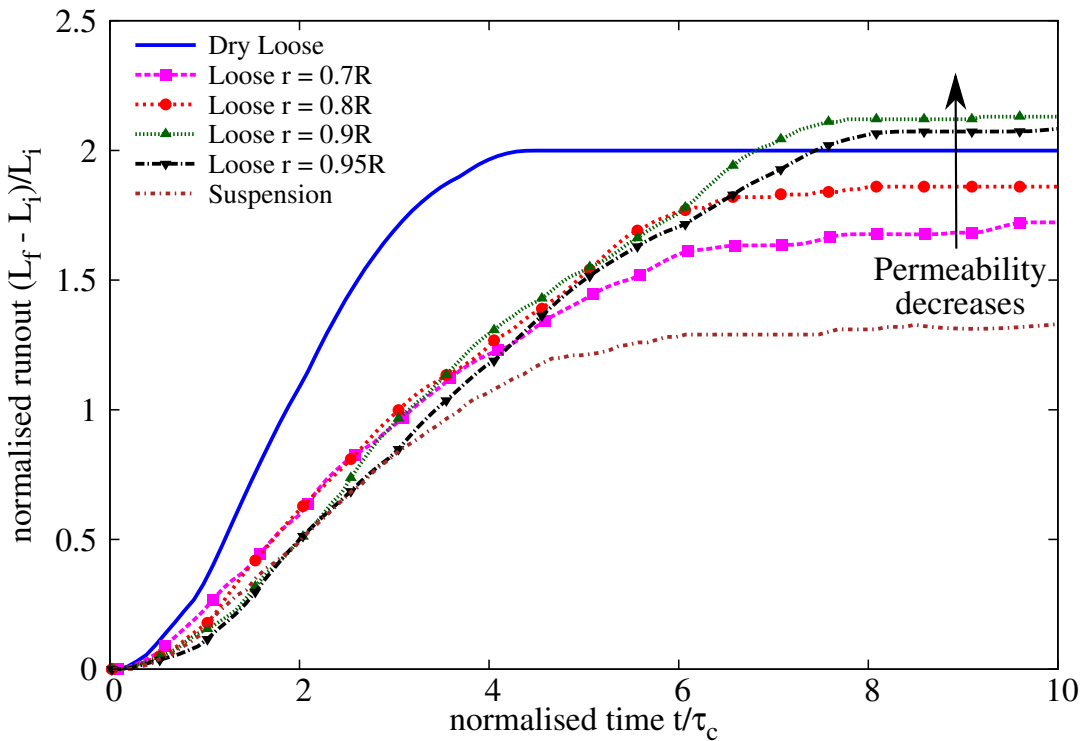


Figure 6.25 Effect of permeability on the evolution of run-out for a column collapse in fluid ( $a = 0.8$  & loose packing)

### <sup>10</sup> 6.2.5 Effect of initial packing density

## <sup>11</sup> 6.3 Submarine granular flows down incline plane

<sup>12</sup> The flow of dense granular material is a common phenomenon in engineering predictions, such  
<sup>13</sup> as avalanches, landslides, and debris-flow modelling. Despite the huge amount of research  
<sup>14</sup> that has gone into describing the behaviour of granular flows, a constitutive equation that  
<sup>15</sup> describes the overall behaviour of a flowing granular material is still lacking. The initiation and  
<sup>16</sup> propagation of submarine granular flows depend mainly on the slope, density, and quantity of  
<sup>17</sup> the material destabilised. Although certain macroscopic models are able to capture the simple  
<sup>18</sup> mechanical behaviours, the complex physical mechanisms that occur at the grain scale, such as  
<sup>19</sup> hydrodynamic instabilities, the formation of clusters, collapse, and transport, have largely been  
<sup>20</sup> ignored (Topin et al., 2011). The momentum transfer between the discrete and the continuous  
<sup>21</sup> phases significantly affects the dynamics of the flow (Peker and Helvacı, 2007). Grain-scale  
<sup>22</sup> description of the granular material enriches the macro-scale variables, which poorly account  
<sup>23</sup> for the local rheology of the materials. In order to describe the mechanism of saturated and/or  
<sup>24</sup> immersed granular flows, it is important to consider both the dynamics of the solid phase and

(a) High permeability ( $r = 0.7 R$ )(b) Low permeability ( $r = 0.95 R$ )

Figure 6.26 Effect of permeability on the excess pore water pressure distribution for a granular column collapse in fluid ( $a = 0.8$  & loose packing) at  $t = \tau_c$

## 6.3 Submarine granular flows down incline plane

209

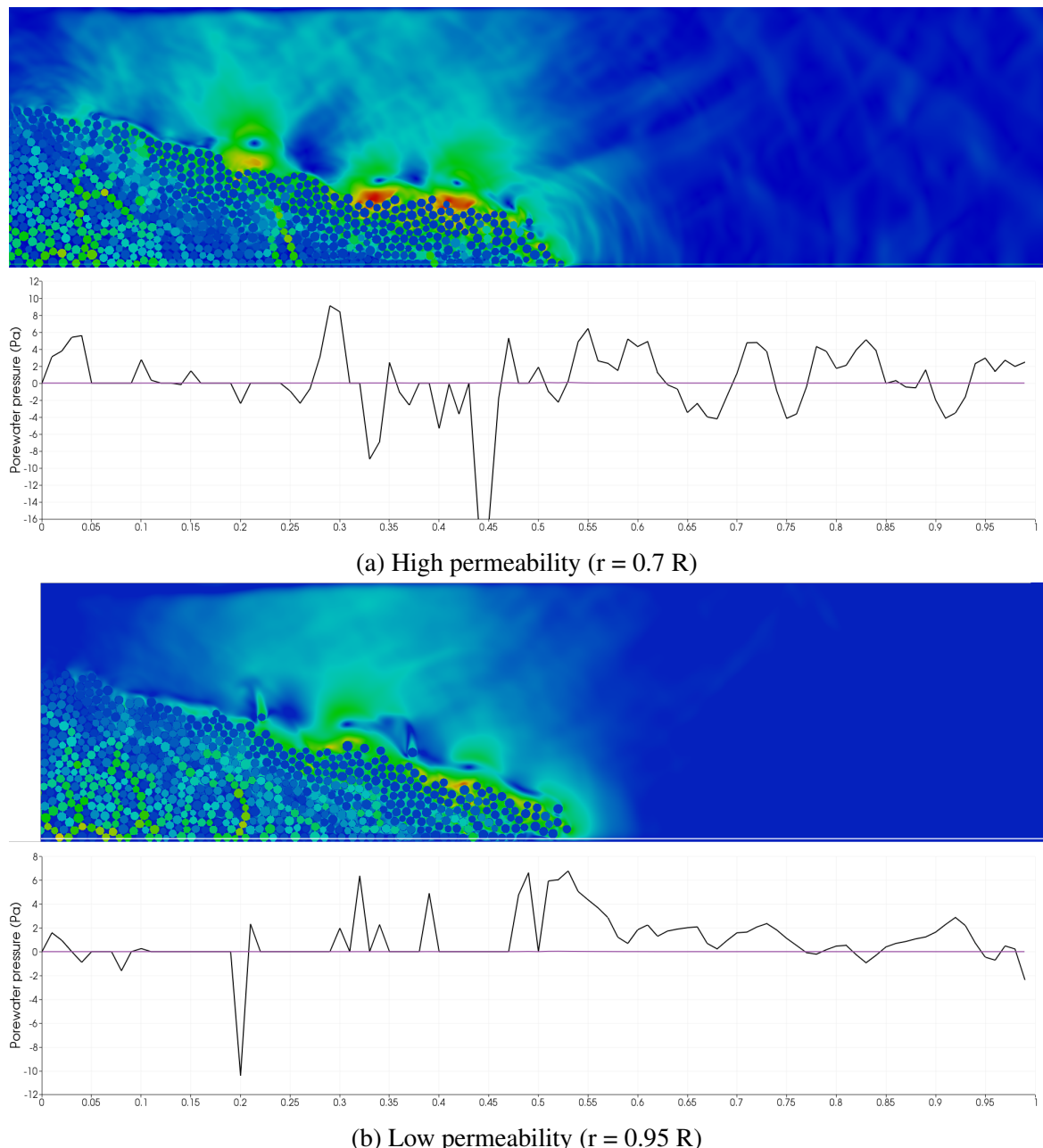


Figure 6.27 Effect of permeability on the excess pore water pressure distribution for a granular column collapse in fluid ( $a = 0.8$  & loose packing) at  $t = 2\tau_c$

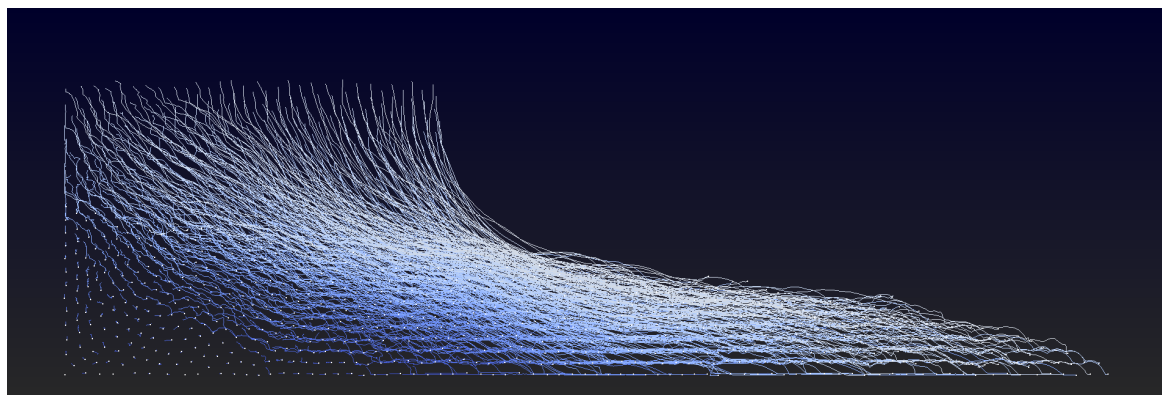
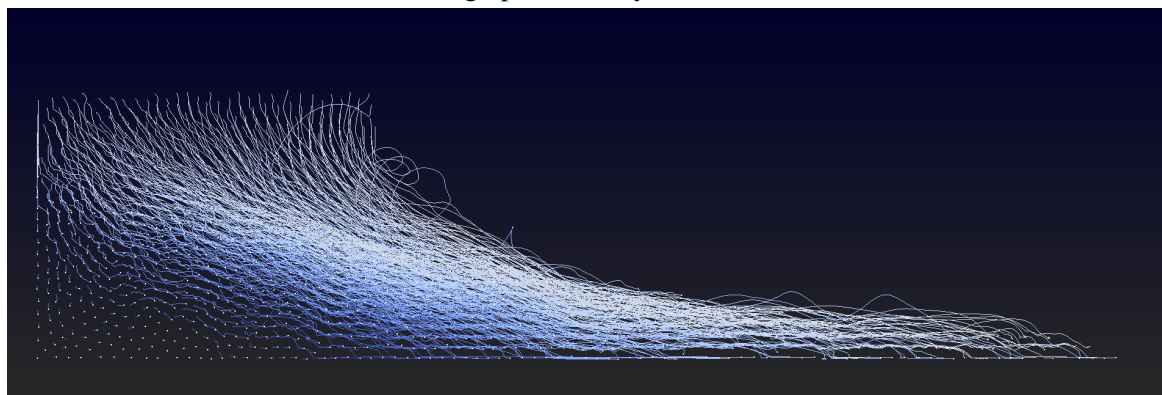
(a) High permeability ( $r = 0.7 R$ )(b) Low permeability ( $r = 0.95 R$ )

Figure 6.28 Particle tracking of the deposit morphology for a granular column collapse in fluid ( $a = 0.8$  & loose packing), influence of permeability

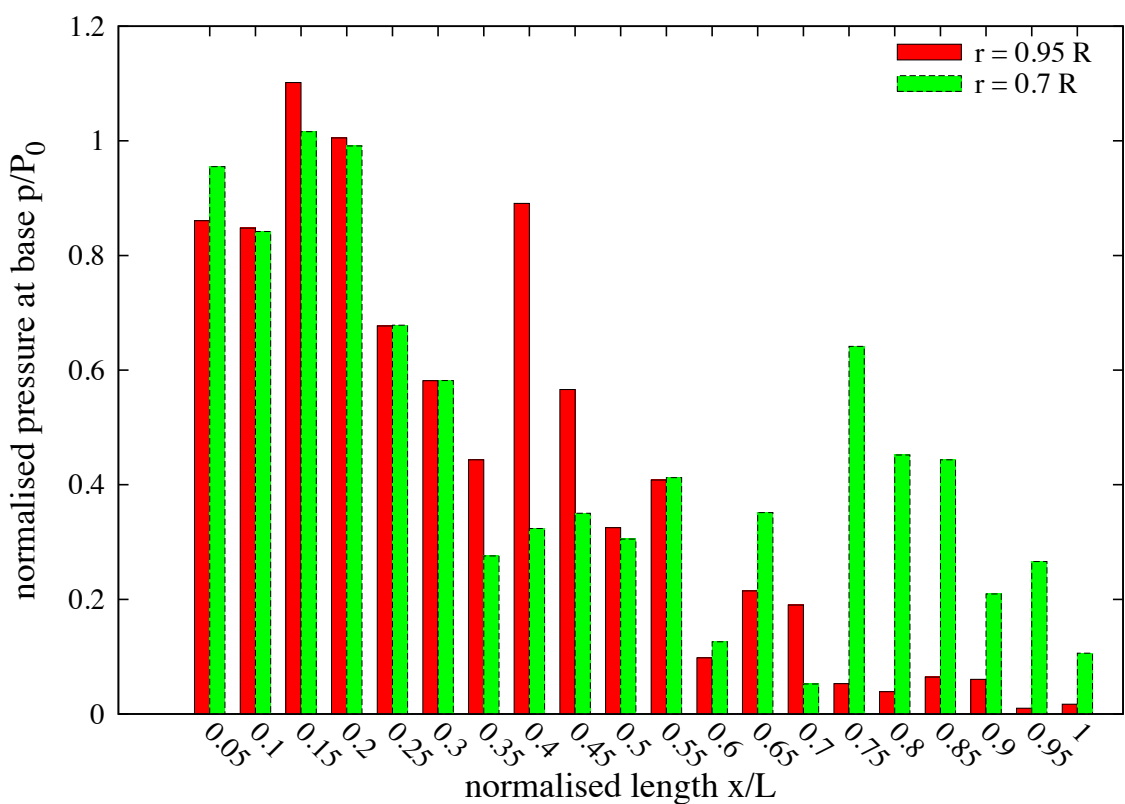
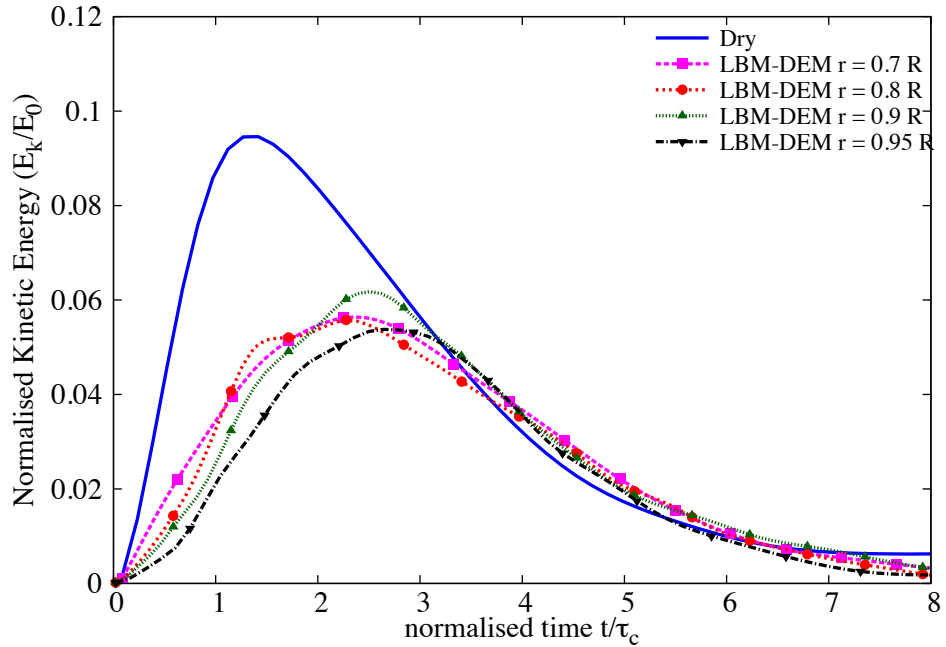
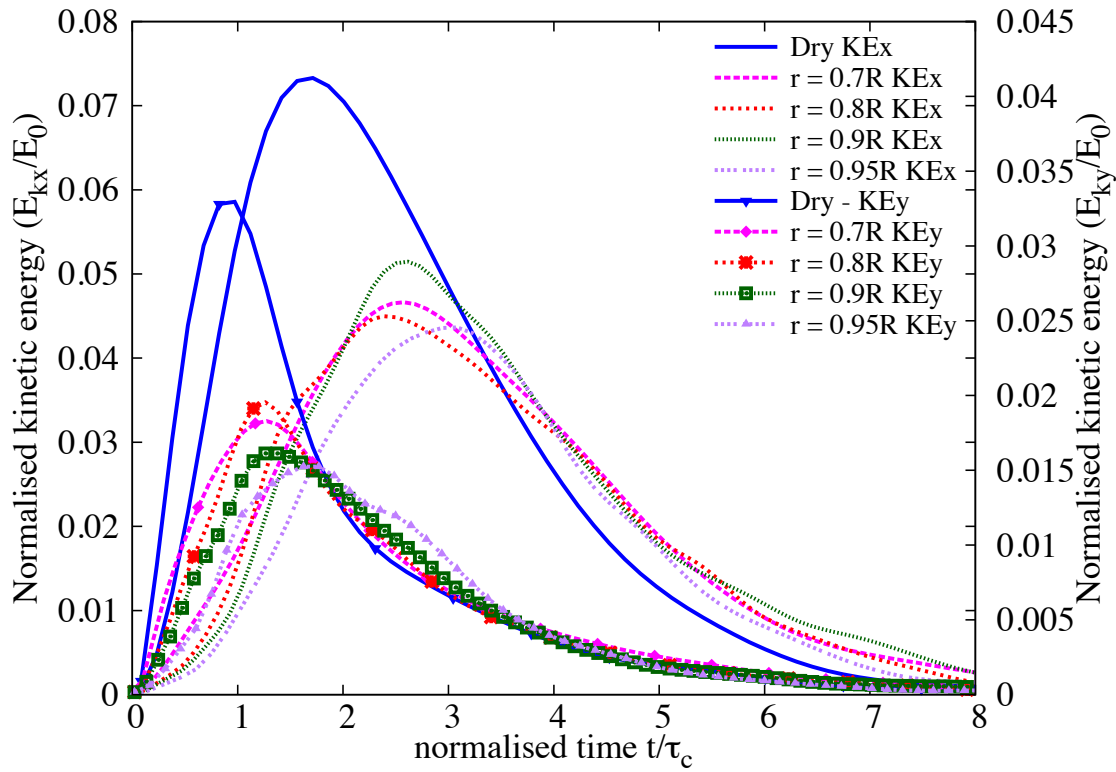


Figure 6.29 Effect of permeability on the normalised effective stress for loose initial packing at  $t = \tau_c$



(a) Evolution of the total kinetic energy



(b) Evolution of horizontal and vertical kinetic energies

Figure 6.30 Effect of permeability on the evolution of kinetic energies with time for a granular column collapse in fluid ( $a = 0.8$  & loose packing)

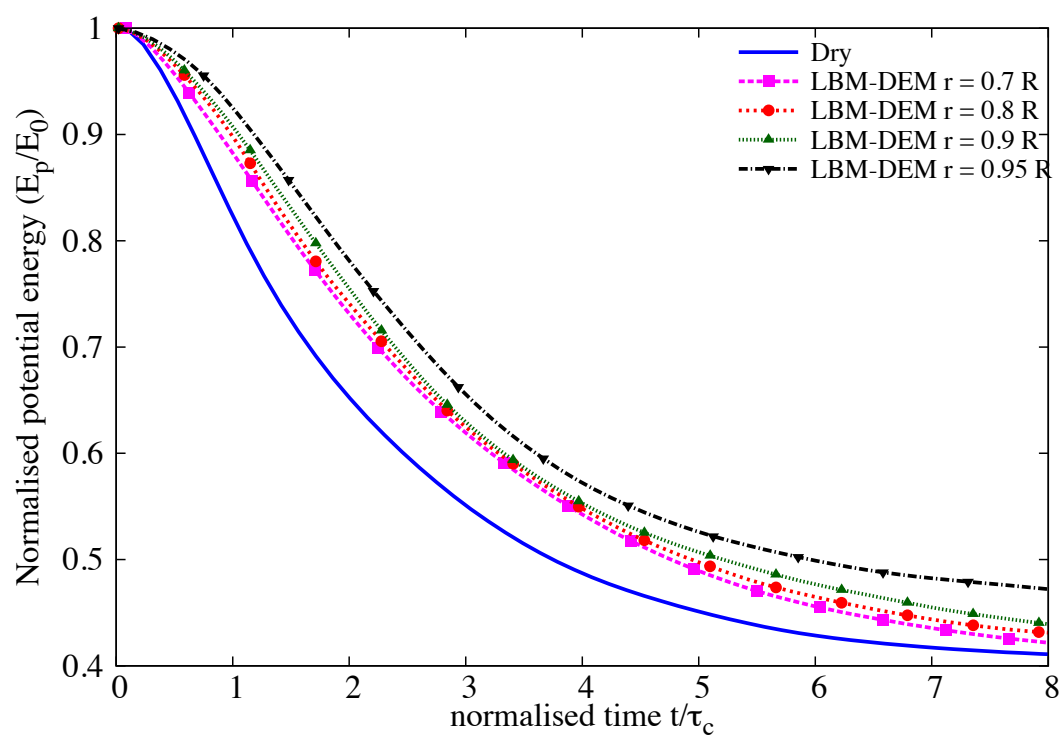


Figure 6.31 Effect of permeability on the evolution of the potential energy with time for a granular column collapse in fluid ( $a = 0.8$  & loose packing)

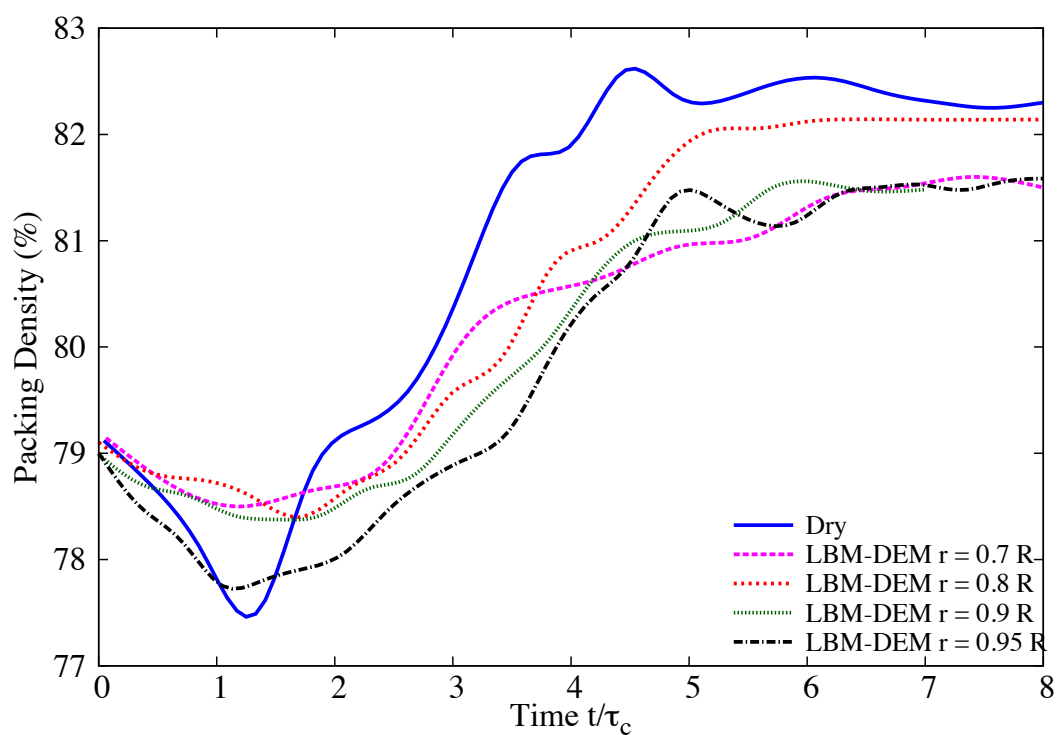
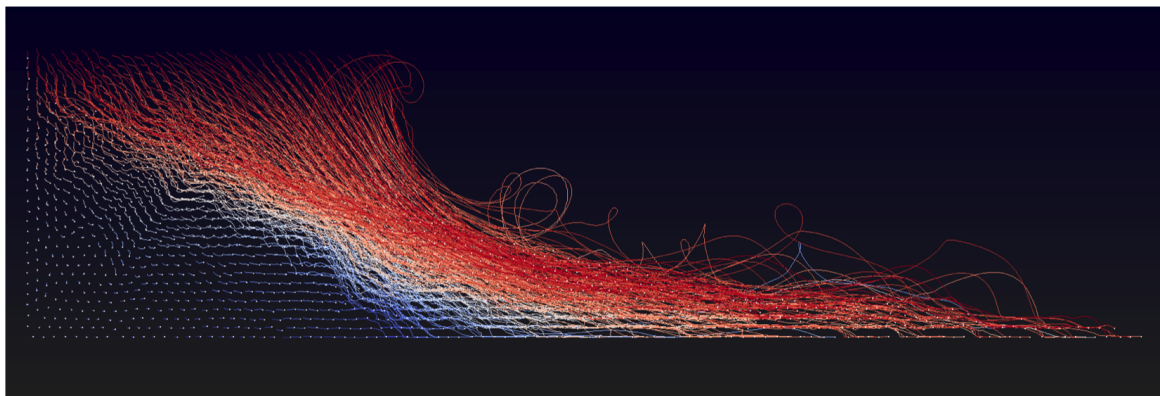
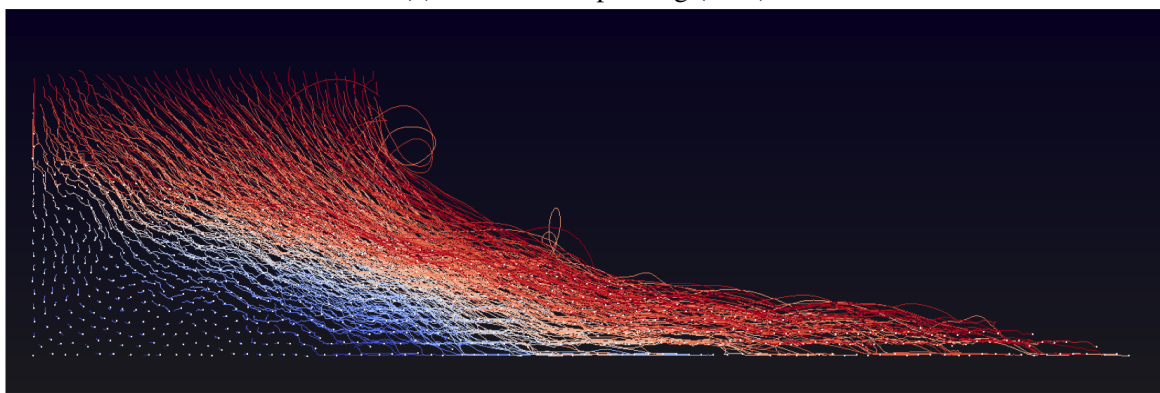


Figure 6.32 Effect of permeability on the evolution of packing density for a granular column collapse in fluid ( $a = 0.8$  & loose initial packing)



(a) Dense initial packing (79%)



(b) Loose initial packing (83%)

Figure 6.33 Effect of initial density on the deposit morphology for a granular column collapse in fluid ( $\alpha = 0.8$ ). Dense vs loose initial packing fraction.



(a) Dense initial packing (83%)



(b) Loose initial packing (79%)

Figure 6.34 Evolution of packing fraction at  $t = \tau_c$  for dense and loose initial packing fraction.

the role of the ambient fluid (Denlinger and Iverson, 2001). In particular, when the solid phase reaches a high volume fraction, it is important to consider the strong heterogeneity arising from the contact forces between the grains, the drag interactions which counteract the movement of the grains, and the hydrodynamic forces that reduce the weight of the solids inducing a transition from dense compacted to a dense suspended flow (Meruane et al., 2010). The case of the collapse in presence of an interstitial fluid has been less studied. In this paper, we study the submarine granular flows in the inclined configuration. We study the effect of permeability, density and slope angle on the run-out evolution.

In this study, a 2D poly-disperse system ( $d_{max}/d_{min} = 1.8$ ) of circular discs in fluid was used to understand the behaviour of granular flows on inclined planes (see ??). The soil column was modelled using 1000 discs of density  $2650 \text{ kg m}^{-3}$  and a contact friction angle of  $26^\circ$ . The collapse of the column was simulated inside a fluid with a density of  $1000 \text{ kg m}^{-3}$  and a kinematic viscosity of  $1 \times 10^{-6} \text{ m}^2 \text{ s}^{-1}$ . The choice of a 2D geometry has the advantage of cheaper computational effort than a 3D case, making it feasible to simulate very large systems. A granular column of aspect ratio ‘a’ of 0.8 was used. A hydrodynamic radius  $r = 0.9R$  was adopted during the LBM computations. Dry analyses were also performed to study the effect of hydrodynamic forces on the run-out distance.

### 6.3.1 Effect of initial density

The morphology of the granular deposits in fluid is shown to be mainly controlled by the initial volume fraction of the granular mass and not by the aspect ratio of the column (Pailha et al., 2008; Rondon et al., 2011). In order to understand the influence of the initial packing density on the run-out behaviour, a dense sand column (initial packing density,  $\Phi = 83\%$ ) and a loose sand column ( $\Phi = 79\%$ ) were used. The granular columns collapse and flow down slopes of varying inclinations ( $2.5^\circ$ ,  $5^\circ$  and  $7.5^\circ$ ).

The evolution of run-out distances for a dense sand column with time in dry and submerged conditions for varying slope inclinations are presented in figure 6.35. The run-out distance is longer in submerged condition than the dry condition for a flow on a horizontal surface. However, with increase in the slope angle the run-out in the fluid decreases.

Dense granular columns in fluid take a longer time to collapse and flow, due to the development of large negative pore-pressure, as the dense granular material dilates during the initial phase of the flow. The morphology of dense granular flows down slopes of varying inclinations at the critical time ( $t = \tau_c = \sqrt{H/g}$ , when the flow is fully mobilised) are shown in figure 6.37.

It can be seen that the viscous drag on the dense column tend to predominate over the influence of hydroplaning on the run-out behaviour. This influence can be observed in the smaller peak kinetic energy for granular column in fluid compared to its dry counterpart

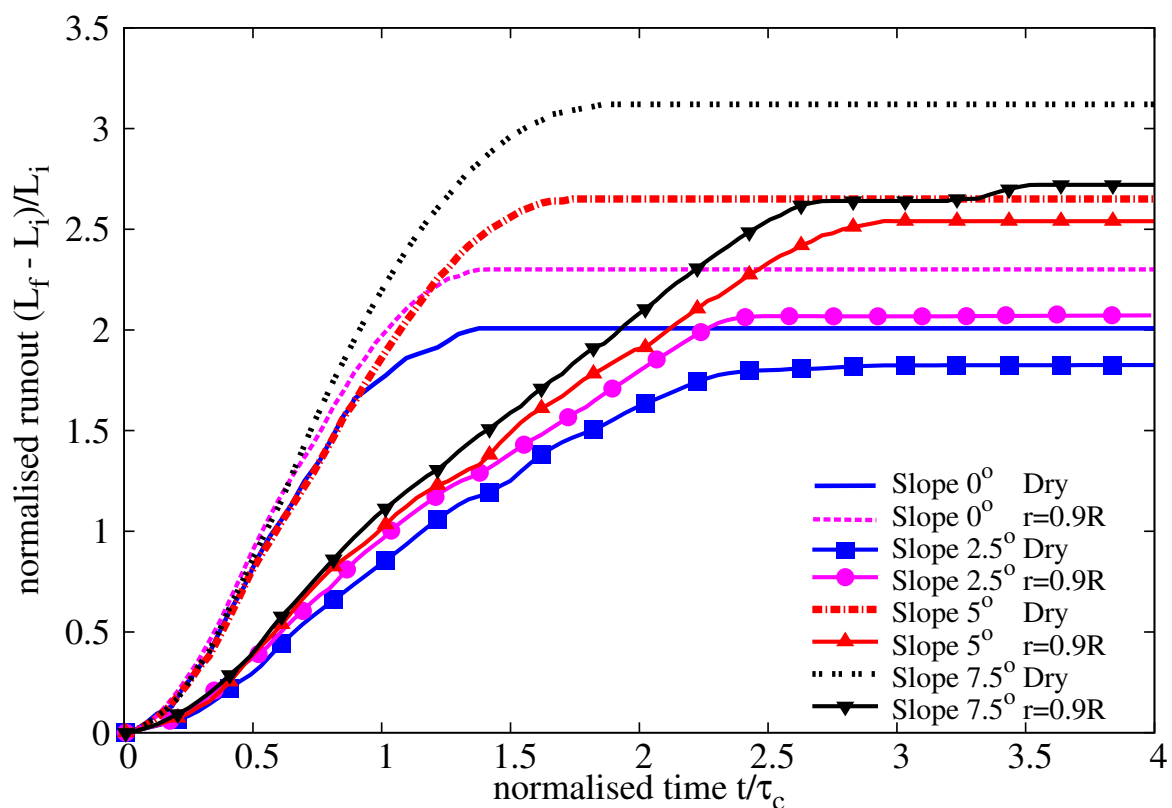


Figure 6.35 Evolution of run-out with time (dense)

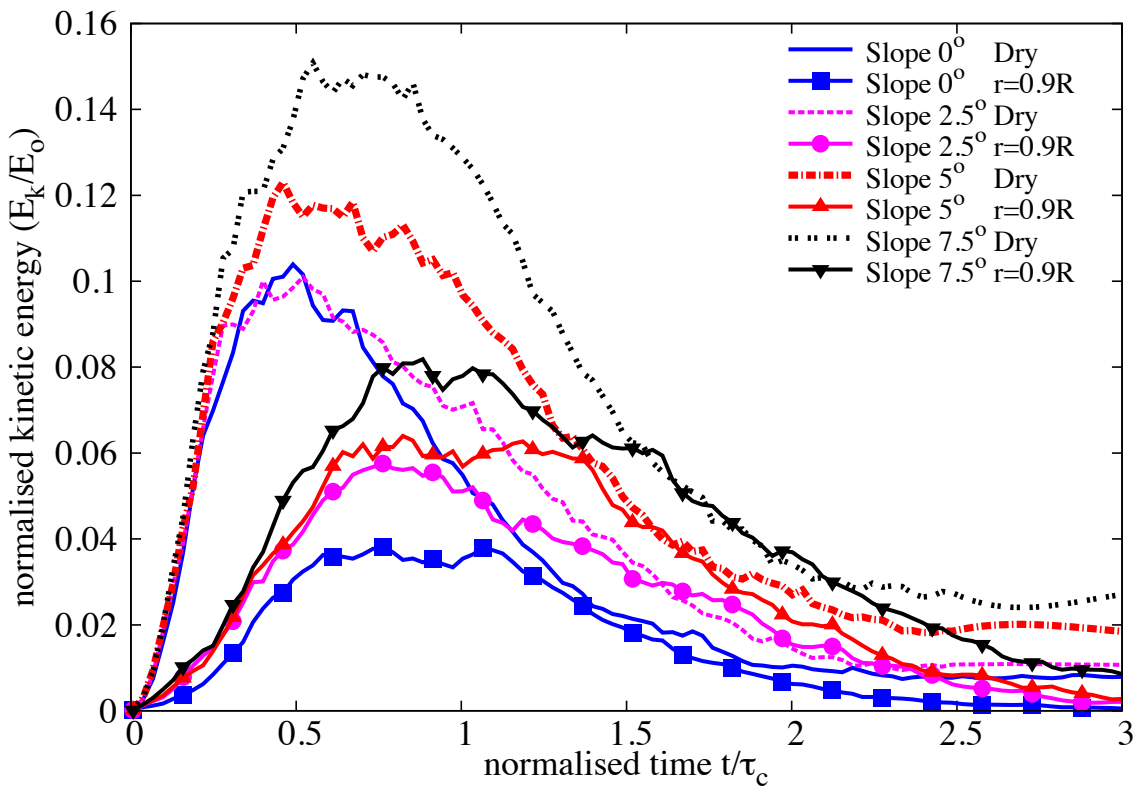


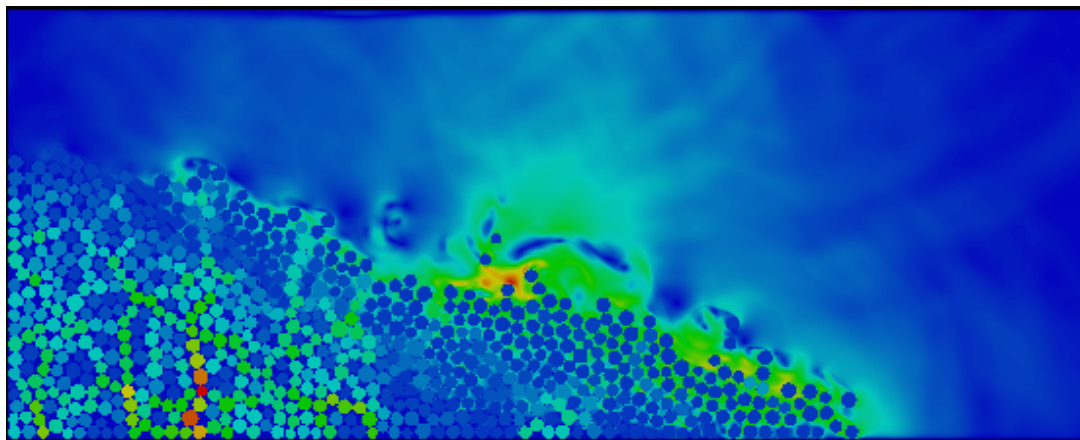
Figure 6.36 Evolution of Kinetic Energy with time (dense case)

(see Figure 6.36). With increase in slope angle, the volume of material that dilates increases. This results in large negative pore pressures and more viscous drag on the granular material. Hence, the difference in the run-out between the dry and the submerged condition, for a dense granular assembly, increases with increase in the slope angle.

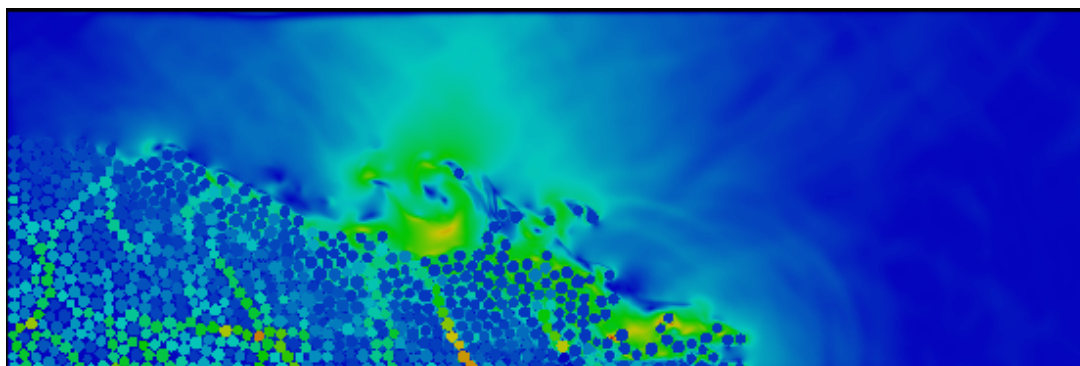
In contrast to the dense granular columns, the loose granular columns (relative density

- <sup>1</sup>  $I_D = 30\%$ ) show longer run-out distance in immersed conditions (see Figure 6.38). The run-out
- <sup>2</sup> distance in fluid increases with increase in the slope angle compared to the dry cases. Loose
- <sup>3</sup> granular material tends to entrain more water at the base of the flow front, creating a lubricating
- <sup>4</sup> surface, which causes longer run-out distance (see Figure 6.39). The hydroplaning effect
- <sup>5</sup> causes an increase in the velocity the loose condition in comparison with the dense condition
- <sup>6</sup> (see Figure 6.40).

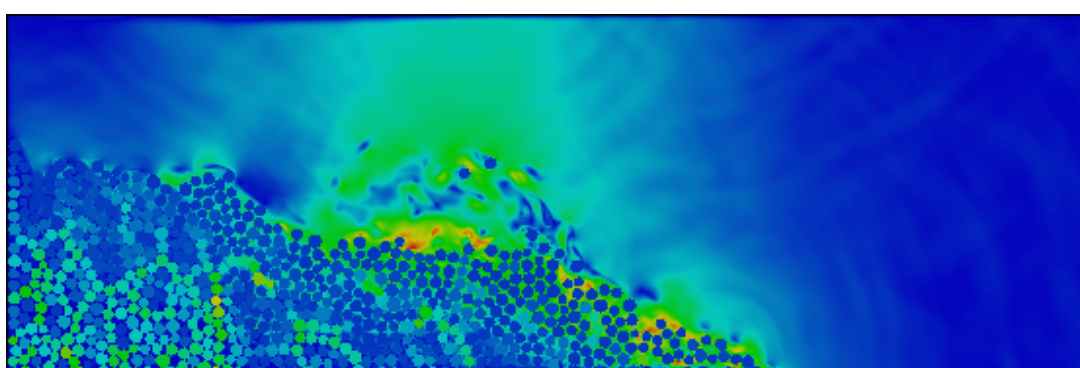
- <sup>7</sup> The evolution of packing density (see Figure 6.41) shows that dense and the loose conditions
- <sup>8</sup> reach similar packing density. This indicates that the dense granular column dilates more and
- <sup>9</sup> is susceptible to higher viscous drag forces. Where as in the loose condition, a positive pore-
- <sup>10</sup> pressure is observed at the base of the flow, indicating entrainment of water at the base, i.e.
- <sup>11</sup> hydroplaning resulting in longer run-out distance.



(a) Slope 2.5



(b) Slope 5.0



(c) Slope 7.5

Figure 6.37 Flow morphology at critical time for different slope angles (dense)

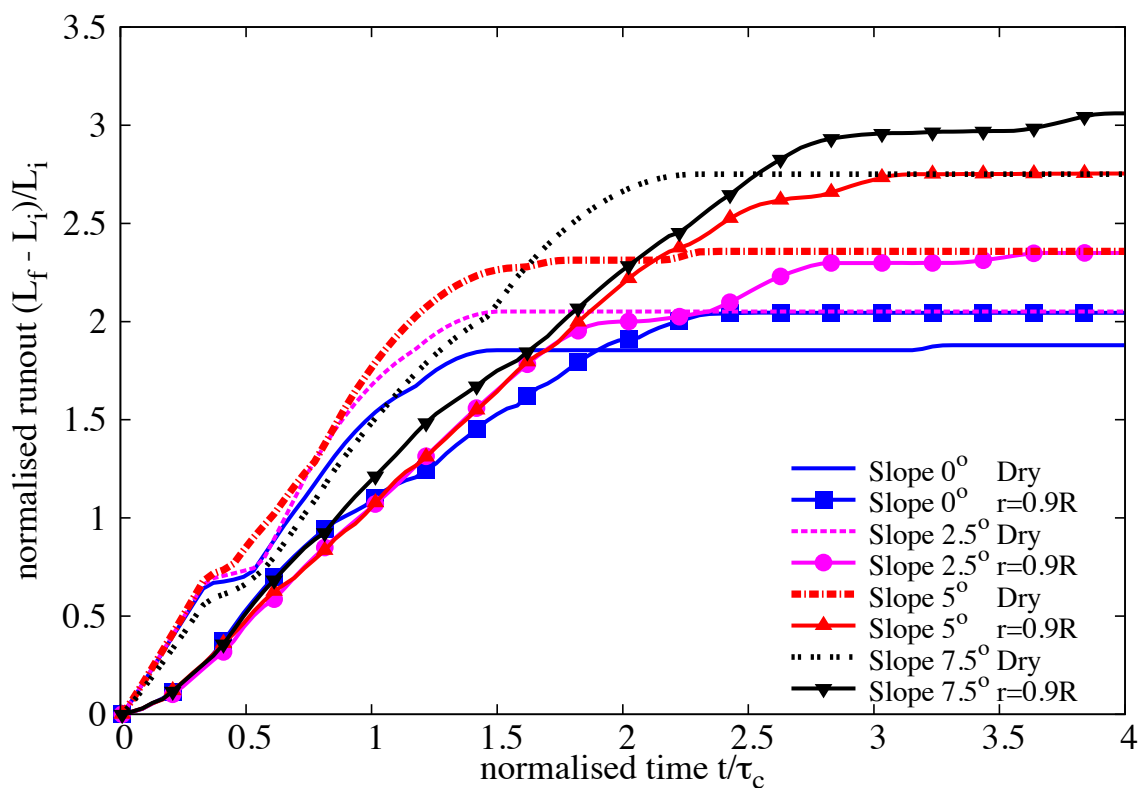
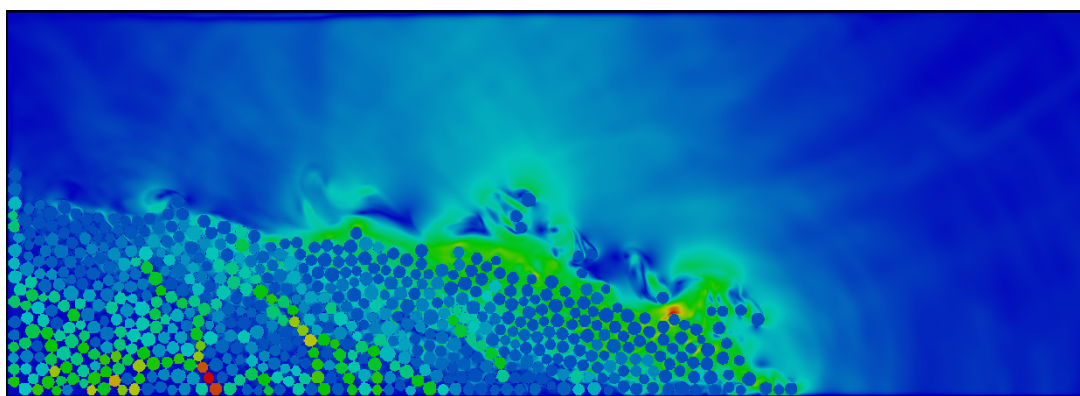
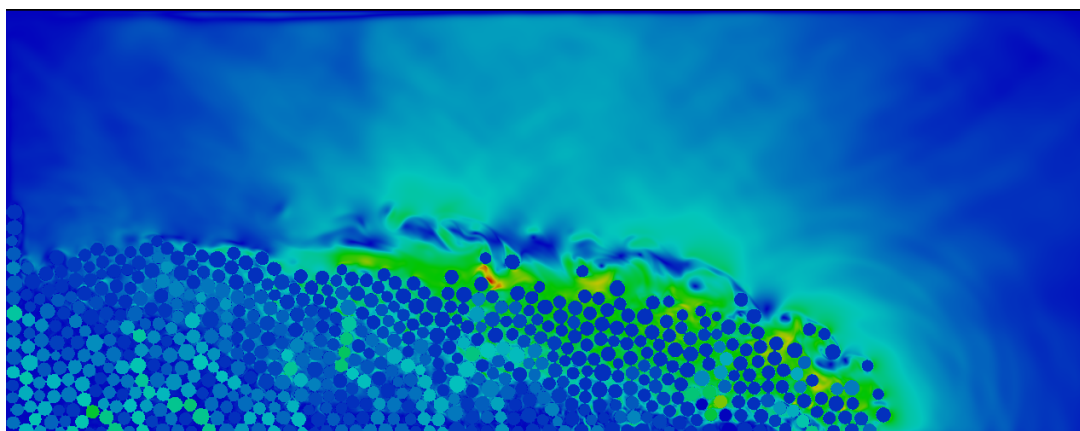


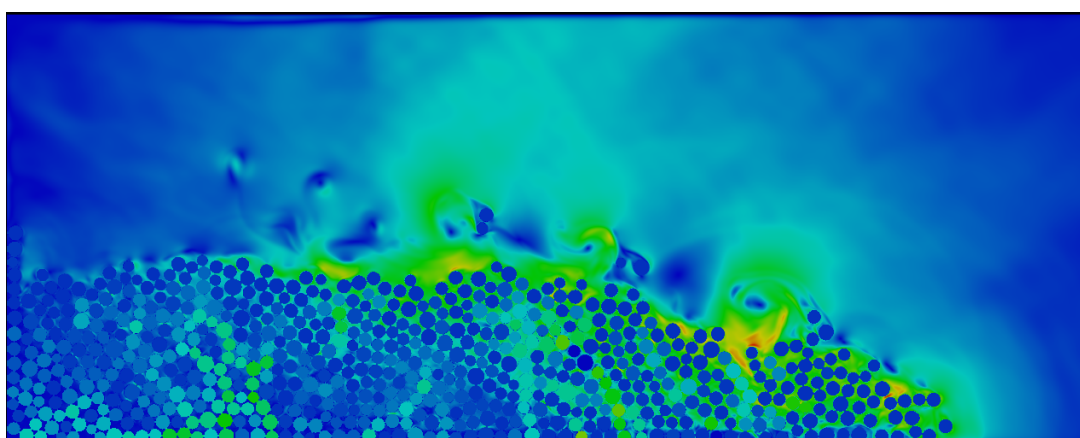
Figure 6.38 Evolution of run-out with time (loose)



(a) Slope 2.5



(b) Slope 5.0



(c) Slope 7.5

Figure 6.39 Flow morphology at critical time for different slope angles (loose)

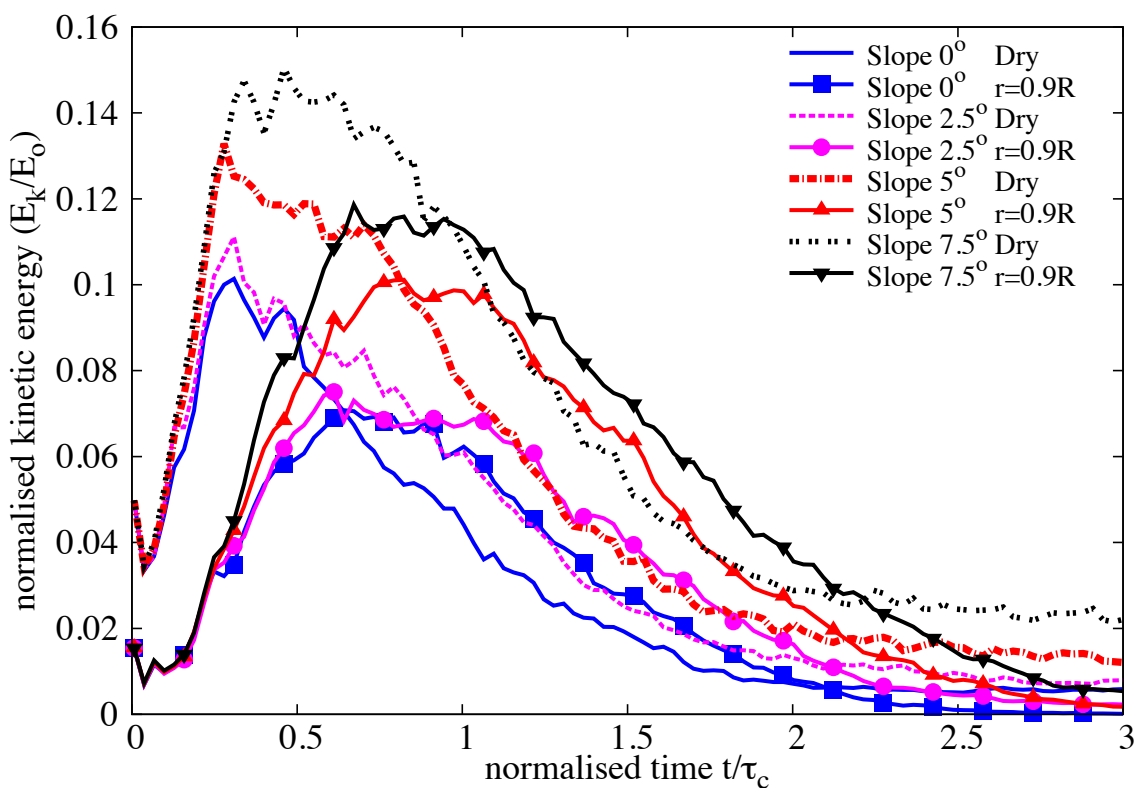


Figure 6.40 Evolution of Kinetic Energy with time (loose)

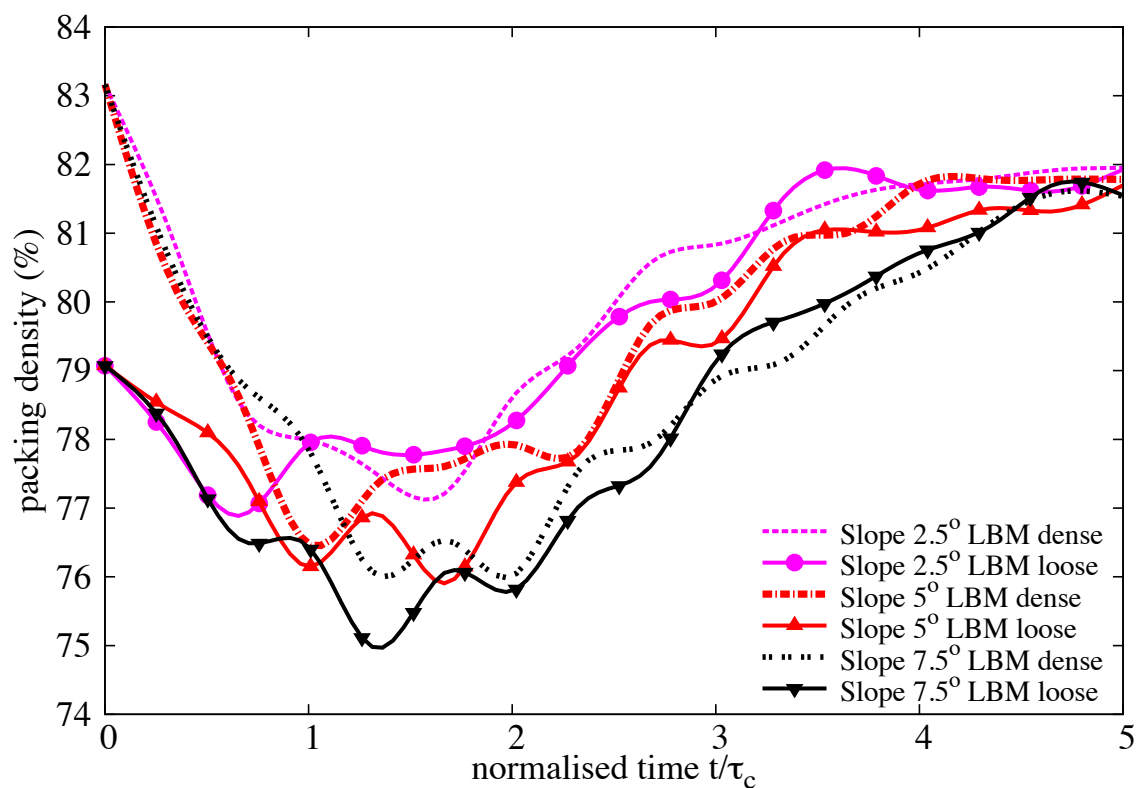


Figure 6.41 Evolution of packing density with time

<sub>12</sub> **6.3.2 Effect of permeability**

<sub>13</sub> In DEM, the grain – grain interaction is described based on the overlap between the grains at the  
<sub>14</sub> contact surface. In a 3D granular assembly, the pore spaces between grains are interconnected.  
<sub>15</sub> Whereas in a 2-D assembly, the grains are in contact with each other that result in a non-  
<sub>16</sub> interconnected pore-fluid space. This causes a no flow condition in a 2-D case. In order to  
<sub>17</sub> overcome this difficulty, a reduction in radius is assumed only during the LBM computation  
<sub>18</sub> phase (fluid and fluid – solid interaction). The reduction in radius allows interconnected pore  
<sub>19</sub> space through which the surrounding fluid can flow. This technique has no effect on the grain –  
<sub>20</sub> grain interactions computed using DEM. See Kumar et al. (2012) for more details about the  
<sub>21</sub> relationship between reduction in radius and permeability of the granular assembly.

<sub>22</sub> For a slope angle of 5°, the hydrodynamic radius of the loosely packed grains was varied  
<sub>23</sub> from  $r = 0.7R$  (high permeability), 0.75R, 0.8R, 0.85R to 0.9R (low permeability). The run-  
<sub>24</sub> out distance is found to increase with decrease in the permeability of the granular assembly  
<sub>25</sub> (see Figure 6.42). The run-out distance for high permeable conditions ( $r = 0.7R – 0.8R$ ) were  
<sub>26</sub> lower than their dry counterparts. Although, decrease in permeability resulted in an increase  
<sub>27</sub> in the run-out distance, no significant change in the run-out behaviour was observed for a  
<sub>28</sub> hydrodynamic radius of up to 0.8R.

<sub>29</sub> With further decrease in permeability ( $r = 0.85R$  and 0.9R), the run-out distance in the fluid  
<sub>30</sub> was greater than the run-out observed in the dry condition. At very low permeability ( $r = 0.9R$ ),  
<sub>31</sub> granular material started to entrain more water at the base, which causes a reduction in the  
<sub>32</sub> effective stress accompanied by a lubrication effect on the flowing granular media. This can be  
<sub>33</sub> seen as a significant increase in the peak kinetic energy and the duration of the peak energy, in  
<sub>34</sub> comparison with dry and high permeable conditions (see Figure 6.44).

<sub>35</sub> The permeability of the granular column did not have an influence on the evolution of  
<sub>36</sub> height during the flow. However, dry granular column tends to collapse more than the immersed  
granular column (see Figure 6.43). 1

<sub>2</sub> Positive pore-pressure generation at the base of the flow was observed for low permeable  
<sub>3</sub> conditions. Inspection of the local packing density showed entrainment of water at the base  
<sub>4</sub> of the flow, which can also be observed by the steep decrease in the packing density (see Fig-  
ure 6.45) for the very low permeability condition ( $r = 0.9R$ ). At the end of the flow ( $t \geq 3 \times \tau_c$ ),  
<sub>5</sub> the excess pore-pressure dissipates and the granular material, irrespective of their permeability,  
<sub>6</sub> reaches almost the same packing density. 7

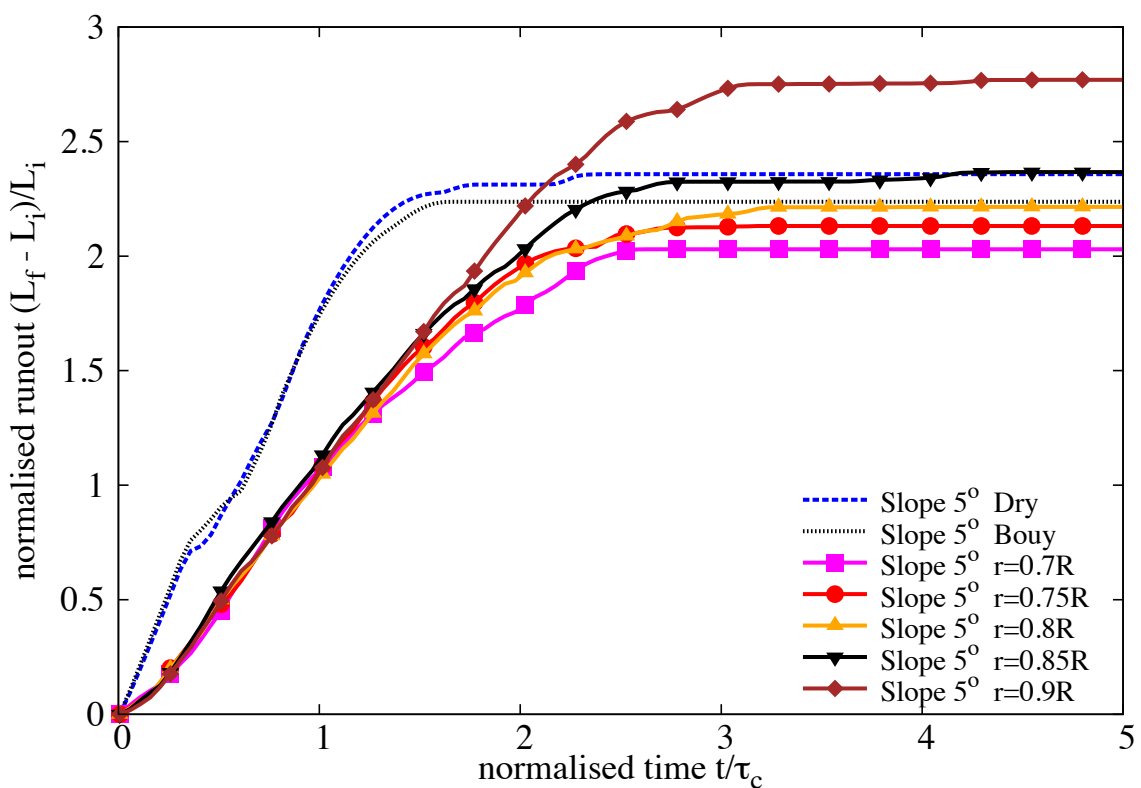


Figure 6.42 Evolution of run-out with time for different permeability (loose slope 5°)

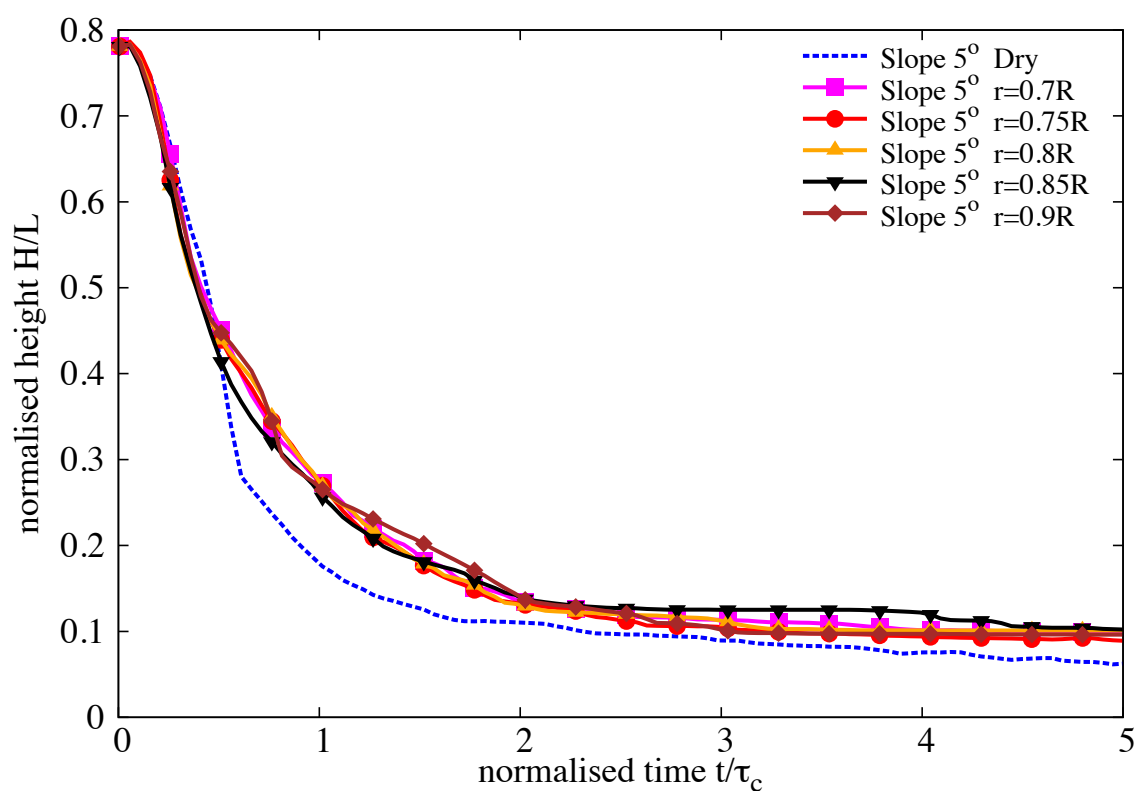


Figure 6.43 Evolution of height with time for different permeability (loose slope  $5^\circ$ )

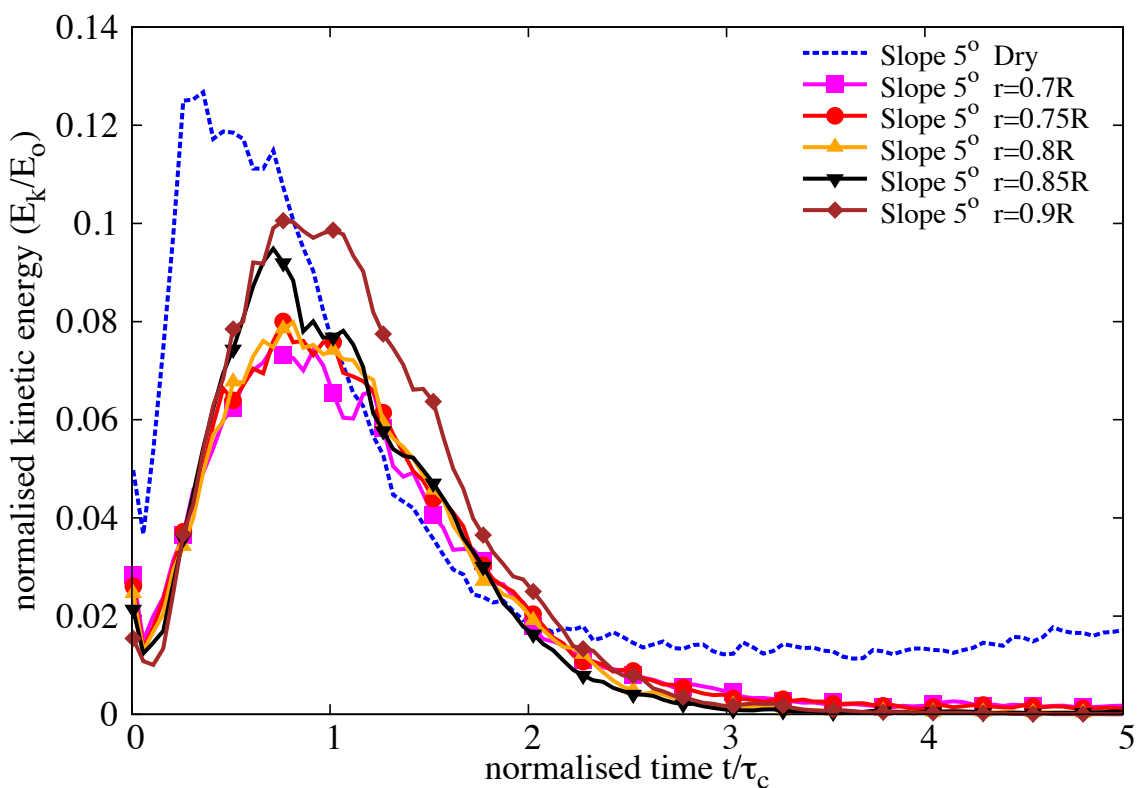


Figure 6.44 Evolution of Kinetic Energy with time for different permeability (loose slope 5°)

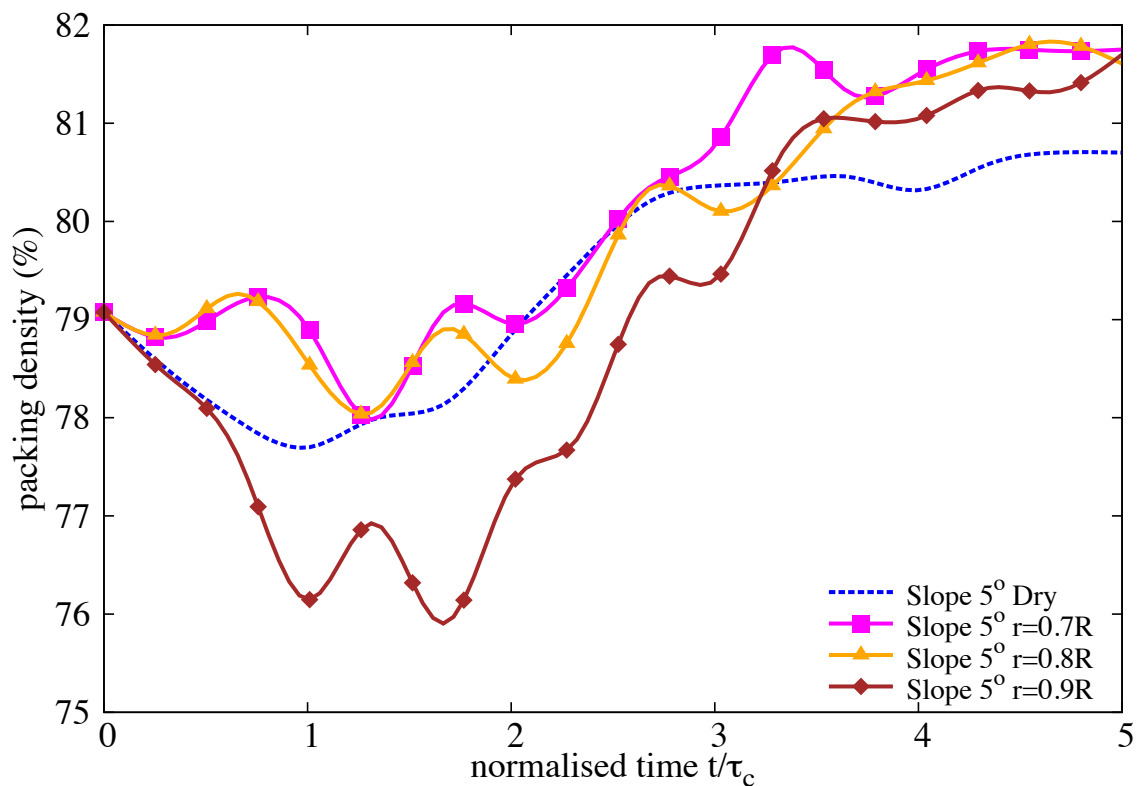


Figure 6.45 Evolution of packing density with time for different permeability (loose slope 5°)

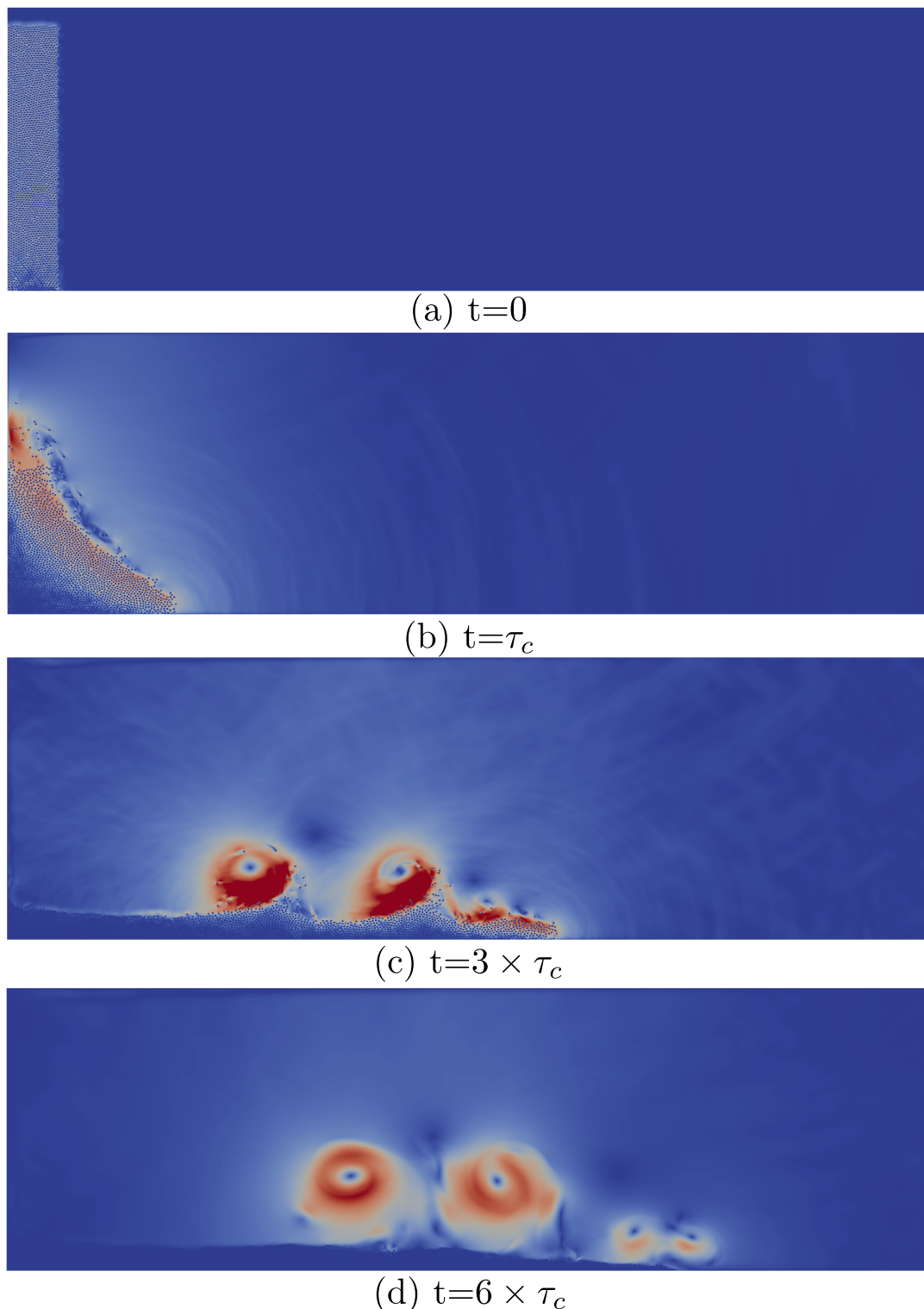
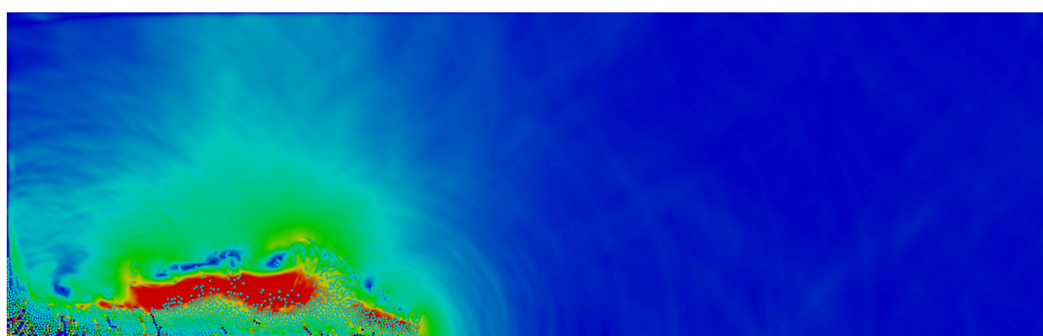


Figure 6.46 Flow evolution of a granular column collapse in fluid ( $a = 6$ ) on a horizontal surface

 $t = 0\tau_c$  $t = 1\tau_c$  $t = 3\tau_c$

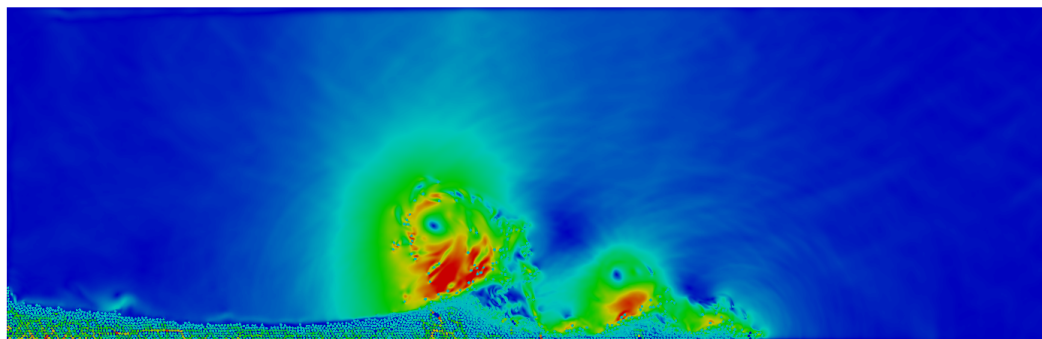
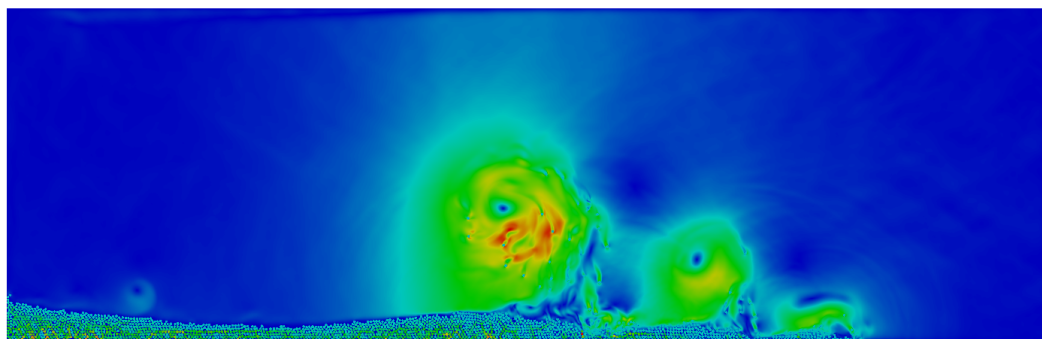
 $t = 6\tau_c$  $t = 8\tau_c$ 

Figure 6.46 Flow evolution of a granular column collapse in fluid ( $a = 6$ ) on a slope of  $5^\circ$ . Shows the velocity profile of fluid due to interaction with the grains (red - higher velocity).

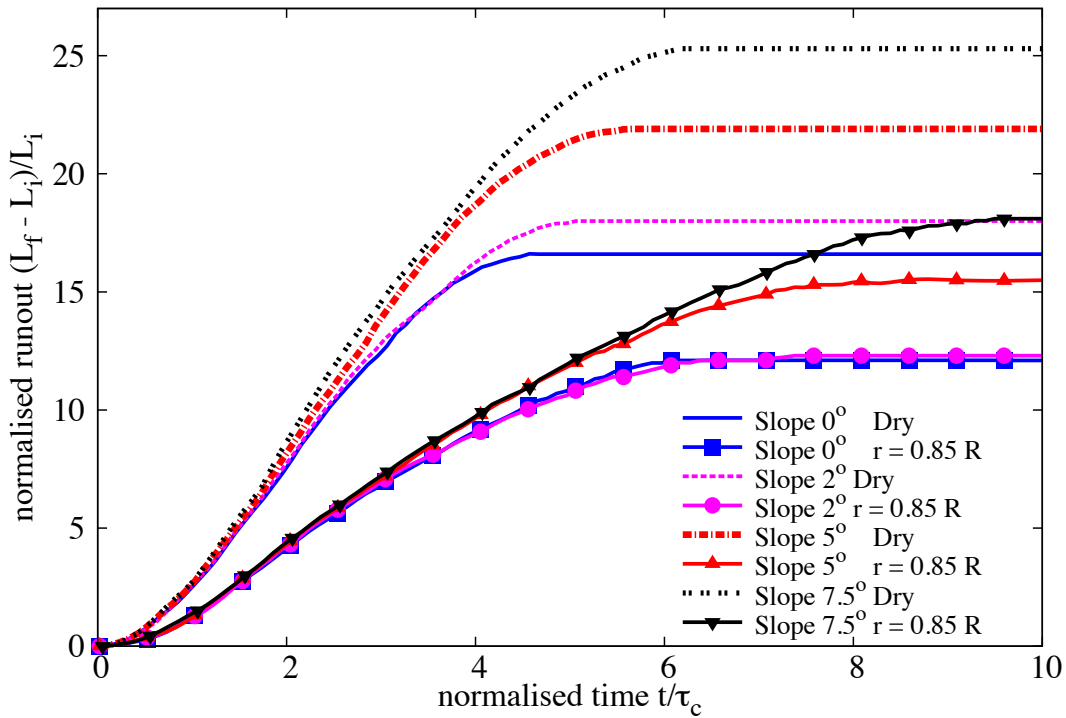


Figure 6.47 Evolution of run-out for a column collapse in fluid ( $a = 6$ ) on a slope of  $5^\circ$

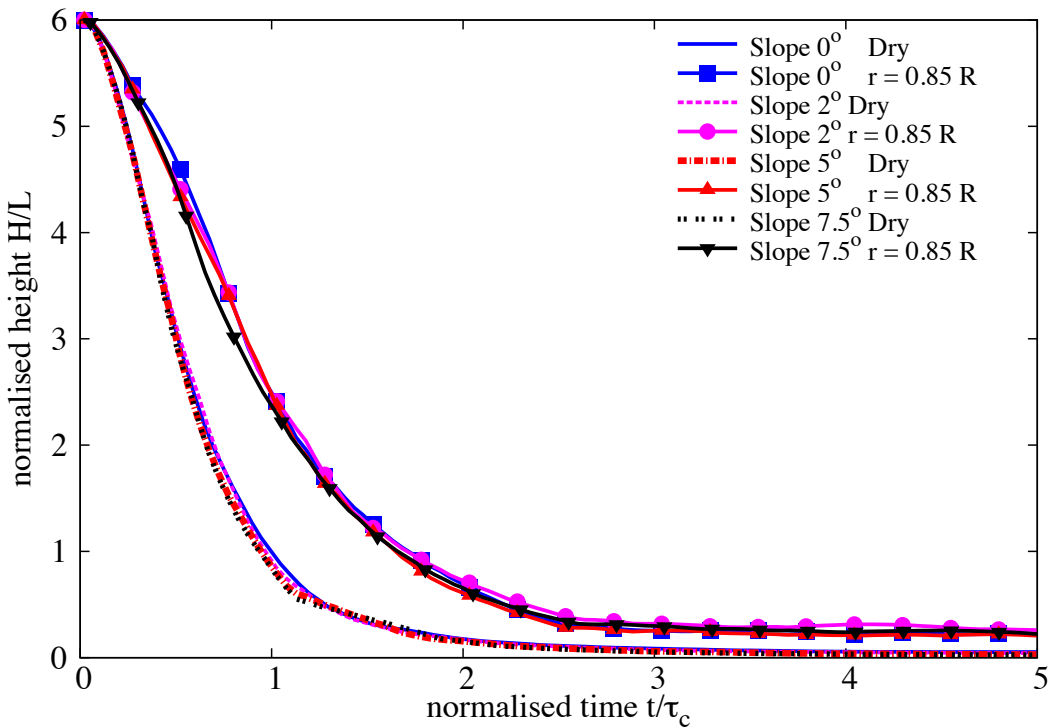
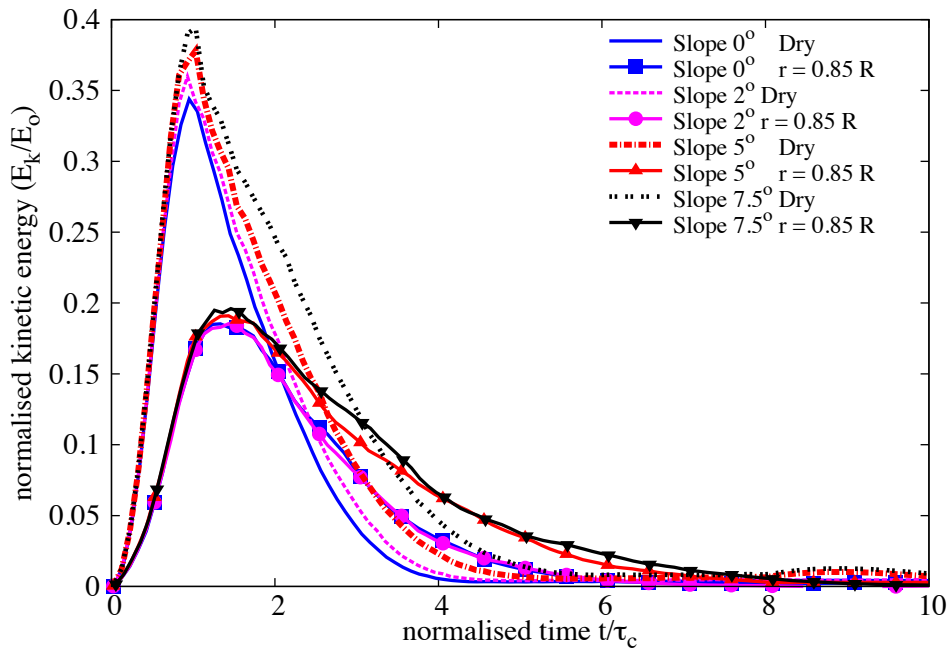
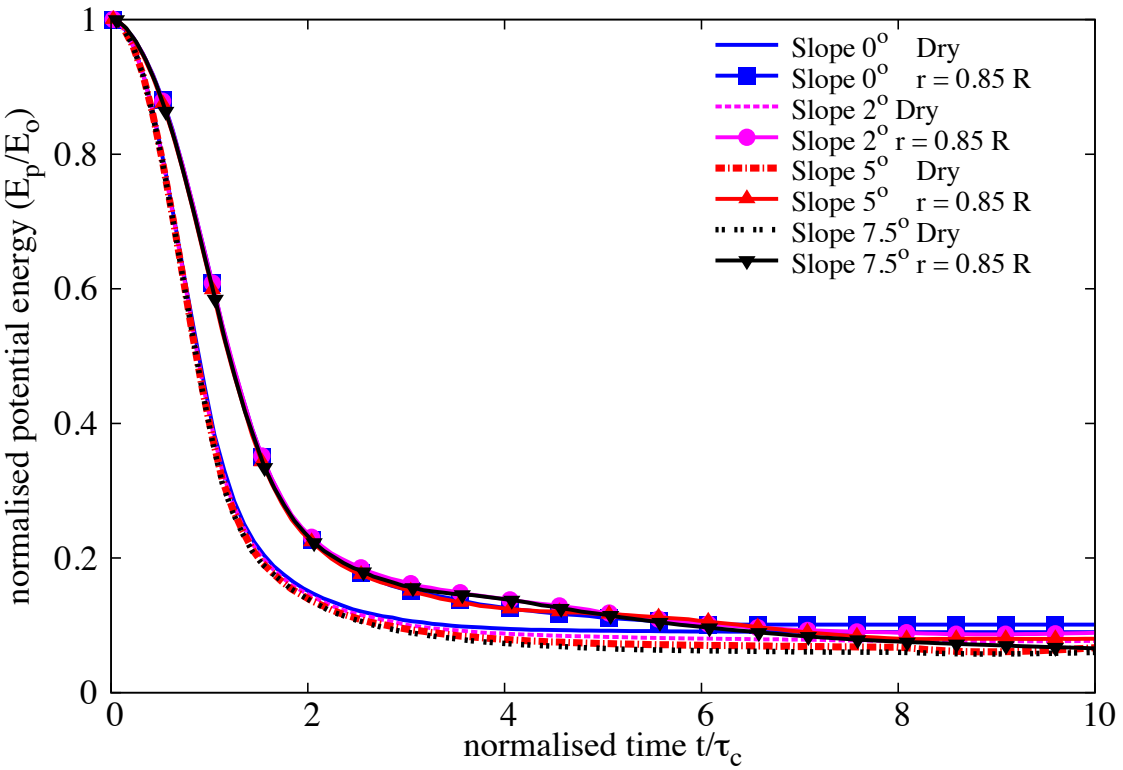


Figure 6.48 Evolution of height with time for a column collapse in fluid ( $a = 6$ ) on a slope of  $5^\circ$

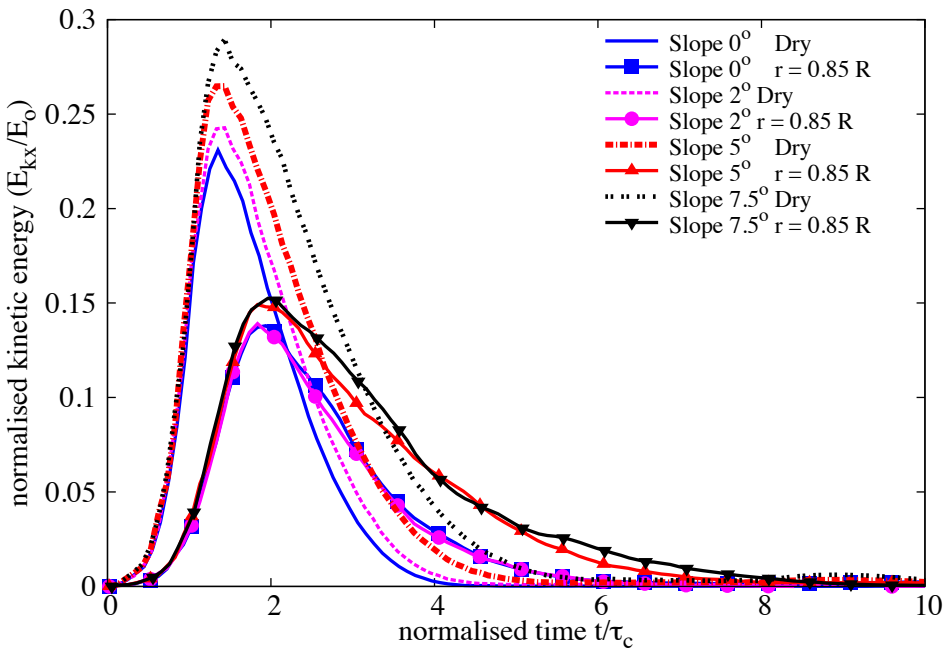


(a) Evolution of the total kinetic energy

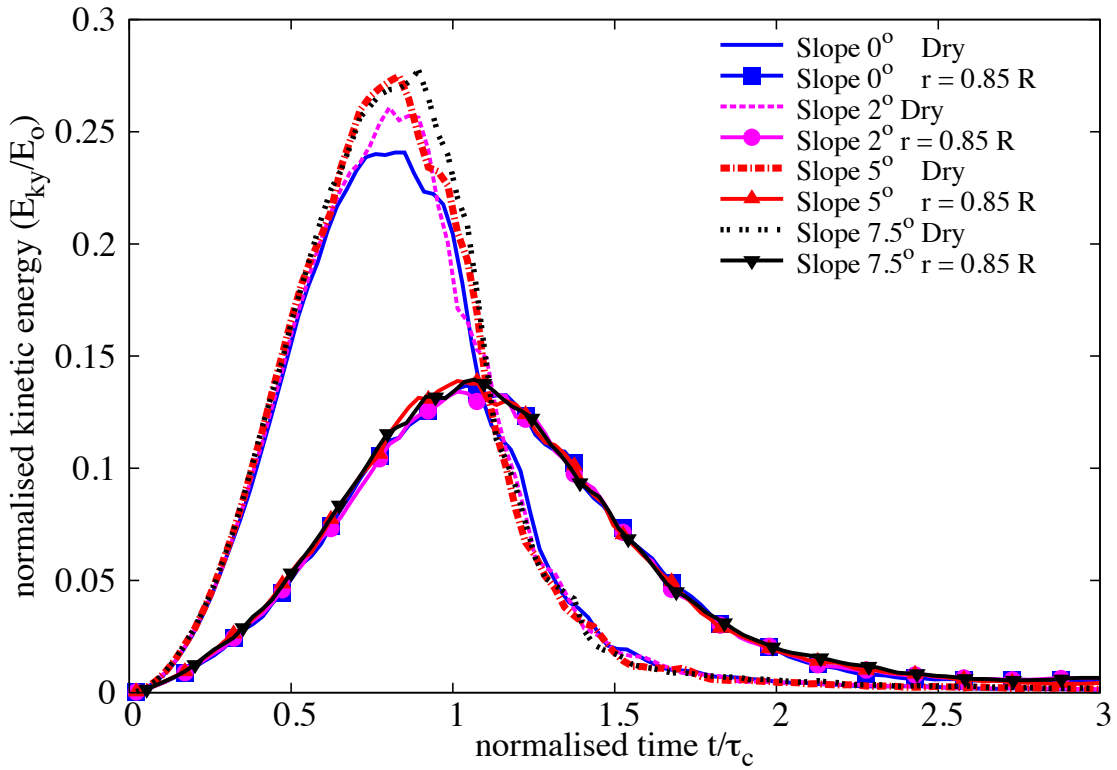


(b) Evolution of the total potential energy

Figure 6.49 Evolution of the kinetic and the potential energy with time for a granular column collapse in fluid ( $a = 6$ ) on a slope of  $5^\circ$



(a) Evolution of the vertical kinetic energy



(b) Evolution of the horizontal kinetic energy

Figure 6.50 Evolution of the kinetic energies with time for a granular column collapse in fluid ( $a = 6$ ) on a slope of  $5^\circ$

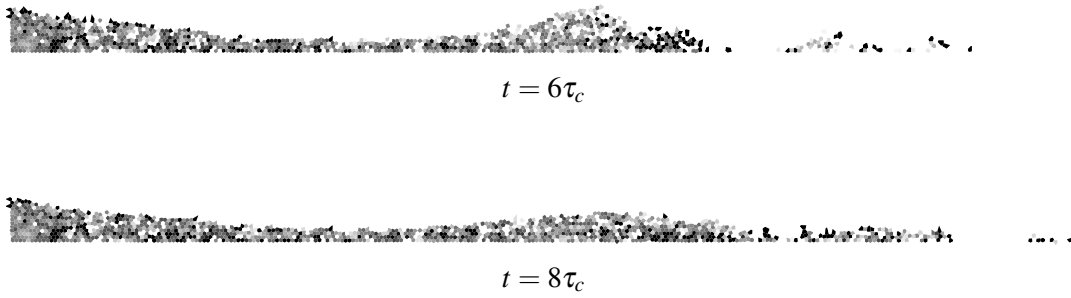


Figure 6.51 Packing density of a granular column collapse in fluid ( $a = 6$ ) on a slope of  $5^\circ$ .

### 6.3.3 Tall columns

#### 6.3.4 Summary

Two-dimensional LB-DEM simulations were performed to understand the behaviour of submarine granular flows. Unlike dry granular collapse, the run-out behaviour in fluid is dictated by the initial volume fraction. Granular columns with loose packing tend to flow longer in comparison to dense columns, due to entrainment of water at the base resulting in lubrication. The loose column when it starts flowing expands and ejects liquid, leading to a partial fluidization of the material. However, with increase in the slope angle, the run-out in fluid is influenced by the viscous drag on the granular materials. The run-out distance in fluid increases with decrease in permeability. More research work is required to characterise the flow behaviour of granular materials, especially in submerged conditions.



# Chapter 7

19

## Conclusions and future work

20

### 7.1 Introduction

21

The Multi-scale modelling of granular flows involves simulating the granular materials in discrete and continuum scales. In the present study, a C++ code has been developed to model the granular materials as discrete-elements using the Discrete Element Method technique. The Material Point Method code, developed in the University of Cambridge, has been adopted to study the flow of granular materials as a continuum. Multi-scale analyses of the collapse of the granular columns with different aspect ratios were performed using continuum and particle-scale approaches. In the present study, the solid-fluid interactions in the Discrete Element approach is modelled by coupling the Lattice Boltzmann Method, a Newtonian fluid solver, with the Discrete Element Method technique. This chapter presents an overview of the future research along with the proposed research schedule. This chapter also presents an outline of the final thesis and the proposed papers based on this research work.

22

23

24

25

26

27

28

29

30

31

32

### 7.2 Recommendations for future research

33

This research work involves the following stages: (1) understanding the limits of the continuum and the discrete-element approaches in modelling the granular flow, and investigating the influence of various microscopic parameters on the macroscopic flow behaviour, (2) understanding the differences in the mechanism of the granular flows in dry and submerged conditions, and (3) Modelling the granular flow behaviour using the  $\mu(I)$  rheology for dry and submerged flow conditions.

34

35

### 5    7.2.1 Multi-scale simulations of granular flows

6    The continuum and discrete-element simulations of the dry and the submerged granular flows  
7    will be performed to understand the differences in their flow mechanism. Multi-scale analyses of  
8    granular flows enable us to understand the limitations of the continuum approach in modelling  
9    large deformation granular flow problems, and help us to identify the micro-scale parameters  
10   responsible for the complex macroscopic behaviour. Multi-scale modelling of the collapse  
11   of a granular columns on a horizontal surface have been performed. Continuum simulations  
12   accurately predict the granular flow behaviour for columns with smaller aspect ratios, however  
13   they fail to capture the dynamics of the flow for columns with larger aspect ratios.

In order to understand the difference in the flow dynamics with increasing aspect ratios,  
further analyses will be performed to study the mechanism of energy dissipation in the particle  
scale, i.e. the evolution of kinetic energy and potential energy with time. A simple mathematical  
relationship based on the initial potential energy of the grains lying above the failure surface  
is being developed to describe the flow dynamics of the granular column collapse problem  
with different aspect ratios. The relationship will enable us to understand the variation in the  
flow dynamics in the continuum and the particle-scale. The continuum description of granular  
column collapse showed non-physical behaviour near the foot of the column, further analyses  
will be carried out to understand the effect of interface properties on the run-out distance.  
Further details on the continuum modelling of granular flow are presented in the next section.  
Micro-scale parameters influencing the flow dynamics will be identified and the influence of  
these parameters on the deposit morphology will be investigated. Multi-scale analysis of large  
deformation flow problem such as flow of dry granular materials down an inclined flume will  
be performed. This analysis will provide an insight on the limits of the continuum approach  
in modelling large deformation problems, which involve large shear-rates. The results from  
the analysis will be compared with the experimental results of Denlinger and Iverson (2001)  
on miniature flume experiments. The influence of parameters, such as particle size, density,  
packing and dilatancy, on the flow dynamics will be explored. These studies will be useful in  
describing the granular flow behaviour using the  $\mu(I)$  rheology.

In order to understand the differences in the mechanism between the dry and the submerged  
granular flows, multi-scale analysis of granular flows in fluid will be performed. In particle-scale  
approach, the Discrete Element Method technique coupled with Lattice Boltzmann approach  
will be adopted to study the collapse of granular columns in fluids. Dynamic fluid-coupling  
in the Material Point Method will be developed to study the behaviour of granular flows in  
fluids. The numerical simulations will be verified with the experimental results of Cassar  
et al. (2005) on immersed granular flows. The effect of packing density of granular material,  
frictional parameters and the viscosity of the fluid on the flow dynamics and the phase-transition

behaviour will also be investigated. The influence of the fluid viscosity on the flow behaviour  
will also be investigated. The variation in the flow dynamic and the deposit morphology for dry  
and submerged granular flows will also be analysed. The parameters that cause a change in the  
flow dynamic between the dry and the submerged flow conditions will be used in extending the  
 $\mu(I)$  rheology for submerged granular flows.

28  
29  
30  
31  
32

### 7.2.2 Developments in Material Point Method

33  
34  
35

The present MPM code is capable of solving the granular flow problems using the Mohr-Coulomb constitutive model. It is also capable of solving seepage problems with static  
1 fluid-solid interface. In the present study, the Material Point Method will be extended to  
2 solve 3D problems and it will be implemented into a standard framework, similar to the Finite  
3 Element framework developed in the University of Cambridge. Constitutive models such as  
4 Nor-Sand and  $\mu(I)$  rheology will be implemented to model the dense granular flows. Modified  
5 Nor-Sand constitutive model ([Robert, 2010](#)) implemented in the present study will be validated  
6 by performing element testing and the results will be verified with the results of ?. The current  
7 MPM code is capable of simulating only small deformation problems, however special attention  
8 is required in modelling large deformation problems, especially those involving two-phase  
9 systems. Objective stress rate such as Jaumann stress rate has been implemented to study large  
10 deformation problems. The dynamic re-meshing technique ([Shin, 2010](#)) will be implemented  
11 to efficiently solve large deformation problems. The dynamic meshing approach is useful for  
12 problems involving motion of a finite size body in unbounded domains, in which the extent of  
13 material run-out and the deformation is unknown a priori. The approach involves searching for  
14 cells that only contain material points, thereby avoiding unnecessary storage and computation.

15 The present fluid coupling algorithm in the MPM involves only static boundaries, and  
conserves the equation of momentum for fluid particles by introducing additional particles  
1 in a cell, when the number of particles decreases. A dynamic solid-fluid interface modelling  
2 in the Material Point Method will be developed. The approach involves the following steps:  
3 identification of the soil particles along the boundary of the current soil domain, obtaining  
4 the nodal numbers for the edges of each soil particle and definition of a new boundary (see  
5 Figure 7.1). The shape of the boundary is approximated by equivalent rectangular grids, similar  
6 to the coupling technique adopted in the discrete-element approach. The procedure is repeated  
7 until the entire boundary is defined. This process is repeated for each time step to simulate the  
8 dynamic boundary behaviour which is common in the case of granular flows in a fluid.  
9

1  
2  
3  
4  
5  
6  
7  
8  
9

10 The MPM code will be extended to include the phase-transition behaviour in a continuum  
domain for partially fluidized granular flows ([Aranson and Tsimring, 2001, 2002; Volfson et al.,](#)  
11 [2003](#)). The theory is based on the hydrodynamics of the flow, coupled with an order parameter

10  
11  
12

equation, which describes the transition between the flowing and the static components of the granular system. The order parameter is defined as a fraction of static contacts among all contacts between particles. The shear stresses in a partially fluidized granular matter is assumed to have two components: the dynamic part that is proportional to the shear strain rate and the strain-independent or the static part. The ratio of these two parts is a function of the order parameter. The relative magnitude of the static shear stress is controlled by the order parameter which varies from 0 in the liquid phase to 1 in the solid phase.

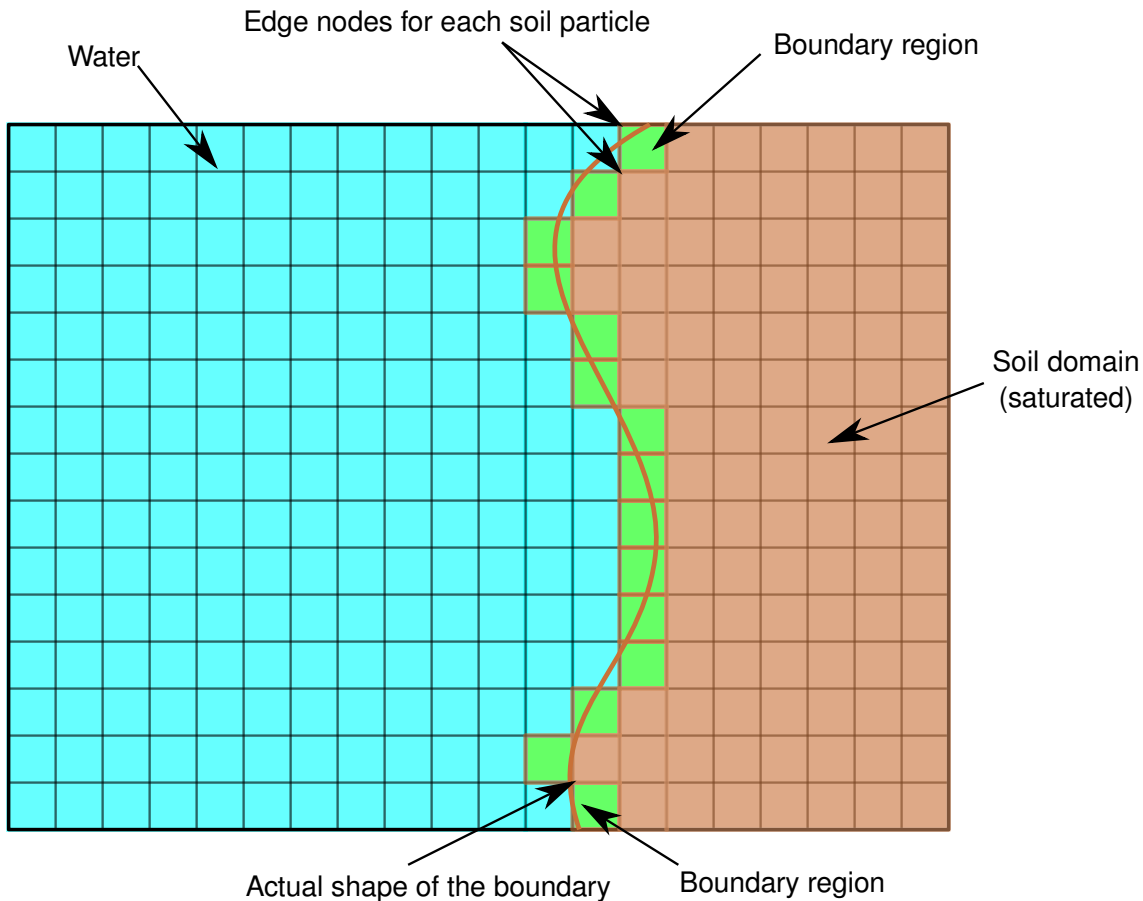


Figure 7.1 Identification of dynamic solid-fluid boundary

### 7.2.3 The I rheology

The  $\mu(I)$  rheology is capable of describing the behaviour of dense granular flows. However, it considers the yield strength as an adjustable rheological property, which contradicts the basic understanding that the strength evolves as the debris-flow motion progresses. Also, the  $\mu(I)$  rheology uses the Mohr-Coulomb constitutive model to describe the yielding of granular materials. In the present study, the evolution of soil strength with time will be considered using

models based on critical state framework. Nor-Sand constitutive model will be implemented in  
26 the present study to describe the plastic flow of granular materials. The  $\mu(I)$  rheology will be  
27 extended to describe the behaviour of granular flows in fluids. In the case of dense granular  
28 flows, the parameter  $I$  is described as the ratio between the time taken for a particle to fall  
29 into the hole,  $t_{micro}$ , and the meantime,  $t_{mean}$ , which is inversely related to the shear rate. If the  
30 velocity of the ambient fluid is low, then the time taken by the particle to fall into a hole, is then  
1 controlled by the viscosity of the ambient fluid (Pouliquen et al., 2005). The  $\mu(I)$  rheology  
2 will be modified to include the effect of fluid viscosity to model granular flows in fluids based  
3 on the parameters identified to control the flow dynamics.  
4

#### 5 7.2.4 Homogenization of granular flows

6 Granular materials are composed of grains in contact, and are therefore discontinuous and  
7 heterogeneous. The macroscopic material properties of these materials are linked to the fabric of  
8 the medium. It is interesting to define the behaviour of granular materials at the macroscopic  
9 scale from characteristics defined at the local scale. This approach has been widely developed  
10 for heterogeneous continuum and is known as the homogenization method. This kind of  
11 approach is different from the phenomenological one, in which the constitutive model is  
12 derived from the general laws of thermodynamics. These phenomenological models introduce  
13 some material parameters whose values are obtained from the simulations performed on  
14 representative volume element. The main objective of the homogenization method is to obtain  
15 a constitutive relation at the scale of a representative volume element, based on the information  
16 on the material behaviour at the micro-scale and the micro-structure. For granular media, the  
17 micro-scale is generally the grain scale. The scale of the representative volume element is of  
18 several orders of magnitude higher. The homogenization process is based on three relations,  
19 a localization operator, a local constitutive law and an averaging operator, see Chapter 6. An  
20 intrinsic difficulty in the case of granular materials arises from the fact that the variables at  
21 the micro-scale and the macro-scale are of different nature. At the micro-scale the material  
22 behaviour is described using vectorial variables such as contact forces, grain displacement and  
23 grain rotation, whereas the macroscopic behaviour law uses tensorial variables (stress tensor,  
24 strain tensor). The micro-polar plasticity constitutive formulation (Suiker et al., 2001) that is  
25 directly related to micro-scale properties, such as contact stiffness, particle density, particle  
26 radius and its micro-structure will be extended to large scale deformation problems which  
27 involves loss or gain of contacts between grains. Discrete Element Method simulations provide  
28 useful insight on the role of contact forces at micro-scale. The macroscopic stress is related  
29 to microscopic contact forces using the virtual work theorem. The microscopic kinematic  
30 variables usually considered are the displacement of the centre of mass of the particle and the

31 ration of the particle. The local phenomena occurring at the micro-scale during the deformation  
32 of granular material are complex. Different approaches have been proposed in the literature  
33 to establish the link between particle-level displacements and macro-scale deformations. The  
34 micro-behaviour is converted into a macroscopic model through the conservation of internal  
35 work. The local constitutive law gives the value of contact forces and the average over the  
sample provides the value of the stress tensor.

1

### 7.2.5 Slope subjected to impact

This work may be pursued along two directions: 1) experimental realization of a similar setup  
with different modes of energy injection and 2) investigating the effect of various particle shapes  
or the presence of an ambient fluid. Although numerical simulations are generally reliable  
with realistic results found in the past studies of steady flows, we believe that the transients are  
more sensitive situations than steady states and the experiments are necessary for checking the  
validation of the results suggested by the simulations. Provided a convenient method is used  
for supplying kinetic energy homogeneously into a pile, our configuration is also interesting  
for the investigation of the behavior of a pile immersed in a viscous fluid.

2

3

4

5

6

7

8

9

10

# References

11

- Abe, K., Soga, K., and Bandara, S. (2013). Material Point Method for Coupled Hydromechanical Problems. *Journal of Geotechnical and Geoenvironmental Engineering*, page 04013033. 12  
13  
14
- Aidun, C., Lu, Y., and Ding, E. (1998). Direct analysis of particulate suspensions with inertia using the discrete Boltzmann equation. *Journal of Fluid Mechanics*, 373(-1):287–311. 15  
16
- Aranson, I. S. and Tsimring, L. S. (2001). Continuum description of avalanches in granular media. *Physical Review E - Statistical, Nonlinear, and Soft Matter Physics*, 64(2 I):203011–203014. 17  
18  
19
- Aranson, I. S. and Tsimring, L. S. (2002). Continuum theory of partially fluidized granular flows. *Physical Review E*, 65(6):061303. 20  
21
- Bagnold, R. (1954). Experiments on a gravity-free dispersion of large solid spheres in a Newtonian fluid under shear. *Proceedings of the Royal Society of London. Series A. Mathematical and Physical Sciences*, 225(1160):49. 22  
23  
24
- Balmforth, N. J. and Kerswell, R. R. (2005). Granular collapse in two dimensions. *Journal of Fluid Mechanics*, 538:399–428. 25  
26
- Bandara, S. (2013). *Material Point Method to simulate Large Deformation Problems in Fluid-saturated Granular Medium*. PhD thesis, University of Cambridge. 27  
28
- Bardenhagen, S. and Kober, E. (2004). The generalized interpolation material point method. *Computer Modeling in Engineering and Sciences*, 5(6):477–496. 29  
30
- Bardenhagen, S. G., Brackbill, J. U., and Sulsky, D. (2000). The material-point method for granular materials. *Computer Methods in Applied Mechanics and Engineering*, 187(3-4):529–541. 31  
32  
33
- Bareschino, P., Lirer, L., Marzocchella, A., Petrosino, P., and Salatino, P. (2008). Self-fluidization of subaerial rapid granular flows. *Powder Technology*, 182(3):323–333. 34  
35
- Bathe, K. and Zhang, H. (2004). Finite element developments for general fluid flows with structural interactions. *International Journal for Numerical Methods in Engineering*, 60(1):213–232. 36  
37
- <sup>2</sup> Bigler, J., Guilkey, J., Gribble, C., Hansen, C., and Parker, S. (2006). A case study: Visualizing material point method data. *Proceedings of Euro Vis 2006*, pages 299–306.
- <sup>3</sup>

- <sup>4</sup> Bonnet, F., Richard, T., and Philippe, P. (2010). Sensitivity to solid volume fraction of  
<sup>5</sup> gravitational instability in a granular medium. *Granular Matter*.
- <sup>6</sup> Breuer, M., Bernsdorf, J., Zeiser, T., and Durst, F. (2000). Accurate computations of the  
<sup>7</sup> laminar flow past a square cylinder based on two different methods: lattice-Boltzmann and  
<sup>8</sup> finite-volume. *Journal of Heat and Fluid Flow*, 21(2):186–196.
- <sup>9</sup> Cambou, B., Jean, M., and Radjaï, F. (2009). *Micromechanics of granular materials*. Wiley-  
<sup>10</sup> ISTE.
- <sup>11</sup> Campbell, C. (1986). The effect of microstructure development on the collisional stress tensor  
<sup>12</sup> in a granular flow. *Acta Mechanica*, 63(1):61–72.
- <sup>13</sup> Campbell, C. and Brennan, C. (1985). Computer simulation of granular shear flows. *Journal*  
<sup>14</sup> *of Fluid Mechanics*, 151:167–88.
- <sup>15</sup> Campbell, C. S. (1990). Rapid Granular Flows. *Annual Review of Fluid Mechanics*, 22(1):57–  
<sup>16</sup> 90.
- <sup>17</sup> Campbell, C. S. (2002). Granular shear flows at the elastic limit. *Journal of Fluid Mechanics*,  
<sup>18</sup> 465:261–291.
- <sup>19</sup> Campbell, C. S. (2006). Granular material flows - An overview. *Powder Technology*,  
<sup>20</sup> 162(3):208–229.
- <sup>21</sup> Capecelatro, J. and Desjardins, O. (2013). An Euler–Lagrange strategy for simulating particle-  
<sup>22</sup> laden flows. *Journal of Computational Physics*, 238(0):1–31.
- <sup>23</sup> Cassar, C., Nicolas, M., and Pouliquen, O. (2005). Submarine granular flows down inclined  
<sup>24</sup> planes. *Physics of Fluids*, 17(10):103301–11.
- <sup>25</sup> Chen, S. and Doolen, G. G. D. (1998). Lattice Boltzmann method for fluid flows. *Annual*  
<sup>26</sup> *review of fluid mechanics*, 30(1):329–364.
- <sup>27</sup> Chen, Z. and Brannon, R. (2002). An evaluation of the material point method. *Sandia National*  
<sup>28</sup> *Laboratories (SAND2002-0482)*.
- <sup>29</sup> Choi, J. (2005). *Transport-limited aggregation and dense granular flow*. PhD thesis.
- <sup>30</sup> Coetzee, C. J., Vermeer, P. A., and Basson, A. H. (2005). The modelling of anchors using  
<sup>31</sup> the material point method. *International Journal for Numerical and Analytical Methods in*  
<sup>32</sup> *Geomechanics*, 29(9):879–895.
- <sup>33</sup> Cook, B., Noble, D., and Williams, J. (2004). A direct simulation method for particle-fluid  
<sup>34</sup> systems. *Engineering Computations*, 21(2/3/4):151–168.
- <sup>35</sup> Coulomb, C. A. (1776). *Essai sur une application des règles de maximis & minimis {à}*  
<sup>36</sup> *quelques problèmes de statique, relatifs à l'architecture*. De l’Imprimerie Royale.
- Crosta, G. B., Imposimato, S., and Roddeman, D. (2009). Numerical modeling of 2-D granular  
step collapse on erodible and nonerodible surface. *J. Geophys. Res.*, 114(F3):F03020.

- Da Cruz, F., Emam, S., Prochnow, M., Roux, J. N., and Chevoir, F. (2005). Rheophysics of dense granular materials: Discrete simulation of plane shear flows. *Physical Review E - Statistical, Nonlinear, and Soft Matter Physics*, 72(2):1–17. 3  
4  
5
- Daerr, A. and Douady, S. (1999). Two types of avalanche behaviour in granular media. *Nature*, 399(6733):241–243. 6  
7
- Daniel, R. C., Poloski, A. P., and Eduardo Saez, A. (2007). A continuum constitutive model for cohesionless granular flows. *Chemical Engineering Science*, 62(5):1343–1350. 8  
9
- Denlinger, R. and Iverson, R. (2001). Flow of variably fluidized granular masses across three-dimensional terrain, ii: Numerical predictions and experimental tests. *J. Geophys. Res.*, 106(B1):553–566. 10  
11  
12
- Du, R., Shi, B., and Chen, X. (2006). Multi-relaxation-time lattice Boltzmann model for incompressible flow. *Physics Letters A*, 359(6):564–572. 13  
14
- Durst, F., Ray, S., Unsal, B., and Bayoumi, O. (2005). The development lengths of laminar pipe and channel flows. *Journal of fluids engineering*, 127:1154. 15  
16
- Estrada, N., Taboada, A., and Radjai, F. (2008). Shear strength and force transmission in granular media with rolling resistance. *Physical Review E*, 78(2):021301. 17  
18
- Feng, Y. T., Han, K., and Owen, D. R. J. (2007). Coupled lattice Boltzmann method and discrete element modelling of particle transport in turbulent fluid flows: Computational issues. *International Journal for Numerical Methods in Engineering*, 72(9):1111–1134. 19  
20  
21
- Forterre, Y. and Pouliquen, O. (2008). Flows of Dense Granular Media. *Annual Review of Fluid Mechanics*, 40(1):1–24. 22  
23
- Fortes, A. (1987). Nonlinear mechanics of fluidization of beds of spherical particles. *Journal of Fluid Mechanics*. 24  
25
- Frisch, U. and Kolmogorov, A. (1995). *Turbulence: the legacy of AN Kolmogorov*. Cambridge University Press. 26  
27
- Girolami, L., Hergault, V., Vinay, G., and Wachs, A. (2012). A three-dimensional discrete-grain model for the simulation of dam-break rectangular collapses: comparison between numerical results and experiments. *Granular Matter*, pages 1–12. 28  
29  
30
- Goldhirsch, I. (2003). Rapid granular flows. *Annual Review of Fluid Mechanics*, 35:267–293. 31
- Grubmuller, H., Heller, H., Windemuth, A., and Schulten, K. (1991). Generalized verlet algorithm for efficient molecular dynamics simulations with long-range interactions. *Molecular simulations*, 6:121–142. 32  
33  
34
- Guilkey, J., Harman, T., Xia, A., Kashiwa, B., and McMurtry, P. (2003). An Eulerian-Lagrangian approach for large deformation fluid structure interaction problems, Part 1: algorithm development. *Advances in Fluid Mechanics*, 36:143–156. 35
- Gumhold, S. (2003). Splatting illuminated ellipsoids with depth correction. volume 2003, pages 245–252. 3
- 4

- 5 Han, K., Feng, Y., and Owen, D. (2007a). Coupled lattice Boltzmann and discrete element  
6 modelling of fluid–particle interaction problems. *Computers & Structures*, 85(11-14):1080–  
7 1088.
- 8 Han, S., Zhu, P., and Lin, Z. (2007b). Two-dimensional interpolation-supplemented and Taylor-  
9 series expansion-based lattice Boltzmann method and its application. *Communications in*  
10 *Nonlinear Science and Numerical Simulationin Nonlinear Science and Numerical Simulation*,  
11 12(7):1162–1171.
- 12 Harlow, F. H. (1964). The particle-in-cell computing method for fluid dynamics. *Computer*  
13 *Methods in Physics*, 3:319–343.
- 14 He, X. and Luo, L. L.-S. (1997a). Theory of the lattice Boltzmann method: From the Boltzmann  
15 equation to the lattice Boltzmann equation. *Physical Review E*, 56(6):6811.
- 16 He, X. and Luo, L.-S. (1997b). A priori derivation of the lattice Boltzmann equation. *Physical*  
17 *Review E*, 55(6):R6333–R6336.
- 18 He, X., Zou, Q., Luo, L. S., and Dembo, M. (1997). Analytic solutions of simple flows and  
19 analysis of nonslip boundary conditions for the lattice Boltzmann BGK model. *Journal of*  
20 *Statistical Physics*, 87(1):115–136.
- 21 Hertz, H. (1882). Über die Berührung fester elastischer Körper. *ournal fur die Reinen und*  
22 *Angewandte Mathematik*, 92:156–171.
- 23 Hogg, A. J. (2007). Two-dimensional granular slumps down slopes. *Physics of Fluids*, 19(9):9.
- 24 Hutter, K., Koch, T., Pluuss, C., and Savage, S. (1995). The dynamics of avalanches of granular  
25 materials from initiation to runout. Part II. Experiments. *Acta Mechanica*, 109(1):127–165.
- 26 Hutter, K., Wang, Y., and Pudasaini, S. P. (2005). The Savage: Hutter Avalanche Model: How  
27 Far Can It be Pushed? *Philosophical Transactions: Mathematical, Physical and Engineering*  
28 *Sciences*, 363(1832):1507–1528.
- 29 Iddir, H. and Arastoopour, H. (2005). Modeling of multitype particle flow using the kinetic  
30 theory approach. *AIChE Journal*, 51(6):1620–1632.
- 31 Igelberger, K., Thurey, N., and Rude, U. (2008). Simulation of moving particles in 3D with the  
32 Lattice Boltzmann method. *Computers & Mathematics with Applications*, 55(7):1461–1468.
- 33 Iverson, R. (2003). The debris-flow rheology myth. pages 303–314.
- 34 Iverson, R. M. (1997). The physics of debris flows. *Rev. Geophys.*, 35(3):245–296.
- 35 Iverson, R. M. (2000). Acute Sensitivity of Landslide Rates to Initial Soil Porosity. *Science*,  
36 290(5491):513–516.
- 37 Jaeger, H., Nagel, S., and Behringer, R. (1996). Granular solids, liquids, and gases. *Reviews of*  
1 *Modern Physics*, 68(4):1259–1273.
- Jean, M. (1999). The non-smooth contact dynamics method. *Computer Methods in Applied*  
2 *Mechanics and Engineering*, 177(3-4):235–257.  
3

- Jenkins, J. T. and Savage, S. B. (1983). A theory for the rapid flow of identical, smooth, nearly elastic, spherical particles. *Journal of Fluid Mechanics*, 130:187–202. 4  
5
- Johnson, A. (1965). *A model for debris flow*. PhD thesis. 6
- Jop, P., Forterre, Y., and Pouliquen, O. (2006). A constitutive law for dense granular flows. 7  
Nature, 441(7094):727–730. 8
- Josserand, C., Lagree, P. Y., and Lhuillier, D. (2004). Stationary shear flows of dense granular 9  
materials: A tentative continuum modelling. *European Physical Journal E*, 14(2):127–135. 10
- Jullien, R., Meakin, P., and Pavlovitch, A. (1992). Random packings of spheres built with 11  
sequential models. *Journal of Applied Physics*, 25:4103. 12
- Kamrin, K. (2008). *Stochastic and deterministic models for dense granular flow*. PhD thesis. 13
- Kamrin, K. (2010). Nonlinear elasto-plastic model for dense granular flow. *International 14  
Journal of Plasticity*, 26(2):167–188. 15
- Kamrin, K., Rycroft, C. H., and Bazant, M. Z. (2007). The stochastic flow rule: a multi- 16  
scale model for granular plasticity. *Modelling and Simulation in Materials Science and 17  
Engineering*, 15(4):S449–S464. 18
- Kerswell, R. (2005). Dam break with Coulomb friction: A model for granular slumping? 19  
*Physics of Fluids*, 17:057101. 20
- Komiwes, V., Mege, P., Meimon, Y., and Herrmann, H. (2005). Simulation of granular flow in 21  
a fluid applied to sedimentation. *Granular Matter*, 8(1):41–54. 22
- Krogh, M., Painter, J., and Hansen, C. (1997). Parallel sphere rendering. *Parallel Computing*, 23  
23(7):961–974. 24
- Kuester, F., Bruckschen, R., Hamann, B., and Joy, K. (2001). Visualization of particle traces in 25  
virtual environments. pages 151–157. 26
- Kumar, K., Soga, K., and Delenne, J.-Y. (2012). *Discrete Element Modelling of Particulate 27  
Media*. Special Publication. Royal Society of Chemistry, Cambridge. 28
- Lacaze, L. and Kerswell, R. R. (2009). Axisymmetric Granular Collapse: A Transient 3D Flow 29  
Test of Viscoplasticity. *Physical Review Letters*, 102(10):108305. 30
- Lacaze, L., Phillips, J. C., and Kerswell, R. R. (2008). Planar collapse of a granular column: 31  
Experiments and discrete element simulations. *Physics of Fluids*, 20(6). 32
- Ladd, A. J. (1994). Numerical simulations of particulate suspensions via a discretized Boltz- 33  
mann equation. Part 1. Theoretical foundation. *Journal of Fluid Mechanics*, 271:285–309. 34
- Ladd, A. J. C. and Verberg, R. (2001). Lattice-Boltzmann Simulations of Particle-Fluid 35  
Suspensions. *Journal of Statistical Physics*, 104(5):1191–1251. 36
- <sup>1</sup> Lajeunesse, E., Mangeney-Castelnau, A., and Vilotte, J. P. (2004). Spreading of a granular  
<sup>2</sup> mass on a horizontal plane. *Physics of Fluids*, 16(7):2371.

- <sup>3</sup> Lajeunesse, E., Monnier, J. B., and Homsy, G. M. (2005). Granular slumping on a horizontal surface. *Physics of Fluids*, 17(10).
- <sup>5</sup> Larrieu, E., Staron, L., and Hinch, E. J. (2006). Raining into shallow water as a description of the collapse of a column of grains. *Journal of Fluid Mechanics*, 554:259–270.
- <sup>7</sup> Lemiale, V., Muhlhaus, H. B., Meriaux, C., Moresi, L., and Hodkinson, L. (2011). Rate effects in dense granular materials: Linear stability analysis and the fall of granular columns. *International Journal for Numerical and Analytical Methods in Geomechanics*, 35(2):293–308.
- <sup>11</sup> Levoy, M. (1988). Display of surfaces from volume data. *Computer Graphics and Applications, IEEE*, 8(3):29–37.
- <sup>13</sup> Li, S. and Liu, W. (2002). Meshfree and particle methods and their applications. *Applied Mechanics Reviews*, 55:1.
- <sup>15</sup> Liu, S. H., Sun, D. A., and Wang, Y. (2003). Numerical study of soil collapse behavior by discrete element modelling. *Computers and Geotechnics*, 30(Compindex):399–408.
- <sup>17</sup> Lo, C. Y., Bolton, M., and Cheng, Y. P. (2009). Discrete element simulation of granular column collapse. In *AIP Conf. Proc. Powders and Grains 2009*, volume 1145 of *6th International Conference on Micromechanics of Granular Media, Powders and Grains 2009*, pages 627–630.
- <sup>21</sup> Lorensen, W. and Cline, H. (1987). Marching cubes: A high resolution 3D surface construction algorithm. *ACM Siggraph Computer Graphics*, 21(4):163–169.
- <sup>23</sup> Lube, G., Huppert, H. E., Sparks, R. S. J., and Freundt, A. (2005). Collapses of two-dimensional granular columns. *Physical Review E - Statistical, Nonlinear, and Soft Matter Physics*, 72(4):1–10.
- <sup>26</sup> Luding, S., Clément, E., and Blumen, A. (1994). Anomalous energy dissipation in molecular-dynamics simulations of grains: The "detachment" effect. *Physical Review*, 50:4113.
- <sup>28</sup> Mangeney, A., Roche, O., and Hungr, O. (2010). Erosion and mobility in granular collapse over sloping beds. *Journal of Geophysical Research*, 115(F3):F03040.
- <sup>30</sup> Mansouri, M., Delenne, J. Y., El Youssoufi, M. S., and Seridi, A. (2009). A 3D DEM-LBM approach for the assessment of the quick condition for sands. *Comptes Rendus Mécanique*, 337(9-10):675–681.
- <sup>33</sup> Meakin, P. and Jullien, R. (1985). Structural readjustment effects in cluster-cluster aggregation. *Journal de Physique*, 46(9):1543–1552.
- <sup>35</sup> Mehta, A. (2011). *Granular Physics*. Cambridge University Press.
- Mehta, A. and Barker, G. (1994). The dynamics of sand. *Reports on Progress in Physics*, 57:383. 1
- Mei, R., Shyy, W., Yu, D., and Luo, L.-S. (2000). Lattice Boltzmann Method for 3-D Flows with Curved Boundary. *Journal of Computational Physics*, 161(2):680–699. 3
- 2
- 4

- Meruane, C., Tamburrino, A., and Roche, O. (2010). On the role of the ambient fluid on gravitational granular flow dynamics. *Journal of Fluid Mechanics*, 648:381–404. 5  
6
- Midi, G. D. R. (2004). On dense granular flows. *European Physical Journal E*, 14(4):341–365. 7
- Mitchell, J. K. and Soga, K. (2005). *Fundamentals of soil behavior*. John Wiley & Sons. 8
- Moreau, J. J. (1993). New computation methods in granular dynamics. In Thornton, C., editor, 9  
*Powders and Grains*, page 227. A. A. Balkema. 10
- Mutabaruka, P. (2013). *Modelisation numerique des milieux granulaires immergés : initiation et propagation des avalanches dans un fluide*. Phd thesis, University of Montpellier 2. 11  
12
- Ng, B. H., Ding, Y., and Ghadiri, M. (2008). Assessment of the kinetic-frictional model for 13  
dense granular flow. *Particuology*, 6(1):50–58. 14
- Noble, D. and Torczynski, J. (1998). A lattice-Boltzmann method for partially saturated 15  
computational cells. *International Journal of Modern Physics C-Physics and Computer*, 16  
9(8):1189–1202. 17
- Obrecht, C. and Kuznik, F. (2011). A new approach to the lattice Boltzmann method for 18  
graphics processing units. *Computers & Mathematics*. 19
- Okada, Y. and Ochiai, H. (2008). Flow characteristics of 2-phase granular mass flows from 20  
model flume tests. *Engineering Geology*, 97(1-2):1–14. 21
- OpenACC-Members (2013). The OpenACC Application Programming Interface Version 2.0 22  
(June, 2013; Corrected: August, 2013). Technical report, OpenMP Standard Group. 23
- Pailha, M., Pouliquen, O., and Nicolas, M. (2008). Initiation of Submarine Granular Avalanches: 24  
Role of the Initial Volume Fraction. *AIP Conference Proceedings*, 1027(1):935–937. 25
- Pan, C., Luo, L., and Miller, C. (2006). An evaluation of lattice Boltzmann schemes for porous 26  
medium flow simulation. *Computers & fluids*, 35(8-9):898–909. 27
- Peker, S. and Helvacı, S. (2007). *Solid-liquid two phase flow*. Elsevier. 28
- Pitman, E. B. and Le, L. (2005). A Two-Fluid Model for Avalanche and Debris Flows. *Philosophical Transactions: Mathematical, Physical and Engineering Sciences*, 363(1832):1573– 29  
1601. 30  
31
- Popken, L. and Cleary, P. W. (1999). Comparison of Kinetic Theory and Discrete Element 32  
Schemes for Modelling Granular Couette Flows. *Journal of Computational Physics*, 155(1):1– 33  
25. 34
- Potapov, A. and Campbell, C. (1996). Computer simulation of hopper flow. *Physics of Fluids*, 35  
8:2884. 36
- <sup>1</sup> Pouliquen, O. (1999). Scaling laws in granular flows down rough inclined planes. *Physics of 37  
Fluids*, 11(3):542–548.
- <sup>3</sup> Pouliquen, O., Cassar, C., Forterre, Y., Jop, P., and Nicolas, M. (2005). How do grains flow: 38  
Towards a simple rheology of dense granular flows.

- <sup>5</sup> Pouliquen, O., Cassar, C., Jop, P., Forterre, Y., and Nicolas, M. (2006). Flow of dense granular  
<sup>6</sup> material: towards simple constitutive laws. *Journal of Statistical Mechanics: Theory and*  
<sup>7</sup> *Experiment*, 2006(07):P07020–P07020.
- <sup>8</sup> Pouliquen, O. and Chevoir, F. (2002). Dense flows of dry granular material. *Comptes Rendus*  
<sup>9</sup> *Physique*, 3(2):163–175.
- <sup>10</sup> Pouliquen, O. and Forterre, Y. (2002). Friction law for dense granular flows: Application to the  
<sup>11</sup> motion of a mass down a rough inclined plane. *Journal of Fluid Mechanics*, 453:133–151.
- <sup>12</sup> Radjai, F. and Dubois, F. (2011). *Discrete-element modeling of granular materials*. ISTE  
<sup>13</sup> Wiley, London; Hoboken, N.J.
- <sup>14</sup> Radjai, F. and Richefeu, V. (2009). Contact dynamics as a nonsmooth discrete element method.  
<sup>15</sup> *Mechanics of Materials*, 41(6):715–728.
- <sup>16</sup> Radjai, F., Schafer, J., Dipple, S., and Wolf, D. (1997). Collective Friction of an Array of  
<sup>17</sup> Particles: A Crucial Test for Numerical Algorithms. *Journal de Physique I*, 7(9):1053–1070.
- <sup>18</sup> Radjai, F., Voivret, C., and McNamara, S. (2011). Discrete-element modelling of granular  
<sup>19</sup> materials. chapter Periodic b, pages 181–198. ISTE Wiley.
- <sup>20</sup> Robert, D. (2010). *Soil-pipeline interaction in unsaturated soil*. PhD thesis.
- <sup>21</sup> Rondon, L., Pouliquen, O., and Aussillous, P. (2011). Granular collapse in a fluid: Role of the  
<sup>22</sup> initial volume fraction. *Physics of Fluids*, 23(7):073301–073301–7.
- <sup>23</sup> Roux, J. and Combe, G. (2002). Quasistatic rheology and the origins of strain. *Comptes Rendus*  
<sup>24</sup> *Physique*, 3(2):131–140.
- <sup>25</sup> Rycroft, C. H., Bazant, M. Z., Grest, G. S., and Landry, J. W. (2006). Dynamics of random  
<sup>26</sup> packings in granular flow. *Physical Review E*, 73(5):051306.
- <sup>27</sup> Rycroft, C. H., Orpe, A. V., and Kudrolli, A. (2009). Physical test of a particle simulation  
<sup>28</sup> model in a sheared granular system. *Physical Review E*, 80(3):031305.
- <sup>29</sup> Savage, S. and Hutter, K. (1991). The dynamics of avalanches of granular materials from  
<sup>30</sup> initiation to runout. Part I: Analysis. *Acta Mechanica*, 86(1):201–223.
- <sup>31</sup> Savage, S. and Jeffrey, D. (1981). The stress tensor in a granular flow at high shear rates.  
<sup>32</sup> *Journal of Fluid Mechanics*, 110(1):255–272.
- <sup>33</sup> Savage, S. and Sayed, M. (1984). Stresses developed by dry cohesionless granular materials  
<sup>34</sup> sheared in an annular shear cell. *Journal of Fluid Mechanics*, 142:391–430.
- <sup>35</sup> Savage, S. B. (1984). The Mechanics of Rapid Granular Flows. *Advances in Applied Mechanics*,  
<sup>36</sup> 24(C):289–366.
- Schaefer, D. G. (1990). Instability and ill-posedness in the deformation of granular materials.  
*International Journal for Numerical and Analytical Methods in Geomechanics*, 14(4):253–  
<sup>1</sup> 278.  
<sup>2</sup>  
<sup>3</sup>

- 
- Schofield, A. and Wroth, P. (1968). *Critical state soil mechanics*. European civil engineering series. McGraw-Hill. 4  
5
- Shin, W. (2010). *Numerical simulation of landslides and debris flows using an enhanced material point method*. PhD thesis. 6  
7
- Smagorinsky, J. (1963). General circulation experiments with the primitive equations. *Monthly weather review*, 91(3):99–164. 8  
9
- Staron, L. and Hinch, E. J. (2005). Study of the collapse of granular columns using two-dimensional discrete-grain simulation. *Journal of Fluid Mechanics*, 545:1–27. 10  
11
- Staron, L. and Hinch, E. J. (2007). The spreading of a granular mass: Role of grain properties and initial conditions. *Granular Matter*, 9(3-4):205–217. 12  
3902
- Staron, L., Radjai, F., and Vilotte, J. P. (2005). Multi-scale analysis of the stress state in a granular slope in transition to failure. *The European physical journal. E, Soft matter*, 18(3):311–20. 3903  
3904  
3905
- Staron, L., Radjai, F., and Vilotte, J.-P. (2006). Granular micro-structure and avalanche precursors. *Journal of Statistical Mechanics: Theory and Experiment*, 2006(07):P07014–P07014. 3906  
3907  
3908
- Steffen, M., Wallstedt, P., Guilkey, J., Kirby, R., and Berzins, M. (2008). Examination and analysis of implementation choices within the material point method. *Computer Modeling in Engineering and Sciences*, 32:107–127. 3909  
3910  
3911
- Succi, S. (2001). *The lattice Boltzmann equation for fluid dynamics and beyond*. Oxford University Press. 3912  
3913
- Succi, S., Foti, E., and Higuera, F. (1989). Three-Dimensional Flows in Complex Geometries with the Lattice Boltzmann Method. *Europhysics Letters (EPL)*, 10(5):433–438. 3914  
3915
- Suiker, A., De Borst, R., and Chang, C. (2001). Micro-mechanical modelling of granular material. Part 1: Derivation of a second-gradient micro-polar constitutive theory. *Acta mechanica*, 149(1):161–180. 3916  
3917  
3918
- Sukop, M. and Thorne, D. (2006). *Lattice Boltzmann modeling: An introduction for geoscientists and engineers*. Springer Verlag. 3919  
3920
- Sulsky, D., Chen, Z., and Schreyer, H. (1994). A particle method for history-dependent materials. *Computer Methods in Applied Mechanics and Engineering*, 118(1-2):179–196. 3921  
3922
- Sulsky, D., Zhou, S.-J., and Schreyer, H. L. (1995). Application of a particle-in-cell method to solid mechanics, volume 87. 3923  
3924
- Sun, X., Sakai, M., and Yamada, Y. (2013). Three-dimensional simulation of a solid–liquid flow by the DEM–SPH method. *Journal of Computational Physics*, 248(0):147–176. 3925  
3926
- Thompson, E. L. and Hupper, H. E. (2007). Granular column collapses: Further experimental results. *Journal of Fluid Mechanics*, 575:177–186. 3927  
3928

- Topin, V., Dubois, F., Monerie, Y., Perales, F., and Wachs, A. (2011). Micro-rheology of dense particulate flows: Application to immersed avalanches. *Journal of Non-Newtonian Fluid Mechanics*, 166(1-2):63–72. 3929
- Topin, V., Monerie, Y., Perales, F., and Radjai, F. (2012). Collapse Dynamics and Runout of Dense Granular Materials in a Fluid. *Physical Review Letters*, 109(18):188001. 3930  
3931
- Utili, S., Zhao, T., and Houslsby, G. (2014). 3D DEM investigation of granular column collapse: Evaluation of debris motion and its destructive power. *Engineering Geology*. 3934  
3935
- Verlet, L. (1967). Computer "Experiments" on Classical Fluids. I. Thermodynamical Properties of Lennard-Jones Molecules. *Phys. Rev.*, 159(1):98. 3936  
3937
- Vold, M. J. (1959). A numerical approach to the problem of sediment volume. *Journal of Colloid Science*, 14(2):168–174. 3938  
3939
- Volfson, D., Tsimring, L. S., and Aranson, I. S. (2003). Partially fluidized shear granular flows: Continuum theory and molecular dynamics simulations. *Physical Review E*, 68(2):021301. 3940  
3941
- Wang, L., Guo, Z., and Mi, J. (2014). Drafting, kissing and tumbling process of two particles with different sizes. *Computers & Fluids*. 3942  
3943
- Ward, S. and Day, S. (2002). Suboceanic landslides. In 2002 Yearbook of Science and Technology. McGraw-Hill, 349:352. 3944  
3945
- Warnett, J. M., Denissenko, P., Thomas, P. J., Kiraci, E., and Williams, M. A. (2013). Scalings of axisymmetric granular column collapse. *Granular Matter*, 16(1):115–124. 3946  
3947
- Willis, A., Peixinho, J., Kerswell, R., and Mullin, T. (2008). Experimental and theoretical progress in pipe flow transition. *Philosophical Transactions of the Royal Society A: Mathematical, Physical and Engineering Sciences*, 366(1876):2671. 3948  
3949  
3950
- Wolfe, M. (2012). PGInsider August 2012: OpenACC Kernels and Parallel Constructs. 3951
- Xiong, Q., Madadi-Kandjani, E., and Lorenzini, G. (2014). A LBM–DEM solver for fast discrete particle simulation of particle–fluid flows. *Continuum Mechanics and Thermodynamics*. 3952  
3953  
3954
- Xu, H., Louge, M., and Reeves, A. (2003). Solutions of the kinetic theory for bounded collisional granular flows. *Continuum Mechanics and Thermodynamics*, 15(4):321–349. 3955  
3956
- Yazdchi, K., Srivastava, S., and Luding, S. (2011). Microstructural effects on the permeability of periodic fibrous porous media. *International Journal of Multiphase Flow*. 3957  
3958
- Yu, D., Mei, R., Luo, L., and Shyy, W. (2003). Viscous flow computations with the method of Lattice Boltzmann equation. *Progress in Aerospace Sciences*, 39(5):329–367. 3959  
3960
- Yu, H., Girimaji, S., and Luo, L. (2005). Lattice Boltzmann simulations of decaying homogeneous isotropic turbulence. *Physical Review E*, 71(1):016708. 3961  
3962
- Zenit, R. (2005). Computer simulations of the collapse of a granular column. *Physics of Fluids*, 17(Compendex):031703–1–031703–4. 3963  
3964

---

References

## 253

- Zhang, Y. and Campbell, C. S. (1992). The interface between fluid-like and solid-like behaviour in two-dimensional granular flows. *Journal of Fluid Mechanics*, 237:541–568. 3965  
3966
- Zhong, Q. and Olson, M. (1991). Finite element–algebraic closure analysis of turbulent separated-reattaching flow around a rectangular body. *Computer methods in applied mechanics and engineering*, 85(2):131–150. 3967  
3968  
3969
- Zhou, H., Mo, G., Wu, F., Zhao, J., Rui, M., and Cen, K. (2012). GPU implementation of lattice Boltzmann method for flows with curved boundaries. *Computer Methods in Applied Mechanics and Engineering*, 225-228(null):65–73. 3970  
3971  
3972
- Ziegler, D. (1993). Boundary conditions for Lattice Boltzmann simulations. *Journal of Statistical Physics*, 71(5):1171–1177. 3973  
3974
- Zou, Q. and He, X. (1997). On pressure and velocity boundary conditions for the Lattice Boltzmann BGK model. *Physics of Fluids*, 9(6):1591–1598. 3975  
3976